Multivariate analysis for lepton identification at CDF

March 2010

Mina Yoshida

A dissertation submitted
in partial fulfillment of the requirements
for the Degree of Master in Science

Graduate School of Science

Osaka City University

Abstract

We search for the neutral higgs production associated with the W boson using hight-p_T like-sign (LS) dilepton events. It is important to distinguish real and fake leptons in this search because fake leptons are one of major backgrounds in the LS dilepton events. At CDF, we usually use cut-based identification (ID) methods for the lepton selection in analyses involving high-p_T physics processes, but given that higgs searches are difficult mainly due to small predicted production cross sections, it is worth to consider more sophisticated lepton selections. This note describes the lepton ID using a likelihood method for electrons or muons. The method combines the probability distribution functions (PDFs) of various lepton ID variables into a likelihood function. We compare efficiencies of the likelihood-based ID with those of the cut-based ID using signal and background samples to estimate improvements. We look at 3 types of signal control samples: Z decays, photon conversions (for electrons), and higgs Monte Carlo (MC) samples, while the background (fake lepton) control samples are inclusive jet data. For the same efficiencies of leptons from Z decays as the cut-based ID, the signal-to-background ratios are found to be improved by factors of 3.8–9.6 for electrons and 1.3–1.9 for muons, depending on the p_T, using the signal PDFs created from Z decays themselves. Using the same PDFs, the efficiency for electrons is increased by a factor of about 1.3, while it is about 1.1 for muons, for the same fake-lepton efficiencies. Our likelihood-based ID is confirmed to be better than the cut-based method for leptons, especially electrons, from Z decays. For the selection of leptons in higgs MC events, the PDFs created from higgs MCs showed better performance than the PDFs by Z events. We try the similar analysis using Boosted decision tree method for electron. The background reduction using Boosted decision tree is better than the likelihood-based method for the Z selection, but we didn't see significant improvements from likelihood method for the higgs selection.

Acknowledgments

I would like to thank everybody for a few years for a constant support and encouraged me. This thesis could not have been completed without the support and encouragement of countless people.

First of all, I would like to than Prof. Toru Okusawa for his excellent education from my undergraduate days. He taught carefully and kindly the basics of elementary particle physics and gave me the precious opportunity to work at the CDF experiment and his great generosity. I am deeply thankful to Prof. Yoshihiro Seiya. He always encourged me providing suggestions and useful comments for this analysis and so on. I was very impressed with his dedicated attitude toward high energy physics and his kindness. I would like to express thanks to Prof. Kazuhiro Yamamoto. He give me advised the physical ideas and offered comfortable study environment. I really enjoyed staying at Fermilab with you. I also would like to thank Dr. Takayuki Wakisaka and Dr. Atunari Hamaguchi. They provided me with a lot of useful advices and gave me clear answers to my questions. I wish to thank members of the Osaka City University high energy physics group for their continuous help. They are very kind and friendly to me. I enjoyed the discussion, lunch and dinner parties and exercises with them.

Finally, I would like to thank my family. They provided me the financial support, and grateful encouragement.

Thank you so much!!

Contents

List of Figures

List of Tables

Chapter 1

Introduction

What's the origin of mass?

Isaac Newton said in his book "Philosophiae naturalis principia mathematica" [1] at 1687,

$$\boldsymbol{F} = m\boldsymbol{a}.$$

It means that mass (m) indicates a physical quantity which is degree of acceleration ($\boldsymbol{a}$) when a boby are applied a force ($\boldsymbol{F}$).

Albert Einstein said in his papers [2, 3] at 1905,

$$E = mc^2.$$

It shows mass-energy equivalence where c is the speed of light in a vacuum.

However now we have understood the mass in sense of physical quantity by their excellent achievements, we do not konw why there is the mass. Particle physics have understood various fundamental physicial picutures in our world. The knowlege will extend the grasp of mass.

Now, Human may be in a ground they can know the origin of mass.

1.1 The standard model

Standard Model (SM) is one of particle physics theories based on gauge field theory which is invariance under the gauge transformation, and extremely well describes the phenomena and properties of the elementary particles which was tested by various experiments. The SM can form three gauge field theories in the framework, the three gauge field theories are "Quantum Electrodynamics (QED)", "Quantum Chromodynamics (QCD)" and "Weak theory". The QED describes the electromagnetic

interaction between charged particles based on $U(1)$ gauge group, the QCD describes the strong interaction between quarks and gluons based on $SU(3)_C$ gauge group, and the Weak theory describes weak interaction where in the nuclei based on $SU(2)$ gauge group. In particular, the QED and the Weak theory are unified in the SM framework as $SU(2)_L \otimes U(1)_Y$ gauge theory. In addition, the "Higgs Mechanism" amazingly plays to give "Mass" to a particle with keeping the gauge invariance in the theory. However, a particle is needed for the mechanism, which is called Higgs boson, the Higgs boson is undiscovered yet experimentally.

1.1.1 Elementary particles in the standard model

In the SM, there are mainly 2 types elementary particles, so-called "Fermion" and "Boson", respectively. The Fermions construct matters in the universe, while the Bosons mediate forces between the elementary particles. The visible complex matters in this world are made up of them. This following section describes the elementary particles in some detail.

Fermion

A particle called Fermion obeys the "Pauli Exclusion Principle", i.e. it has half-integral spin. In the SM, the Fermions are classified into six leptons and six quarks. The three of the six leptons are charged lepton, which are "electron", "muon", and "tau", they have different mass, respectively, however its spin, weak isospin, and electric charge are same. The remaining three leptons have no electric charge so-called "neutrino", they have a lepton flavor (lepton number) same as corresponding charged lepton, when electron has $+1$ electron number, the corresponding neutrino so-called "electron neutrino" has $+1$ electron number.

The three of the six quarks have $2/3$ electric charge, so-called "up", "charm", and "top" quark respectively, they are collectively called "up-type quark" while the other three quarks is $-1/3$ electric charge called "down", "strange", and "bottom", collectively "down-type quark". They also have color charge which is source of the strong interaction.

In addition, there are antiparticle for each fermion, which have opposite quantum numbers corresponding to the each fermion. Table 1.1 shows the list of the leptons and the quarks.

Boson

The Bosons play a role in mediating force between the elementary particles corresponding to type of forces. Such bosons are especially called "gauge boson". In the present, it is believed that there are at least 4 kind of force, "Electromagnetic", "Weak", "Strong", and "Gravity", however the Gravity force is excluded in the SM due to normalization problem, and its extremely small affect in the particle world. The electromagnetic forces are propagated via "photon" by feeling electric charge which is gauge boson in

the electromagnetic field. The photon has spin 1, and massless means that the force caries to infinity. The weak force interactions are mediated by $W^{\pm}$ and Z^0 bosons have 80 and 91 GeV/c^2 mass, respectively, unlike electromagnetic force, it can effect within short range ($\sim 10^{-16}$ cm). The strong force interactions are occurred by exchanging gauge boson so-called "gluon" via color charge, which can propagate within finite range due to "asymptotic freedom". The color charge are conventionally expressed as 3 colors, "red (r)", "blue (b)", and "green (g)", which is introduced by taking Pauli Exclusion Principle in Hadrons (Baryons and Mesons) into account, for example Δ^{++} particle is constructed by 3 up-quarks, it can be expressed as (u_r, u_b, u_g). The force mediating particles, i.e. gauge bosons, are shown in Table 1.2 [4].

Name	Symbol	Mass		Charge ($Q/\|e\|$)	Spin	Weak Isospin
		Leptons				
electron	e	0.509	MeV/c^2	-1	1/2	$+1/2$
electron neutrino	ν_e	<225(95%CL)	eV/c^2	0	1/2	$-1/2$
muon	μ	105.7	MeV/c^2	-1	1/2	$+1/2$
muon neutrino	ν_μ	<0.19(90%CL)	MeV/c^2	0	1/2	$-1/2$
tau	τ	1776.8	MeV/c^2	-1	1/2	$+1/2$
tau neutrino	ν_τ	<18.2(95%CL)	MeV/c^2	0	1/2	$-1/2$
		Quarks				
up	u	$2.55^{+0.75}_{-1.05}$	MeV/c^2	$+2/3$	1/2	$+1/2$
down	d	$5.04^{+0.96}_{-1.54}$	MeV/c^2	$-1/3$	1/2	$-1/2$
charm	c	$1.27^{+0.07}_{-0.11}$	GeV/c^2	$+2/3$	1/2	$+1/2$
strange	s	104^{+26}_{-34}	MeV/c^2	$-1/3$	1/2	$-1/2$
top	t	171.2 ± 2.1	GeV/c^2	$+2/3$	1/2	$+1/2$
bottm	b	$4.20^{+0.17}_{-0.07}$	GeV/c^2	$-1/3$	1/2	$-1/2$

Table 1.1: List of the leptons and quarks and its properties in the Standard Model [4].

Interaction	Gauge boson (symbol)	Mass (GeV/c^2)	Effective coupling	Range [cm]	Typical time [s]
Electromagnetic	photon (γ)	0	1/137	∞	10^{-20}
Weak	$W^{\pm}$, Z^0	80.4, 91.2	10^{-5}	10^{-16}	10^{-10}
Strong	gluon (g)	0	~ 1	10^{-13}	10^{-23}

Table 1.2: Summry of the forces and gauge bosons in the Standard Model.

1.1.2 Quantum electrodynamics: $U(1)$

Quantum Electrodynamics (QED) is relativistic quantum field theory of the classical electromagnetism [5]. QED has the structure of an Abelian gauge theory with a $U(1)$ gauge group. The gauge field, which mediates the interaction between the charged 1/2 spin fields, is the electromagnetic field. An electron is described by a complex field and the Lagrangian is written as follows,

$$\mathscr{L} = i\bar{\psi}\gamma_\mu\partial^\mu\psi - m\psi\bar{\psi}. \tag{1.1}$$

The Lagrangian is invariant under the phase transformation,

$$\psi \to e^{i\alpha}\psi, \tag{1.2}$$

where α is a real constant. The family of phase transformations $U(\alpha) \equiv e^{i\alpha}$ forms a unitary Abelian group known as the $U(1)$ group. Using Neother's theorem, this invariant implies the existence of a conserved current and charge,

$$\partial_\mu j^\mu = 0,\ j^\mu = -e\bar{\psi}\gamma^\mu\psi,\ Q = \int d^3x j^0. \tag{1.3}$$

In addition, the local gauge transformation is generalized as

$$\psi \to e^{i\alpha(x)}\psi, \tag{1.4}$$

where $\alpha(x)$ depends on space and time in a completely arbitrary way. Now, the Lagrangian (1.1) is not invariant under such phase transformation. Using (1.4),

$$\bar{\psi} \to e^{-i\alpha(x)}\bar{\psi}, \tag{1.5}$$

the last term of the Lagrangian is invariant, however the term of derivative ψ is not as follows,

$$\partial_\mu\psi \to e^{i\alpha(x)}\partial_\mu\psi + ie^{i\alpha(x)}\psi\partial_\mu\alpha, \tag{1.6}$$

and the $\partial_\mu\alpha$ term breaks the invariant of the Lagrangian. To impose invariance of the Lagrangian under local gauge transformation, the derivative ∂_μ is modified as D_μ, the treatment covariantly transforms the Lagrangian under the phase transformation,

$$D_\mu\psi \to e^{i\alpha(x)}D_\mu\psi, \tag{1.7}$$

$$D_\mu \equiv \partial_\mu - ieA_\mu, \tag{1.8}$$

where a vector field A_μ is introduced to cancel the unwanted term in (1.6), and the vector field transforms as,

$$A_\mu \to A_\mu + \frac{1}{e}\partial_\mu\alpha. \tag{1.9}$$

Invariance of the Lagrangian (1.1) under the local gauge transformation (1.4) is achieved by replacing ∂_μ by D_μ,

$$\begin{aligned}\mathscr{L} &= i\bar{\psi}\gamma_\mu D^\mu\psi - m\psi\bar{\psi} \\ &= \bar{\psi}(i\gamma^\mu\partial_\mu - m)\psi + e\bar{\psi}\gamma^\mu\psi A_\mu. \end{aligned} \tag{1.10}$$

By demanding local phase invariance, it forces to introduce a vector field A_μ, i.e. gauge field in QED. If the additional field is regarded as the physical photon field, the Lagrangian is added a term corresponding to its kinetic energy. Since the kinetic term must be invariant under (1.9), it can only involve the gauge invariant field strength tensor

$$F_{\mu\nu} = \partial_\mu A_\nu - \partial_\nu A_\mu. \tag{1.11}$$

Finally, the Lagrangian of QED is expressed as follows,

$$\mathscr{L} = \bar{\psi}(i\gamma^\mu\partial_\mu - m)\psi + e\bar{\psi}\gamma^\mu\psi A_\mu - \frac{1}{4}F_{\mu\nu}F^{\mu\nu}. \tag{1.12}$$

The addition of a mass term $(1/2)m^2 A_\mu A^\mu$ is prohibited by gauge invariance. The gauge particle must be massless and the gauge field can propagate to an infinite range.

1.1.3 Quantum chromodynamics: $SU(3)_C$

Quantum Chromodynamics (QCD) is the gauge theory for strong interactions [5]. QCD is based on the extension of the QED idea, however it has a gauge transformation invariant under $SU(3)$ group on quark color fields. The Lagrangian is written in the following,

$$\mathscr{L} = \bar{q}_j(i\gamma^\mu\partial_\mu - m)q_j, \tag{1.13}$$

where $q_j (j = 1, 2, 3)$ denotes the three color fields. The Lagrangian (1.13) is to be invariant under local phase transformations as follows,

$$q(x) \to Uq(x) \equiv e^{i\alpha_a(x)T_a}q(x), \tag{1.14}$$

where U is an arbitrary 3×3 unitary matrix, it has the summation over the repeated suffix a. $T_a (a = 1, \cdots, 8)$ is a set of linearly independent traceless 3×3 matrices, and α_a are the group parameters. The group is non-Abelian since the generators T_a do not commute with each other,

$$[T_a, T_b] = if_{abc}T_c, \tag{1.15}$$

where f_{abc} are real constants called the structure constants of the group. To impose $SU(3)$ local gauge invariance on the Lagrangian (1.13), the infinitesimal phase transformation is introduced,

$$q(x) \to [1 + i\alpha_a(x)T_a]q(x), \tag{1.16}$$

$$\partial_\mu q \to (1 + i\alpha_a T_a)\partial_\mu q + iT_a q\partial_\mu\alpha_a. \tag{1.17}$$

The last term spoils the invariance of Lagrangian. The 8 gauge fields G^a_μ are constructed by requiring the invariance of the Lagrangian under the local gauge transformation,

$$G^a_\mu \to G^a_\mu - \frac{1}{g}\partial_\mu \alpha_a - f_{abc}\alpha_b G^c_\mu, \tag{1.18}$$

and form a covariant derivative,

$$D_\mu = \partial_\mu + igT_a G^a_\mu. \tag{1.19}$$

The gauge invariant QCD Lagrangian is formed by the replacement $\partial_\mu \to D_\mu$ in the Lagrangian (1.13), and adding a gauge invariant kinetic energy term for each of the G^a_μ fields,

$$\mathscr{L} = \bar{q}(i\gamma^\mu \partial_\mu - m)q - g(\bar{q}\gamma^\mu T_a q)G^a_\mu - \frac{1}{4}G^a_{\mu\nu}G^{\mu\nu}_a, \tag{1.20}$$

$$G^a_{\mu\nu} = \partial_\mu G^a_\nu - \partial_\nu G^a_\mu - g f_{abc} G^b_\mu G^c_\nu, \tag{1.21}$$

(1.20) is the Lagrangian for interacting colored quarks q and vector gluons G_μ, with coupling specified by g. The local gauge invariance requires the gluons to be massless. The field strength $G^a_{\mu\nu}$ has a remarkable new property as shown in the last term in (1.21). Imposing the gauge symmetry has required that the kinetic energy term in Lagrangian is not purely kinetic but includes an induced self-interaction between the gauge bosons and reflects the fact that gluons themselves carry color charge.

1.1.4 Electroweak theory: $SU(2)_L \otimes U(1)_Y$

The electroweak theory is a gauge theory unified the electromagnetic $U(1)$ and weak interactions $SU(2)$. The weak interaction typically occurs in β decay in nuclei ($n \to p + \ell + \nu_\ell$) via a W boson which is weak gauge boson. The weak interaction acts only left-handed fermions, so-called $V-A$ structure, and based on $SU(2)$ isospin group with three vector bosons. The electroweak theory is suggested by Glashow [6], Weinberg [7], and Salam [8].

By demanding weak interaction, the quark fields are expressed as follows,

$$\psi_L = \begin{pmatrix} q_u \\ q_d \end{pmatrix}_L, \ \psi_R = q_R. \tag{1.22}$$

The left-handed quark fields can be expressed in doublets, while the right-handed quark fields in singlets, where q_u is up-type quarks (u, c, t), q_d is down-type quarks (d, s, b), and q_R is six quark flavours (u, d, c, s, t, b). The lepton fields are also expressed by,

$$\psi_L = \begin{pmatrix} \nu_\ell \\ \ell^- \end{pmatrix}_L, \ \psi_R = \ell_R, \tag{1.23}$$

where ℓ means three lepton flavours i.e. e, μ, and τ. Note that there are no right-handed neutrino fields due to satisfying $V-A$ structure in the weak interaction. Here, the free Lagrangian for the lepton and the quark fields is written in,

$$\mathscr{L} = \sum_{j=L,R} i\bar{\psi}_j \gamma^\mu \partial_\mu \psi_j. \tag{1.24}$$

The Lagrangian (1.24) is invariant under global transformation,

$$\psi_L \to e^{i\alpha_a T^a + i\beta Y}\psi_L, \tag{1.25}$$
$$\psi_R \to e^{i\beta Y}\psi_R, \tag{1.26}$$

where the parameter Y is hypercharge for $U(1)_Y$ phase transformation, the T^a is defined by using Pauli matrices as follows,

$$T^a = \frac{\tau^a}{2},\ \tau^1 = \begin{pmatrix} 0 & 1 \\ 1 & 0 \end{pmatrix},\ \tau^2 = \begin{pmatrix} 0 & -i \\ i & 0 \end{pmatrix},\ \tau^3 = \begin{pmatrix} 1 & 0 \\ 0 & -1 \end{pmatrix}, \tag{1.27}$$

and it is under $SU(2)_L$ transformation. The Lagrangian should be invariant under local $SU(2)_L \otimes U(1)_Y$ gauge transformation,

$$\psi_L \to e^{i\alpha_a(x) T^a + i\beta(x) Y}\psi_L, \tag{1.28}$$
$$\psi_R \to e^{i\beta(x) Y}\psi_R. \tag{1.29}$$

To achieve the local gauge invariance in the Lagrangian, the derivative is replaced by covariant derivatives,

$$D_{\mu L} \equiv \partial_\mu + igT_a W^a_\mu, + i\frac{g'}{2}B_\mu Y \tag{1.30}$$

$$D_{\mu R} \equiv \partial_\mu + i\frac{g'}{2}B_\mu Y, \tag{1.31}$$

$D_{\mu L}(D_{\mu R})$ is for the left(right)-handed fermion fields, g is the coupling constant of $SU(2)_L$ and g' is of $U(1)_Y$. The covariant derivatives have gauge fields, $W^a_\mu (a = 1, 2, 3)$ for $SU(2)_L$, and B_μ for $U(1)_Y$. The gauge fields also transform as,

$$B_\mu \to B_\mu - \frac{1}{g'}\partial_\mu \beta, \tag{1.32}$$

$$\boldsymbol{W}_\mu \to \boldsymbol{W}_\mu - \frac{1}{g}\partial_\mu \boldsymbol{\alpha} - \boldsymbol{\alpha} \times \boldsymbol{W}_\mu. \tag{1.33}$$

In addition, the gauge field strength tensors are introduced by requiring the local gauge invariant,

$$B_{\mu\nu} \equiv \partial_\mu B_\nu - \partial_\nu B_\mu, \tag{1.34}$$
$$W^a_{\mu\nu} \equiv \partial_\mu W^a_\nu - \partial_\nu W^a_\mu - g\varepsilon_{abc} W^b_\mu W^c_\nu. \tag{1.35}$$

Finally, the Lagrangian under local gauge invariant in electroweak interaction can be written as,

$$\mathscr{L} = \sum_{j=L,R} i\bar{\psi}_j \gamma^\mu D_{\mu,j} \psi_j - \frac{1}{4} W^a_{\mu\nu} W^{\mu\nu}_a - \frac{1}{4} B_{\mu\nu} B_{\mu\nu}, \tag{1.36}$$

Although the weak and electromagnetic interactions coexist in the $SU(2)_L \otimes U(1)_Y$ gauge symmetry, it describes no realistic world, because there are no mass terms for fermions and weak gauge bosons which are known that they are massive, and weak interaction only affects in short range. However introducing the mass terms such as $\frac{1}{2} M_W^2 W_\mu W^\mu$ in the Lagrangian breaks the gauge symmetry. The fermion terms also break due to different transformation between the left-handed and right-handed fermion fields,

$$m_f \bar{f} f = m_f (\bar{f}_R f_L + \bar{f}_L f_R), \tag{1.37}$$

using the left-handed and right handed relation equations,

$$f_L = \frac{1}{2}(1 - \gamma^5) f, \;\; f_R = \frac{1}{2}(1 + \gamma^5) f. \tag{1.38}$$

Fortunately, the nature have a solution(mechanism) to be invariant under gauge transformation when the Lagrangian has a mass terms for fermion and weak gauge boson, so-called "Spontaneous symmetry breaking".

1.1.5 Spontaneous symmetry breaking

To give mass to the gauge bosons and fermions, the electroweak gauge symmetry are hidden. Here let us start by introducing the scalar real field ϕ as simple example, and its Lagrangian is written by,

$$\mathscr{L} = \frac{1}{2} \partial_\mu \phi \partial^\mu \phi - V(\phi), \tag{1.39}$$

$$V(\phi) = \frac{1}{2} \mu^2 \phi^2 + \frac{1}{4} \lambda \phi^4, \tag{1.40}$$

where $\lambda > 0$, the Lagrangian is invariant under the symmetry operation: $\phi \to -\phi$.

If $\mu^2 > 0$, it can be regarded that the Lagrangian describes a scalar fields with mass μ, the ϕ^4 terms means self-interaction with coupling λ, and the minimum of the potential $V(\phi)$ is,

$$\langle 0|\phi|0\rangle \equiv \phi_0 = 0, \tag{1.41}$$

as shown in the left side of Figure 1.1.5. On the other hand, if $\mu^2 < 0$, the potential $V(\phi)$ has a minimum when,

$$\frac{\partial V}{\partial \phi} = \mu^2 \phi + \lambda \phi^3 = 0, \tag{1.42}$$

$$\langle 0|\phi^2|0\rangle \equiv \phi_0^2 = -\frac{\mu^2}{\lambda} \equiv v^2, \tag{1.43}$$

as shown in the right side of Figure 1.1.5. The value $v = \sqrt{\mu^2/\lambda}$ is called "vacuum expectation value" of the scalar field ϕ. Here the field ϕ is expanded around the minimum value v with the quantum fluctuation η,

$$\phi = v + \eta. \tag{1.44}$$

From this, the Lagrangian (1.40) becomes

$$\mathscr{L} = \frac{1}{2}\partial_\mu\eta\partial^\mu\eta - \lambda v^2\eta^2 - \lambda v\eta^3 - \frac{1}{4}\eta^4 + \text{const}, \tag{1.45}$$

where a scalar field η with mass $m_\eta = \sqrt{-2\mu^2}$ appears in the Lagrangian (1.45), and there are self-interaction terms η^3 and η^4, in particular, the cubic term breaks the symmetry in the Lagrangian without external operation, it is called "Spontaneous Symmetry Breaking (SSB)". Next step, let us introduce the SSB to electroweak symmetry to get the true world picture, that is, the weak bosons and the fermions are massive.

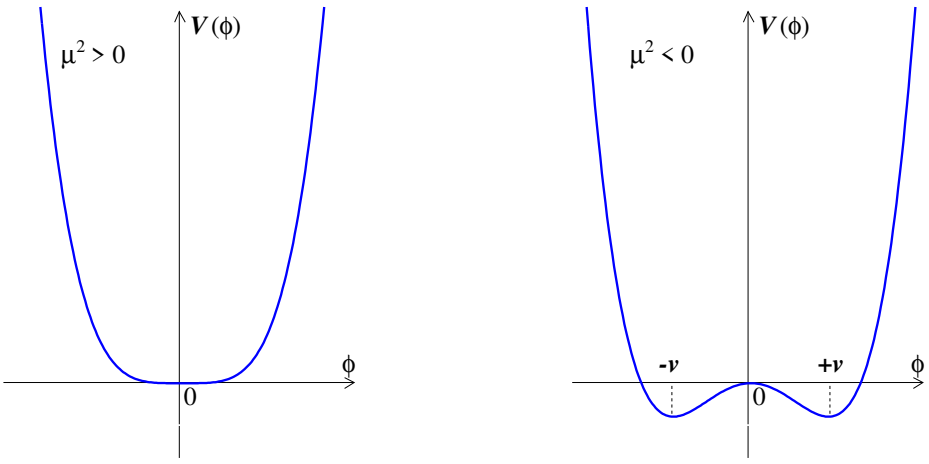

Figure 1.1: The potential $V(\phi)$ of the scalar field ϕ in the case $\mu^2 > 0$ (left) and $\mu^2 < 0$ (right).

1.1.6 Higgs mechanism

As described in §1.1.4, however the Lagrangian (1.36) is invariant under local gauge invariant, the Lagrangian describes the no real world picture because the weak gauge bosons and fermions have no mass in the Lagrangian. But the Lagrangian is broken by including the mass terms. Now, let us show that the Lagrangian becomes the real

world Lagrangian by using the symmetry breaking [9, 10, 11]. By introducing complex scalar doublet,

$$\phi = \begin{pmatrix} \phi^+ \\ \phi^0 \end{pmatrix} = \frac{1}{\sqrt{2}} \begin{pmatrix} \phi_1 + i\phi_2 \\ \phi_3 + i\phi_4 \end{pmatrix}, \; Y_\phi = +1, \tag{1.46}$$

where the hypercharge is 1 for the scalar fields, the Lagrangian can be written by

$$\mathscr{L} = (\partial_\mu \phi)^\dagger (\partial^\mu \phi) - \mu^2 \phi^\dagger \phi - \lambda (\phi^\dagger \phi)^2. \tag{1.47}$$

In this case, if $\mu^2 < 0$, the vacuum expectation value and the scalar field after the symmetry breaking with the real scalar field h become as follows,

$$\phi^\dagger \phi = \frac{\phi_1^2 + \phi_2^2 + \phi_3^2 + \phi_4^2}{2} = \frac{-\mu^2}{2\lambda} \equiv \frac{v^2}{2}, \tag{1.48}$$

$$\phi = \frac{1}{\sqrt{2}} \begin{pmatrix} 0 \\ v + h \end{pmatrix}, \tag{1.49}$$

where the scalar fields are chosen as $\phi^1 = \phi^2 = \phi^4 = 0$, and $\phi^3 = v$. Let us expand the first term of the Lagrangian (1.47), i.e. the kinematical terms,

$$\begin{aligned} |D_\mu \phi|^2 &= \left| \left(\partial_\mu - igT^a W_\mu^a + i\frac{g'}{2} B_\mu \right) \phi \right|^2 \\ &= \frac{1}{2}(\partial_\mu h)^2 + \frac{g^2 v^2}{4} \left| \frac{W_\mu^1 + iW_\mu^2}{2} \right|^2 + \frac{v^2}{8} |gW_\mu^3 - g' B_\mu|^2 + \text{interaction terms} \end{aligned} \tag{1.50}$$

where the derivative is replaced to covariant derivative (1.31), and define the field $W_\mu^\pm$, Z_μ and A_μ written as follows,

$$W_\mu^\pm = \frac{1}{\sqrt{2}}(W_\mu^1 \pm iW_\mu^2), \tag{1.51}$$

$$Z_\mu = W_\mu^3 \cos\theta_W - B_\mu \sin\theta_W, \tag{1.52}$$

$$A_\mu = W_\mu^3 \sin\theta_W + B_\mu \cos\theta_W, \tag{1.53}$$

where weak mixing angle θ_W is defined as $g' = g \tan\theta_W$, the A_μ field is the orthogonal field to the Z_μ field, and the masses of fields can be expressed as respectively,

$$M_W = \frac{1}{2} v g, \; M_Z = \frac{1}{2} v \sqrt{g^2 + g'^2}, \; M_A = 0. \tag{1.54}$$

Note that the W_μ and the Z_μ fields become massive, while the A_μ field is still massless, that is, the weak gauge bosons can have desirable mass by introducing the SSB, in particular, it is called "Higgs Mechanism". By using the weak mixing angle θ_W, the W_μ field is related to Z_μ field as follows,

$$M_W = M_Z \cos\theta_W. \tag{1.55}$$

The fermion fields should be massive to achieve the true world in the electroweak Lagrangian. The Higgs mechanism also gives a mass to the fermions under the local gauge invariant. The Lagrangian with fermion fields is written by,

$$\mathscr{L}_{Yukawa} = -G_f \bar{\psi}_L \phi \psi_R - G_f \bar{\psi}_R \phi^\dagger \psi_L, \tag{1.56}$$

where G_f is arbitrary constant for each fermion. First, the lepton sector Lagrangian becomes,

$$\begin{aligned}
\mathscr{L}_{\text{lepton}} &= -G_\ell \left[(\bar{\nu}_\ell, \bar{\ell})_L \begin{pmatrix} \psi^+ \\ \psi^0 \end{pmatrix} \ell_R + \bar{\ell}_R (\psi^-, \bar{\psi}^0) \begin{pmatrix} \nu_\ell \\ \ell \end{pmatrix}_L \right] \\
&= -\frac{G_\ell}{\sqrt{2}} v (\bar{\ell}_L \ell_R + \bar{\ell}_R \ell_L) - \frac{G_\ell}{\sqrt{2}} (\bar{\ell}_L \ell_R + \bar{\ell}_R \ell_L) h \\
&= -m_\ell \bar{\ell}\ell - \frac{m_\ell}{v} \bar{\ell}\ell h,
\end{aligned} \tag{1.57}$$

using (1.38) and $m_\ell = G_\ell v/\sqrt{2}$ is defined as the lepton mass. The lepton sector Lagrangian (1.57) then keeps the gauge symmetry under the local transformation. Let us show that the quark sector Lagrangian also becomes the invariant. In the quark sector, the new higgs doublet must be introduced by using ϕ to give the the up-type quark mass,

$$\phi_c = i\tau_2 \phi = \begin{pmatrix} -\bar{\phi}^0 \\ \phi^- \end{pmatrix}, \tag{1.58}$$

the higgs doublet is chosen the following after the symmetry breaking,

$$\phi_c = \frac{1}{\sqrt{2}} \begin{pmatrix} v + h \\ 0 \end{pmatrix}. \tag{1.59}$$

The quark sector Lagrangian is formed by

$$\begin{aligned}
\mathscr{L}_{\text{quark}} &= -G_d (\bar{u}, \bar{d})_L \begin{pmatrix} \psi^+ \\ \psi^0 \end{pmatrix} d_R - G_u (\bar{u}, \bar{d})_L \begin{pmatrix} -\bar{\psi}^0 \\ \psi^- \end{pmatrix} u_R + h.c. \\
&= -m_d \bar{d}d - m_u \bar{u}u - \frac{m_d}{v} \bar{d}dh - \frac{m_u}{v} \bar{u}uh,
\end{aligned} \tag{1.60}$$

where the down-type and the up-type quark masses are defined as $m_d = G_d v/\sqrt{2}$ and $m_u = G_u v/\sqrt{2}$ respectively. The quark sector Lagrangian also preserves the gauge invariant after the symmetry breaking.

The Higgs Mechanism gives us the electroweak Lagrangian with relevant field mass terms under the gauge symmetry. However the fermions masses are not predicted in the Lagrangian because of general fermion coupling G_f's are arbitrary constant, and the Higgs mass and its potential structure are also unknown. They need to be revealed by a experiment.

1.1.7 Two higgs doublet model

In the previous section, the minimal SM higgs is considered, however the scalar field doublet can be introduced as two, and more doublets to break the electroweak symmetry. Then, Let us introduce the two complex doublet scalar fields ϕ_1 and ϕ_2 so-called "Two Higgs Doublet Model (2HDM)",

$$\phi_1 = \begin{pmatrix} \phi_1^+ \\ \phi_1^0 \end{pmatrix}, \ \phi_2 = \begin{pmatrix} \phi_2^+ \\ \phi_2^0 \end{pmatrix}, \tag{1.61}$$

The 2HDM have mainly two scenarios, named "Type-I" and "Type-II", respectively. In the "Type-I", the scalar fields ϕ_1 do not couple to any quarks and leptons, while the other scalar fields ϕ_2 couple to them. In the "Type-II", the first scalar fields ϕ_1 couple only to down-type quarks and leptons, while the second scalar fields ϕ_2 couple only to up-type quarks. In this thesis, the Type-I scenario is noticed [13, 14].

First, let us start to introduce the most general potential written as,

$$\begin{aligned} V(\phi_1, \phi_2) =& \lambda_1(\phi_1^\dagger\phi_1 - v_1^2)^2 + \lambda_2(\phi_2^\dagger\phi_2 - v_2^2)^2 \\ &+ \lambda_3\left[(\phi_1^\dagger\phi_1 - v_1^2) + (\phi_2^\dagger\phi_2 - v_2^2)\right]^2 \\ &+ \lambda_4\left[(\phi_1^\dagger\phi_1)(\phi_2^\dagger\phi_2) - (\phi_1^\dagger\phi_2)(\phi_2^\dagger\phi_1)\right] \\ &+ \lambda_5\left[\mathrm{Re}(\phi_1^\dagger\phi_2) - v_1v_2\cos\xi\right]^2 + \lambda_6\left[\mathrm{Im}(\phi_1^\dagger\phi_2) - v_1v_2\sin\xi\right]^2 \\ &+ \lambda_7\left[\mathrm{Re}(\phi_1^\dagger\phi_2) - v_1v_2\cos\xi\right]\left[\mathrm{Im}(\phi_1^\dagger\phi_2) - v_1v_2\sin\xi\right] \end{aligned} \tag{1.62}$$

where λ_i are real parameters, and the potential has a discrete symmetry, $\phi_1 \to -\phi_1$, only broken softly. The last term with λ_7 can be eliminated by defining the phases of the scalar fields or demanding the CP-conservation which is assumed in this section.

The vacuum expectation values for the two scalar fields after symmetry breaking are formed as follows,

$$\langle\phi_1\rangle = \begin{pmatrix} 0 \\ v_1 \end{pmatrix}, \ \langle\phi_2\rangle = \begin{pmatrix} 0 \\ v_2 \end{pmatrix}, \tag{1.63}$$

where $v_{1,2}$ are real, in addition, the vacuum expectation values are defined by,

$$\tan\beta \equiv \frac{v_2}{v_1}, \ v^2 \equiv v_1^2 + v_2^2 = \frac{2m_W^2}{g^2} = (173\ \mathrm{GeV})^2, \tag{1.64}$$

as discussed below, the parameter β serves as key role in the model. In this model, there are five Higgs boson (h^0, H^0, A^0, and $H^\pm$) and three Goldstone bosons (G^0 and $G^\pm$) which give a mass to weak bosons. The charged Goldstone boson $G^\pm$ is orthogonal to the charged Higgs boson $H^\pm$, and the charged sector are expressed by,

$$G^\pm = \phi_1^\pm\cos\beta + \phi_2^\pm\sin\beta, \tag{1.65}$$

$$H^\pm = -\phi_1^\pm\sin\beta + \phi_2^\pm\cos\beta. \tag{1.66}$$

By demanding the CP-conservation, the imaginary parts and the real parts of the neutral scalar fields decouple. The neutral Goldstone boson is orthogonal to the one of the neutral higgs bosons, the imaginary sector (CP-odd) are obtained as,

$$G^0 = \sqrt{2}\left[\mathrm{Im}(\phi_1^0)\cos\beta + \mathrm{Im}(\phi_2^0)\sin\beta\right], \tag{1.67}$$

$$A^0 = \sqrt{2}\left[-\mathrm{Im}(\phi_1^0)\sin\beta + \mathrm{Im}(\phi_2^0)\cos\beta\right], \tag{1.68}$$

while the real sector (CP-even) are expressed by as follows,

$$H^0 = \sqrt{2}\left[(\mathrm{Re}(\phi_1^0) - v_1)\cos\alpha + (\mathrm{Re}(\phi_2^0) - v_2)\sin\alpha\right], \tag{1.69}$$

$$h^0 = \sqrt{2}\left[-(\mathrm{Re}(\phi_1^0) - v_1)\sin\alpha + (\mathrm{Re}(\phi_2^0) - v_2)\cos\alpha\right], \tag{1.70}$$

where the neutral higgs scalars are related with the mixing angle α which is defined as,

$$\sin 2\alpha = \frac{2\mathcal{M}_{12}}{\sqrt{(\mathcal{M}_{11} - \mathcal{M}_{22})^2 + 4\mathcal{M}_{12}^2}}, \tag{1.71}$$

$$\cos 2\alpha = \frac{\mathcal{M}_{11} - \mathcal{M}_{22}}{\sqrt{(\mathcal{M}_{11} - \mathcal{M}_{22})^2 + 4\mathcal{M}_{12}^2}}, \tag{1.72}$$

then, the scalar masses can be obtained by diagonalizing the Higgs boson matrix, $M_{ij}^2 = \frac{\partial^2 V}{\partial\phi_i\partial\phi_j}$, the Higgs masses are respectively written as,

$$M_{H^0,h^0}^2 = \frac{1}{2}\left[\mathcal{M}_{11} + \mathcal{M}_{22} \pm \sqrt{(\mathcal{M}_{11} - \mathcal{M}_{22})^2 + 4\mathcal{M}_{12}^2}\right], \tag{1.73}$$

$$M_{H^\pm}^2 = \lambda_4(v_1^2 + v_2^2),\ M_{A^0}^2 = \lambda_6(v_1^2 + v_2^2), \tag{1.74}$$

where using the mass matrices defined as follows,

$$\mathcal{M} = \begin{pmatrix} \mathcal{M}_{11} & \mathcal{M}_{12} \\ \mathcal{M}_{12} & \mathcal{M}_{22} \end{pmatrix} = \begin{pmatrix} 4v_1^2(\lambda_1 + \lambda_3) + v_2^2\lambda_5 & (4\lambda_3 + \lambda_5)v_1v_2 \\ (4\lambda_3 + \lambda_5)v_1v_2 & 4v_2^2(\lambda_2 + \lambda_3) + v_1^2\lambda_5 \end{pmatrix}. \tag{1.75}$$

The neutral Higgs boson couplings relate to the vacuum expectation value ratio β and the mixing angle α, the coupling can be repressed by,

$$\frac{g_{h^0VV}}{g_{\phi^0VV}} = \sin(\beta - \alpha),\ \frac{g_{H^0VV}}{g_{\phi^0VV}} = \cos(\beta - \alpha), \tag{1.76}$$

where ϕ^0 is minimal SM Higgs boson, and $V = W^\pm, Z$. Note that the remaining neutral Higgs boson A^0 couples to no gauge boson.

Next, let us show the Higgs-fermion interaction in the Type-I. The interaction is formed as,

$$\begin{aligned}\mathscr{L}_{\text{fermion}} =& -\frac{g}{2M_W\sin\beta}\bar{D}M_D D(H^0\sin\alpha + h^0\cos\alpha) - \frac{ig\cot\beta}{2M_W}\bar{D}M_D\gamma^5 DA^0 \\ &- \frac{g}{2M_W\sin\beta}\bar{U}M_U U(H^0\sin\alpha + h^0\cos\alpha) + \frac{ig\cot\beta}{2M_W}\bar{U}M_U\gamma^5 UA^0 \\ &+ \frac{g\cot\beta}{2\sqrt{2}M_W}(\bar{U}[M_U K(1-\gamma^5) - KM_D(1+\gamma^5)]DH^+ + h.c.) + \text{leptonic sector}.\end{aligned} \tag{1.77}$$

where M_U and M_D are diagonal quark matrices, K is Kobayashi-Maskawa mixing matrix. The Higgs-lepton couplings can be expressed by replacing U, D and the quark mass matrices with the corresponding lepton fields and lepton matrices and setting $K = 1$. The neutral Higgs boson couplings to gauge bosons and fermions are shown in Table 1.3. In particular, the "fermiophobic Higgs (h_F)" appears in the 2HDM Type-I by setting the mixing angle,

$$\alpha = \frac{\pi}{2}, \tag{1.78}$$

as seen in (1.77), so-called "fermiophobia". The "fermiophobic Higgs" becomes only coupling to the bosons.

ϕ	H^0	h^0	A^0
$g_{\phi VV}$	$\cos(\beta-\alpha)$	$\sin(\beta-\alpha)$	0
$g_{\phi\bar{u}u}$	$\frac{\sin\alpha}{\sin\beta}$	$\frac{\cos\alpha}{\sin\beta}$	$\cot\beta$
$g_{\phi\bar{d}d}$	$\frac{\sin\alpha}{\sin\beta}$	$\frac{\cos\alpha}{\sin\beta}$	$\cot\beta$
$g_{\phi\bar{e}e}$	$\frac{\sin\alpha}{\sin\beta}$	$\frac{\cos\alpha}{\sin\beta}$	$\cot\beta$

Table 1.3: The neutral Higgs boson couplings to gauge bosons ($V = W^{\pm}, Z$) and fermions in 2HDM Type-I.

1.2 Production of the higgs boson at tevatron

As mentioned before, the SM Higgs boson is that particle give a mass to any particles except for weak gauge boson photon and neutrinos, that is, the higgs boson couples to the massive particles with its production and decay. The strength of the process depend on higgs mass and relevant particle masses.

The main production mechanisms for the SM Higgs at hadron collider uses coupling to the heavy particles, i.e. W, Z bosons, and top quark. There are 4 dominant SM Higgs boson production modes in the Tevatron, the gluon-gluon fusion production, the associated production with the weak boson, the vector boson fusion (VBF) production, and the associated production with top quark, as shown in Figure 1.2. However there are also several mechanisms for the pair Higgs boson production, the mechanism is not useful production in the Tevatron because the production cross-section will extremely become small by the additional coupling.

In this section, the production mechanisms are described, and also its cross-sections in the Tevatron are mentioned which are taken QCD correction on NLO into account [15, 16].

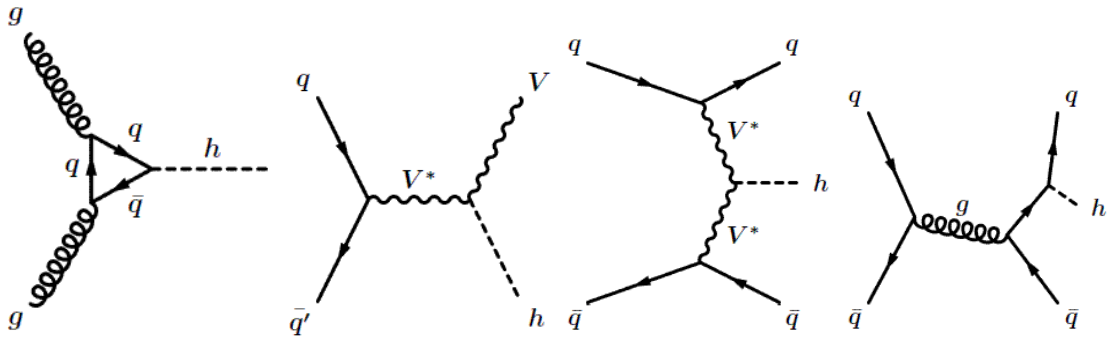

Figure 1.2: Feynman diagrams for the Higgs boson production mechanism (from left to right: the gluon-gluon fusion, the associated production with vector boson, the vector boson fusion, and the associated production with heavy quarks).

1.2.1 The gluon-gluon fusion production

The Higgs boson production in the gluon-gluon fusion mechanism is mediated by triangular loop of the heavy quarks, in the SM, the top quarks mostly contribute the process, while the bottom quark loop is also non-negligible contribution. In the single Higgs production, the two loop QCD radiative corrections enhance the cross-section 60-100%. The production process is the largest cross-section in the Tevatron, as shown in Figure 1.2.4, 1.0-0.2 pb from 100 to 200 GeV/c^2.

1.2.2 The associated production with vector boson

The associated production process goes on with $q\bar{q}$ annihilation into a virtual vector boson V^*, and then, do the "Higgs-strahlung". The QCD corrections increases the cross-section 30%. The cross-section for a virtual W^* process, $q\bar{q} \to Wh$, is roughly a factor of two higher than for a virtual Z ones, as shown in Figure 1.2.4. The cross-section for Wh mechanism is 0.3-0.02 pb from 100 to 200 GeV/c^2, and for Zh, 0.2-0.01 pb. The production mechanism is most promising discovery ones for $M_h < 130$ GeV/c^2.

1.2.3 The vector boson fusion production

The vector boson fusion mechanism is that the quark and anti-quark both radiate virtual bosons, and then the bosons annihilate to produce the Higgs boson. The QCD corrections enhance the cross-section by about 10%. The cross-section is 0.1-0.02 pb from 100 to 200 GeV/c^2. In this production process, there are two forward jets, it can somewhat suppress the QCD backgrounds by using the distinct kinematics.

1.2.4 The associated production with heavy quarks

The production process where Higgs is produced association with heavy quark pairs with the final state quarks being either the top or the bottom quark. At tree-level, it

originates from $q\bar{q}$ annihilation into heavy quarks with the Higgs boson emitted from the quarks lines which is the mains source at the Tevatron. Figure 1.2.4 shows of the top quark pairs, the QCD corrections are taken the limit of $M_h \ll M_t$ into account.

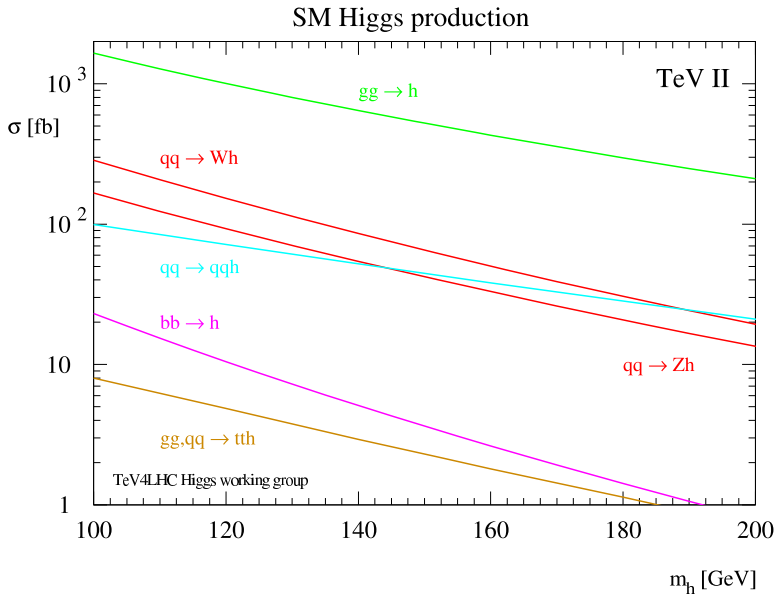

Figure 1.3: Production cross-section of the SM Higgs boson in several processes at the Tevatron.

1.3 Decay of the higgs boson at Tevatron

In the decay process, the Higgs boson has the tendency to decay into the heaviest particles allowed by phase space, because the Higgs couplings to gauge bosons and fermions are proportional to the masses of the particles.

The branching fractions for the dominant decay modes of the Higgs boson are varied by the Higgs-self mass. In the Tevatron, the Higgs hunters chose the best set of the Higgs decay mode and production mechanism as mentioned previous section to maximally get the discovery chance.

In this below section, the several decay modes are discussed, which are used in the Higgs search at the Tevatron. Figure 1.3.3 shows the branching fraction of the dominant decay modes of the minimal Standard Model Higgs boson and the fermiophobic Higgs in 2HDM Type-I.

1.3.1 $h \to f\bar{f}$ Mode

The decay mode $h \to b\bar{b}$ dominates for the minimal SM Higgs boson below about 130 GeV/c^2. The $b\bar{b}$ decay mode is ubiquitous employed in the Higgs search at the Tevatron, in particular, in the associated production with vector boson channel, because there are distinctive signatures in the final state, i.e. leptons plus two-bjets, which lead to not too large backgrounds, and the valid feature can reconstructs the $b\bar{b}$ invariant mass peak using flavour tagging (b-tagging) to reject the background such as $Wb\bar{b}$ and $t\bar{t}$ production event. The decay mode $h \to \tau\tau$ also is somewhat valid with respect to its high branching fraction for low mass minimal SM Higgs boson if enough luminosity is available, however needs a significant improvement of τ identification.

1.3.2 $h \to WW^{(*)}$ Mode

The decay mode has one of the most promising detection and the potential discovery final state $\ell^+\nu\ell^-\nu$ for the minimal SM Higgs boson $M_h > 135$ GeV/c^2 combination using gluon-gluon fusion production in the Tevatron. The dominant background source is WW and $t\bar{t}$ production. The decay process in the latter involves $t \to bW$, i.e. become 2-lepton plus 2-bjets final state, although 2-bjets non-requirement can greatly removes the background. The former can be removed by using the characteristic spin-correlations in the Higgs channel. With associated production with vector boson, the decay mode will be significance detection channel using like-sign dilepton event in the final state, which excellently remove the QCD and electroweak backgrounds. The combination channel are employed in this thesis, and also useful to search for the fermiophobic Higgs from its low mass region due to its feature, as shown in the right-hand side of Figure 1.3.3.

1.3.3 $h \to \gamma\gamma$ Mode

Although the two photon decay mode is extremely rare for the minimal SM Higgs boson at the Tevatron, for low mass fermiophobic Higgs will be useful, which will be dominant mode, as shown in Figure 1.3.3. And the mode give a narrow mass peak which can effectively reject the backgrounds.

1.4 Higgs boson mass constraints

As mentioned before, the Higgs boson mass are not given in the SM framework while predicted the existence of the Higgs boson. However the Higgs boson mass can be constraint by taking into account adaptive limit for perturbation theory. In additional, the passed experiment results have constrained the Higgs boson mass. In this section, the constraints on the Higgs boson mass are discussed in both theoretical and experimental point of view.

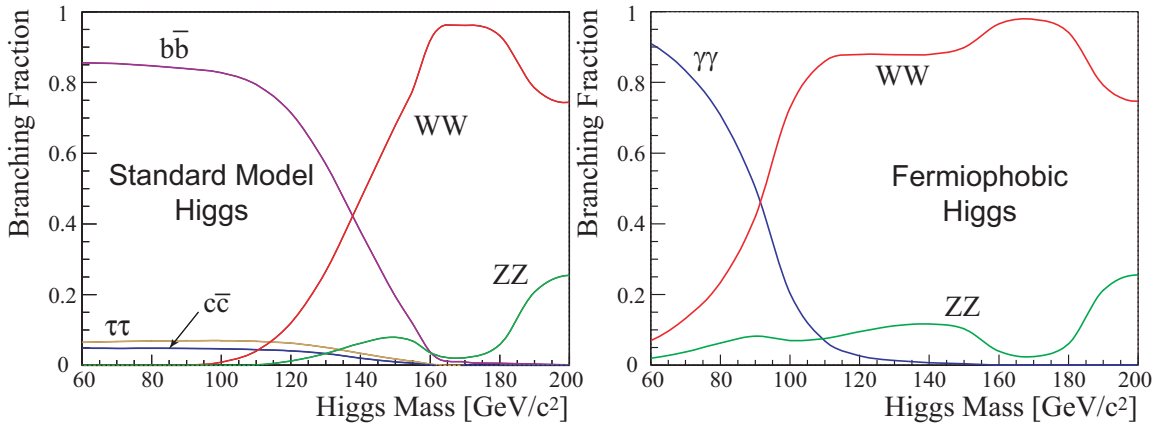

Figure 1.4: The branching fraction on the minimal SM Higgs boson (left-side) and the Fermiophobic Higgs boson in 2HDM Type-I (right-side).

1.4.1 Theoretical higgs boson mass constraints

The Higgs mass and its coupling depend on the considered energy because of quantum (radiative) corrections. The Higgs mass can be limited by taking into account the energy scale from upper side (triviality bound) and lower side (vacuum stability bound) where the SM is valid within perturbation theory. In this section, let us see the theoretical constraint of the Higgs boson mass. Figure 1.4.1 shows the upper bound and the lower bound on the Higgs boson mass as a function of the energy scale Λ_c.

Triviality bound

First, let us take the one-loop radiative correction to the Higgs boson quartic coupling for the contributions to the Higgs boson. The Feynman diagrams for the tree-level and the one-loop corrections to the Higgs boson self-coupling are shown in Figure 1.4.1. The variation of the quartic Higgs coupling with the energy scale Q is described by the Renormalization Group Equation (RGE),

$$\frac{d\lambda(Q^2)}{dQ^2} = \frac{3}{4\pi^2}\lambda^2(Q^2) + \text{higher order}. \tag{1.79}$$

The solution of the equation by selecting a energy point to be the electroweak symmetry breaking scale $Q_0 = v$ can be written by,

$$\lambda(Q^2) = \lambda(v^2)\left[1 - \frac{3}{4\pi^2}\lambda(v^2)\log\frac{Q^2}{v^2}\right]^{-1}. \tag{1.80}$$

The quartic couplings varies logarithmically with the squared energy Q^2. From (1.80), if the energy is much smaller than the electroweak breaking scale, $Q^2 \ll v^2$, the quartic coupling becomes extremely small and eventually vanishes, i.e. the theory is trivially

non-interacting, $\lambda(Q^0) \sim 0$. While when the energy is much higher than electroweak scale, $Q^2 \gg v^2$, the quartic coupling grows and eventually becomes infinite $\lambda(Q^2) \gg 1$ which is called Landau Pole, i.e. the coupling becomes infinite at the energy,

$$\Lambda_c = v \exp\left(\frac{4\pi^2 v^2}{M_h^2}\right). \tag{1.81}$$

The energy point Λ_c is corresponding to the Higgs mass upper limit to avoid the Landau pole as seen in (1.81). For instance, if the energy $\Lambda_c \sim 10^{16}$, the Higgs boson mass need to be light, $M_h < 200$ GeV/c^2, while when the energy $\Lambda_c \sim 10^3$, the Higgs boson mass is allowed to be the order of 1 TeV/c^2.

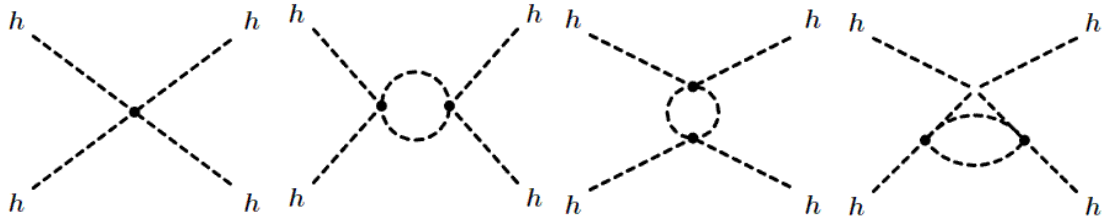

Figure 1.5: Feynman diagrams for the tree-level and one-loop Higgs self-coupling.

Stability bound

Next, the Higgs boson coupling needs to also include the contribution from fermion and gauge bosons. In this case, only the contribution of top quark and massive gauge bosons are taken into account because the Higgs boson coupling are proportional to the particle masses. The Feynman diagrams for the top quark and gauge boson contribution are shown in Figure 1.4.1. The one-loop RGE for the quartic coupling including the additional contribution can be obtained by,

$$\frac{d\lambda}{d\log Q^2} \simeq \frac{1}{16\pi^2}\left[12\lambda^2 - \frac{12M_t^4}{v^4} + \frac{3}{16}(2g_2^4 + (g^2 + g^1)^2)\right], \tag{1.82}$$

where the top quark Yukawa coupling is $\lambda_t = \sqrt{2}m_t/v$. The solution taking the electroweak breaking scale same as the case of Higgs self-coupling,

$$\lambda(Q^2) = \lambda(v^2) + \frac{1}{16\pi^2}\left[-\frac{12M_t^4}{v^4} + \frac{3}{16}(2g_2^4 + (g_2^2 + g_1^2)^2)\right]\log\frac{Q^2}{v^2}. \tag{1.83}$$

If the coupling λ is too small, the top quark contribution can be dominant and could result a negative value $\lambda(Q^2) < 0$ which is eventually leading to a scalar potential $V(Q^2) < V(v)$, and it can say that the vacuum is stable since it has no minimum. From the stability perspective, that is, to keep $\lambda(Q^2) > 0$, the Higgs boson mass need to be larger than a value as written in the following,

$$M_h^2 > \frac{v^2}{8\pi^2}\left[-\frac{12M_t^4}{v^4} + \frac{3}{16}(2g_2^4 + (g_2^2 + g_1^2)^2)\right]\log\frac{Q^2}{v^2}. \tag{1.84}$$

The lower constraint on Higgs boson mass depends on the value of the energy scale Λ_c, if the value $\Lambda_c \sim 10^3$, the Higgs boson mass should be larger than 70 GeV/c^2, and if $\Lambda_c \sim 10^{16}$, the Higgs boson mass is larger than 130 GeV/c^2.

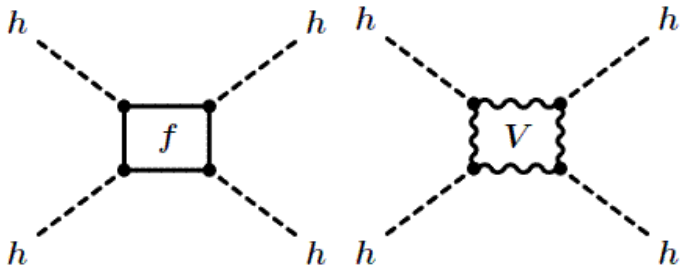

Figure 1.6: Feynman diagrams for the one-loop contribution of fermion and gauge boson to the Higgs coupling λ.

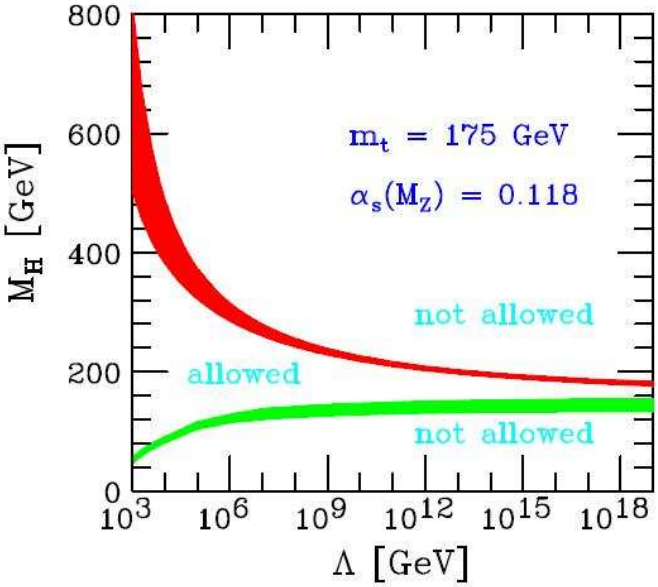

Figure 1.7: The triviality (upper) bound and the vacuum stability (lower) bound on the Higgs boson mass as a function of the cut-off scale Λ for a top quark mass $M_t = 175 \pm 6$ GeV/c^2 and $\alpha_s(M_Z) = 0.118 \pm 0.002$.

1.4.2 Experimental higgs boson mass constraints

The Higgs searches have performed and are going on with the various experiments in the whole world. The experiments results give us the constraint of the Higgs mass, directly and indirectly. The letter constraints are set by using precision electroweak measurements taking top quark and Higgs boson radiative correction into account. The

four LEP collaborations performed the Higgs direct searches at LEP1 and LEP2 from 1989 to 2000. The collaborations reported the combined lower limits on the mass of SM Higgs boson, also set the lower limit on the mass of the fermiophobic Higgs boson. In this section, The experimental Higgs mass constraints are discussed.

The electroweak precision measurements

The electroweak parameters, the vector boson and top quark mass and its width, forward-backward asymmetry, and so on, are precisely measured by various experiments (ALEPH, DELPHI, L3, OPAL, SLD, CDF, DØ and NuTeV) in the world. The precision electroweak results have the sensitivity to the masses of the top and the Higgs boson through radiative (loop) corrections as shown in Figure 1.4.2. The parameter indicating the relation of the W boson and the Z boson mass with weak mixing angle at one loop is,

$$\rho = \frac{M_W^2}{M_Z^2(1-\sin^2\theta_W)} \equiv 1 + \Delta r, \tag{1.85}$$

and a radiative correction are written by,

$$\Delta r = \frac{3G_F}{8\pi^2\sqrt{2}} m_t^2 + \frac{\sqrt{2}G_F}{16\pi^2} M_W^2 \left[\frac{11}{3} \ln\left(\frac{M_h^2}{M_W^2}\right) + \cdots \right] + \cdots , \tag{1.86}$$

which is quadratic in the top quark mass, while the dependence on the mass of the Higgs boson is only logarithmic, therefore the top quark mass, especially if large, is the dominant parameter in the correction to electroweak processes [17].

The electroweak precision measurements allow the constraint on the SM Higgs boson mass [18]. The Figure 1.4.2 shows the $\Delta\chi^2$ of the fit to all electroweak measurements as a function of SM Higgs Mass. From the fitting, the constraint SM Higgs mass with the experiment uncertainties are obtained as,

$$M_h = 84^{+34}_{-26}\ \mathrm{GeV}/c^2, \tag{1.87}$$

the shaded band represents the uncertainty due to uncalculated higher-order corrections. And the 95% one-sided confidence level upper limits on the SM Higgs mass is,

$$M_h < 154\ \mathrm{GeV}/c^2, \tag{1.88}$$

when the 95% confidence level lower limits on the SM Higgs mass 114.4 GeV/c^2 from direct searches as discussed in the following section is included, the upper limit increases to 185 GeV/c^2.

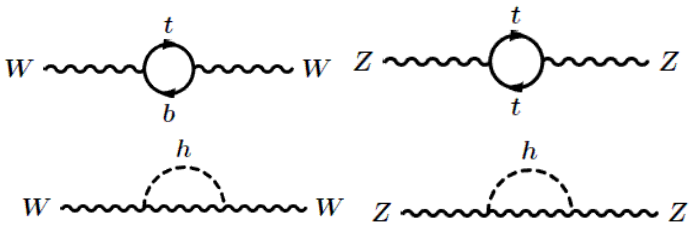

Figure 1.8: Radiative loop correction for electroweak processes.

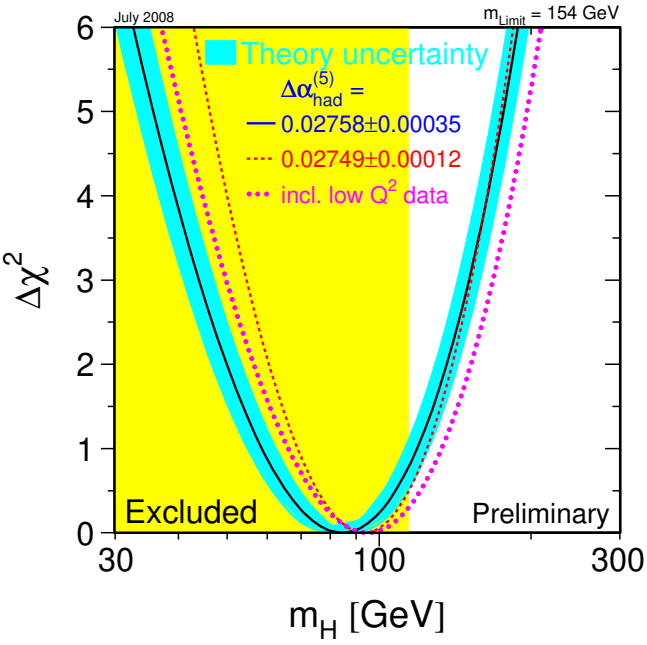

Figure 1.9: The $\Delta\chi^2$ of the fit to the electroweak precision data as a function of SM Higgs mass. The solid line results by including all data, and the blue band is the estimated theoretical error from missing higher-order corrections.

The SM higgs boson searches at LEP

The four LEP collaborations, ALEPH, DELPHI, L3, and OPAL set a lower bound of the SM Higgs bosons at 95% confidence level using the combined result [19]. The LEP collaborations have collected a total of 2461 pb^{-1} of e^+e^- collision data at $\sqrt{s} = 189 - 209$ GeV which are used to search for the SM Higgs boson. The four results are combined and examined in a likelihood test for their consistency with two hypotheses, the background hypothesis and the signal plus background hypothesis.

The SM Higgs boson is expected to be produced mainly in association with Z as $e^+e^- \to Zh$, and the SM Higgs boson is expected to decay mainly into $b\bar{b}$ pairs. The target final state are the 4-jets event ($Zh \to q\bar{q}b\bar{b}$), the missing energy event

($Zh \to \nu\bar{\nu}b\bar{b}$), the leptonic event ($Zh \to \ell^+\ell^- b\bar{b}$, $\ell = e, \mu$), and the tau lepton event ($Zh \to \tau^+\tau^- b\bar{b}$).

The ratio $CL_s = CL_{s+b}/CL_b$ is used to drive a lower bound on the SM Higgs boson mass, where CL_{s+b} means the compatibility for the observation and signal + background hypothesis, and CL_b is the compatibility for the observation and background hypothesis. Using The quantity for setting exclusion limits by taken a mass hypothesis into account to be excluded at the 95% confidence level if the corresponding value of CL_s is less than 0.05. The combined the final results from the four LEP experiments is a lower bound of 114.4 GeV/c^2 on the mass of the SM Higgs boson at the 95% confidence level as shown in Figure 1.4.2.

The fermiophobic higgs boson searches at LEP

The LEP collaborations also set a lower bound on the "benchmark" fermiophobic Higgs boson at the 95% confidence level assuming Standard Model production rates [20]. The four experiments searched for hadronic, leptonic, and missing energy decay mode of the associated Z boson in the production Zh^0 with $h^0 \to \gamma\gamma$. For the combined data from the four experiments, the 95% confidence level lower mass limit for a benchmark fermiophobic Higgs boson is set at 109.7 GeV/c^2. Figure 1.4.2 shows the combined upper limit on $B(h^0 \to \gamma\gamma) \times \sigma(e^+e^- \to h^0 Z)/\sigma(\mathrm{SM})$ at 95% confidence level.

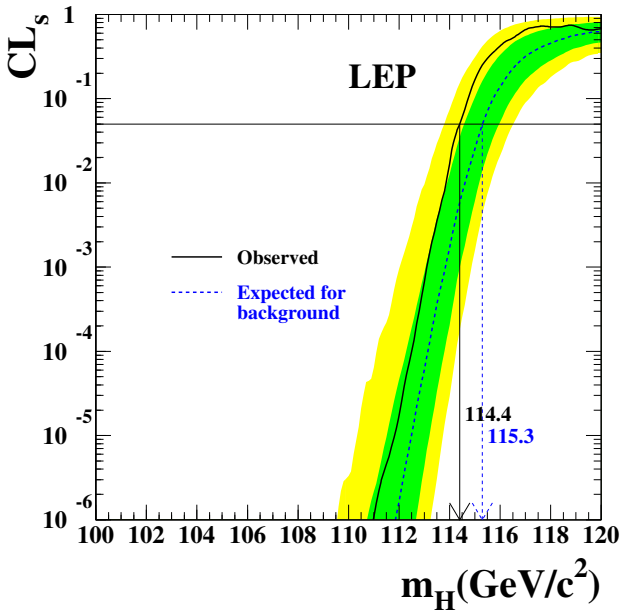

Figure 1.10: Confidence Level CL_s for the signal+background hypothesis in Higgs production at LEP2. The yellow green and yellow band around the median expected line correspond to the 68% and 95% probability bands, respectively.

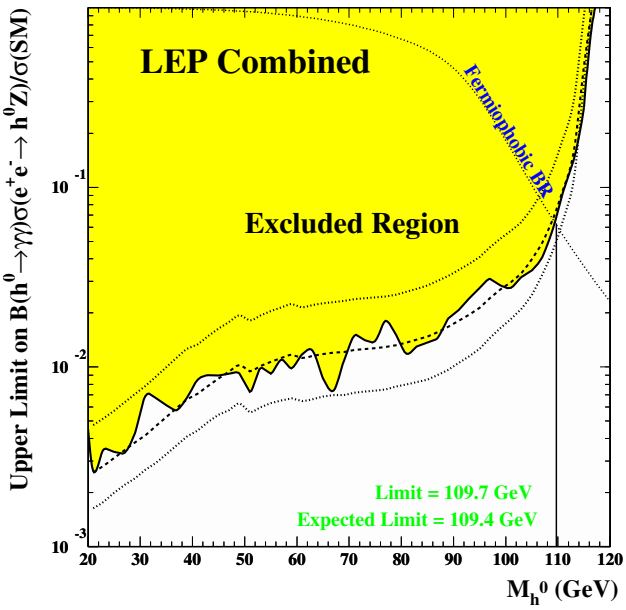

Figure 1.11: Combined LEP experiment upper limits for the Higgs bosons decaying into di-photons $B(h^0 \to \gamma\gamma) \times \sigma(e^+e^- \to h^0 Z)/\sigma(\mathrm{SM})$ as a function of Higgs mass at 95% confidence level.

1.5 Higgs boson searches at Tevatron

The two Tevatron collaboration, CDF and DØ, are performing not the SM Higgs boson searches but also the extended SM Higgs and the MSSM Higgs searches. At the present day, the Tevatron are already here that give us the new knowledge for the SM Higgs bosons for the first times in 5 years from the LEP result. In this section, let us discuss the performing SM Higgs searches and also fermiophobic searches at two Tevatron collaborations.

The SM higgs boson searches

The CDF and the DØ collaborations are searching the SM Higgs boson by looking at several Higgs production and decay modes as described §1.2 and §1.3 with too efforts. The CDF experiment searches the SM Higgs Boson under mainly six channels [21, 22, 23, 24, 25, 26], the four of them are sensitive to low mass SM Higgs ($M_h < 135$ GeV/c^2) because of the looking for $H \to b\bar{b}$ and $\tau^+\tau^-$ decay mode ($WH \to \ell\nu b\bar{b}$, $ZH \to \ell\ell b\bar{b}$, $VH \to \nu\bar{\nu}b\bar{b}$, and $H \to \tau^+\tau^-$), while the remaining two channels are sensitive to the high mass SM Higgs ($M_h > 135$ GeV/c^2) because of the looking for $H \to WW$ ($gg \to H \to WW \to \ell^\pm\nu\ell^\mp\nu$ and $WH \to WWW \to \ell^\pm\nu\ell^\pm\nu$ that is this study channel), they contribute to the combined Tevatron (CDF and DØ) upper limits on the SM Higgs boson production. The latest result (2009 winter) will show in §5.

Also the several SM Higgs search channels (total 6 channels [27, 28, 29, 30, 31, 32]) in the DØ experiment contribute to the Tevatron limits, in this case, included channel $H \to \gamma\gamma$ instead of $H \to \tau^+\tau^-$ channel. It is necessary to emphasize that the Tevatron combined result using 2.0-3.0 fb^{-1}, at 2008 Summer, excluded the SM Higgs mass 170 GeV/c^2 at 95% confidence level. Figure 1.5 shows the Tevatron combined upper limit on the ratios to the SM Higgs boson production in the high Higgs mass region [33].

The fermiophobic higgs boson searches

The Tevatron experiments, CDF and DØ also search for the fermiophobic Higgs boson. In 1st period run, so-called Run-I, the CDF collaboration set a lower mass limit by looking at di-photon events ($h_f \to \gamma\gamma$) at $\sqrt{s} = 1.8$ TeV with 100 pb^{-1} data [34]. The Higgs boson production considers the associated production with W and Z boson. The lower limit on the mass of the fermiophobic Higgs is 82 GeV/c^2 at 95% confidence level. The DØ collaboration also reported the lower limit on the mass at Run-I [35]. The limit are set by using the associated production with vector boson and vector boson fusion production and looking at di-photon plus 2-jets final state ($h_f \to \gamma\gamma$, $Z/W \to jj$). The DØ collaboration set the lower limits on the fermiophobic Higgs mass of 85 GeV/c^2 at 95% confidence level. Now, in the Run-II, the CDF and the DØ collaborations are also searching for the fermiophobic Higgs boson by using several the Higgs production and decay modes, for instance di-photon channel [36] and 3 or 4-photons channel [37], and also $Wh \to WWW$ channel as discussed this thesis has discovery potential.

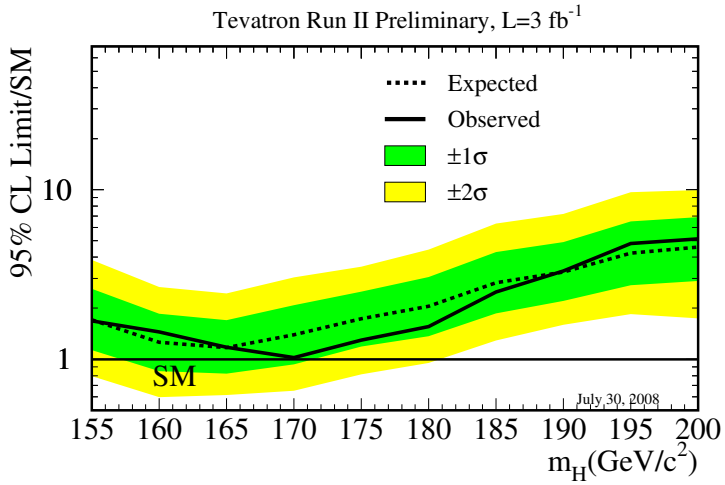

Figure 1.12: Tevatron combined upper limit on the ratios to the SM Higgs boson production as a function of the Higgs mass at 95% confidence level. The green and yellow bands indicate the 68% and 95% probability regions, respectively.

Chapter 2

Experimental apparatus

The experimental apparatus is located at the Fermi National Accelerator Laboratory (Fermilab) in Batavia, Illinois(USA). The Tevatron Collider represents the high energy frontier accelerator in particle physics. It is currently the source of the world highest energy proton-antiproton ($p\bar{p}$) collisions, and the only apparatus capable of probing the Higgs boson directly. The center-of-mass energy of the $p\bar{p}$ collision is $\sqrt{s} = 1.96$ TeV. The collisions occur at two points on an underground ring, which has a radius about 1km. There are two collision points at the Tevatron, each with its own associated experiment. hey are named the Coolider Detector at Fermilab (CDF II) and DØ. This analysis uses data collected with the CDF II Detector. The CDF II is a general purpose solenoidal detector which combines precision charged particle tracking, scintillator based calorimetry, and muon detection chambers and scintillators. Protons and antiprotons are bound states of quarks; thus because quarks participate in the strong, weak and electromagnetic interactions, each of these forces can be probed in a $p\bar{p}$ collision. The high energy collisions allow for the production of such exotic particles as $W^{\pm}$ and Z bosons and the top quark and so on. In this capter, we describe the collider apparatus and the CDF II detector design.

2.1 The accelerator complex

The Tevatron is the final stage in a chain of accelerators. With the accelerator complex, protons and antiprotons are create and gradually accelerated to collide at two designated points. The accelerator complex consists of several components. Figure 2.1 shows an aerial view of the Fermilab and accelerator complex. A diagram of the Tevatron is shown in Figure 2.1. The proton antiproton beams are created and accelerated in the chain of accelerators step-by-step. Each step of this production and acceleration is described in the following section.

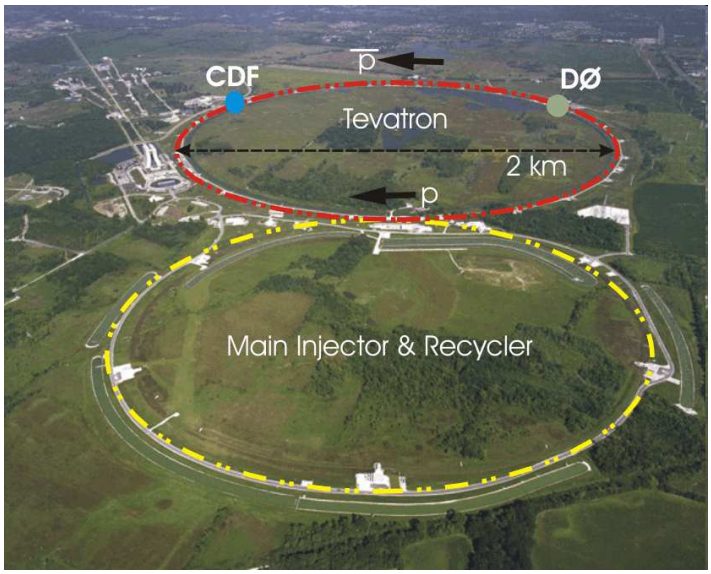

Figure 2.1: Aerial view of the accelerator complex at the FNAL. The upper ring is the Tevatron, and lower is the main injector.

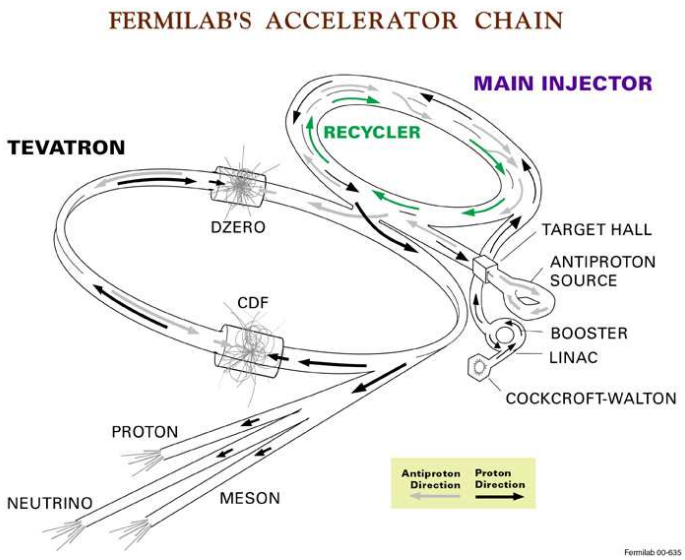

Figure 2.2: Diagram of the Tevatron. There are eight accelerators. They consist of linear accelerator and synchrotrons.

2.1.1 Proton production and boosting

The Cockcroft-Walton pre-accelerator provides the first stage of acceleration. It consists of a source housed in an electrically charged dome. The source converts hydrogen

gas to ionized gas H^- and accelerates to an energy of 750 keV of kinetic energy every 66 ms (15 Hz). The hydrogen gas is placed in an electric field which strips the hydrogen atoms of an electron to become H^+. These protons (H^+) are then attracted to a cesium anode where they attach and acquire two electrons to become H^- which is then repelled by the anode. These H^- ions are then accelerated by the Cockcroft-Walton to 750 keV.

After beam exits the accelerating column, it travels a transfer line called the 750 keV line and these ions are fed into the linear accelerator (Linac) in bunches at a rate of 201.24 MHz. The Linac is a circular synchrotron, approximately 150 m long which is the nest level of acceleration for the negatively charged hydrogen ions. It takes the ions with an evergy of 750 keV and accelerates them to an energy of 400 MeV. The acceleration in the Linac in done by a series of "kicks" from Radio Frequency (RF) cavities. The Linac can accelerate beam once every 66 ms (15 Hz). These bunches of accelerated ions are then injected into the Booster.

At injection, these ions are stripped of their electrons by passing them through a thin carbon foil, leaving behind protons. The proton accelerated from 400 MeV to 8 GeV with a series of magnets around a 75-meter radius circle with 18 RF cavities interspersed.

After leaving the Booster, protons are transferred to the Main Injector, a newly built circular accelerator that replaced the older Main Ring.

2.1.2 Main injector

The Main Injector (MI) is a circular synchrotron seven times the circumference of the Booster and slightly more than half the circumference of the Tevatron. Main Injector has 18 accelerating cavities. It can accelerate 8 GeV protons from the Booster to either 120 GeV or 150 GeV, depending on their destination. When used to stack antiprotons, the final energy is 120 GeV. When used to inject into the Tevatron, the final beam energy is 150 GeV. As well as accepting protons from Booster, the Main Injector can accept antiprotons from the Antiproton Source. The Main Injector can accelerate beam as fast as every 2.2 seconds.

2.1.3 Antiproton source and recycler

In order to produce antiprotons, the protons with 120 GeV are extracted from the MI and strike a nickel target at the Antiproton source. These high-energy protons striking the target produce a spray of all sorts of secondary particles. Using magnets to choose which momentum and charge we can collect 8 GeV antiprotons from this spray. Approximately one antiproton is produced per 10^5 protons. These antiprotons are directed into the Debuncher.

The Debuncher is a rounded triangular-shaped synchrotron with a mean radius of 90m. It can accept 8 GeV antiprotons from the target station, and maintain the beam at a energy of 8 GeV. Its primary purpose is to efficiently capture the high

momentum spread antiprotons coming from the target using a RF manipulation called bunch rotation which reduce the antiproton momentum spread. The reduction is done to improve the Debuncher to Accumulator transfer because of the limited momentum aperture of the Accumulator at injection.

The Accumulator is also triangular-shaped synchrotron and is mounted in the same tunnel as the Debuncher. It is the storage ring for antiprotons, all of the antiprotons made are stored here at 8 GeV and cooled until need.

The Recycler is an antiproton storage ring installed in the same tunnel as the MI. The proposed purpose of the Recycler was to recycle the antiproton from a Tevatron store, cooling them and storing them alongside those sent from the Antiproton Source. This was abandoned after early problems in RunII. The Recycler now accepts transfers only from the Antiproton Source and cools them further than the antiprotons Accumulator is capable. The Recycler uses both a stochastic cooling system and an electron cooling system. Stochastic cooling is used to cool the beam in Recycler, but loses its effectiveness with higher intensities. Once above 2×10^{12} antiprotons in the Recycler, Electron cooling is required. Electron cooling works on the principle of momentum transfer between electrons and antiprotons, a highly concentrated, cool beam of electrons is driven at the same energy as the antiprotons and laid overtop of the antiprotons. The resulting glancing collisions between electrons and antiprotons transfer some of the momentum from the "hot" antiprotons to the "cool" electrons. With enough electrons, a substantial longitudinal cooling force is produced by absorbing momenta from the antiprotons allowing for more compact, brighter bunches to send to the Tevatron.

2.1.4 Tevatron

The Tevatron is the final stage of Fermilab accelerator chain, with a circumference of approximately 6 km long. It is a circular synchrotron with a 1 km radius. It is composed of eight accelerating cavities, quadrupole and dipole focusing magnets.

The Tevatron receives protons and antiprotons infected from the MI or the Recycler at 150 GeV and accelerates them to a beam energy of 980 GeV. Since the antiprotons and protons are oppositely charged, they circle in opposite directions in the magnetic field, and are housed in the same ring. The Tevatron can sustain both beams over 1 day at onece. The protons and antiprotons are bunched into 36 bunches each, separated into 3 groups of 12 bunches. Within a group, each set of bunches is separated by 396 ns, with longer intervals between groups.

The Tevatron is cryogenically cooled to 4 K, and the acceleration cavities are made of superconductiong materials. It is desirable to use superconducting magnets because the very large fields necessary to maintain TeV-scale energies would require currents so large that it is not affordable for ordinary resistive magnets. The superconducting dipole magnets are used to steer the beams and quadrupole magnets are located near the two interaction regions at BØ and DØ to reduce the transverse beam size before collision.

The Tevatron is not a perfect circle. These are six sectors from A to F and each one has five service buildings (0-4). The "0" sections have large straight sections. The A0 is where the Tevatron tunnel connects to the proton injection point. It also contains one of the two beam aborts. At BØ and DØ, the colliding beams are focused into very narrow beam lines of order 32 μm. C0 is the location of the other beam abort. F0 houses the RF stations which "kick" the beam back into position if it has wandered off its axis. It is also where the transfer lines from the MI connect with the Tevatron. It also houses the transfer line to the antiproton source.

In normal operation, protons and antiprotons are injected into the Tevatron and circulate for up to a day in a "store", until beam losses and $p\bar{p}$ collisions have reduced the interaction rate sufficiently that the beams are dumped, at which point preparations for a new store begin. While a store is circulating in the Tevatron, the antiproton systems build up a new stack of antiprotons. If a store terminates abnormally (usually due to a "quench", when a superconducting magnet loses superconductivity, forcing the beam to be dumped), the Tevatron often must sitidle while the antiproton stack is built up again.

2.1.5 Luminosity

The luminosity of collisions can be expressed as:

$$\mathcal{L} = \frac{f N_B N_p N_{\bar{p}}}{2\pi(\sigma_p^2 + \sigma_{\bar{p}}^2)} F\left(\frac{\sigma_l}{\beta^*}\right), \tag{2.1}$$

where f is the frequency of bunch collisions, N_B is the number of bunched, $N_{p(\bar{p})}$ is the number of protons (antiprotons) per bunch, and $\sigma_{p(\bar{p})}$ is the protrons (antiprotons) RMS beam size at the interaction point. F is a form factor which corrects for the bunch shape and depends on the ratio of σ_l, the bunch length to β^*, the beta function, at the interaction point. The beta function is a measure of the beam width, and it is proportional to the beam's x and y extent in phase space. Table 2.1 shows the accelerator parameter in the current run (Run II). The current peak luminosity is $\sim 3.6 \times 10^{32}$ cm^{-2}s^{-1}. The delivered luminosity is 5.4 fb^{-1} and actual recorded luminosity is 4.5 fb^{-1}, which is collected between February 2002 and December 2008. Figure 2.1.5 shows peak and integrated luminosity measured with CDF.

2.2 The Collider Detector at Fermilab

The CDF Run II detector is an azimuthally and forward-backward symmetric apparatus designed to study $p\bar{p}$ collisions at the Tevatron. It is a general purpose solenoidal detector which combines precision charged particle tracking with fast projective calorimetry and fine grained muon detection. The detector is cylindrically symmeetric about about the beamline and extends for several meters through the BØ interaction region. The detector shown in a schematic view in Figure 2.2. Figure 2.2 show a elevation

Parameter	Run II
Number of bunhes (N_B)	36
Bunch length [m]	0.37
Bunch spacing [ns]	396
Protons/bunch (N_p)	2.7×10^{11}
Antiprotons/bunch ($N_{\bar{p}}$)	3.0×10^{10}
Total antiprotons	1.1×10^{12}
β^* [cm]	35
Interactions/crossing	2.3

Table 2.1: Accelerator parameters for Run II configurations.

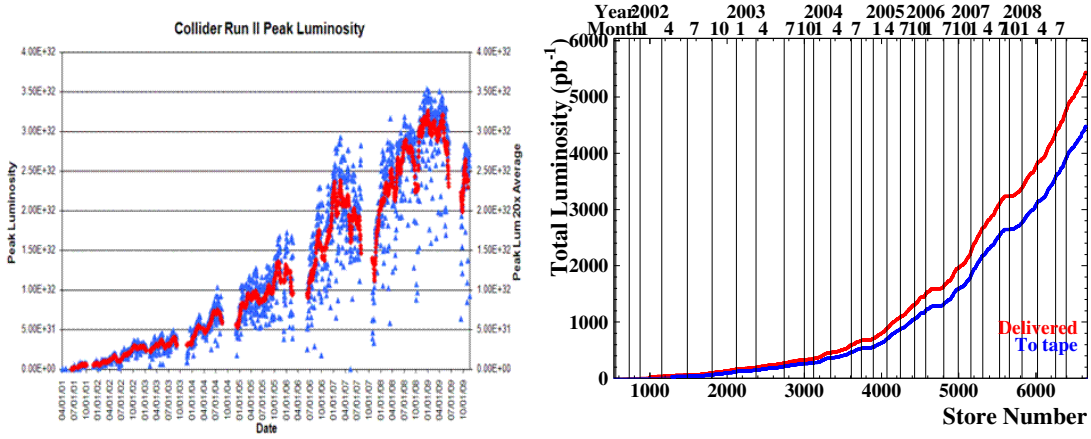

Figure 2.3: Left: CDF peak luminosity for each store. Right: Integrated luminosity as a function of store number observed at CDF over the Run II period for the Tevatron.

view of the CDFII detector. It is composed of several detectors which play a role in the detection of the particles

The inner detector is composed of the Silicon Vertex Detector and the Central Outer Tracker (COT) that surrounds the silicon detector inside a 1.4 T superconduction solenoid magnetic field parallel to the beam axis. These systems from a tracking system to measure precise tranjectories and momenta of charged particles and reconstruct primary and secondary veritices. Figure 2.4 is show the tracking detectors. A Time Of Flight (TOF) detector located outside the COT. Segmented electromagnetic and hadronic sampling calorimeters surround the tracking system and measure the energy flow of interaction particles. Charged particles in the volume will travel on helical trajectories and the curvature of these orbits which are measured. Measuring the curvature is equivalent to measuring the momentum of these particles. The muon system resides beyound the calorimetry and detects muons that escape the calorimeters. Muon Chambers detect the particles penetrating both Tracking Systems and Calorime-

try Systems. Muons deposit small amount of ionization energy in the material because they act as minimally ionizing particles (MIP), that is, the penetrating particles are mostly muons. The beam luminosity is determined by using Cerenkov counters located near beam.

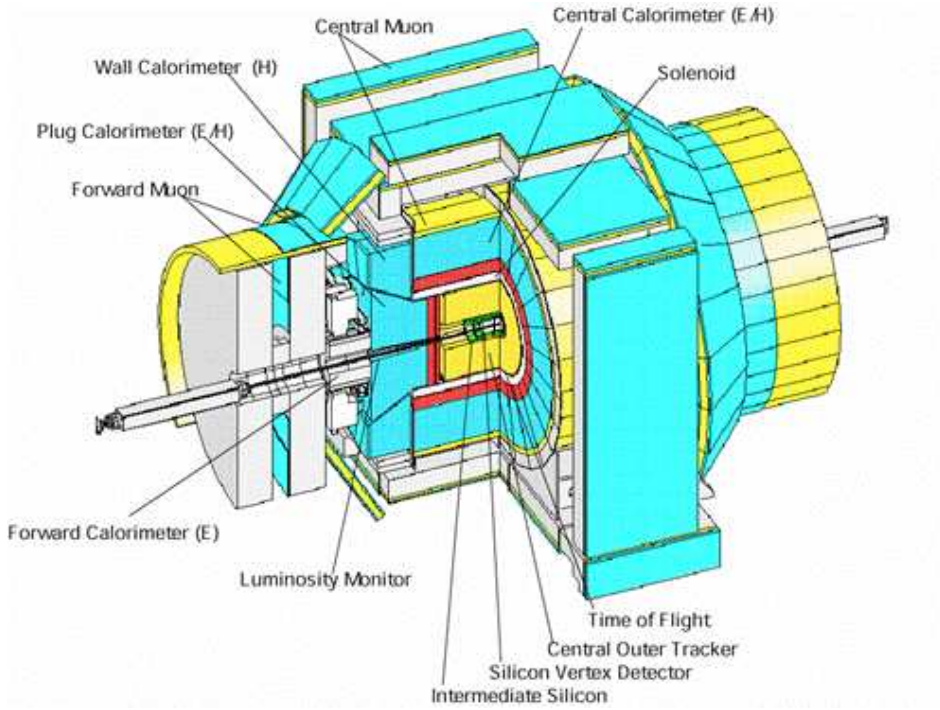

Figure 2.4: Cut away view of the CDF II detector.

2.3 Coordinate system in the CDF

The CDF has both azimuthal and forward-backward symmetry about the transverse plane passing through the interaction point, which results in the naturally arising cylindrical coordinate system. The standard coordinate system to be used in the CDF is the right-handed coordinate system. The z-axis is oriented along the colliding beams, and the positive z-direction is in the direction of the proton beam at the normal (z_0) collision point. The x-axis points toward the outside of the Tevatron ring (roughly northwest) and the y-axis is difined to point vertically upwards, where unit vectors satisfy $\hat{z} = \hat{x} \times \hat{y}$. It is convenient to work in cylindrical (r, z, ϕ) or polar (r, θ, ϕ) coordinates, where the azimuthal angle ϕ is the $x - y$ plane angle around the beam line. The polar angle θ is measured starting from the z-axis, and often replaced by pseude-rapidity:

$$\eta = -\ln\left(\tan\frac{\theta}{2}\right) \tag{2.2}$$

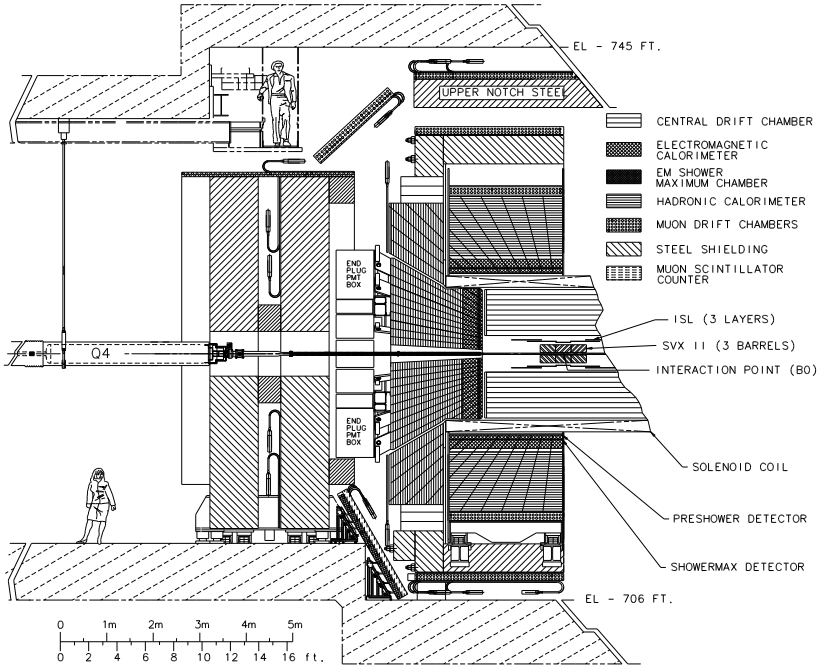

Figure 2.5: Elevation view of the CDF II detector.

The pseudo-rapidity is explained as the relativistic or mass less particle approximation of real rapidity

$$y \equiv \frac{1}{2}\ln\left(\frac{E+p_z}{E-p_z}\right). \tag{2.3}$$

where E is the energy of the particle and p_z is its longitudinal momentum. At the high energy limit, $E \sim p$ and $p_z = p\cos\theta$, pseudo-rapidity is same as real rapidity.

Many particles from the underlying event occur along the beam line from processes such as spectator quarks, beam halo, and initial radiation. For those particles, the transverse energies and momenta are small and are not very interesting to us. Hence, the transverse components of an event are important at CDF. The transverse momentum, p_{T} and the transverse energy, E_T are difined as follows.

$$p_{\mathrm{T}} \equiv p\ \sin\theta \tag{2.4}$$

$$E_{\mathrm{T}} \equiv E\ \sin\theta \tag{2.5}$$

where p is the magnitude of the momentum.

2.4 Tracking systems

The "integrated tracking system" at CDF, shown in Figure 2.4. The detector has a sylindrical tracking system surrounded in a 1.4 T solenoidal magnetic field for measurement of cahrged-particle momenta.

CDF II detector has an new open cell drift chamber, the Central Outer Tracker (COT) covers the region $|\eta| \leq 1.0$. Inside the COT, a silicon "inner tracker" is built from three components. Layer 00 (L00) is mounted on the beam pipe, very close to the beam line. Its primary purpose is to improve the impact parameter resolution. A micro-vertex detector at very small radii, so-called Silicon Vertex Detector (SVX-II), establishes the ultimate impact parameter resolution. Two additional silicon layers at intermediate radii, so-called Intermediate Silicon Layers (ISL), provides p_T resolution and b-tagging in the forward region $1.0 \leq |\eta| \leq 2.0$, and stand-alone silicon tracking over the full region $|\eta| \leq 2.0$. The stand-alone silicon segments allow integrated tracking algorithms which maximize tracking performance over the whole region $\eta \leq 2.0$. In the central region ($\eta \leq 1.0$), the stand-alone silicon segment can be linked to the fill COT track to give excellent p_T and impact parameter resolution.

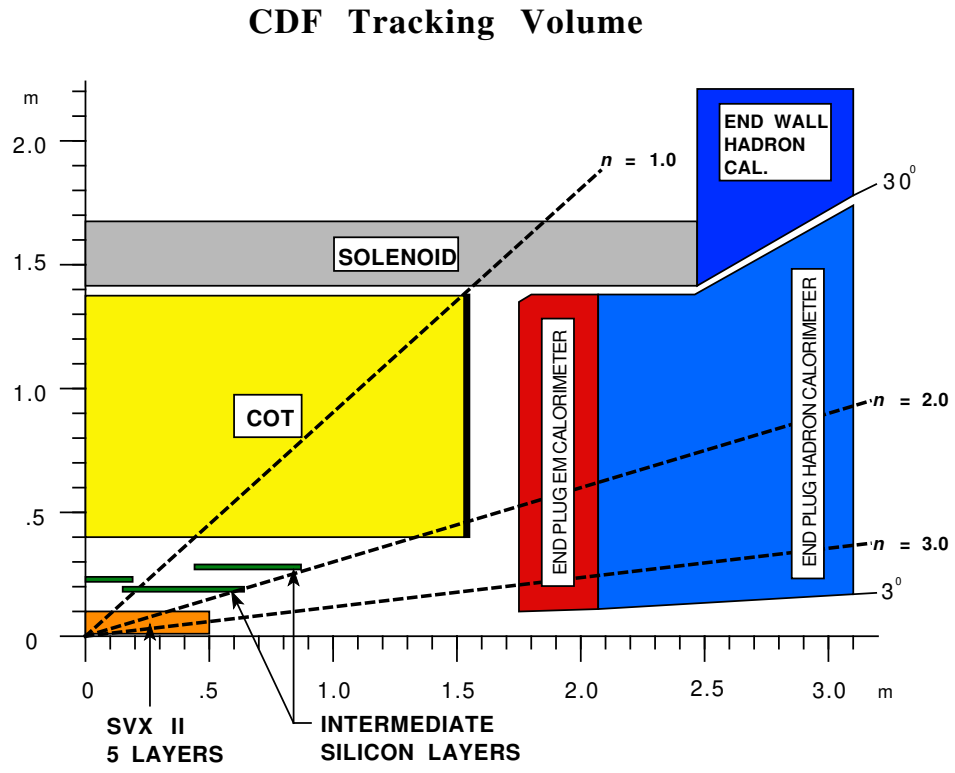

Figure 2.6: Longitudinal view of the CDF II detector tracking volume and plug calorimeter.

2.4.1 Layer 00

Layer 00 [39, 40] is installed directly in the beam pipe. L00 was added at beginning of RunII for two reasons. Firstly to improve the impact parameter resolution of the CDF detector. Placement of a minimal material silicon layer at a smaller radius provides a

precise measurement. Secondly, L00 was installed to extend the useful lifetime of the silicon system. The inner layers SVX-II will have a limited lifetime due to radiation damage. The design has six narrow (128 channels) and six wide (256 channels) groups in θ at $r = 1.35$cm and $r = 1.62$cm respectively. There are six readout modules in z, with two sensors bounded together in each module for a total length of 95cm. The sensors are single-sided p-in-n silicon with a 25(50)μm implant(readout) pitch. These have been produced by Hamamatsu Photonics (HPK), SGS-Thompson (ST) and Micron. These sensors can be biased up to 500V, limited by the maximum range of the power supplies. Figure 2.4.1 shows the end view of L00 and a part of SVX-II (L0 and L1).

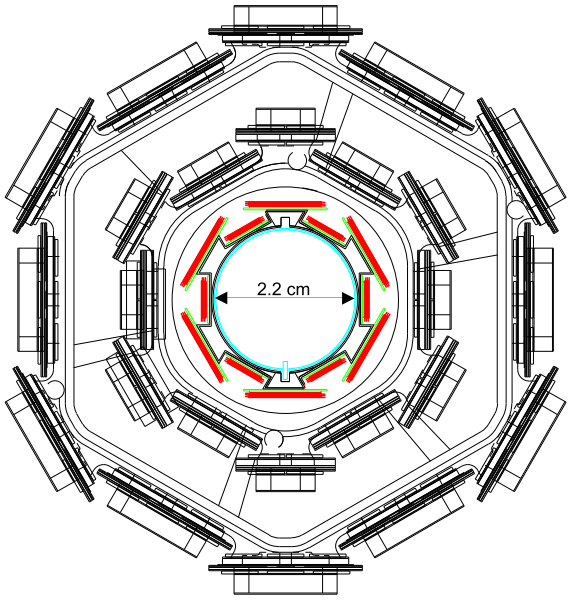

Figure 2.7: End view of Layer 00 (colored), also showing a part of SVX-II (un-colored).

2.4.2 Silicon Vertex Detector

Silicon Vertex Detector (SVX, SVX-II) [41] is the core detector for silicon tracking and for a trigger on tracks with large impact parameter with respect to the interaction point [42]. The SVX-II detector has 5 layers of double-sided sensors surround the L00 at radii from 2.5 to 10.6cm. Three layers (L0, L1, and L3) are made of Hamamatsu silicon with the n strips perpendicular to the p strips. The remaining two layers (L2 and L4) are Micron sensors with a stereo angle of 1.2° between the n and p strips. The strip pitch varies between 60 to 140μm, depending on the layer radius. The maximum bias voltages that can be applied to Hamamatsu and Micron sensors are 170 V and 70 V respectively, limited by the breakdown voltage of the integrated coupling capacitors and subtle sensor effects. The SVX-II can provide track information to $|\eta| < 2.0$.

Table 2.2 shows the design parameters of the SVX-II. Figure 2.4.2 shows 3D view and $r - \phi$ view for SVX-II.

Parameter	Layer 0 (L0)	Layer 1 (L1)	Layer 2 (L2)	Layer 3 (L3)	Layer 4 (L4)
Number of ϕ strips	256	384	640	768	896
Number of z strips	512	576	640	512	896
stereo angle (degree)	90	90	+1.2	90	−1.2
ϕ strip pitch [μm]	60	62	60	60	65
z strip pitch [μm]	141	125.5	60	141	65
Total width [mm]	171.140	25.594	40.300	47.860	60.170
Total length [mm]	74.3	74.3	74.3	74.3	74.3
Active width [mm]	15.300	23.746	38.340	46.020	58.175
Active length [mm]	72.43	72.43	72.38	72.43	72.38
Number of sensors	144	144	144	144	144

Table 2.2: Design parameters of the Silicon Vertex Detector.

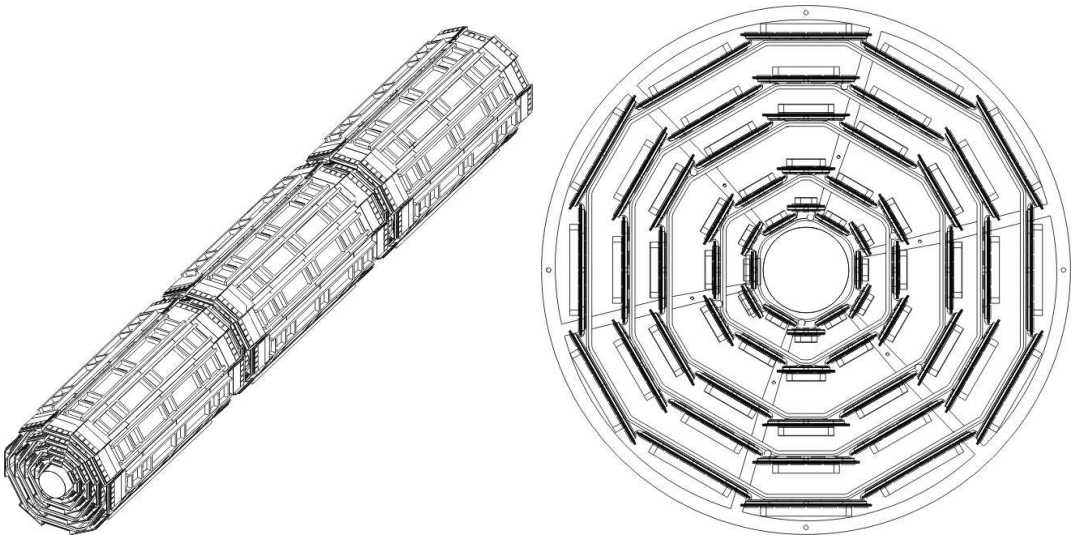

Figure 2.8: 3D view of the three barrels (left) and $r - \phi$ view of the barrel showing the 12 wedges with the 5 layers.

2.4.3 Intermediate Silicon Layers

Intermediate Silicon Layers (ISL) [43, 44] provides an extended forward coverage and links tracks between the COT and The SVX-II, and also can provide stand-alone 3D

track information in the forward region. The ISL detector has one central layer at radius of 22cm covering $|\eta| < 1.0$, and two forward layers at radii of 22cm and 28cm covering $1 < |\eta| < 2$, with total length of 3m. It is made of double-sided silicon with strips at a stereo angle of 1.2°, and a strip of 112μm. The breakdown voltage of the sensors is 100V limited by the breakdown voltage of the coupling capacitors.

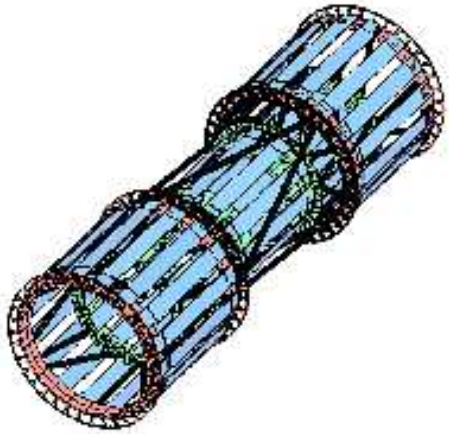

Figure 2.9: 3D veiw of the ISL spaceframe.

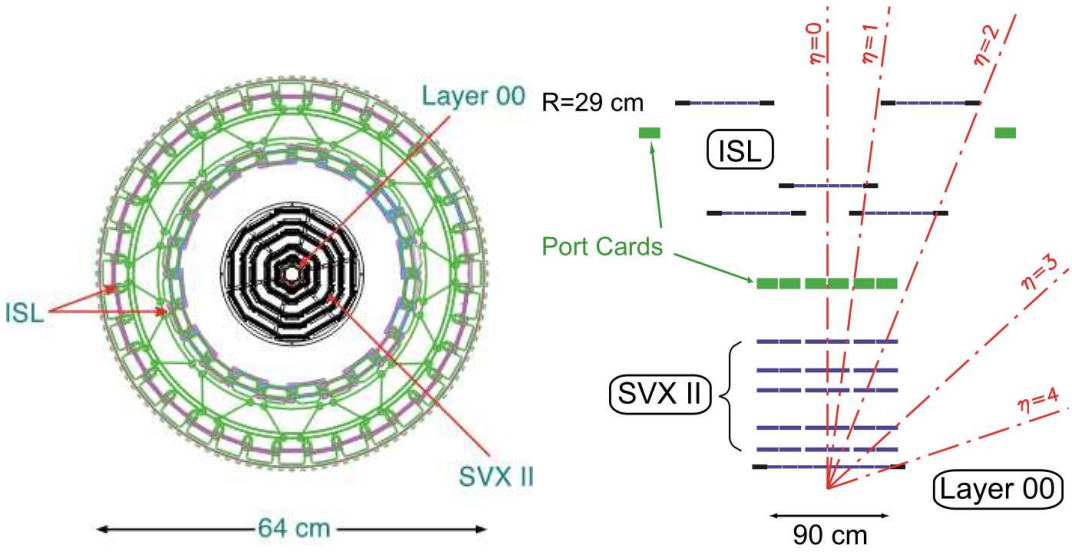

Figure 2.10: $r - \phi$ veiw (left) and $r - z$ view (right) of the silicon detectors.

2.4.4 Central Outer Tracker

The Central Outer Tracker (COT) [45] is a cylindrical open-cell drift chamber spanning from 44 to 132cm in radii, and 310cm long. It operates inside a 1.4 Tesla solenoidal magnetic field and is designed to find charged tracks in the region $|\eta| \leq 1.0$. The hit position resolution is approximately 140μm and the momentum resolution $\sigma(p_T) = 0.0015\ (\mathrm{GeV}/c)^{-1}$. The COT is segmented into 8 super-layers alternating stereo and axial, with a stereo angle of $\pm 2°$. Each super-layer contains 12 sense wires alternated with 13 potential wires which provide the field shaping within the cell yielding a total of 96 measurement layers. For the entire cell chamber, there are 30,240 sense wires and 32,760 potential wires. Operating with an Argon-Ethane (50:50) gas mixture the maximum drift time is approximately 180 ns. The cells ate tilted at 35° to account for the Lorentz angle such that the drift direction is azimuthal. Tracks originating from the interaction point which have $|\eta| < 1$ pass through all 8 superlayers of the COT. Tracks which have $|\eta| < 1.3$ pass through 4 or more superlayers. Table 2.3 shows a mechanical summary of the COT. Figure 2.4.4 shows cell layout for super-layer 2 (SL2). Figure 2.4.4 shows the east endplate slots sense and field planes.

Parameter	
Gas (Argon:Ethane)	(50:50)
Number of Layers	96
Number of Super-layers	8
Stereo Angle (degree)	+2, 0, −2, 0, +2, 0, −2, 0
Cells/Layers	168, 192, 240, 288, 336, 384, 432, 480
Sense Wires/Cell	12, 12, 12, 12, 12, 12, 12, 12
Radius at Center of SL (cm)	46, 58, 70, 82, 94, 106, 117, 129
Tilt Angle	35°
Material Thickness	1.6% X_0
Drift Field	1.9 kV/cm
Maximum Drift Distance	0.88 cm
Maximun Drift Time	177 ns
Number of Channels	30,240

Table 2.3: Design parameters of the Central Outer Tracker.

2.5 Calorimeter Systems

Segmented electromagnetic and hadron sampling calorimeters surround the tracking system and measure the energy flow of interacting particles in the $|\eta| < 3.6$. The calorimeter systems are divided into 2 systems with respect to the pseudo-rapidity range, central and plug(forward) region. The Central Electromagnetic Calorimeter

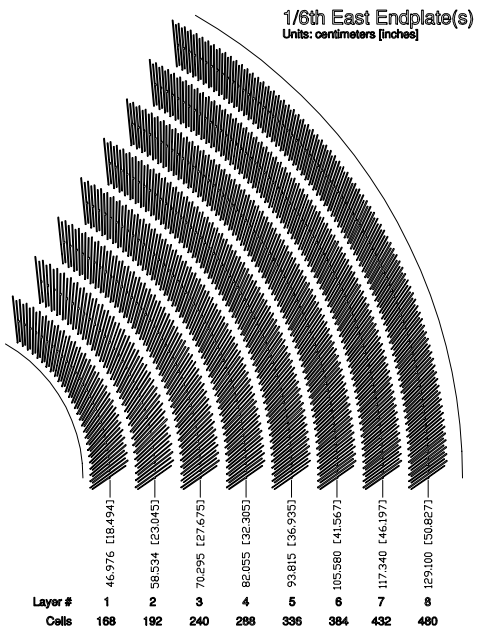

Figure 2.11: East endplate slots sense and field planes are at the clock-wise edge of each slot.

(CEM) covers the $|\eta| < 1.1$, which uses lead sheets interspersed with polystyrene scintillator as the active medium and employs phototube readout. The Central Hadronic Calorimeter (CHA) covers the $|\eta| < 0.9$, which uses steel absorber interspersed with acrylic scintillator as the active medium. The plug calorimeters, Plug Electromagnetic Calorimeter (PEM) and Plug hadron calorimeter (PHA), cover the $1.1 < |\eta| < 3.6$. They are sampling scintillator calorimeters which are read out with plastic fibers and phototubes.

2.5.1 Central Calorimeter

The Central Electromagnetic Calorimeter [46] detects electrons and photons and measures their energy. It is a lead-scintillator sampling system with tower segmentation, the each tower is 15° in $r - \phi$ plane. The CEM total thickness is 18 radiation length (32cm), to make sure that 99.7% of the electrons energy will be deposited. The CEM energy resolution is

$$\frac{\sigma_E}{E} = \frac{13.5\%}{\sqrt{E_T}} \oplus 2\% \tag{2.6}$$

where E_T is the transverse energy in GeV, $\oplus$ symbol means that the constant term is added in quadrature to the resolution, and position resolution is typically 2mm for 50 GeV/c electrons.

The Central Electromagnetic Showermax Chamber (CES) is used to identify electrons and photons using the position measurement to match with tracks, the transverse

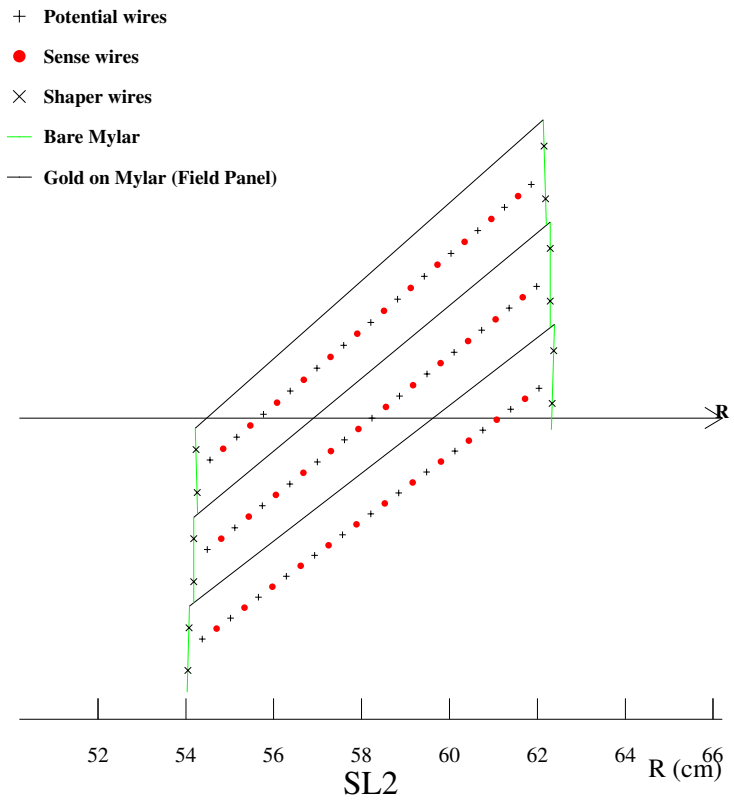

Figure 2.12: Nominal cell layout for SL2.

shower profile to separate photon from π^0s, and pulse hight to help identify electromagnetic showers. The CES is located at approximately 6 radiation lengths deep at the expected shower maximum of particles in the EM calorimeter. The CES module is a multi-wire proportional chamber with 64 anode wires parallel to the beam axis.

The Central Preshower Detector (CPR) [48] is located at between the front face of the EM calorimeter and the magnet coil. The CPR can be useful in the $\pi-$photon separation and electron identification. The CPR was replaced the slow gas chamber with a faster scintillator version which has a better segmentation during RunII in 2004. The new CPR is used to improve the jet energy resolution.

The Central Hadronic Calorimeter [47] is an iron-scintillator sampling calorimeter, covering range $|\eta| < 0.9$, approximately 4.5 λ_0 interaction length, and the energy resolution is

$$\frac{\sigma_E}{E} = \frac{50.0\%}{\sqrt{E_T}} \oplus 3\%. \tag{2.7}$$

The Wall Hadronic Calorimeter (WHA) also an iron-scintillator sampling calorimeter, covering range $0.7 < |\eta| < 1.3$. The WHA is 4.5 λ_0 interaction length, and the

energy resolution is

$$\frac{\sigma_E}{E} = \frac{75.0\%}{\sqrt{E_T}} \oplus 4\%. \tag{2.8}$$

2.5.2 Plug Calorimeter

The plug calorimeter covers $1.1 < |\eta| < 3.6$, corresponding to polar angles $3^\circ < \theta < 37^\circ$ as shown in Figure 2.5.2. Each plug wedge spans 15° in azimuth, however from $1.1 < |\eta| < 2.11$ (37° to 14°) the segmentation in ϕ is doubled, and each tower spans only 7.5°. There is an electromagnetic section (PEM) with a shower position detector (PES), followed by a hadronic section (PHA).

The PEM [49] is lead-scintillator sampling calorimeter, with unit layers composed of 4.5mm lead and 4mm scintillator. There are 23 layers in depth for a total thickness of about 21 X_0 radiation length at normal incidence. The PEM has an energy resolution is

$$\frac{\sigma_E}{E} = \frac{16\%}{\sqrt{E_T}} \oplus 1\%. \tag{2.9}$$

The PHA is an iron-scintillator sampling calorimeter, approximately 7 λ_0 in depth, and has an energy resolution of

$$\frac{\sigma_E}{E} = \frac{80\%}{\sqrt{E_T}} \oplus 5\%. \tag{2.10}$$

The PEM shower maximum detector is located about 6 λ_0 deep within the PEM, and is constructed of two layers of scintillating strips. The strips are 5mm wide, and roughly square in cross section. Position resolution of the PES is about 1mm. The summaries of design parameters for the calorimeter are shown in Table 2.4.

Calorimeter	Coverage	Energy Resolution (%)	Thickness	Absorber
CEM	$\|\eta\| < 1.1$	$13.5/\sqrt{E_T} \oplus 2$	18 X_0	3.18 mm lead
PEM	$1.1 < \|\eta\| < 3.6$	$16.0/\sqrt{E_T} \oplus 1$	21 X_0	4.5 mm lead
CHA	$\|\eta\| < 0.9$	$50.0/\sqrt{E_T} \oplus 3$	4.5 λ	2.5 cm iron
WHA	$0.7 < \|\eta\| < 1.3$	$75.0/\sqrt{E_T} \oplus 4$	4.5 λ	5.0 cm iron
PHA	$1.3 < \|\eta\| < 3.6$	$80.0/\sqrt{E_T} \oplus 5$	7.0 λ	5.08 cm iron

Table 2.4: Design parameters of the calorimeter.

2.6 Muon Detectors

Muons penetrate the tracking systems and the calorimeters leaving very little energy. The reason is muons produce much less bremsstrahlung than electrons and therefore do not produce electromagnetic showers, due to their larger mass. The CDF muon

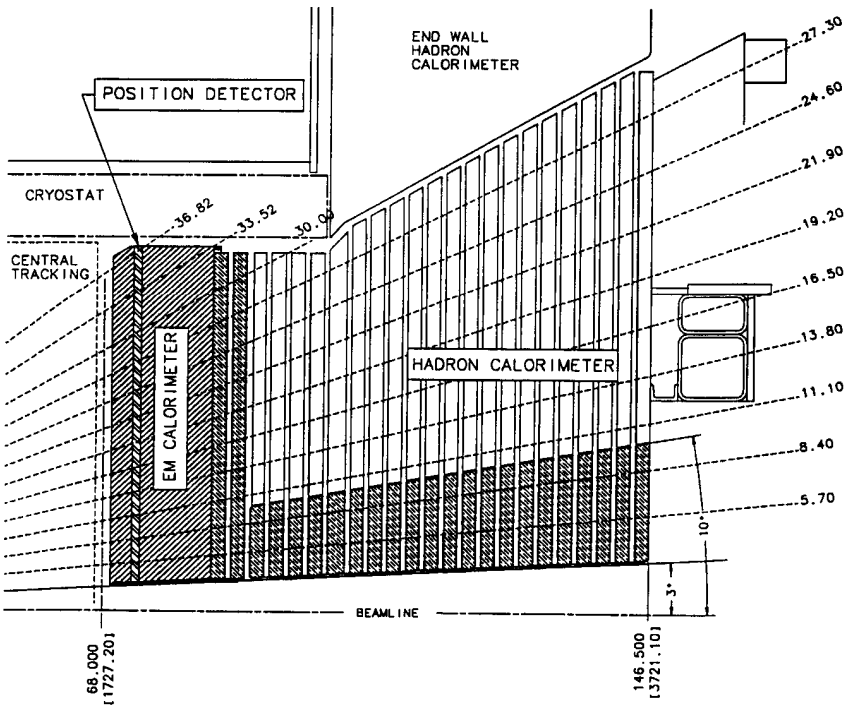

Figure 2.13: Cross section of the plug calorimeter (PEM and PHA).

systems [38] use this property by placing detectors behind enough material. Muons deposit minimum ionizing energy in the calorimeters matched with a track in the COT. The momentum of these muons is measured by their bend in the solenoidal field using the COT. The central muon system is capable of detecting with transverse momentum $p_T \geq 1.4$ GeV, through their interaction with the gas and subsequent drift on the produced electrons toward the anode wires. The muon detectors consist of four separate subsystems: the central muon chambers (CMU), the central upgrade (CMP), the central muon extension (CMX), and the barrel muon detector (BMU). Table 2.5 shows design parameters of the muon detector. Figure 2.6 shows the effective muon detector coverage in $\eta - \phi$ plane.

The CMU detector locates directly outside of the central hadron calorimeter, 35 m from the interaction point, and covers the region of $|\eta| \leq 0.6$. It is divided into 24 east and 24 west 15° wedges. Each wedge contains three muon chambers and each muon chamber consists of four layers of four rectangular drift cells staggered in order to eliminate hit position ambiguities. A stainless steel sense wire a diameter of 50μm is located in the center of each cell. A muon object is created by forming a "stub" from hits in the muon chambers matching it to an extrapolated COT tracks.

The CMP consists of a second set of muon chambers behind additional 60cm of

steel in the region $55° \leq \phi \leq 90°$. The chambers are fixed length in z and form box around the central detector. The pseudorapidity coverage thus varies with azimuth as shown in Figure 2.6.

The central extension consist of conical section of drift tubes (CMX) in polar angle from 42° to 55° ($0.6 \leq |\eta| \leq 1.0$). The top two wedges (Wedge 5 and 6) of the west CMX is called the "Keystone". There are no top 2 wedge on the east CMX due to cryogenic utilities servicing the solenoid. The bottom 6 wedges (Wedge 15-20) are called "Miniskirt". The design parameters of the muon detector are shown in Table 2.5.

Muon detector	CMU	CMP	CMX
Coverage	$\|\eta\| < 0.6$	$\|\eta\| < 0.6$	$0.6 < \|\eta\| < 1.0$
Drift tube length [cm]	226	640	180
Max drift time [μs]	0.8	1.4	1.4
Total drift tubes	2304	1076	2208
Pion interation length (λ)	5.5	7.8	6.2
Minimum detectable muon p_T (GeV/c)	1.4	2.2	1.4

Table 2.5: Design parameters of the moun detector.

2.7 Luminosity Monitor

The beam luminosity has been measured using the process of inelastic $p\bar{p}$ scattering. The cross section is $\sigma_{\text{in}} \sim 60$ mb. The rate of inelastic $p\bar{p}$ interaction is given by

$$\mu f_{\text{BC}} = \sigma_{\text{in}} L \tag{2.11}$$

where L is the instantaneous luminosity, f_{BC} is the rate of bunch crossing in the Tevatron and μ is the average number of $p\bar{p}$ interaction per bunch crossing. In CDF Run II, Cherenkov luminosity counters (CLC) [50, 51] is used to measure the luminosity by counting number of $p\bar{p}$ interaction μ accurately.

The detector consists of two modules which are located in the "3 degree holes" inside the end-plug calorimeter in the forward and backward region and which cover $3.7 < |\eta| < 4.7$ range. Each CLC detector module consists of 48 thin, long, conical, gas-filled Cherenkov counters. The counters arranged around the beam pipe in three concentric layers, with 16 counters each, and pointing to the center of the interaction region. They are built with reflective aluminized mylar sheets of 0.1mm thick and have a conical shape. The cones in two outer layers are about 180cm long and the inner layer counters have the length of 110cm. The Cherenkov light is detected with fast, 2.5cm diameter, photomultiplier tubes. The tubes have a concave-convex, 1mm thick, quartz window for efficient collection of the ultra-violet part of Cherenkov spectra and operate at a gain of 2×10^5. The counters are mounted inside a thin pressure

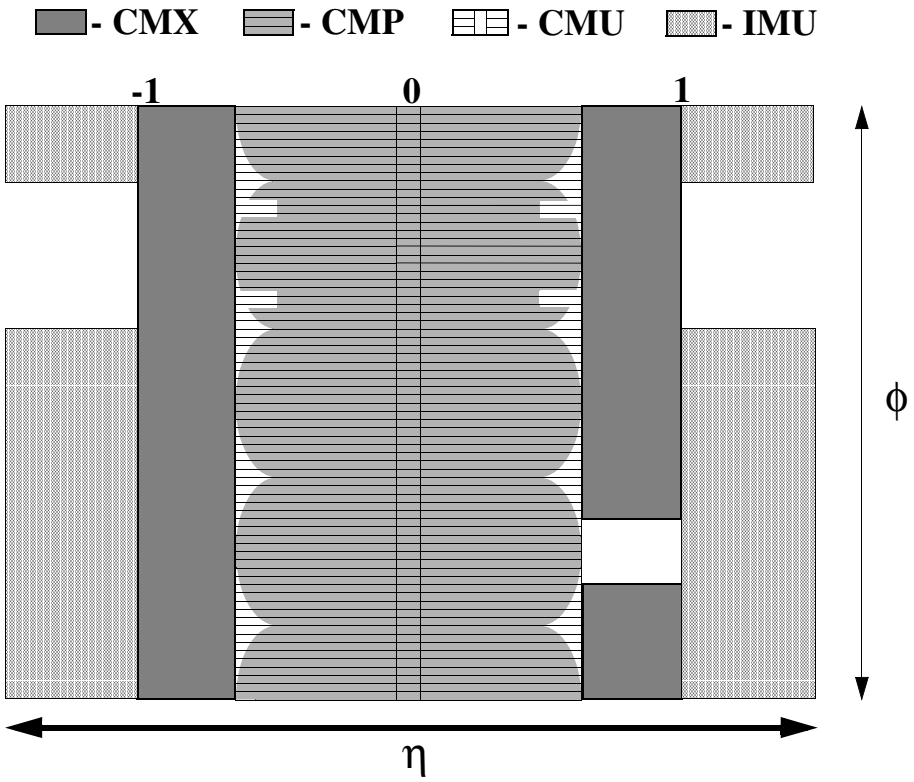

Figure 2.14: Muon detector coverage in $\eta - \phi$ plane.

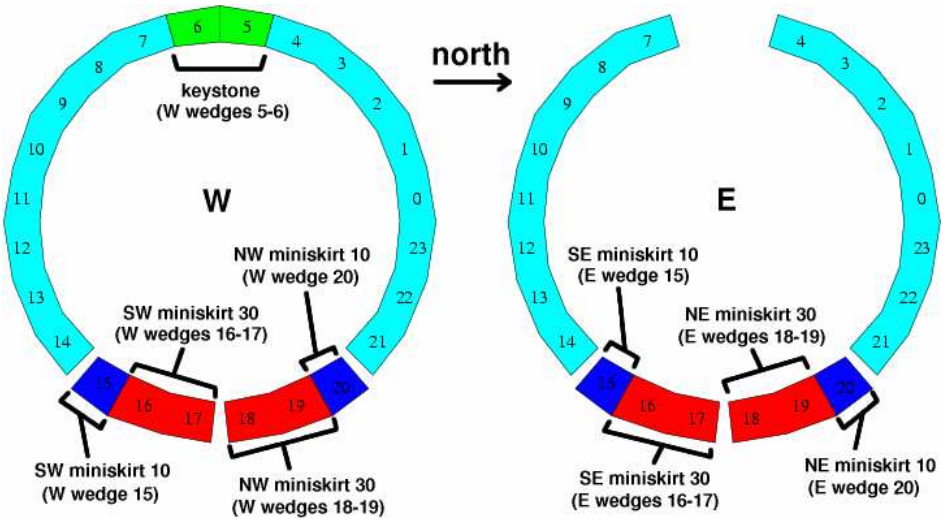

Figure 2.15: CMX detector in $r - \phi$ plane.

vessel made of aluminum and filled with isobutane. The systematic uncertainty of the luminosity measurement is dominantly coming from the uncertainty of the inelastic $p\bar{p}$ cross section ($\sim 3\%$), the CLC acceptance ($\sim 2\%$), and the non-lineality of the CLC acceptance due to CLC occupancy saturates as growing luminosity due to the finite number of counters ($< 2\%$).

2.8 Trigger Systems

The trigger plays an important role on hadron collider experiment because the collision rate is much higher than the rate as which data can be stored on tape. The crossing rate of the Tevatron under 36 on 36 bunch operation is 7.6MHz, corresponding to 396 ns collision separation. The role of the trigger is to effectively extract the most interesting physics events from the large number of minimum bias events. For Run II, CDF employs a three-level trigger system to selectively capture interesting events. The levels are denoted simply as "L1", "L2" and "L3", with each subsequent level making more complicated decisions and requiring successively longer processing times. Figure 2.8 shows schematic of the CDF trigger system.

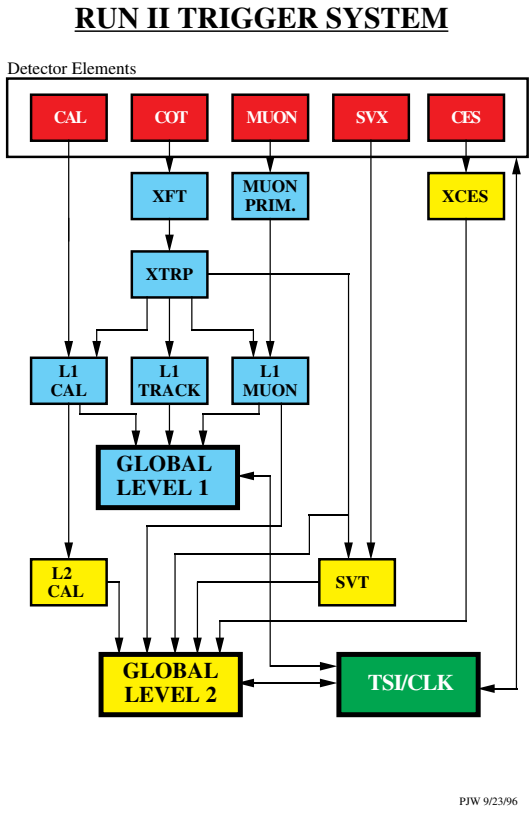

Figure 2.16: Book diagram of the trigger pass for Level 1 and Level 2.

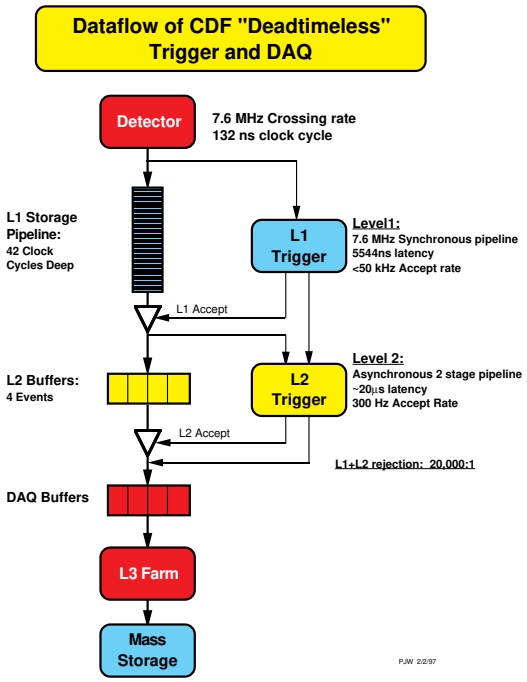

Figure 2.17: Schamatic diagram of the trigger and DAQ.

2.8.1 Level-1

The first level of trigger selection Level-1 (L1) uses custom designed hardware to find physics objects based on a subset of the detector information and then makes a decision based on simple counting of these objects. The input to the L1 hardware comes from the calorimeters, tracking chambers and muon detectors. The decision to retain an event for further processing is based on the number and energies of the electron, jet and muon candidates as well as the missing energy in the event, or on the kinematic properties of few of these objects. The L1 hardware consists of three parallel synchronous processing streams which feed inputs of the single Global Level-1 decision unit. One stream finds calorimeter objects, another finds muons and the third finds tracks in the central region. The L1 trigger can be formed using these streams singularly as well as AND or OR combinations of them. All elements of the L1 trigger are synchronized to the same 132ns clock, with a decision made every 132ns by Global L1. In the period of the data taking considered in this analysis the accelerator was the two intermediate clock cycles automatically rejected. The maximum L1 accept rate is 20kHz, while the typical one is 12kHz.

2.8.2 Level-2

Events accepted by L1 are processed by the second level of trigger Level-2 (L2), which is composed of several asynchronous subsystems. These provide input data to pro-

grammable L2 processors on the Global L2 crate, which determine if any of the L2 trigger are satisfied. Processing for L2 trigger decision starts after the event written into one of the four L2 buffers by a L1 accept. When L2 is analyzing the event in one of the buffers, that buffer cannot be used additional L1 accept. If all the four are full, the deadtime of the data acquisition is increased. It follows that the time required for a L2 decision needs to be less than about 80% of the average time between L1 accepts in order to keep the deadtime as low as possible. For this purpose L2 has been pipelined into two stages each taking approximately 10μs, which is sufficient to keep the deadtime at a minimum, even if L1 had an accept-rate of 50kHz. The L2 buffers perform a limited event reconstruction using essentially all the information used in L1, but with higher precision. In addition, at L2, data from the central shower-max detector and the SVX are available, which improve respectively the identification of electrons and photons and the reconstruction of the secondary vertices. Furthermore, a jet reconstruction algorithm is provided by the L2 cluster finder. After all of the data are stored in the processors, the event is examined to check if the criteria of any of the L2 triggers have been satisfied. This operation can be performed while the new events are being loaded into memory, thus not affecting the dead time. The typical L2 accept rate, as of this writing, is between 100 and 300Hz, depending on the initial luminosity.

2.8.3 Level-3

The Level-3 (L3) trigger subsystem is composed of two main components, the Event Builder (EVB) and the Level-3 Farm. Level-1 and Level-2 systems need to make their decisions at very high rate which makes it impossible to fully reconstruct each event. While Level-1 and Level-2 algorithms use small predefined pieces of event data to make their decision, the event pieces are stored in the buffers of the 140 Front End crates which constitute the EVB. After a L2 decision is made, the Event Builder assembles all event fragments from the Front End crates into one data block.

The 16 subfarms which compose the L3 Farm receive event fragments from the EVB and build complete events into the appropriate data structure for analysis. Since it takes about one second for one computer unit to make a trigger decision on one event, it takes a large farm of 250 Dual Pentiun Linux personal 5computers (called "processors") to ensure the required input rate. Each subfarm contains between 14 and 18 processor nodes and one "converter" node, which acts as "farm input" distributing the data flow coming from the EVB.

The events are then passed to a trigger algorithm (a different one for each processor) that categorizes the event and makes the decision as to whether or not to permanently store it. The selected event are passed to the Data Logger subsystem. During the building processing, the event integrity is checked. The L3 algorithms take advantage of the full detector information and improved resolution unavailable to lower trigger levels. This includes full three-dimensional track reconstruction and tight matching of tracks to calorimeter and muon-system information. Results from the lower level are used or drive the algorithms, which are based on the off-line analysis packages. This

is a modular and separated filter modules for specific triggers. L3 accept events with a rate of approximately 75Hz.

Chapter 3

Likelihood-based lepton identification

Our physics objective is to search for the low-mass fermiophobic higgs and the high-mass Standard Model (SM) higgs boson using like-sign (LS) dilepton events produced by the process

$$qq' \to W^{\pm}h \to W^{\pm}W^{*}W^{*} \to \ell^{\pm}\ell^{\pm} + X \,, \tag{3.1}$$

where the leptonic decay of two W bosons with the same electric charge makes the LS dilepton final state. The relevant higgs boson mass region is above 160 GeV/c^2 for the SM higgs boson where the branching fraction of $H \to WW^*$ supersedes that of $H \to b\bar{b}$. However, the search for this signature in low-mass regions is also important because we need to investigate various higgs boson couplings as an essential test to convince that signals are attributed to the higgs boson production as we expect. This channel also covers the case beyond the SM that the higgs boson couples only to the gauge bosons, which is referred to as the fermiophobic Higgs boson. On the experimental side, the LS dilepton event is one of the cleanest signature in hadron collisions. This analysis is therefore expected to have a high potential of the sensitivity to search for the higgs boson.

The LS requirement is quite effective to suppress QCD and known electroweak processes, however fake-lepton backgrounds still remain at a considerable level. We traditionally use cut-based identification (ID) methods for the lepton selection in high-p_T physics analyses, but given that the higgs search is difficult mainly due to small predicted production cross-sections, developments of more sophisticated ID methods are worth to pursue. In this study, we investigate a likelihood-based lepton ID (LLID) which combines various lepton ID variables into a single likelihood function and compare efficiencies with those of our cut-based ID method (CLID) which is fairly standard.

3.1 Likelihood function

With control samples of real and fake leptons, we separately normalize distributions of ID variables, taking into account of the bin widths of histograms[1], to obtain the probability distribution functions (PDFs). We define the likelihood that a lepton candidate is indeed a real lepton to be

$$S = \prod_{i=1}^{n} S_i \,, \tag{3.2}$$

ignoring any correlations between the ID variables, where S_i is the PDF of real leptons for the i-th ID variable. The likelihood that the lepton candidate is a fake lepton is similarly given as

$$B = \prod_{i=1}^{n} B_i \,. \tag{3.3}$$

The final likelihood estimator is constructed as:

$$L = \frac{S}{S+B} \,. \tag{3.4}$$

We expect that lepton candidates with values of L close to unity are real leptons, while values close to zero indicate most probably fake leptons.

3.2 Lepton identification variables

3.2.1 Electron

We choose 8 variables for our likelihood method.

- E/p
  This is defined by the ratio of the cluster energy to the beam constrained COT track momentum. If the object pointing calorimeter cluster is an electron, its momentum measured by the COT track should match with the energy measured for the calorimeter cluster, i.e. $E/p \simeq 1$.

- χ^2_{strip}
  The pulse height shape in the strip view (r-z) of the CES detector is compared to the same profile extracted from test-beam data of electrons using χ^2 test. To allow for a comparison that is valid for energies lower than 10 GeV, the raw χ^2_{strip} is multipied by $(p/10.0)^{\alpha}$, where the p is the track momentum and α is given by

$$\alpha = 0.85 + 0.15\exp(-p/15.0) - p/1000 \,. \tag{3.5}$$

[1] As long as we use the same binning for a given variable between the signal and background, which we actually do, the bin width cancels out in the final likelihood estimator.

- HA/EM
  This quantity is the ratio of 2-tower hadronic energy deposited in the hadronic calorimeter (CHA and WHA) to the 2-tower electromagnetic energy deposited in the central electromagnetic calorimeter (CEM). This ratio should be small, that is, the energy deposition in the electromagnetic calorimeter is much higher than that in the hadronic calorimeter.

- $L_{\rm shr}$
  The purpose of this quantity is to provide some discrimination of electrons and photons from hadronic showers faking these particles in the CEM. This is done by comparing the observed energy sharing between towers to that expected for a true electromagnetic shower, taken with test-beam data:

$$L_{\rm shr} = 0.14 \sum_i \frac{E_i^{\rm adj} - E_i^{\rm exp}}{\sqrt{(0.14\sqrt{E})^2 + (\Delta E_i^{\rm exp})^2}} \,, \tag{3.6}$$

  where $E_i^{\rm adj}$ is the measured energy in towers adjacent to the seed tower, $E_i^{\rm exp}$ is the expected energy in the adjacent tower from test beam data, $\Delta E_i^{\rm exp}$ is the error on the energy estimate.

- $Q \times \Delta x_{\rm CES}$:
  The $\Delta x_{\rm CES}$ is the distance, in units of cm, in the transverse plane (r-$\phi(x)$) between the track extrapolated to the radius of the CES and the actual cluster position measured by the CES. We sign it with the charge of the candidate track.

- $\Delta z_{\rm CES}$:
  This variable is the distance, in units of cm, in the r-z plane between the track extrapolated to the CES radius and the actual cluster position measured by the CES.

- $E_{\rm CES}/p^*$
  This is the ratio of the wire cluster pulse height measured in the Central Electromagnetic Showe-Max (CES), corrected for chamber warps, to the $p^* = 10(p/10)^\alpha$, where the p is the track momentum and α is defined in Eq. (3.5). The value for a real electron is expecteed to be around 1.

- CPR or CP2
  The response of the Central Pre-Radiator detector (CPR) or upgraded detector (CP2) detector corresponding to an electron cluster in units of the number of minimum-ionizing-particles (MIPs).

3.2.2 Muon

We choose 4 and 3 variables to define our likelihood function for CMUP and CMX muons, respectively.

- EM and HA
  Muon deposite small energies in the calorimeters due to the ionization. So as to maintain good efficiencies for high energy muons, the cuts are dependent on the momentum.

- $r \times \Delta\phi$
  This quantity is the track-stub matching in the r-ϕ plane and defined for the CMU, CMP, and CMX muon detectors.

3.3 Real-lepton samples

3.3.1 Leptons from Z decays

A natural choice of real-lepton control sample is the leptons from Z decays. The high-p_T inclusive lepton samples, `bhel*` and `bhmu*`, corresponding to an integrated luminosity of 4.8 pb^{-1} are used to select these leptons. We apply the same asymmetric kinematical cuts, where the high-p_T cut is $E_T > 20$ GeV ($p_T > 10$ GeV/c) for leading electrons or $p_T > 20$ GeV/c for muons, while the low-p_T cut is $E_T > 6$ GeV ($p_T > 6$ GeV) for electrons or $p_T > 6$ GeV for muons. The leading lepton is required to fully pass other lepton selection using our CLID which is listed in Table 3.1. The 2nd lepton, which serves as a probe, is required to pass the track quality and isolation cuts. The conversion veto is also applied if it is an electron. In order to ensure leptons be originating from Z decays, we require the two leptons have opposite charges and the invariant mass in a Z-mass window 81–101 GeV/c^2.

Figures 3.1 and 3.2 show E_T and p_T distributions of probe leptons from Z decays. Although the kinematical cut on the probe leptons is $p_T > 6$ GeV/c, the leptons from Z decays have much higher typical p_T because of the heavy mass of the Z boson. The distributions from the higgs Monte Carlo (MC) samples for the mass of 110 GeV/c^2 and 160 GeV/c^2 are also included in the figures. As we see, the leptons from the higgs boson that we want to search do not necessarily have such high p_T as Z leptons. Since the lepton ID variables have energy dependences in general[2], mismatches of the p_T region between the sample used to construct the PDFs and that the LLID is applied to would introduce inefficiencies.

3.3.2 Electrons from photon conversions

As an attempt to create PDFs covering relatively low-p_T electrons, we collect conversion electrons with the same 6 GeV/c cut in the high-p_T inclusive electron samples. The E_T and p_T distributions are already shown in Fig. 3.1. We have more electrons in lower p_T regions comapred to the Z electrons but the situation that there are mismatches in the p_T regions is basically the same. We might have to use low-p_T inclusive lepton samples if we want to pursue this direction of the analysis, which we do not include.

[2]For example, HA/EM or CPR responses.

3.3.3 Leptons from higgs Monte Carlo samples

What happens if we directly use higgs MCs to create signal PDFs? This is probably a new idea at CDF. We usually use signal MCs to contruct final discriminants based on various kinematical/topological information to separate signals from backgrounds in the final samples, but usually do not for the event selection at lower levels such as the lepton ID. Immediate issues are, of course, possible mis-modeling of the ID variables by the MCs. Here, they particularly result in over-efficiencies for the higgs MC-events compared to real higgs-events that might exist in the data. But one can see that the issues are not special to this scheme. We have to deal with any aspects of mis-modeling by the MCs anyways no matter what kind of event selection we perform and we argue that the situation is the same as the usual CLID case. Effects of mis-modeling are, then, to be absorbed in the relevant, the so-called, scale factors. Final checks can be done by measuring cross-section of known physics processes, and comparing background expectations with the data in control and/or pilot regions with various kinematical biases. It is we think interesting to see if this scheme works.

3.4 Fake-lepton samples

The words "fake leptons" here are used to mean rather generic objects including non-prompt real leptons such as those coming from (semi-)leptonic decays of heavy-flavor hadrons as well as literal fake leptons. The same selection as is used for the probe leptons of the signal samples is applied to QCD jet samples and resulting "lepton" candidates are considered to form the fake-lepton control samples. The jet samples are collected with the so-called `Jet20`, `Jet50`, `Jet70`, and `Jet100` triggers, and the corresponding integrated luminosity is 4.8 pb^{-1}. The events from different triggers are combined with the weights reflecting the trigger pre-scales, as shown in Fig. 3.3.

3.5 Probability distribution functions

Figures 3.4–3.8 compares the signal and background PDFs, where the signal leptons come from Z decays.

The effects of mis-modeling the signal distributions by the MCs will be corrected for by scale factors which are obtained by comparing efficiencies between real data and MCs for known processes which are usually Z events.

Since the CPR/CP2 and E_{CES}/p^* have especially different distributions between real data and MCs, we implement rescaling factors for MCs. The CPR/CP2 for electron are 2 types, CPR responses from CDF EM objects bg(EM) and tracks associated to EM showers (TR). Figures 3.9–3.11 shows the CPR/CP2 and E_{CES}/p^* for electron and CPR/CP2 for muon distributions before scaling. In the case of E_{CES}/p^*, the p^* have the similar shape, so we rescale E_{CES} only. The χ^2 plots for these scaling and the

distributions after rescaled are shown in Figs. 3.12–3.15. The MCs rescaling factor is listed in Table 3.2.

We compare signal PDFs between Z events of the data and MCs in Figs. 3.16–3.20. We consider not only electrons from Z decays but also conversion electrons as a signal sample. The PDFs from the Z and conversions are compared in Figs. 3.21–3.23. Distributions look similar due to the similar p_T regions we are looking at for the two samples.

Figures 3.24–3.28 compare the lepton PDFs of the MCs between the Z and higgs events. The differences seen in the figures represent the MC predictions of p_T dependence of the ID variables.

The ratio of Z events of the data and MCs are shown in Figs. 3.29–3.31. Figures. 3.32–3.49 are the correlation between two variables for the electron events Z data and the fake electron in the `Jet20`.

3.6 Efficiency

Figure 3.50–3.52 shows normalized likelihood distributions for signal and background samples, where the signal samples are Z, conversion electrons, higgs MCs for the mass of 110 GeV/c^2, and 160 GeV/c^2. The signal PDFs correspond to each type of samples, namely, the PDFs created from Z events are used for the plot of Z events, and so on.

3.6.1 Electron

The CLID efficiencies for electrons in the Z data, higgs MC samples, and fake electrons in jet samples are shown in Table 3.3. We estimate the efficiency as the following simple fraction:

$$\varepsilon = \frac{\text{The number of events after cut} > L}{\text{The number of all events}} \,. \tag{3.7}$$

It is therefore the event efficiency rather than the efficiency per lepton. The efficiency for the Z electrons is 0.776, while it is 0.185 for the fake electrons in the `Jet20` sample.

The cut values for the likelihood that give the same CLID background-efficiencies and the corresponding LLID signal-efficiencies are listed in Table 3.4. We see about 30% gains for Z electrons with the LLID. The likelihood cut-values giving the same CLID signal-efficiencies and the corresponding LLID background-efficiencies are also included in the table. For example, the fake efficiency is reduced from 0.185 to 0.019 for the `Jet20`, the signal-to-background ratio (S/B) is thus improved by a factor of 9.6. According to the table, the S/B improvement is gradually reduced as the jet trigger E_T becomes higher. Similar analyses for the higgs MCs of the mass 110 GeV/c^2 and 160 GeV/c^2 are also shown in the table.

Figure 3.53 compares the signal-efficiency vs. the background-efficiency curves for 3 samples: Z, higgs with the mass 110 GeV/c^2, and 160 GeV/c^2, for a given type of the PDFs, where the background sample is fixed to be the `Jet20`. Figure 3.54 compares the same curves using the different signal PDFs for a given sample.

We confirm that the LLID is better than the CLID for electrons. Using the PDFs created from higgs MCs showed better performance than using the PDFs from Z data to apply for higgs MCs.

Tables 3.6–3.11 are the LLID performances when we use the likelihood function w/o CPR and w/ CPR or CP2. The CPR/CP2 are very strong discriminator between electrons and fake electrons.

3.6.2 Muon

The same analysis is performed for muons. The results are shown in Tables 3.12–3.16. The improvements by the LLID are moderate compared to the electron case: $\simeq 10\%$ gains in signal efficiencies for the same background levels as the CLID, while a factor of $\simeq 1.5$ reduction of backgrounds for the same signal efficiency as the CLID.

3.7 Cut optimization

We discussed the LLID performance in the previous section using the CLID efficiencies as the reference. If we consider, however, the limits on the higgs production as a measure of the performance, the conclusions are not necessarily the same. We compute limits based on counting experiments.

3.7.1 Electron

We compare the limits on the higgs production using the signal PDFs based on Z decays, photon conversions, and higgs MCs, as a function of cut value for the likelihood. The limits for the higgs MC of 110 GeV/c^2 and 160 GeV/c^2 are shown in Fig. 3.55. Figures 3.56–3.57 show the limits for all the other higgs-mass points. The best performance is obtained by using the PDFs based on the higgs MCs themselves.

3.7.2 Muon

The limits for muon analysis are shown in Figs. 3.58–3.60 for the CMUP and 3.61–3.63 for the CMX. The performances of using the PDFs based on Z decays and the higgs MCs themselves show similar findings to the limits.

Event pre-selection	
$\lvert z_{\rm pv}\rvert < 60$ cm	
Cosmic-ray veto	
Electron selection	**Muon selection**
Geometrical and kinematical cuts	
CEM	CMUP or CMX
Fiducial	Fiducial (CMUP), $\rho_{\rm COT} > 140$ cm (CMX)
	Blue-beam veto, keystone veto, miniskirt veto
$E_T^{\ell_1} > 20$ GeV ($p_T > 10$ GeV/c)	$p_T^{\ell_1} > 20$ GeV/c
$E_T^{\ell_2} > 6$ GeV ($p_T > 6$ GeV/c)	$p_T^{\ell_2} > 6$ GeV/c
Track quality cuts	
Axial ≥ 3 and stereo ≥ 3 (≥ 7 hits)	
$\lvert z_0 - z_{\rm pv}\rvert < 2$ cm	
$\lvert d_0\rvert < 0.02$ cm	
Isolation cut	
$\mathrm{ISO}_{0.4}^{\rm cal} < 2$ GeV	
Identification cuts	
HAD/EM $< 0.055 + 0.00045 \times E$	EM $< \max(2, 2 + 0.0115 \times (p - 100))$ GeV
$L_{\rm shr} < 0.2$ ($E_T < 70$ GeV)	HAD $< \max(6, 6 + 0.0280 \times (p - 100))$ GeV
$E/p < 2$ ($E_T < 50$ GeV)	$\lvert r \times \Delta\phi\rvert < 3$, 5, 6 cm (CMU, P, X)
$\chi^2_{\rm strip} < 10$	
$\lvert\Delta z_{\rm CES}\rvert < 3$ cm	
$-3.0 < Q \times \Delta x_{\rm CES} < 1.5$ cm	
Other cuts	
Conversion removal	

Table 3.1: Event pre-selection and lepton selection cuts.

variables	electron		muon
CPR	0.671 (EM)	0.649 (TR)	1.203 (TR)
CP2	0.421 (EM)	0.459 (TR)	1.516 (TR)
E_{CES}	0.754		–

Table 3.2: The scale factor for the MC CPR/CP2 and E_{CES} responces.

Sample	total	pass	efficiency
EL	59368	46057	0.776 ± 0.002
Wh110	14689	11441	0.779 ± 0.003
Wh120	15619	11777	0.754 ± 0.003
Wh130	16637	12429	0.747 ± 0.003
Wh140	17843	13281	0.744 ± 0.003
Wh150	18494	13653	0.738 ± 0.003
Wh160	18223	13236	0.726 ± 0.003
Wh170	18693	13567	0.726 ± 0.003
Wh180	19672	14435	0.734 ± 0.003
Wh190	20564	15073	0.733 ± 0.003
Wh200	21011	15341	0.730 ± 0.003
JT20	58933	10880	0.185 ± 0.002
JT50	21821	3563	0.163 ± 0.003
JT70	28838	5195	0.180 ± 0.002
JT100	28338	5565	0.196 ± 0.002

Table 3.3: Cut-based efficiency for signal and background samples.

Sample	Same background efficiency			Same signal efficiency		
	L cut	new el efficiency	improvement	L cut	new jt efficiency	reduction
JT20	0.04	0.987 ± 0.000	× 1.3	0.99	0.019 ± 0.001	× 9.6
JT50	0.16	0.979 ± 0.001	× 1.3	0.99	0.029 ± 0.001	× 5.5
JT70	0.17	0.978 ± 0.001	× 1.3	0.99	0.039 ± 0.001	× 4.6
JT100	0.19	0.977 ± 0.001	× 1.3	0.99	0.052 ± 0.001	× 3.8

	L cut	new wh110 efficiency	improvement	L cut	new jt efficiency	reduction
JT20	0.04	0.892 ± 0.003	× 1.1	0.76	0.074 ± 0.001	× 2.5
JT50	0.16	0.873 ± 0.003	× 1.1	0.76	0.091 ± 0.002	× 1.8
JT70	0.17	0.872 ± 0.003	× 1.1	0.76	0.108 ± 0.002	× 1.7
JT100	0.19	0.870 ± 0.003	× 1.1	0.76	0.127 ± 0.002	× 1.5

	L cut	new wh160 efficiency	improvement	L cut	new jt efficiency	reduction
JT20	0.04	0.866 ± 0.003	× 1.2	0.93	0.045 ± 0.001	× 4.1
JT50	0.16	0.855 ± 0.003	× 1.2	0.93	0.062 ± 0.002	× 2.6
JT70	0.17	0.854 ± 0.003	× 1.2	0.93	0.076 ± 0.002	× 2.4
JT100	0.19	0.852 ± 0.003	× 1.2	0.93	0.093 ± 0.002	× 2.1

Table 3.4: The efficiency performance for LLID using Z PDFs. The signal samples are Z, the higgs MCs for the mass of 110 GeV/c^2 and 160 GeV/c^2.

Sample	Same background efficiency			Same signal efficiency		
	L cut	new wh110 efficiency	improvement	L cut	new jt efficiency	reduction
JT20	0.31	0.907 ± 0.002	× 1.2	0.95	0.065 ± 0.001	× 2.9
JT50	0.56	0.893 ± 0.003	× 1.1	0.95	0.075 ± 0.002	× 2.2
JT70	0.60	0.890 ± 0.003	× 1.1	0.95	0.091 ± 0.002	× 2.0
JT100	0.63	0.886 ± 0.003	× 1.1	0.95	0.112 ± 0.002	× 1.8

	L cut	new wh160 efficiency	improvement	L cut	new jt efficiency	reduction
JT20	0.27	0.892 ± 0.002	× 1.2	0.97	0.041 ± 0.001	× 4.5
JT50	0.59	0.869 ± 0.002	× 1.2	0.97	0.057 ± 0.002	× 2.9
JT70	0.63	0.866 ± 0.003	× 1.2	0.97	0.071 ± 0.002	× 2.5
JT100	0.67	0.862 ± 0.003	× 1.2	0.97	0.089 ± 0.002	× 2.2

Table 3.5: The efficiency performance for LLID using the PDFs based the higgs MCs themselves. The signal samples are the higgs MCs for the mass of 110 GeV/c^2 and 160 GeV/c^2.

Sample	Same background efficiency			Same signal efficiency		
	L cut	new el efficiency	improvement	L cut	new jt efficiency	reduction
JT20	0.10	0.980 ± 0.001	× 1.3	0.98	0.029 ± 0.001	× 6.3
JT50	0.24	0.971 ± 0.001	× 1.3	0.98	0.038 ± 0.001	× 4.3
JT70	0.25	0.971 ± 0.001	× 1.3	0.98	0.048 ± 0.001	× 3.7
JT100	0.26	0.970 ± 0.001	× 1.3	0.98	0.061 ± 0.001	× 3.2

	L cut	new wh110 efficiency	improvement	L cut	new jt efficiency	reduction
JT20	0.10	0.891 ± 0.003	× 1.1	0.83	0.075 ± 0.001	× 2.5
JT50	0.24	0.876 ± 0.003	× 1.1	0.83	0.086 ± 0.002	× 1.9
JT70	0.25	0.875 ± 0.003	× 1.1	0.83	0.102 ± 0.002	× 1.8
JT100	0.26	0.874 ± 0.003	× 1.1	0.83	0.120 ± 0.002	× 1.6

	L cut	new wh160 efficiency	improvement	L cut	new jt efficiency	reduction
JT20	0.10	0.866 ± 0.003	× 1.2	0.93	0.053 ± 0.001	× 3.5
JT50	0.24	0.856 ± 0.003	× 1.2	0.93	0.062 ± 0.002	× 2.6
JT70	0.25	0.855 ± 0.003	× 1.2	0.93	0.076 ± 0.002	× 2.4
JT100	0.26	0.855 ± 0.003	× 1.2	0.93	0.092 ± 0.002	× 2.1

Table 3.6: The efficiency performance for LLID (w/o CPR) using Z PDFs. The signal samples are Z, the higgs MCs for the mass of 110 GeV/c^2 and 160 GeV/c^2.

Sample	Same background efficiency			Same signal efficiency		
	L cut	new wh110 efficiency	improvement	L cut	new jt efficiency	reduction
JT20	0.38	0.903 ± 0.002	× 1.2	0.94	0.071 ± 0.001	× 2.6
JT50	0.57	0.890 ± 0.003	× 1.1	0.94	0.078 ± 0.002	× 2.1
JT70	0.60	0.888 ± 0.003	× 1.1	0.94	0.093 ± 0.002	× 1.9
JT100	0.62	0.886 ± 0.003	× 1.1	0.94	0.110 ± 0.002	× 1.8

	L cut	new wh160 efficiency	improvement	L cut	new jt efficiency	reduction
JT20	0.34	0.889 ± 0.002	× 1.2	0.96	0.049 ± 0.001	× 3.8
JT50	0.59	0.869 ± 0.003	× 1.2	0.96	0.058 ± 0.002	× 2.8
JT70	0.61	0.867 ± 0.003	× 1.2	0.96	0.074 ± 0.002	× 2.4
JT100	0.63	0.865 ± 0.003	× 1.2	0.96	0.089 ± 0.002	× 2.2

Table 3.7: The efficiency performance for LLID (w/o CPR) using the PDFs based the higgs MCs themselves. The signal samples are the higgs MCs for the mass of 110 GeV/c^2 and 160 GeV/c^2.

Sample	Same background efficiency			Same signal efficiency		
	L cut	new el efficiency	improvement	L cut	new jt efficiency	reduction
JT20	0.05	0.990 ± 0.001	× 1.3	0.99	0.022 ± 0.001	× 8.4
JT50	0.20	0.982 ± 0.002	× 1.3	0.99	0.029 ± 0.002	× 5.7
JT70	0.20	0.982 ± 0.002	× 1.3	0.99	0.038 ± 0.004	× 4.8
JT100	0.24	0.980 ± 0.002	× 1.3	0.99	0.061 ± 0.005	× 3.2
	L cut	new wh110 efficiency	improvement	L cut	new jt efficiency	reduction
JT20	0.05	0.890 ± 0.003	× 1.1	0.76	0.081 ± 0.002	× 2.3
JT50	0.20	0.869 ± 0.003	× 1.1	0.76	0.095 ± 0.004	× 1.7
JT70	0.20	0.869 ± 0.003	× 1.1	0.76	0.119 ± 0.007	× 1.5
JT100	0.24	0.865 ± 0.003	× 1.1	0.76	0.143 ± 0.007	× 1.4
	L cut	new wh160 efficiency	improvement	L cut	new jt efficiency	reduction
JT20	0.05	0.865 ± 0.003	× 1.2	0.93	0.052 ± 0.002	× 3.6
JT50	0.20	0.851 ± 0.003	× 1.2	0.93	0.064 ± 0.004	× 2.5
JT70	0.20	0.851 ± 0.003	× 1.2	0.93	0.089 ± 0.006	× 2.0
JT100	0.24	0.848 ± 0.003	× 1.2	0.93	0.111 ± 0.007	× 1.8

Table 3.8: The efficiency performance for LLID (w/ CPR) using Z PDFs. The signal samples are Z, the higgs MCs for the mass of 110 GeV/c^2 and 160 GeV/c^2.

Sample	Same background efficiency			Same signal efficiency		
	L cut	new wh110 efficiency	improvement	L cut	new jt efficiency	reduction
JT20	0.34	0.906 ± 0.002	× 1.2	0.95	0.069 ± 0.002	× 2.7
JT50	0.55	0.894 ± 0.003	× 1.1	0.95	0.081 ± 0.004	× 2.0
JT70	0.61	0.889 ± 0.003	× 1.1	0.95	0.092 ± 0.006	× 2.0
JT100	0.65	0.884 ± 0.003	× 1.1	0.95	0.124 ± 0.007	× 1.6
	L cut	new wh160 efficiency	improvement	L cut	new jt efficiency	reduction
JT20	0.33	0.887 ± 0.002	× 1.2	0.97	0.049 ± 0.002	× 3.8
JT50	0.61	0.868 ± 0.003	× 1.2	0.97	0.065 ± 0.004	× 2.5
JT70	0.68	0.861 ± 0.003	× 1.2	0.97	0.077 ± 0.006	× 2.3
JT100	0.73	0.855 ± 0.003	× 1.2	0.97	0.102 ± 0.006	× 1.9

Table 3.9: The efficiency performance for LLID (w/ CPR) using the PDFs based the higgs MCs themselves. The signal samples are the higgs MCs for the mass of 110 GeV/c^2 and 160 GeV/c^2.

Sample	Same background efficiency			Same signal efficiency		
	L cut	new el efficiency	improvement	L cut	new jt efficiency	reduction
JT20	0.04	0.987 ± 0.0004	× 1.3	0.99	0.018 ± 0.001	× 10
JT50	0.15	0.979 ± 0.001	× 1.3	0.99	0.030 ± 0.001	× 5.5
JT70	0.17	0.978 ± 0.001	× 1.3	0.99	0.039 ± 0.001	× 4.6
JT100	0.18	0.977 ± 0.001	× 1.3	0.99	0.051 ± 0.001	× 3.9

	L cut	new wh110 efficiency	improvement	L cut	new jt efficiency	reduction
JT20	0.04	0.892 ± 0.003	× 1.1	0.76	0.072 ± 0.001	× 2.6
JT50	0.15	0.875 ± 0.003	× 1.1	0.76	0.090 ± 0.002	× 1.8
JT70	0.17	0.872 ± 0.003	× 1.1	0.76	0.107 ± 0.002	× 1.7
JT100	0.18	0.871 ± 0.003	× 1.1	0.76	0.126 ± 0.002	× 1.6

	L cut	new wh160 efficiency	improvement	L cut	new jt efficiency	reduction
JT20	0.04	0.866 ± 0.003	× 1.2	0.93	0.043 ± 0.001	× 4.3
JT50	0.15	0.856 ± 0.003	× 1.2	0.93	0.061 ± 0.002	× 2.7
JT70	0.17	0.854 ± 0.003	× 1.2	0.93	0.075 ± 0.002	× 2.4
JT100	0.18	0.853 ± 0.003	× 1.2	0.93	0.092 ± 0.002	× 2.1

Table 3.10: The efficiency parformance for LLID (w/ CP2) using Z PDFs. The signal samples are Z, the higgs MCs for the mass of 110 GeV/c^2 and 160 GeV/c^2.

Sample	Same background efficiency			Same signal efficiency		
	L cut	new wh110 efficiency	improvement	L cut	new jt efficiency	reduction
JT20	0.30	0.907 ± 0.002	× 1.2	0.95	0.063 ± 0.001	× 2.9
JT50	0.56	0.893 ± 0.003	× 1.1	0.95	0.073 ± 0.002	× 2.2
JT70	0.60	0.890 ± 0.003	× 1.1	0.95	0.091 ± 0.002	× 2.0
JT100	0.63	0.886 ± 0.003	× 1.1	0.95	0.111 ± 0.002	× 1.8

	L cut	new wh160 efficiency	improvement	L cut	new jt efficiency	reduction
JT20	0.25	0.893 ± 0.002	× 1.2	0.97	0.039 ± 0.001	× 4.8
JT50	0.58	0.870 ± 0.002	× 1.2	0.97	0.055 ± 0.002	× 3.0
JT70	0.63	0.866 ± 0.003	× 1.2	0.97	0.071 ± 0.002	× 2.5
JT100	0.66	0.863 ± 0.003	× 1.2	0.97	0.087 ± 0.002	× 2.2

Table 3.11: The efficiency parformance for LLID (w/ CP2) using the PDFs based the higgs MCs themselves. The signal samples are the higgs MCs for the mass of 110 GeV/c^2 and 160 GeV/c^2.

Sample	total	pass	efficiency
MU	29068	23063	0.793 ± 0.002
Wh110	9639	7282	0.755 ± 0.004
Wh120	10089	7724	0.766 ± 0.004
Wh130	10710	8340	0.779 ± 0.004
Wh140	11216	8848	0.789 ± 0.004
Wh150	11413	8963	0.785 ± 0.004
Wh160	11522	9103	0.790 ± 0.004
Wh170	11864	9384	0.791 ± 0.004
Wh180	12447	9838	0.790 ± 0.004
Wh190	13239	10550	0.797 ± 0.003
Wh200	13698	10836	0.791 ± 0.003
JT20	8773	2324	0.265 ± 0.005
JT50	4043	916	0.227 ± 0.007
JT70	5823	1367	0.235 ± 0.006
JT100	6137	1460	0.238 ± 0.005

Table 3.12: Cut-based efficiency for signal and background samples.

Sample	Same background efficiency			Same signal efficiency		
	L cut	new mu efficiency	improvement	L cut	new jt efficiency	reduction
JT20	0.34	0.934 ± 0.001	× 1.2	0.73	0.141 ± 0.004	× 1.9
JT50	0.49	0.894 ± 0.002	× 1.1	0.73	0.147 ± 0.006	× 1.5
JT70	0.48	0.897 ± 0.002	× 1.1	0.73	0.154 ± 0.005	× 1.5
JT100	0.58	0.863 ± 0.002	× 1.1	0.73	0.183 ± 0.005	× 1.3
	L cut	new wh110 efficiency	improvement	L cut	new jt efficiency	reduction
JT20	0.34	0.759 ± 0.004	× 1.0	0.35	0.261 ± 0.005	× 1.0
JT50	0.49	0.716 ± 0.005	× 0.9	0.35	0.275 ± 0.007	× 0.8
JT70	0.48	0.719 ± 0.005	× 1.0	0.35	0.284 ± 0.006	× 0.8
JT100	0.58	0.687 ± 0.005	× 0.9	0.35	0.321 ± 0.006	× 0.7
	L cut	new wh160 efficiency	improvement	L cut	new jt efficiency	reduction
JT20	0.34	0.867 ± 0.003	× 1.1	0.66	0.163 ± 0.004	× 1.6
JT50	0.49	0.835 ± 0.003	× 1.1	0.66	0.174 ± 0.006	× 1.3
JT70	0.48	0.838 ± 0.003	× 1.1	0.66	0.176 ± 0.005	× 1.3
JT100	0.58	0.814 ± 0.004	× 1.0	0.66	0.206 ± 0.005	× 1.2

Table 3.13: The efficiency performance for LLID using Z PDFs. The signal samples are Z, the higgs MCs for the mass of 110 GeV/c^2 and 160 GeV/c^2.

Sample	Same background efficiency			Same signal efficiency		
	L cut	new wh110 efficiency	improvement	L cut	new jt efficiency	reduction
JT20	0.60	0.783 ± 0.004	× 1.0	0.64	0.240 ± 0.005	× 1.1
JT50	0.64	0.759 ± 0.004	× 1.0	0.64	0.226 ± 0.007	× 1.0
JT70	0.65	0.755 ± 0.004	× 1.0	0.64	0.238 ± 0.006	× 1.0
JT100	0.68	0.735 ± 0.004	× 1.0	0.64	0.260 ± 0.006	× 0.9
	L cut	new wh160 efficiency	improvement	L cut	new jt efficiency	reduction
JT20	0.44	0.879 ± 0.003	× 1.1	0.71	0.168 ± 0.004	× 1.6
JT50	0.59	0.837 ± 0.003	× 1.1	0.71	0.174 ± 0.006	× 1.3
JT70	0.58	0.840 ± 0.003	× 1.1	0.71	0.187 ± 0.005	× 1.3
JT100	0.64	0.822 ± 0.004	× 1.0	0.71	0.208 ± 0.005	× 1.1

Table 3.14: The efficiency performance for LLID using the PDFs based the higgs MCs themselves. The signal samples are the higgs MCs for the mass of 110 GeV/c^2 and 160 GeV/c^2.

Sample	total	pass	efficiency
MU	18836	16356	0.868 ± 0.002
Wh110	4853	3902	0.804 ± 0.006
Wh120	5250	4243	0.808 ± 0.005
Wh130	5559	4583	0.824 ± 0.005
Wh140	5773	4776	0.827 ± 0.005
Wh150	6014	4872	0.810 ± 0.005
Wh160	6079	5074	0.835 ± 0.005
Wh170	6124	5086	0.831 ± 0.005
Wh180	6442	5370	0.834 ± 0.005
Wh190	6827	5606	0.821 ± 0.005
Wh200	6881	5687	0.826 ± 0.005
JT20	6955	2007	0.289 ± 0.005
JT50	2944	817	0.278 ± 0.008
JT70	4107	1159	0.282 ± 0.007
JT100	4069	1228	0.302 ± 0.007

Table 3.15: Cut-based efficiency for signal and background samples.

Sample	Same background efficiency			Same signal efficiency		
	L cut	new mu efficiency	improvement	L cut	new jt efficiency	reduction
JT20	0.19	0.967 ± 0.001	× 1.1	0.58	0.174 ± 0.005	× 1.7
JT50	0.27	0.956 ± 0.001	× 1.1	0.58	0.180 ± 0.007	× 1.5
JT70	0.28	0.954 ± 0.002	× 1.1	0.58	0.183 ± 0.006	× 1.5
JT100	0.25	0.959 ± 0.001	× 1.1	0.58	0.196 ± 0.006	× 1.5
	L cut	new wh110 efficiency	improvement	L cut	new jt efficiency	reduction
JT20	0.19	0.851 ± 0.005	× 1.1	0.35	0.238 ± 0.005	× 1.2
JT50	0.27	0.827 ± 0.005	× 1.0	0.35	0.252 ± 0.008	× 1.1
JT70	0.28	0.825 ± 0.005	× 1.0	0.35	0.260 ± 0.007	× 1.1
JT100	0.25	0.833 ± 0.005	× 1.0	0.35	0.270 ± 0.007	× 1.1
	L cut	new wh160 efficiency	improvement	L cut	new jt efficiency	reduction
JT20	0.19	0.922 ± 0.003	× 1.1	0.48	0.198 ± 0.005	× 1.5
JT50	0.27	0.904 ± 0.004	× 1.1	0.48	0.203 ± 0.007	× 1.4
JT70	0.28	0.901 ± 0.004	× 1.1	0.48	0.216 ± 0.006	× 1.3
JT100	0.25	0.910 ± 0.004	× 1.1	0.48	0.225 ± 0.007	× 1.3

Table 3.16: The efficiency performance for LLID using Z PDFs. The signal samples are Z, the higgs MCs for the mass of 110 GeV/c^2 and 160 GeV/c^2.

Sample	Same background efficiency			Same signal efficiency		
	L cut	new wh110 efficiency	improvement	L cut	new jt efficiency	reduction
JT20	0.44	0.883 ± 0.005	× 1.1	0.56	0.216 ± 0.005	× 1.3
JT50	0.49	0.855 ± 0.005	× 1.1	0.56	0.233 ± 0.008	× 1.2
JT70	0.48	0.862 ± 0.005	× 1.1	0.56	0.243 ± 0.007	× 1.2
JT100	0.47	0.868 ± 0.005	× 1.1	0.56	0.254 ± 0.007	× 1.2
	L cut	new wh160 efficiency	improvement	L cut	new jt efficiency	reduction
JT20	0.36	0.936 ± 0.003	× 1.1	0.58	0.186 ± 0.005	× 1.6
JT50	0.42	0.917 ± 0.004	× 1.1	0.58	0.206 ± 0.007	× 1.3
JT70	0.44	0.910 ± 0.004	× 1.1	0.58	0.210 ± 0.006	× 1.3
JT100	0.44	0.910 ± 0.004	× 1.1	0.58	0.225 ± 0.007	× 1.3

Table 3.17: The efficiency performance for LLID using the PDFs based the higgs MCs themselves. The signal samples are the higgs MCs for the mass of 110 GeV/c^2 and 160 GeV/c^2.

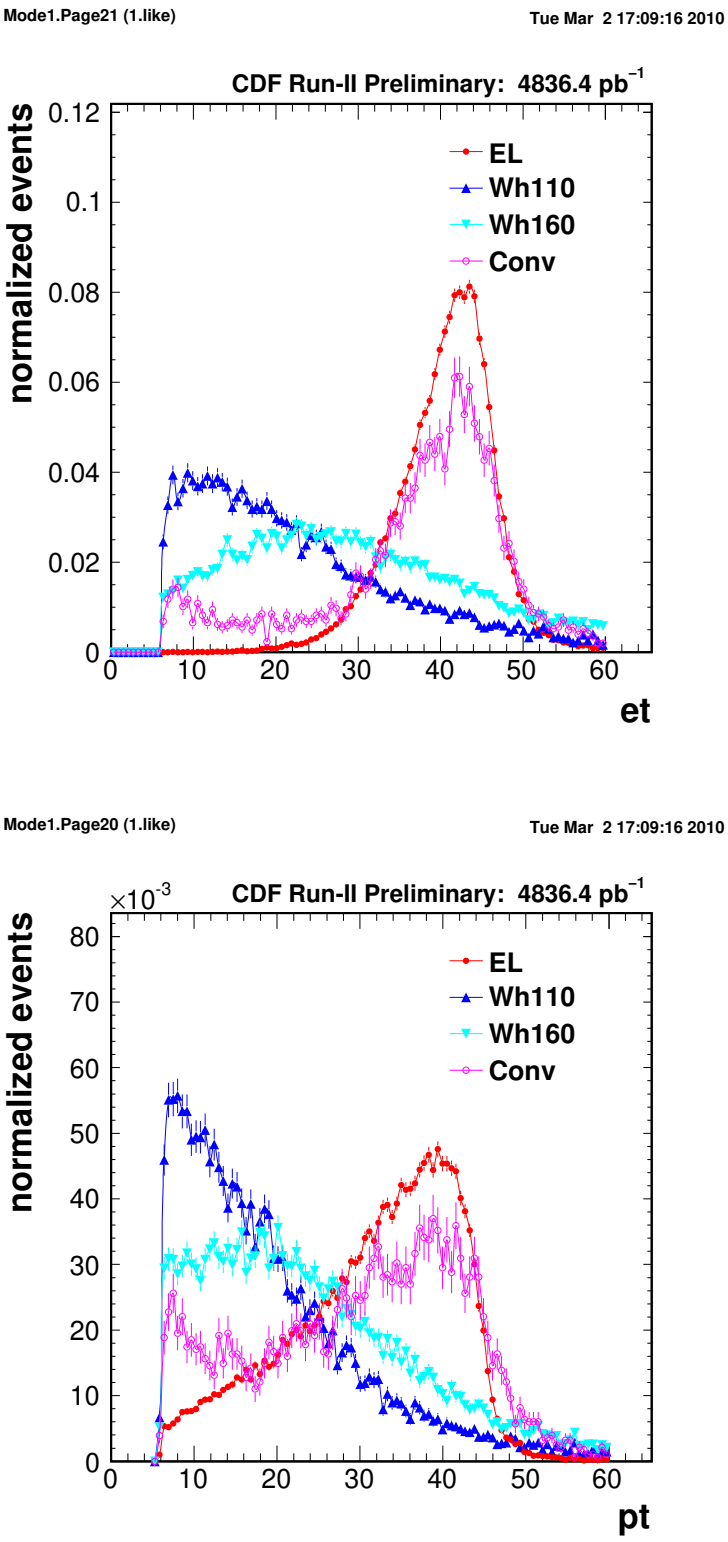

Figure 3.1: The E_T (top) and p_T (bottom) spectra of electrons for the samples of Z, photon conversions, and higgs Monte Carlos.

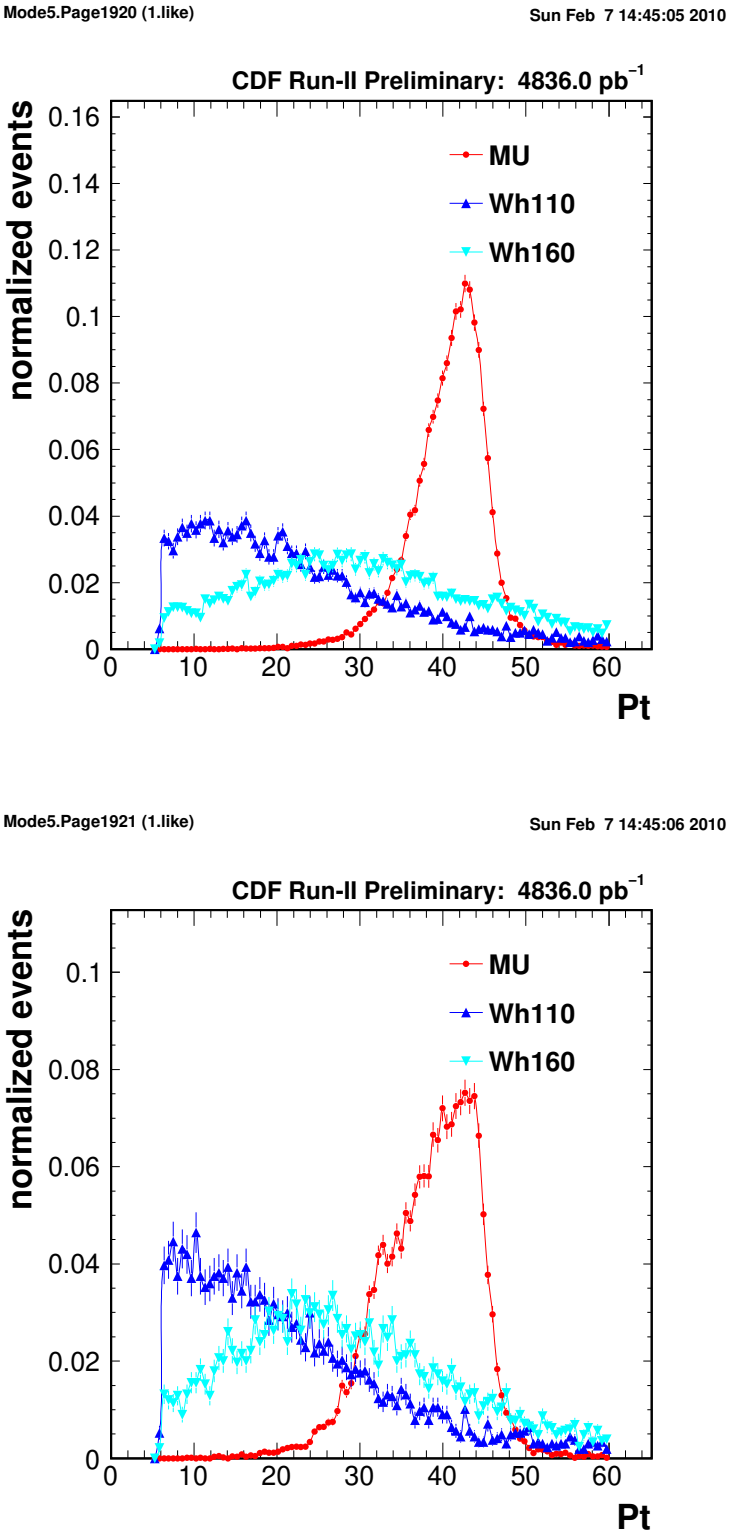

Figure 3.2: The p_T spectra of CMUP muons (top) and CMX muons (bottom) for the samples of Z and higgs Monte Carlos.

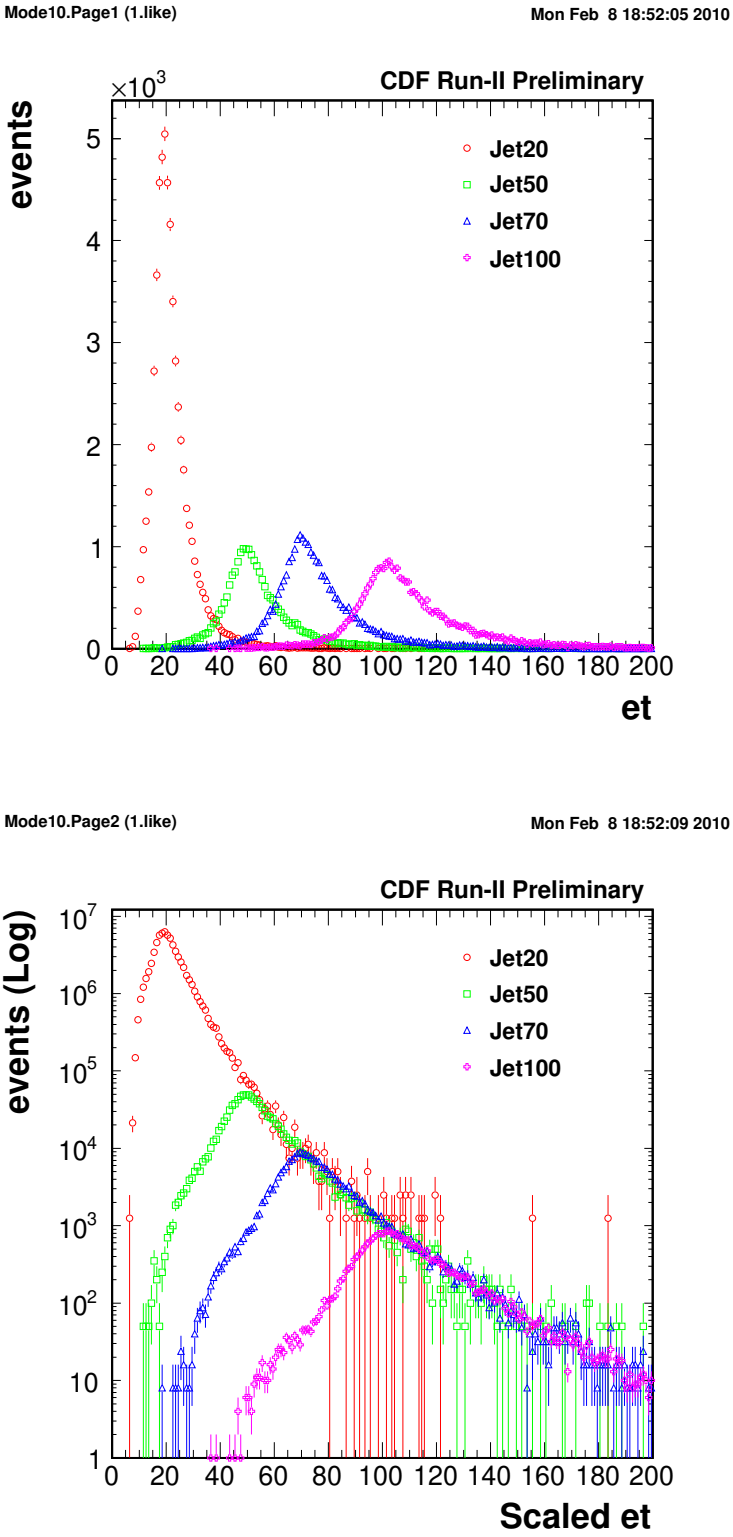

Figure 3.3: E_T dependence of jet sample. The right figure is the vertical axis of the left figure to a logarithm. The background sample PDFs are made with pre-scale weighted jet samples, $\times$ 1250 for Jet20, $\times$ 50 for Jet50, $\times$ 8 for Jet70, and $\times$ 1 for Jet100.

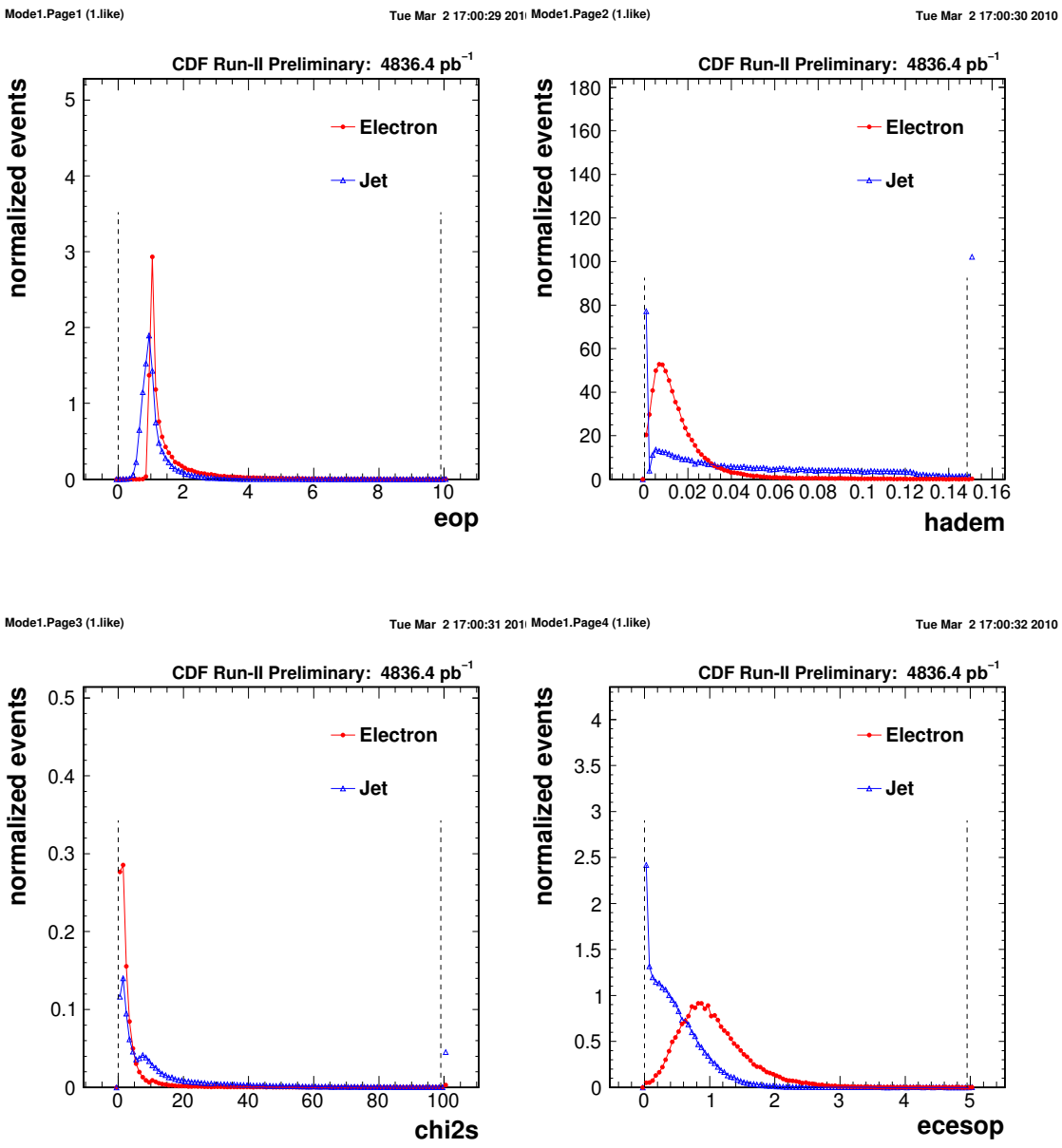

Figure 3.4: These distributions are the identification variables of the electrons from Z decays and jet control samples.

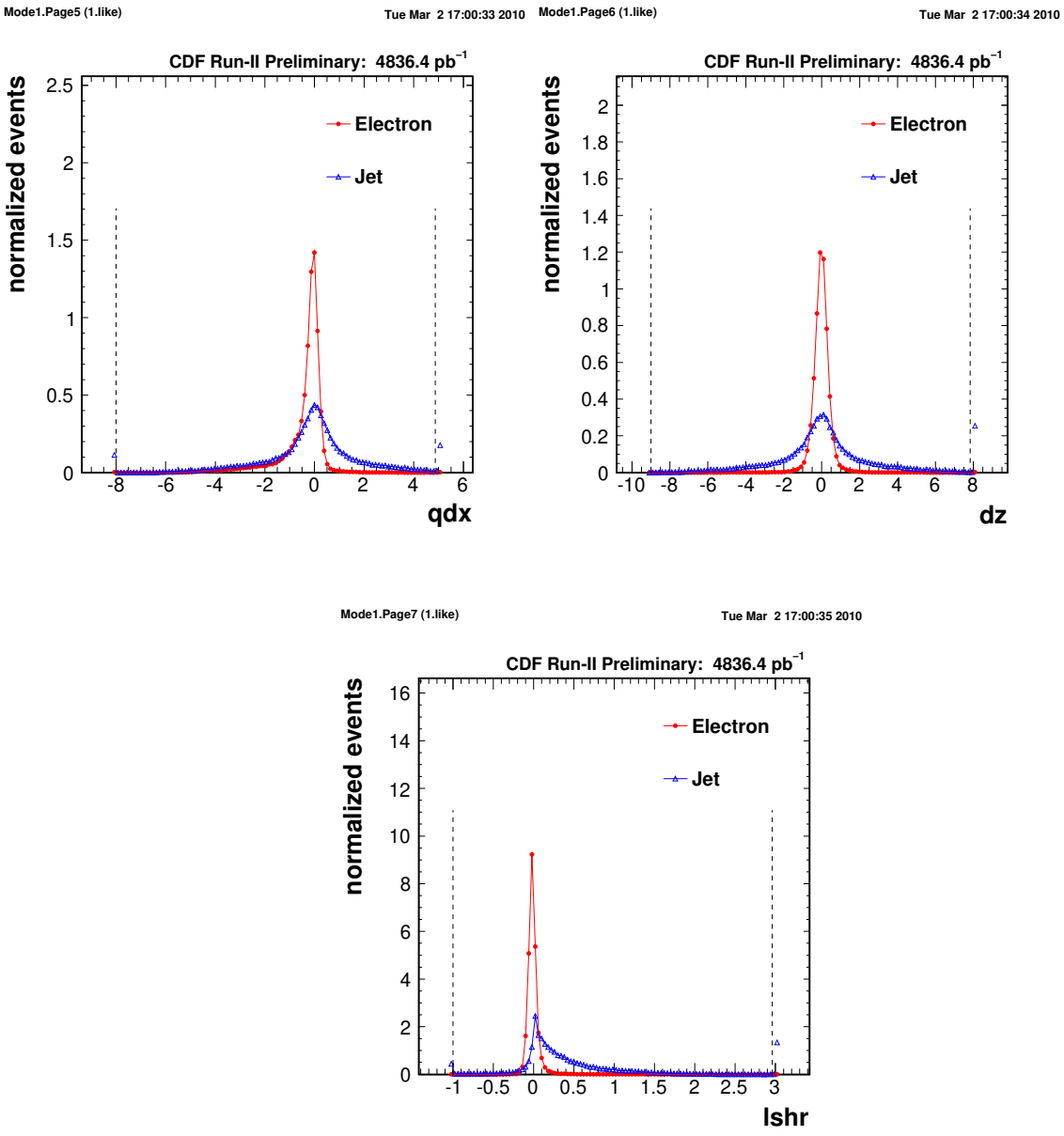

Figure 3.5: These distributions are the identification variables of the electrons from Z decays and jet control samples.

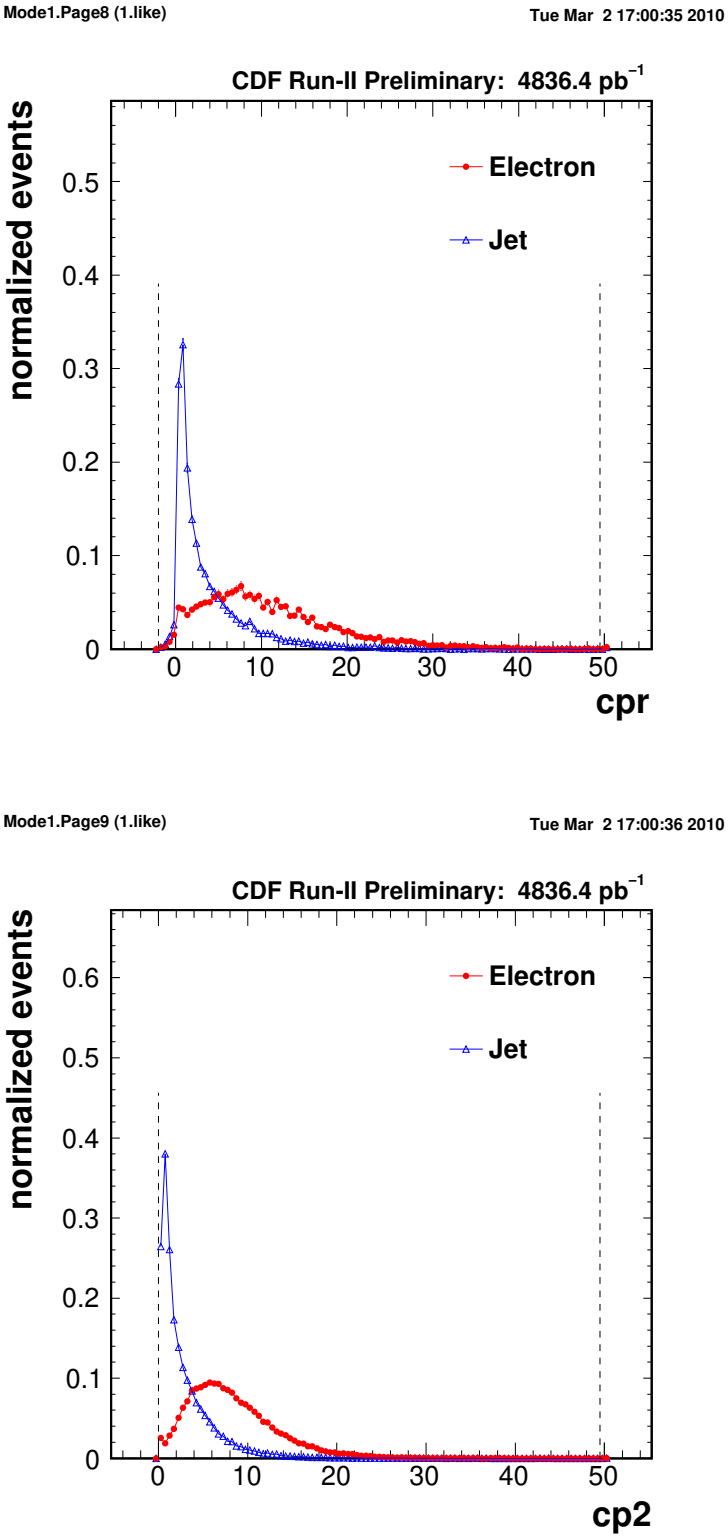

Figure 3.6: These distributions are the identification variables of the electrons from Z decays and jet control samples.

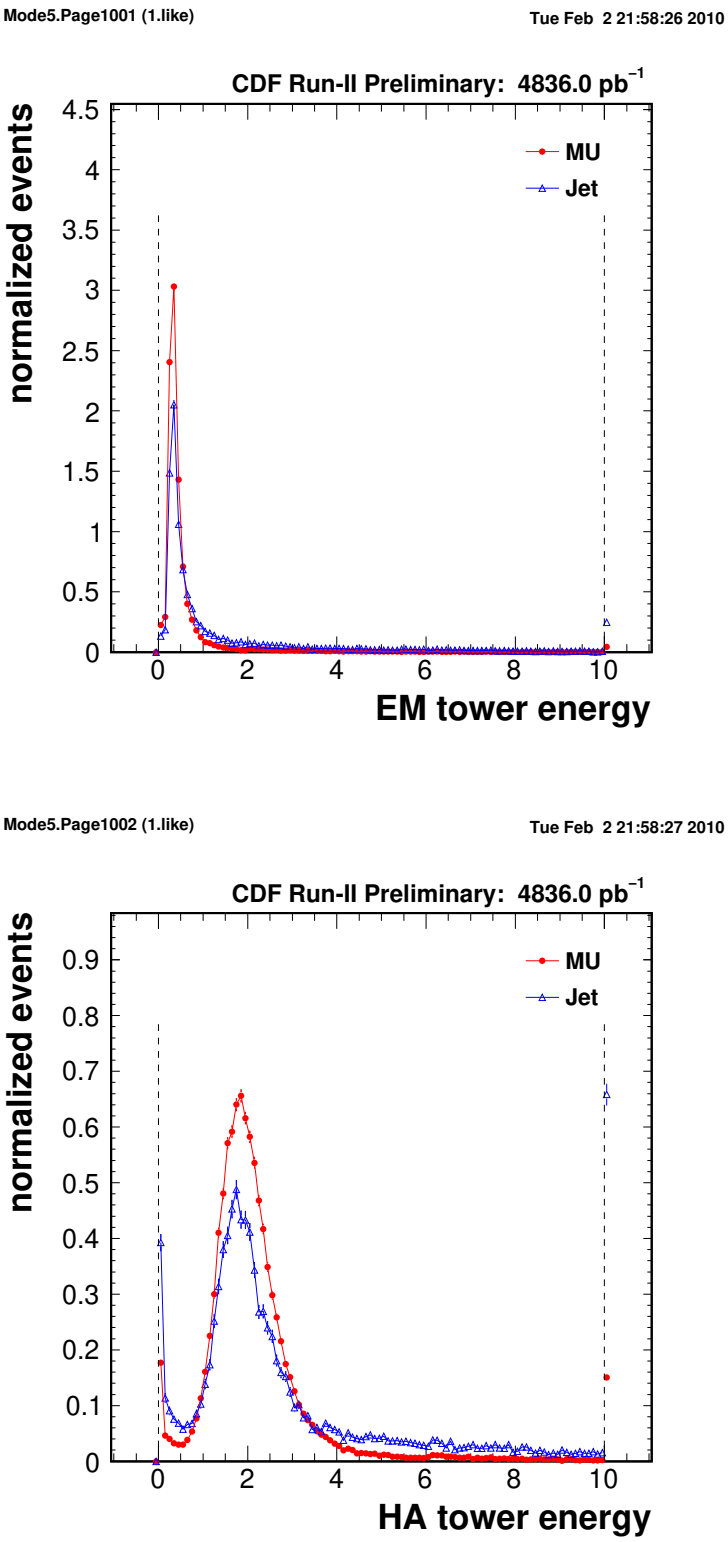

Figure 3.7: These distributions of the identification variables for muon and jet control samples.

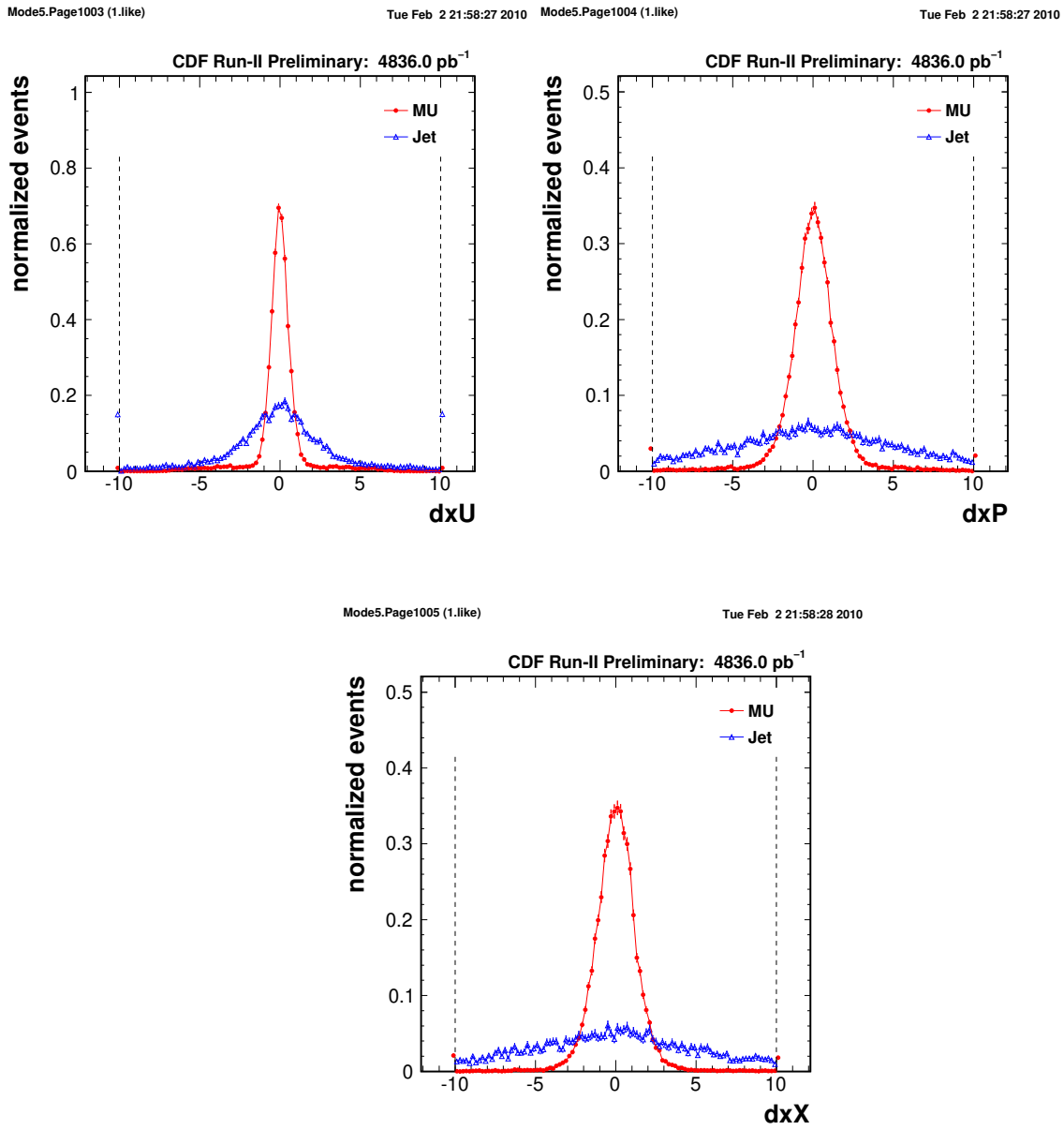

Figure 3.8: These distributions of the identification variables for muon and jet control samples.

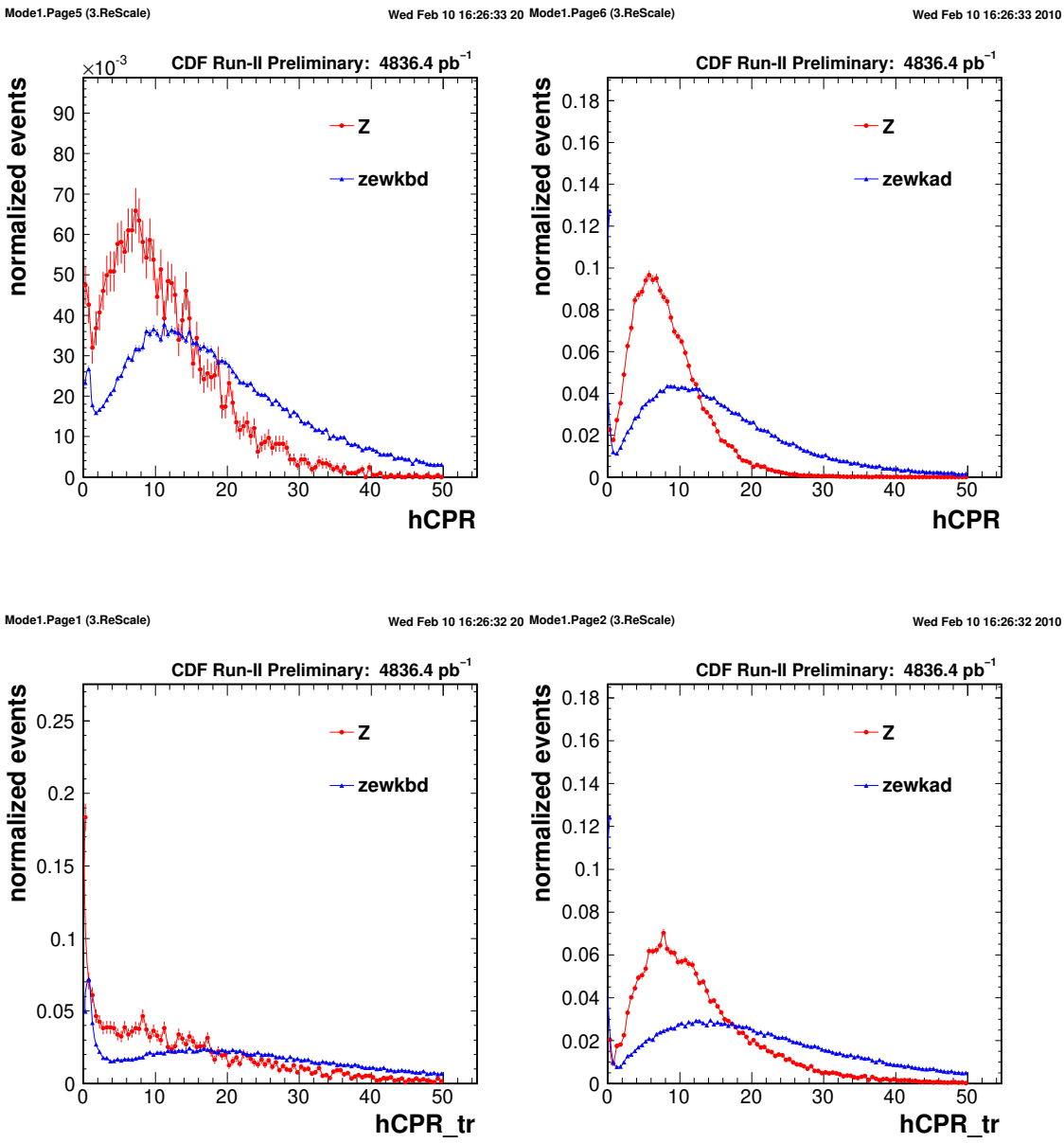

Figure 3.9: The CPR/CP2 responses from CDF EM objects(top) and tracks associated to EM showers(bottom). The samples are real Z electron data and MCs.

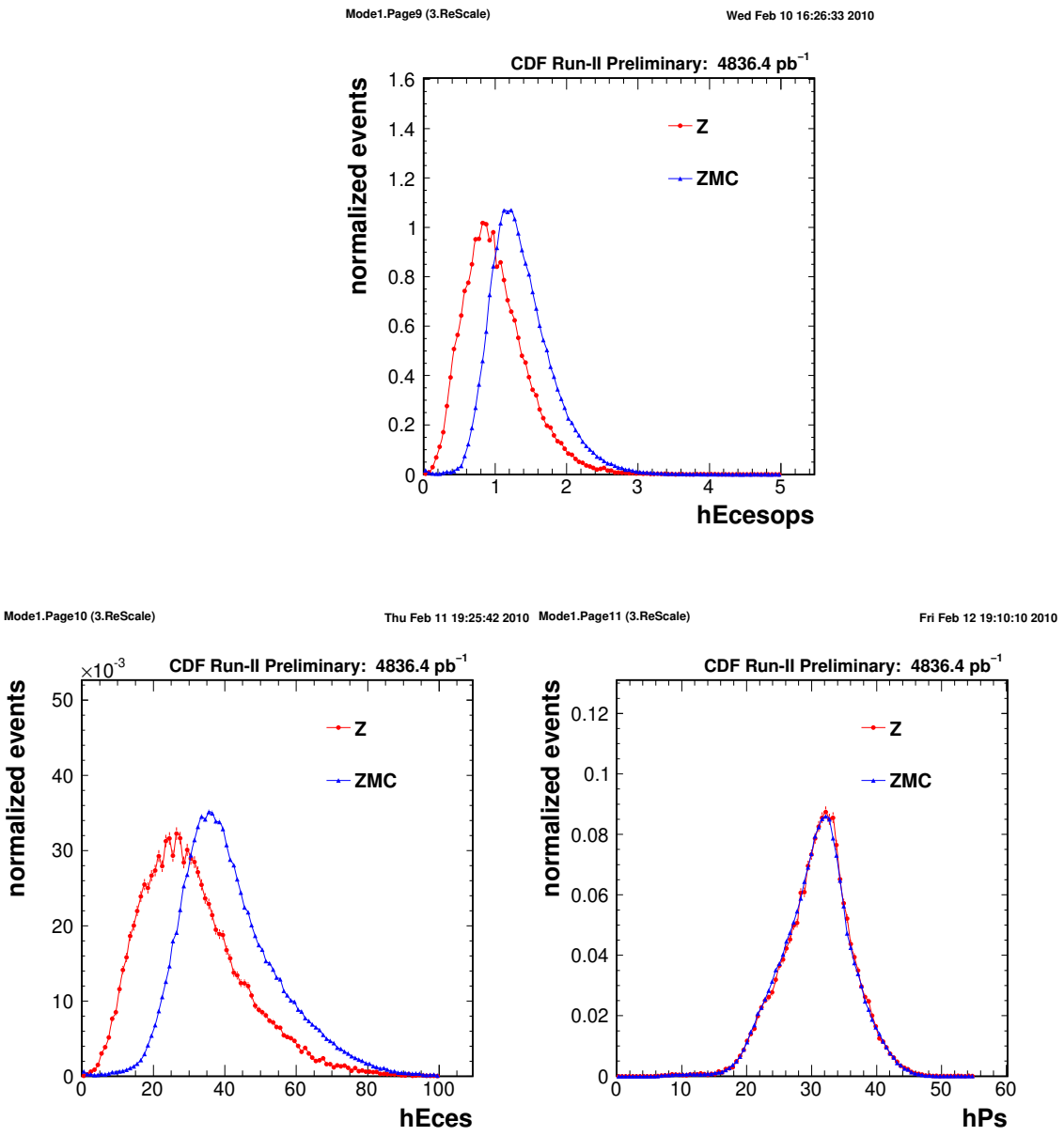

Figure 3.10: The $E_{\rm CES}/p^*$ (top), $E_{\rm CES}$ (bottom-left) and p^* distributions for real Z electron data and MCs.

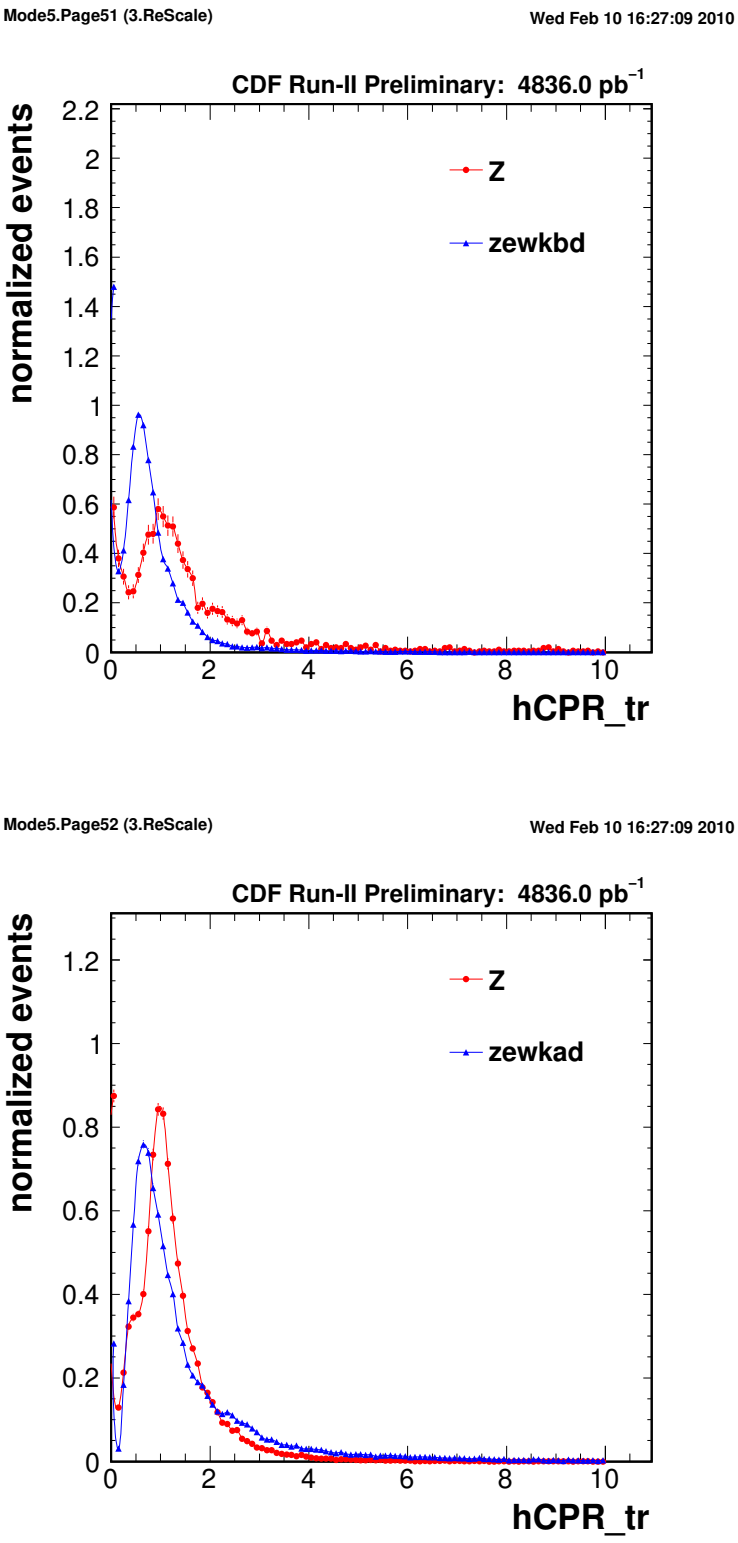

Figure 3.11: The CPR/CP2 responses tracks associated to EM showers for real Z muon data and MCs.

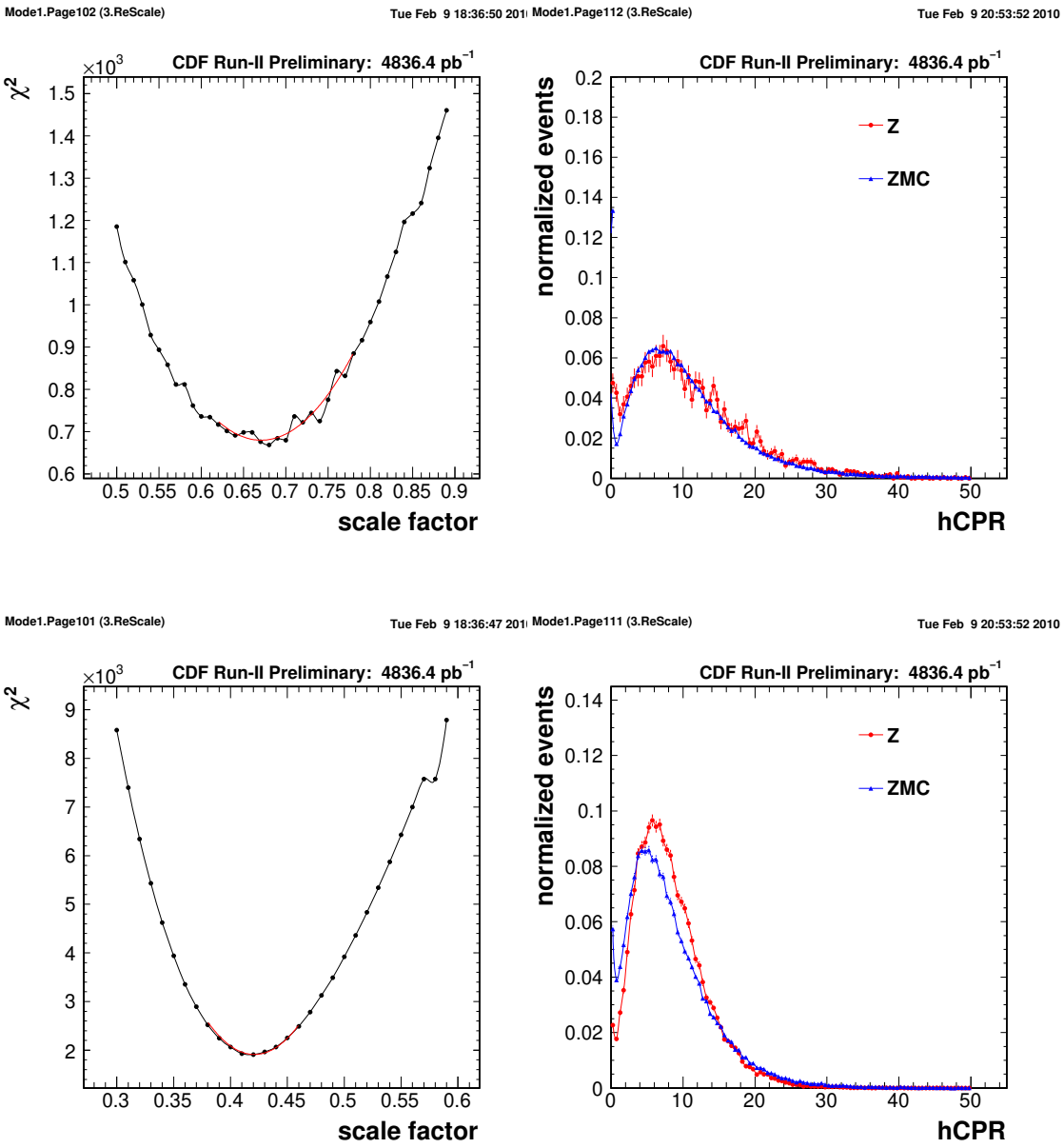

Figure 3.12: The left plots are χ^2 distributions of the CPR/CP2 (EM) rescaling for electron and the right are the CPR/CP2 responses after rescaled. The results for CPR on the top and CP2 on the bottom.

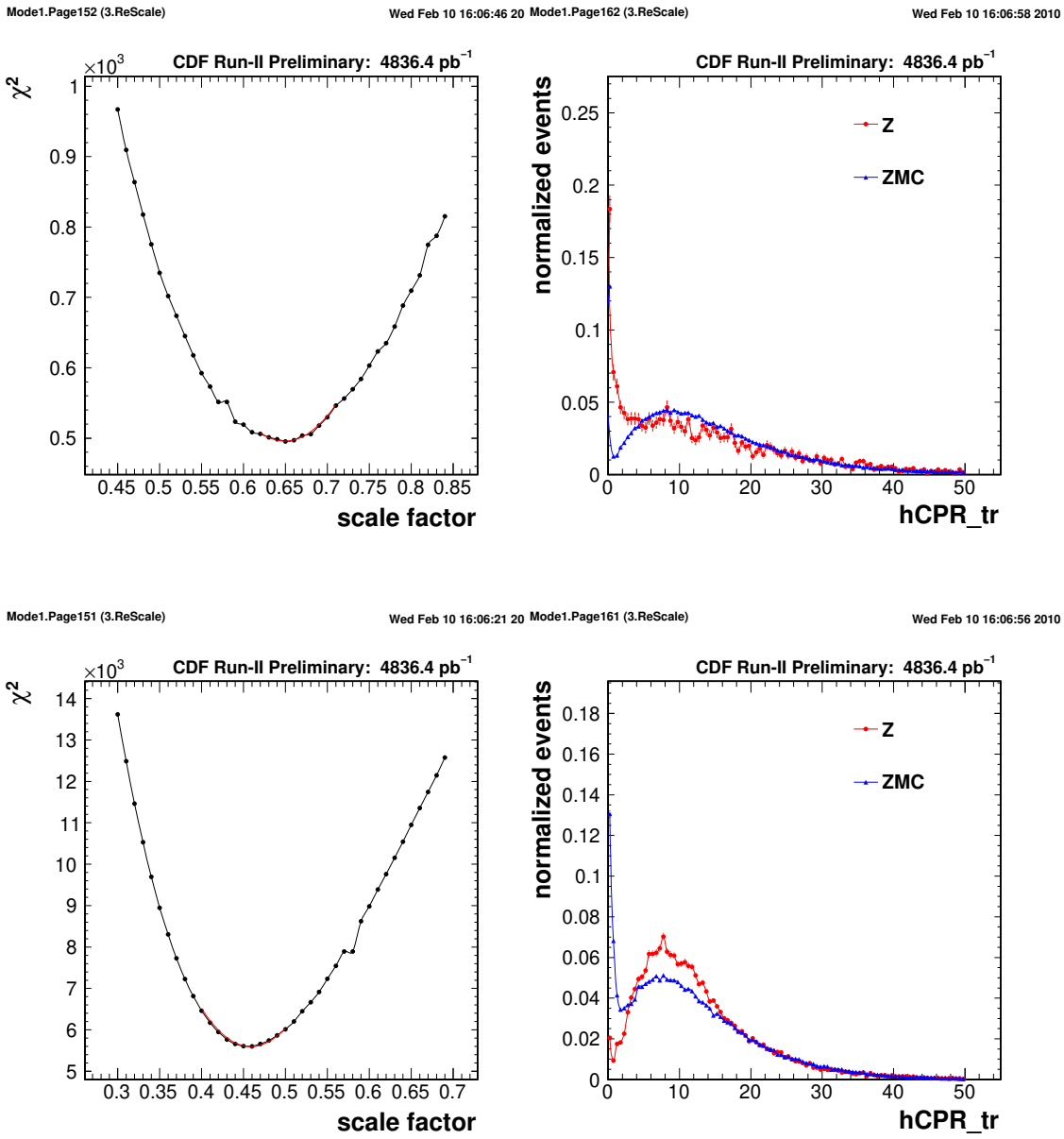

Figure 3.13: The left plots are χ^2 distributions of the CPR/CP2 (TR) rescaling for electron and the right are the CPR/CP2 responses after rescaled. The results for CPR on the top and CP2 on the bottom.

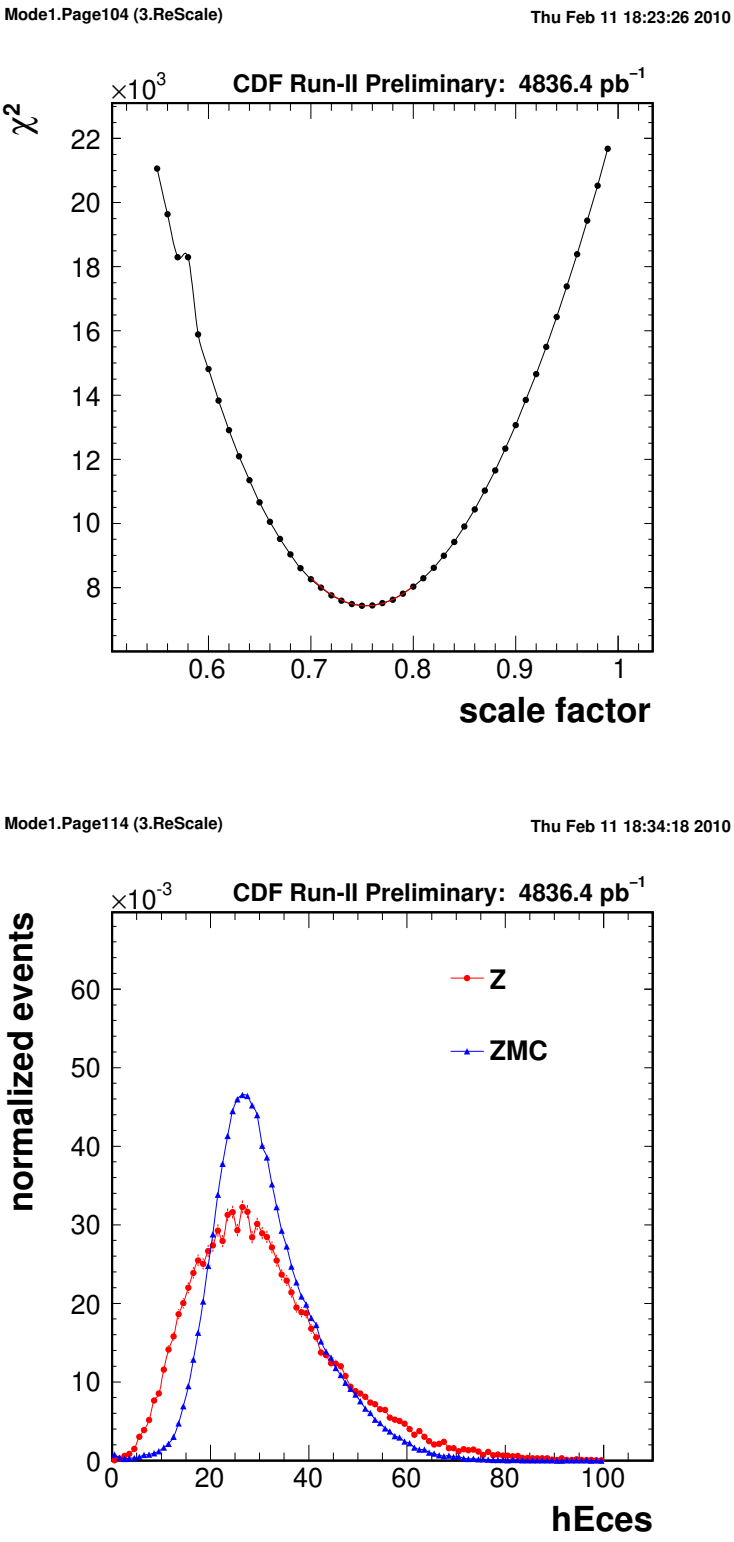

Figure 3.14: The χ^2 distribution for E_{CES} rescaling and the responce after recaled.

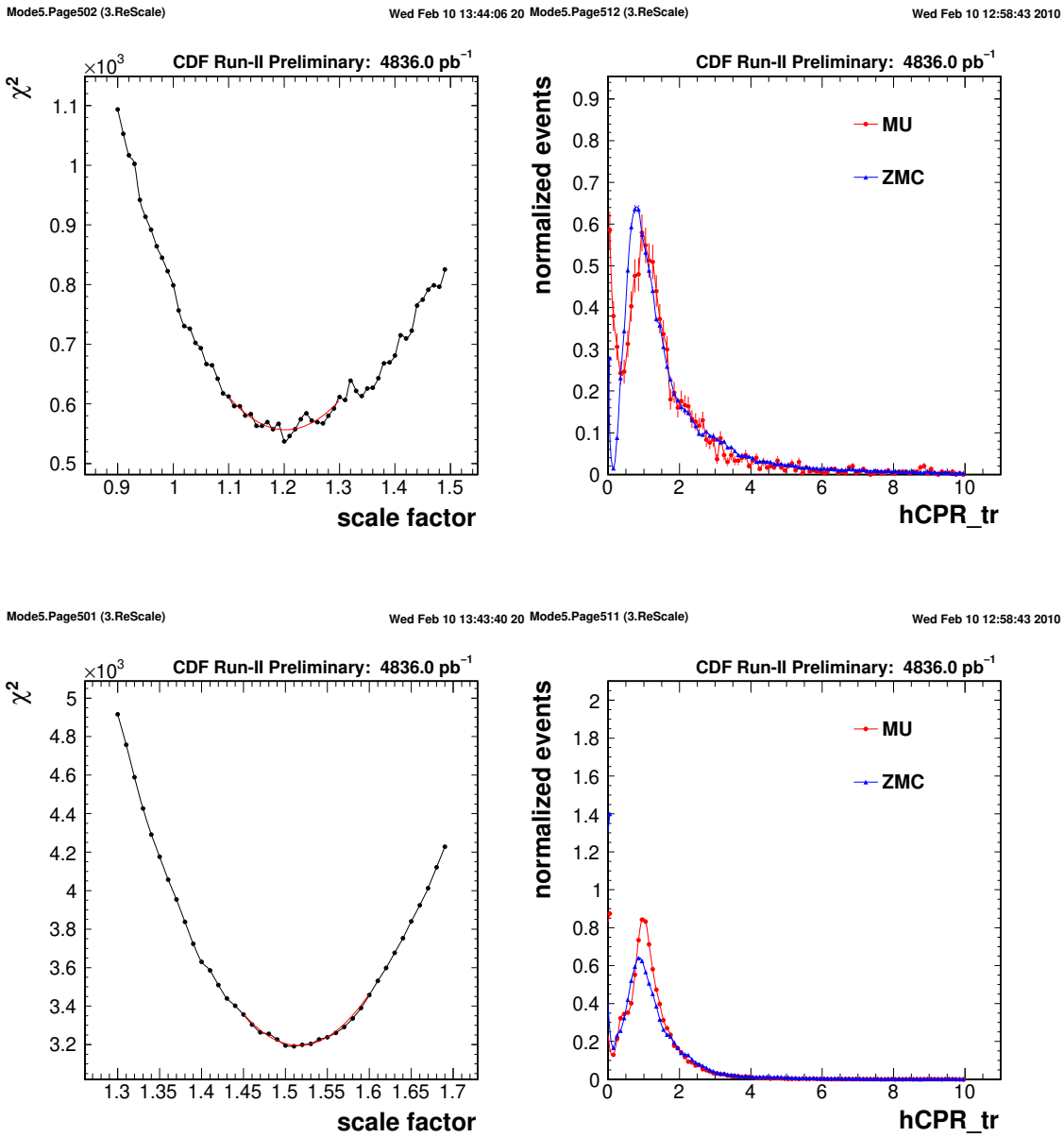

Figure 3.15: The left plots are χ^2 distributions of the CPR/CP2 (TR) rescaling for muon and the right are the CPR/CP2 responses after rescaled. The results for CPR on the top and CP2 on the bottom.

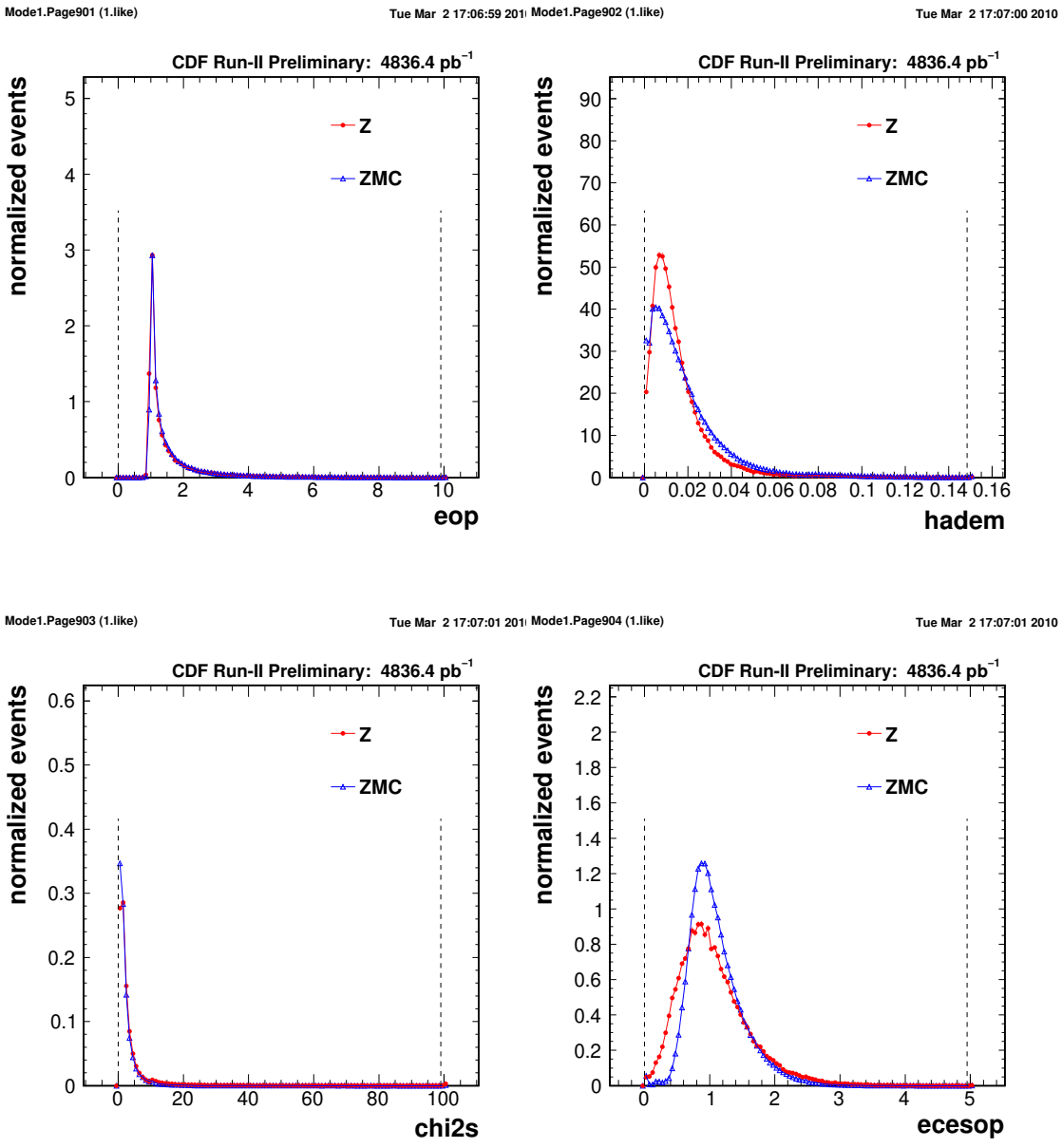

Figure 3.16: The lepton PDFs of the Z data and Z MCs.

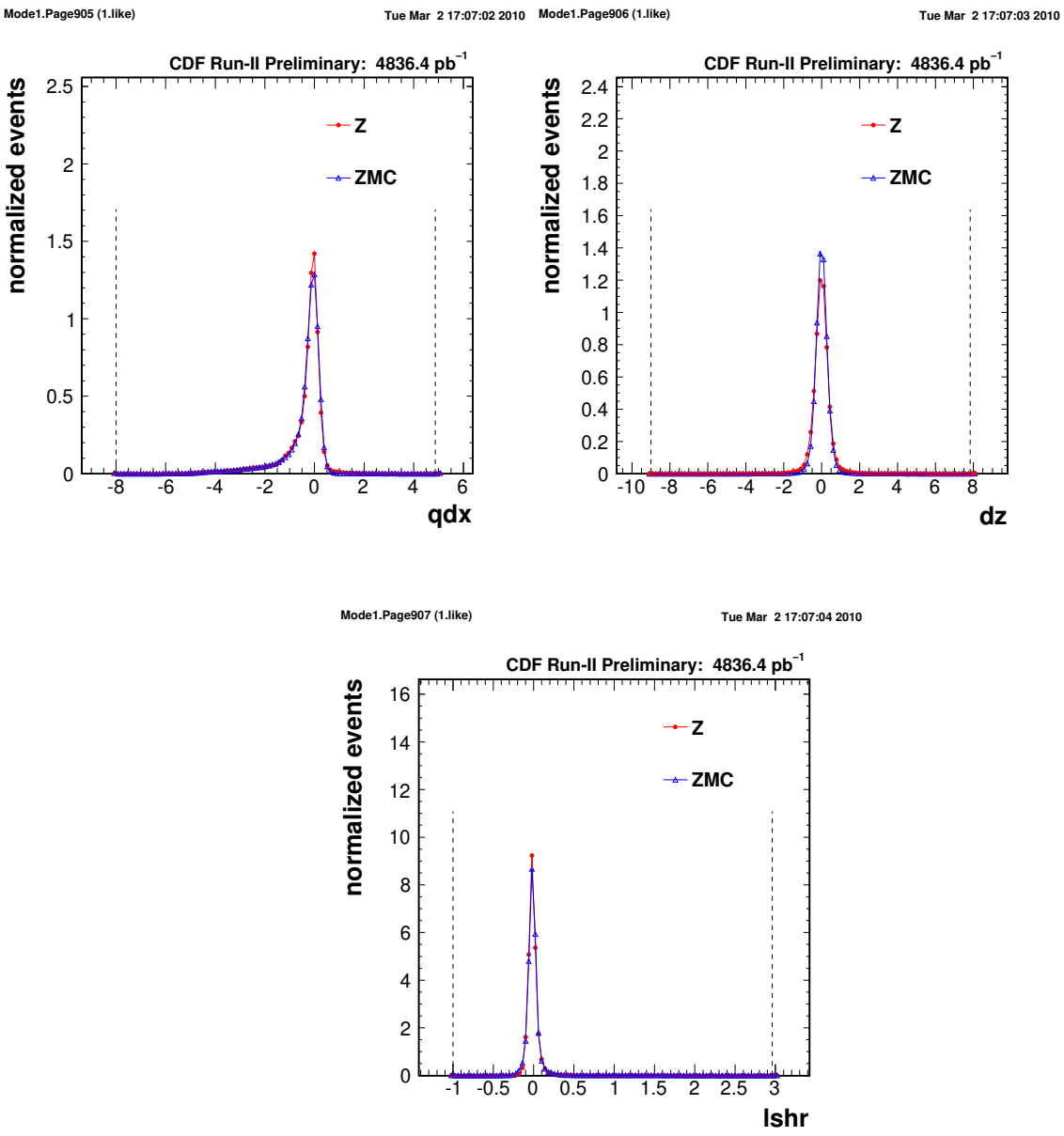

Figure 3.17: The lepton PDFs of the Z data and Z MCs.

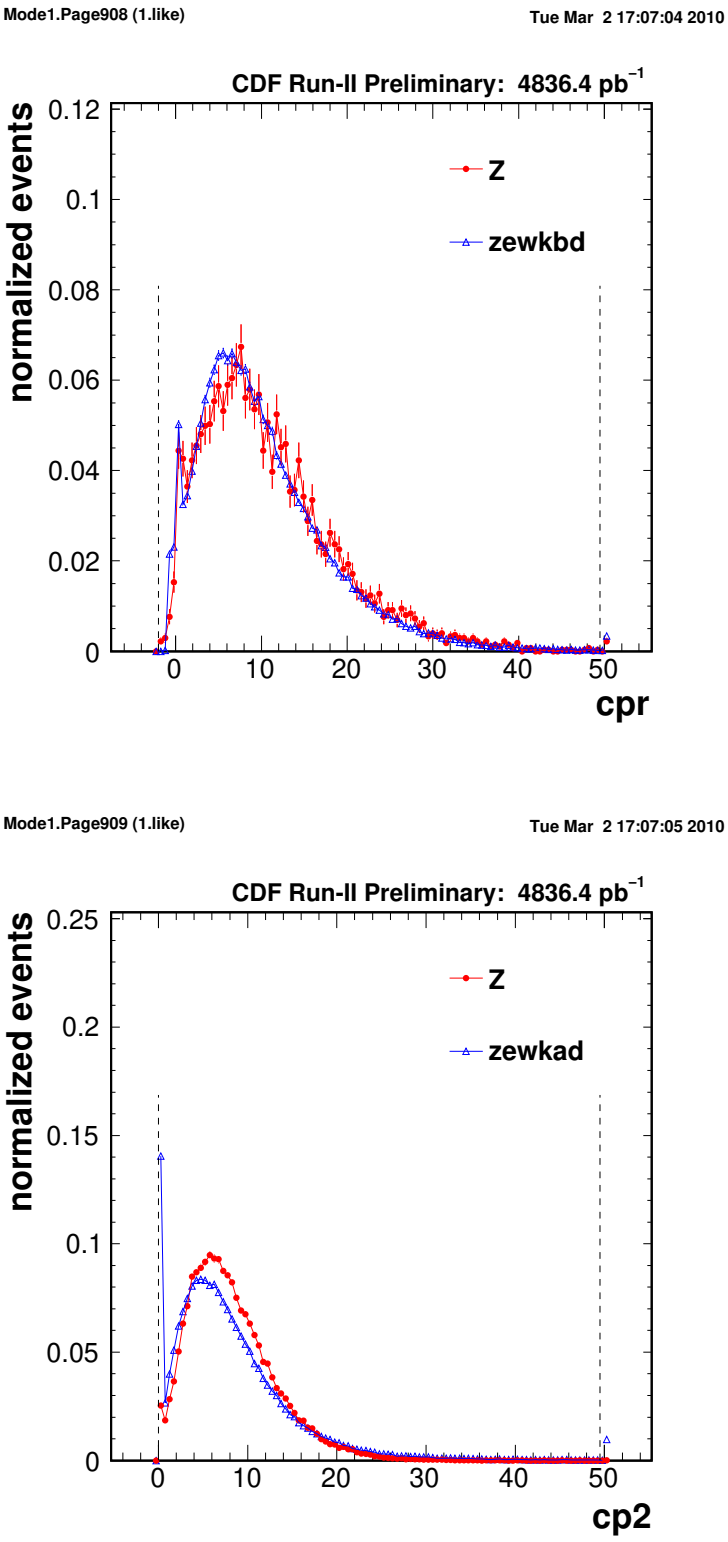

Figure 3.18: The lepton PDFs of the Z data and Z MCs.

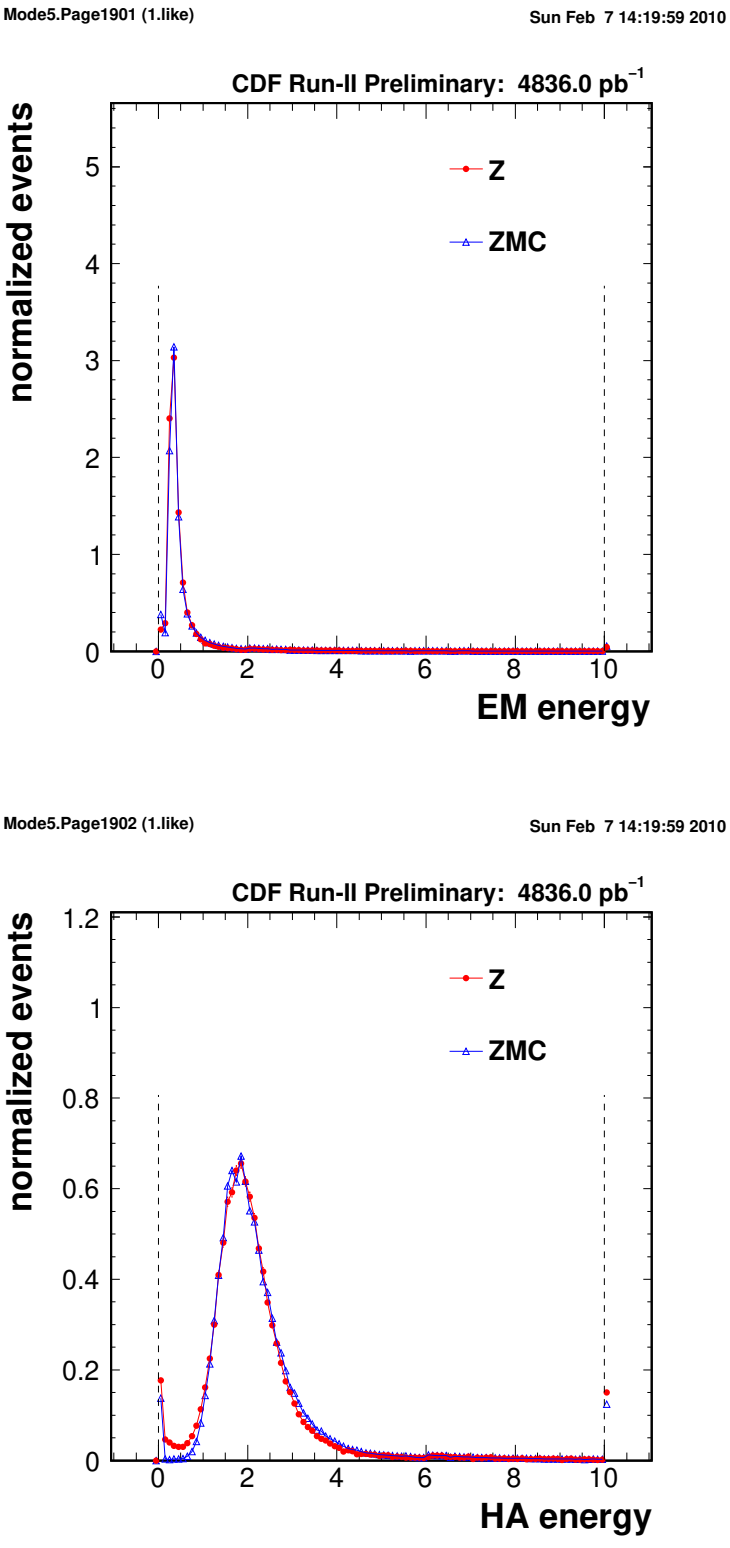

Figure 3.19: The lepton PDFs of the Z data and Z MCs.

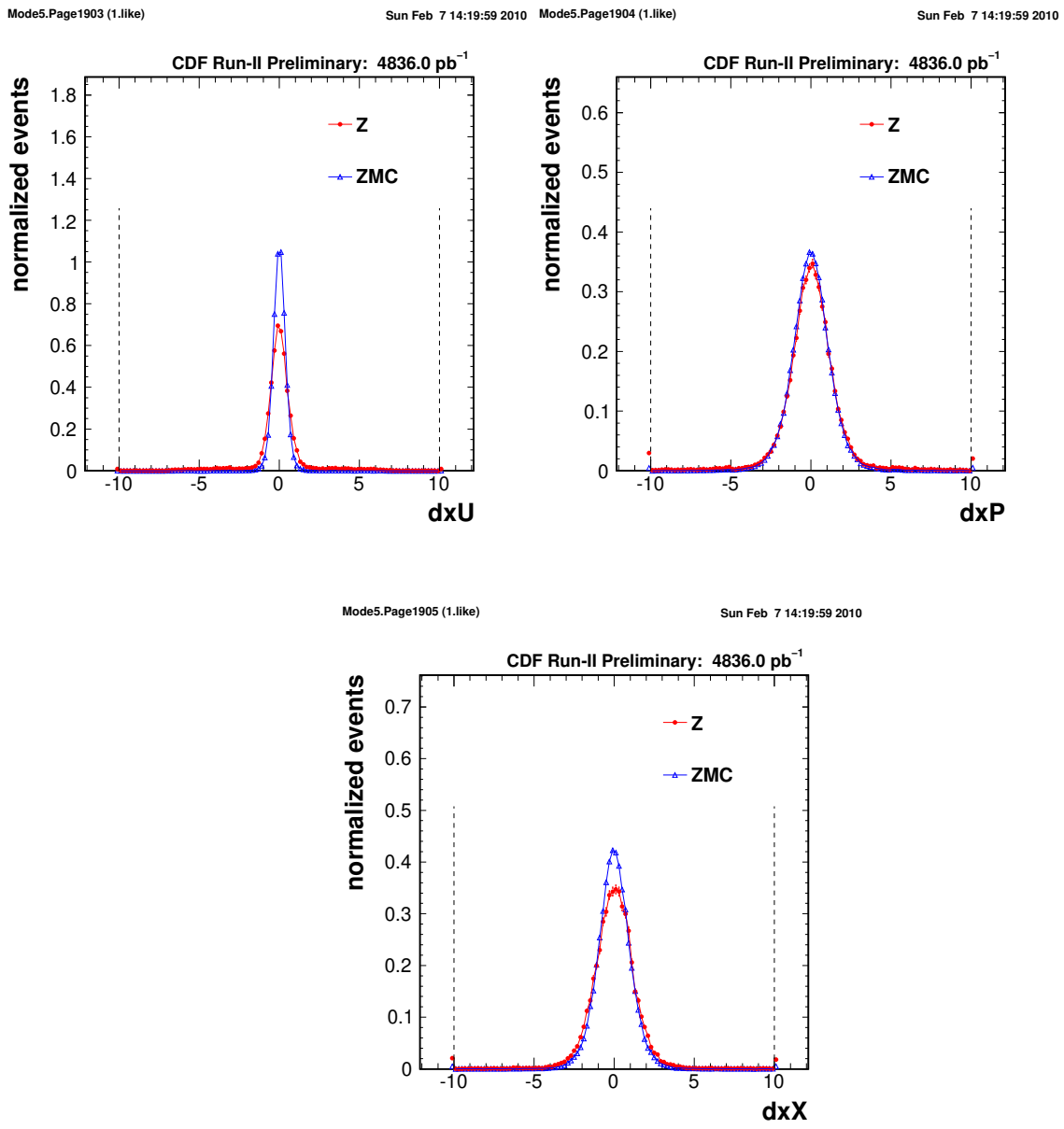

Figure 3.20: The lepton PDFs of the Z data and Z MCs.

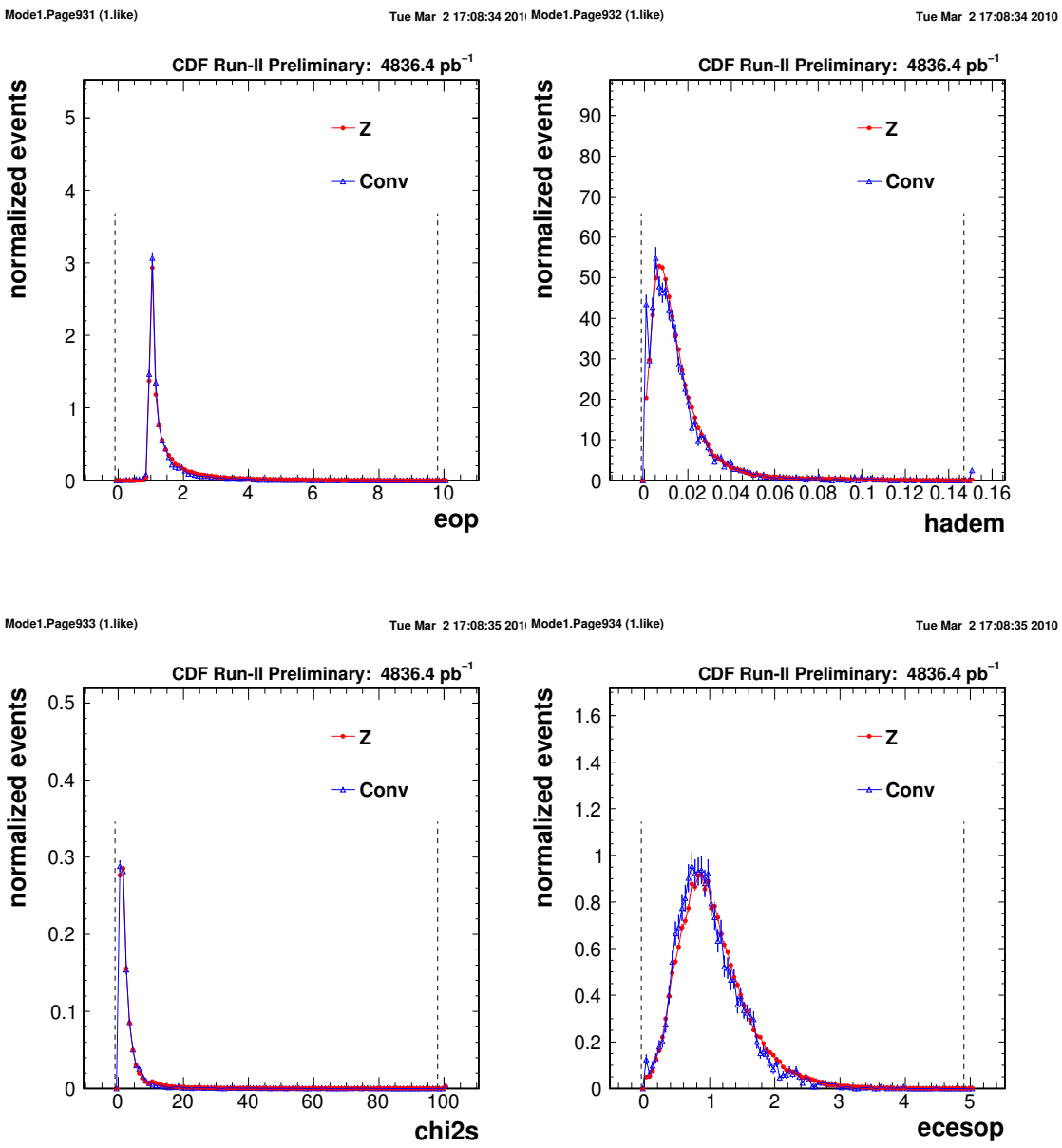

Figure 3.21: The lepton PDFs of electron from Z decays and photon conversion.

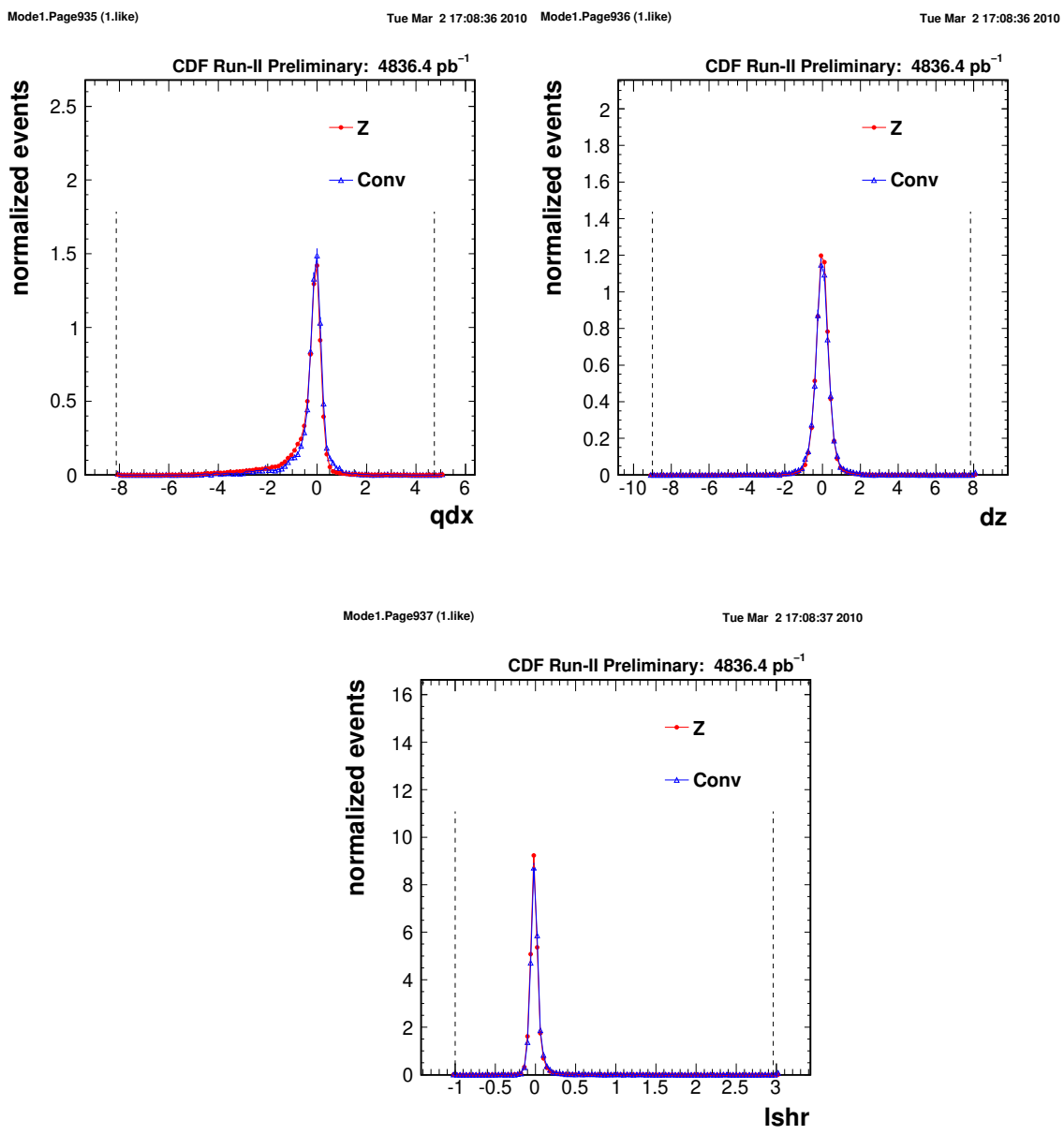

Figure 3.22: The lepton PDFs of electron from Z decays and photon conversion.

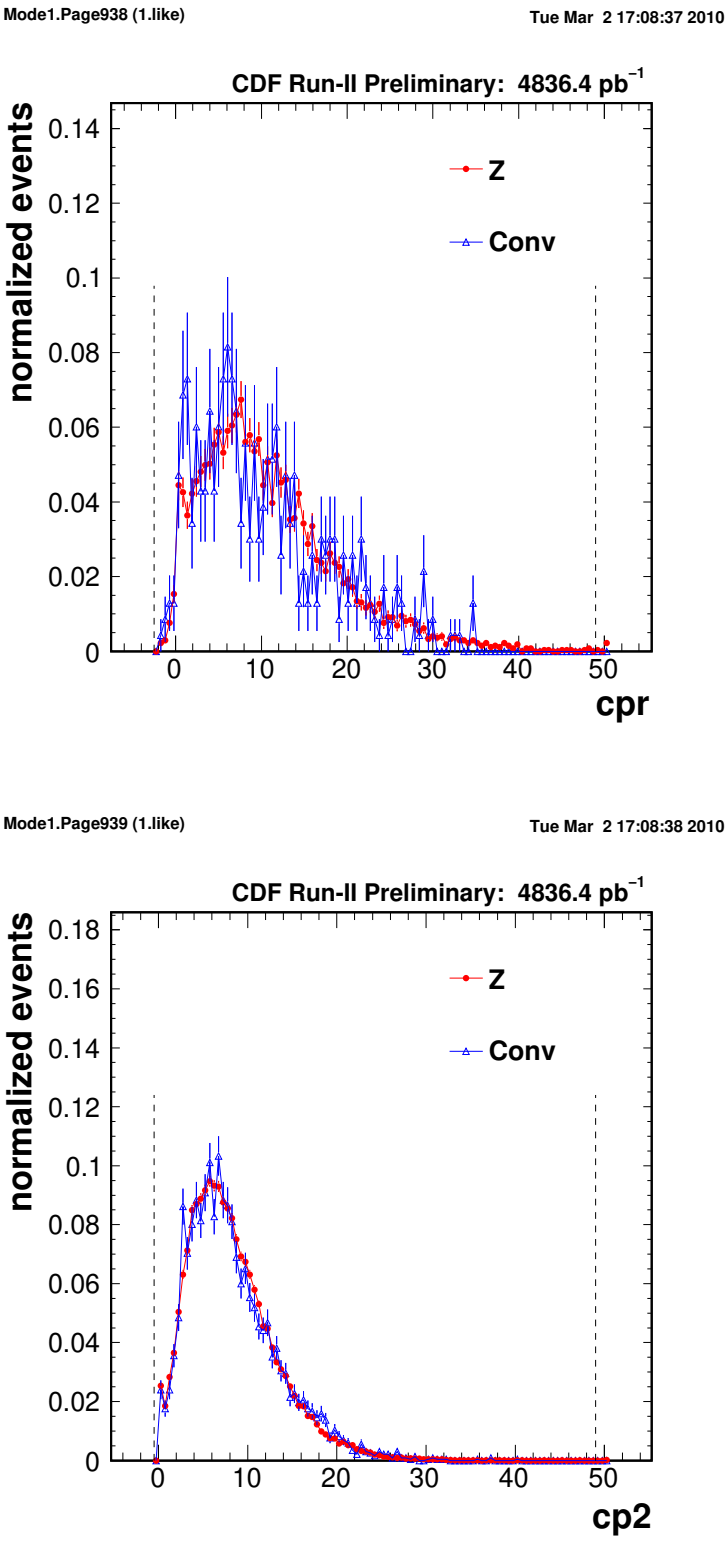

Figure 3.23: The lepton PDFs of electron from Z decays and photon conversion.

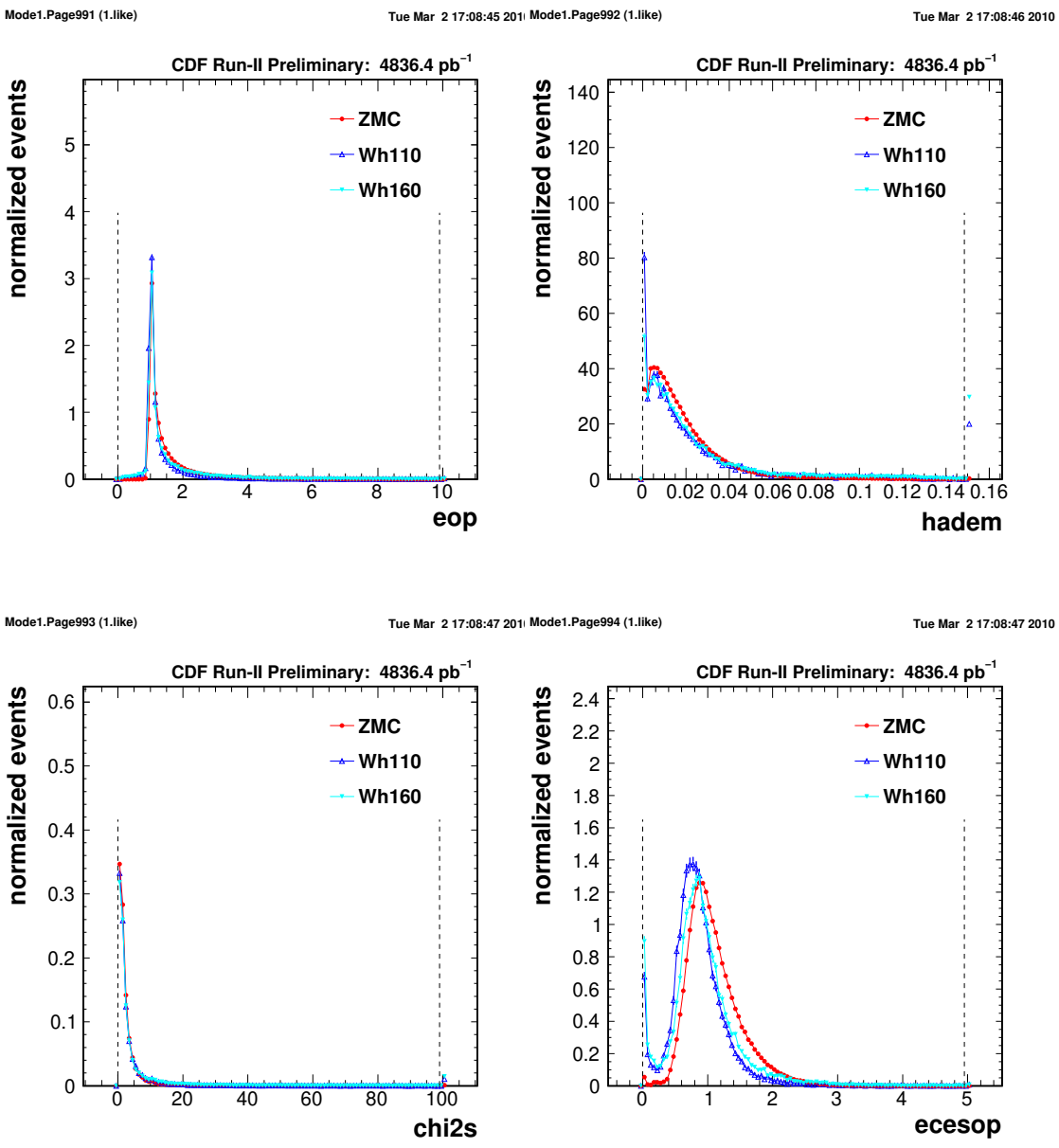

Figure 3.24: The lepton PDFs of the Z and higgs MCs.

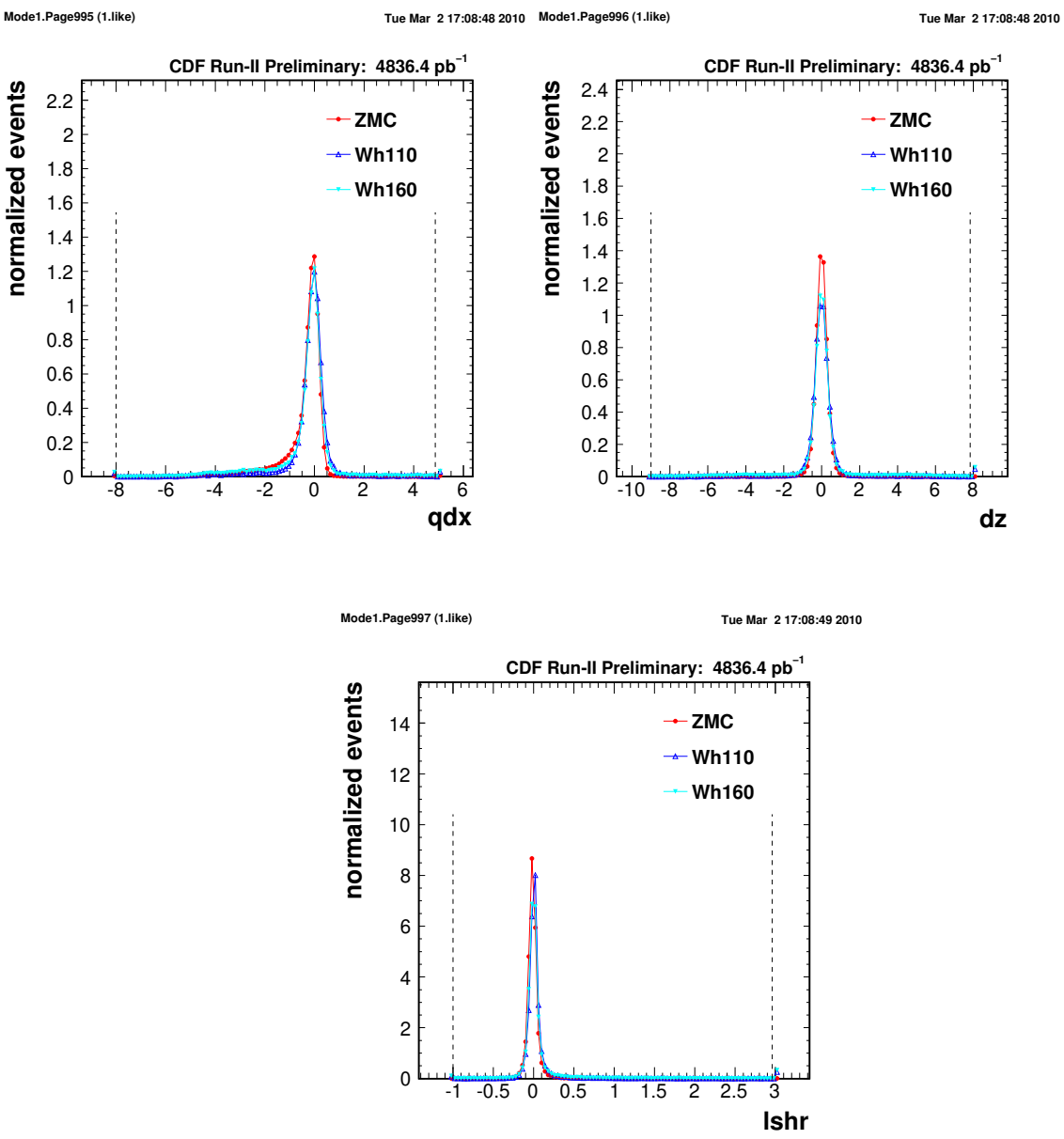

Figure 3.25: The lepton PDFs of the Z and higgs MCs.

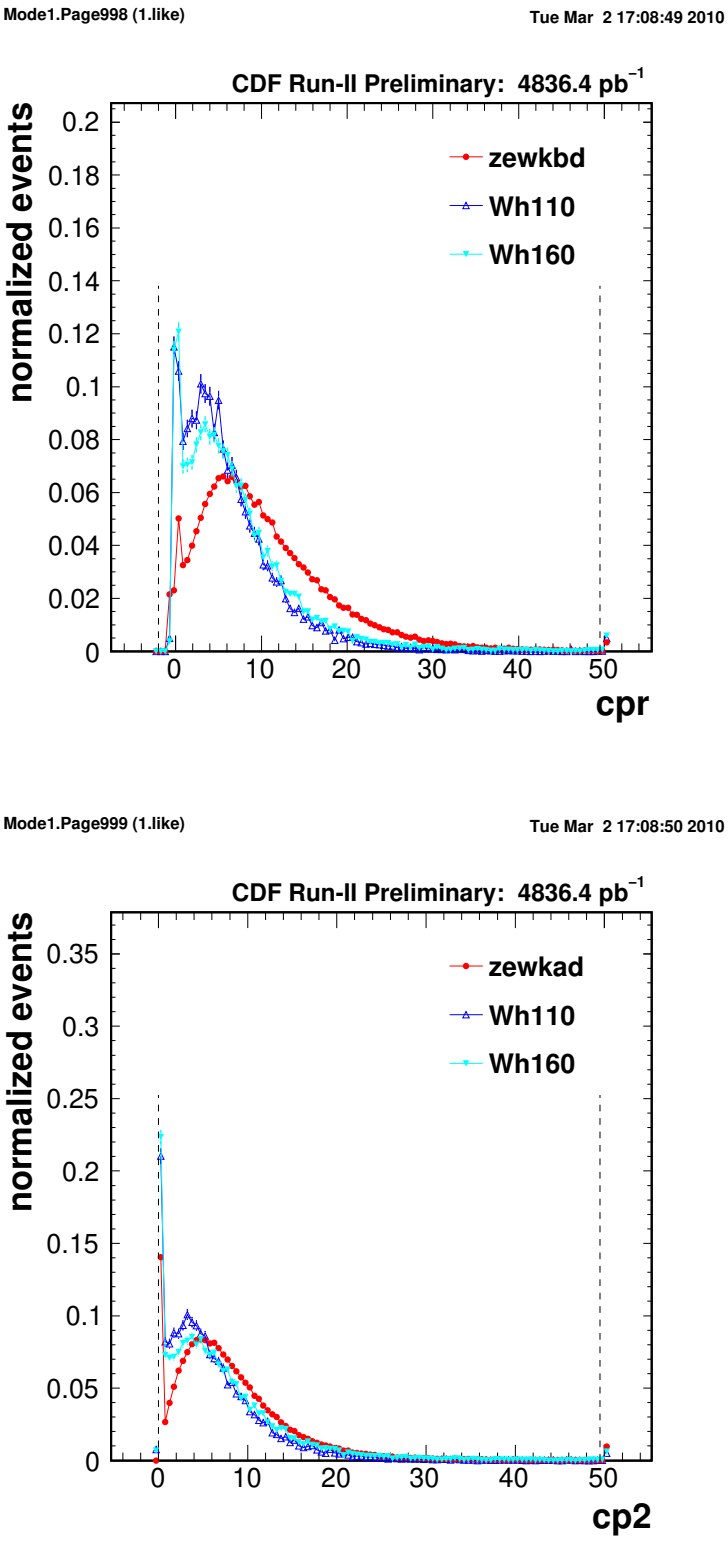

Figure 3.26: The lepton PDFs of the Z and higgs MCs.

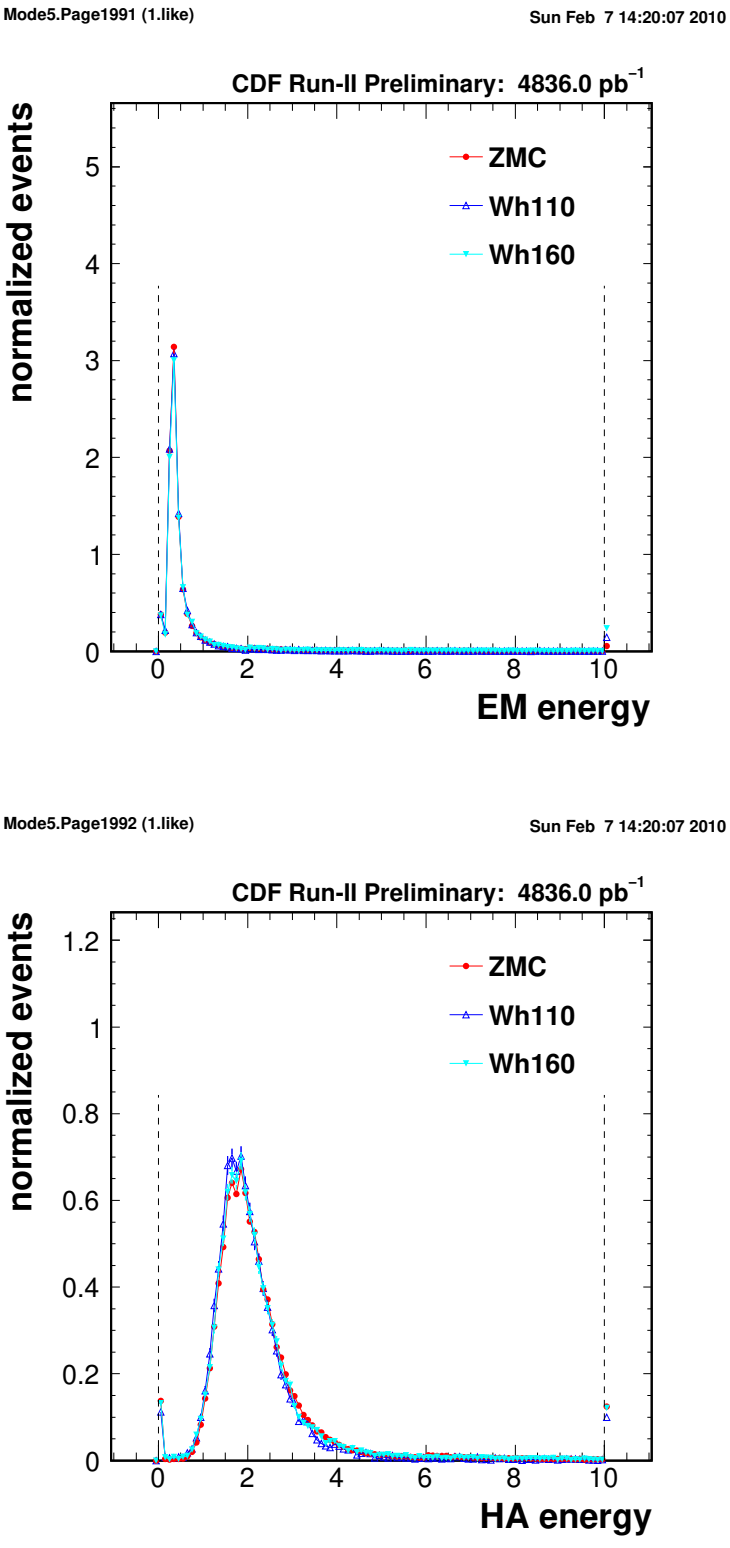

Figure 3.27: The lepton PDFs of the Z and higgs MCs.

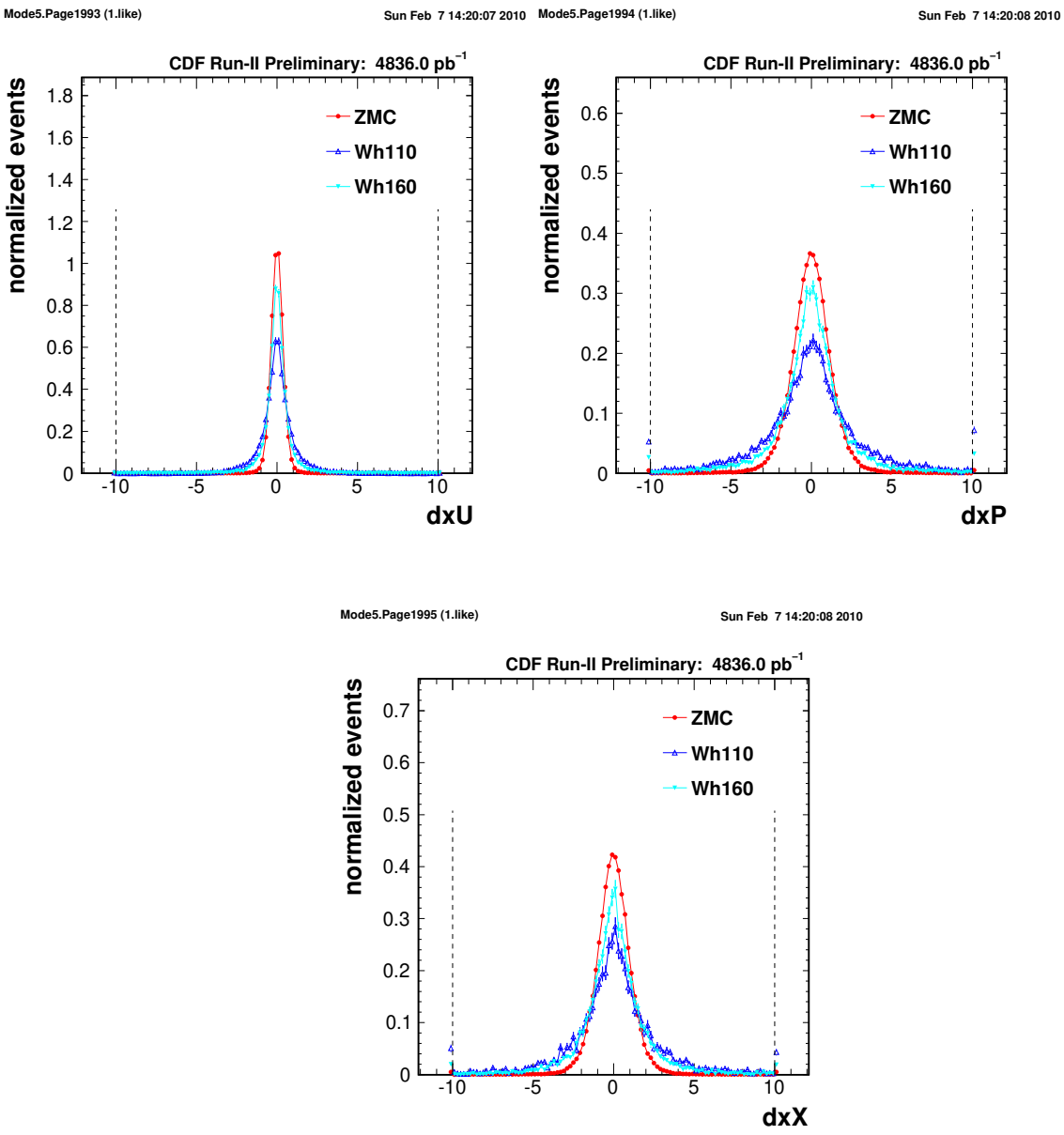

Figure 3.28: The lepton PDFs of the Z and higgs MCs.

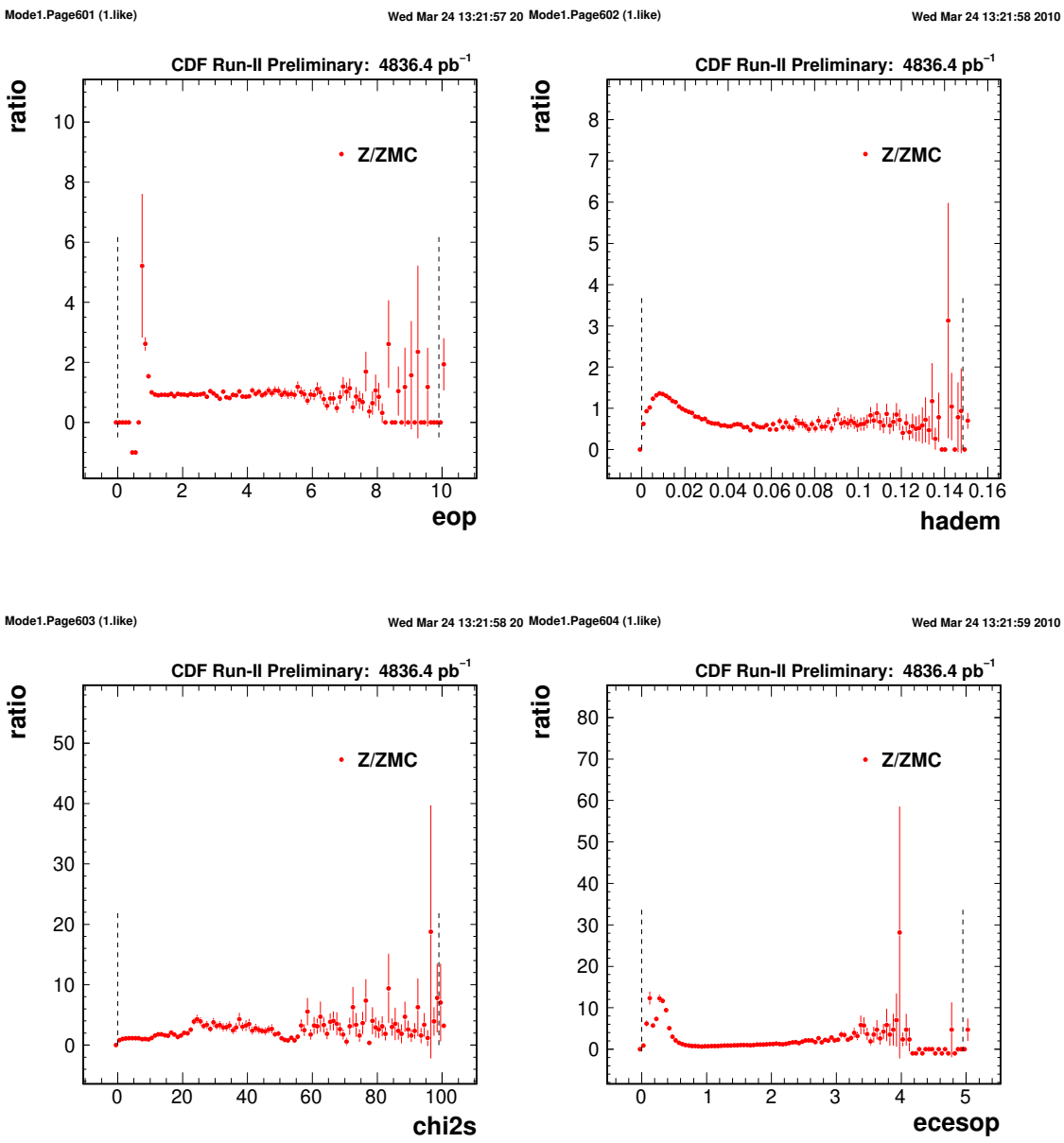

Figure 3.29: The ratio between lepton PDFs of the Z data and Z MCs.

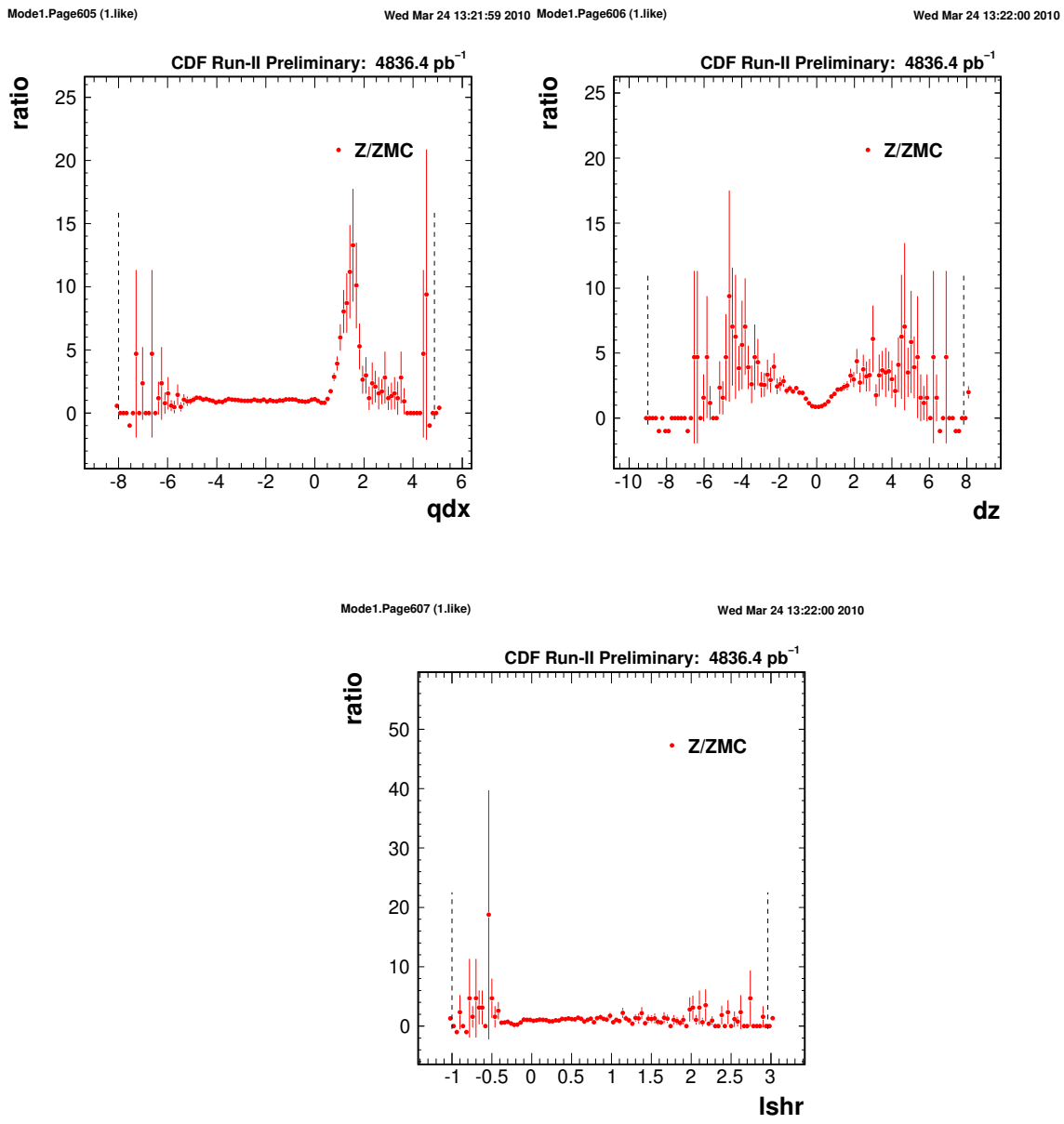

Figure 3.30: The ratio between lepton PDFs of the Z data and Z MCs.

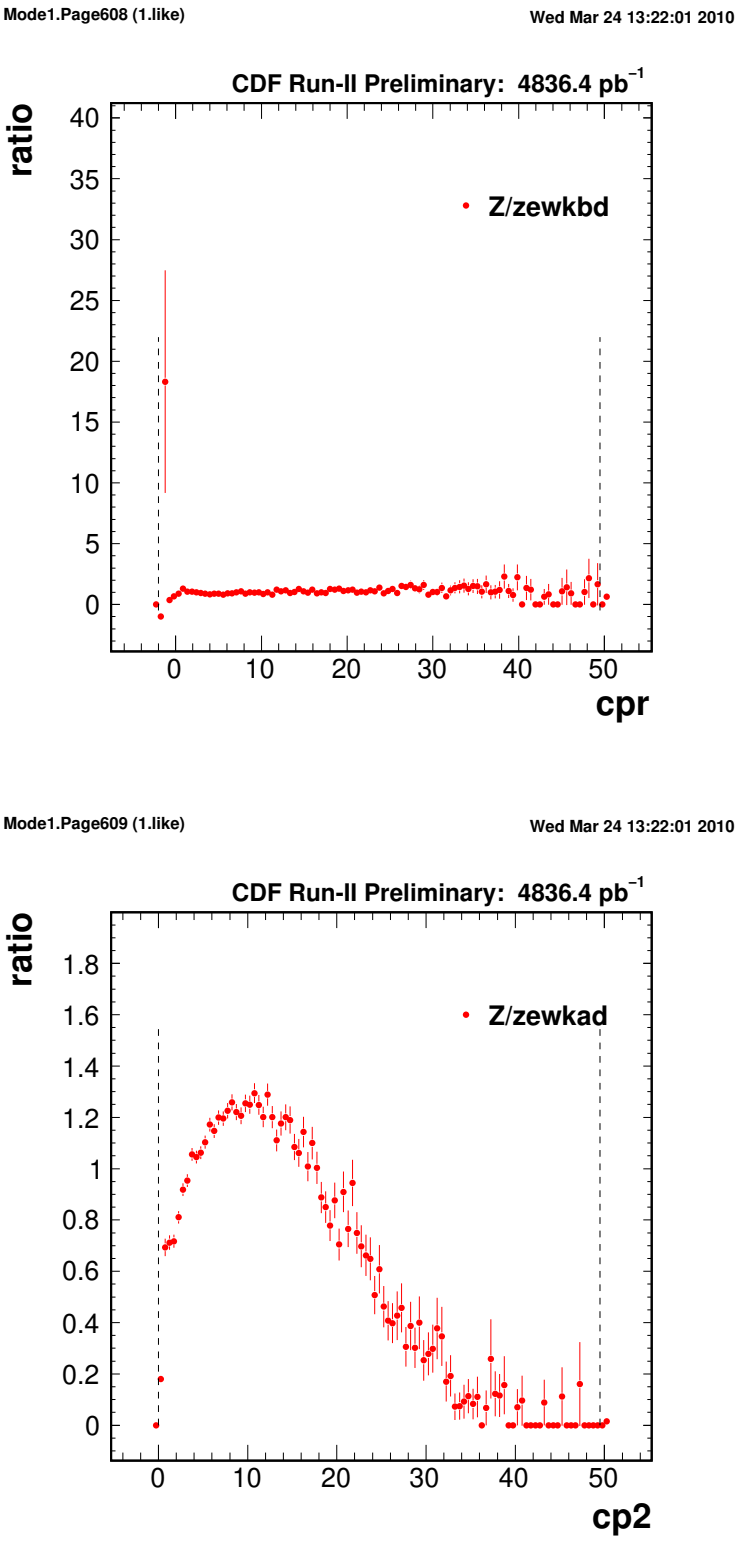

Figure 3.31: The ratio between lepton PDFs of the Z data and Z MCs.

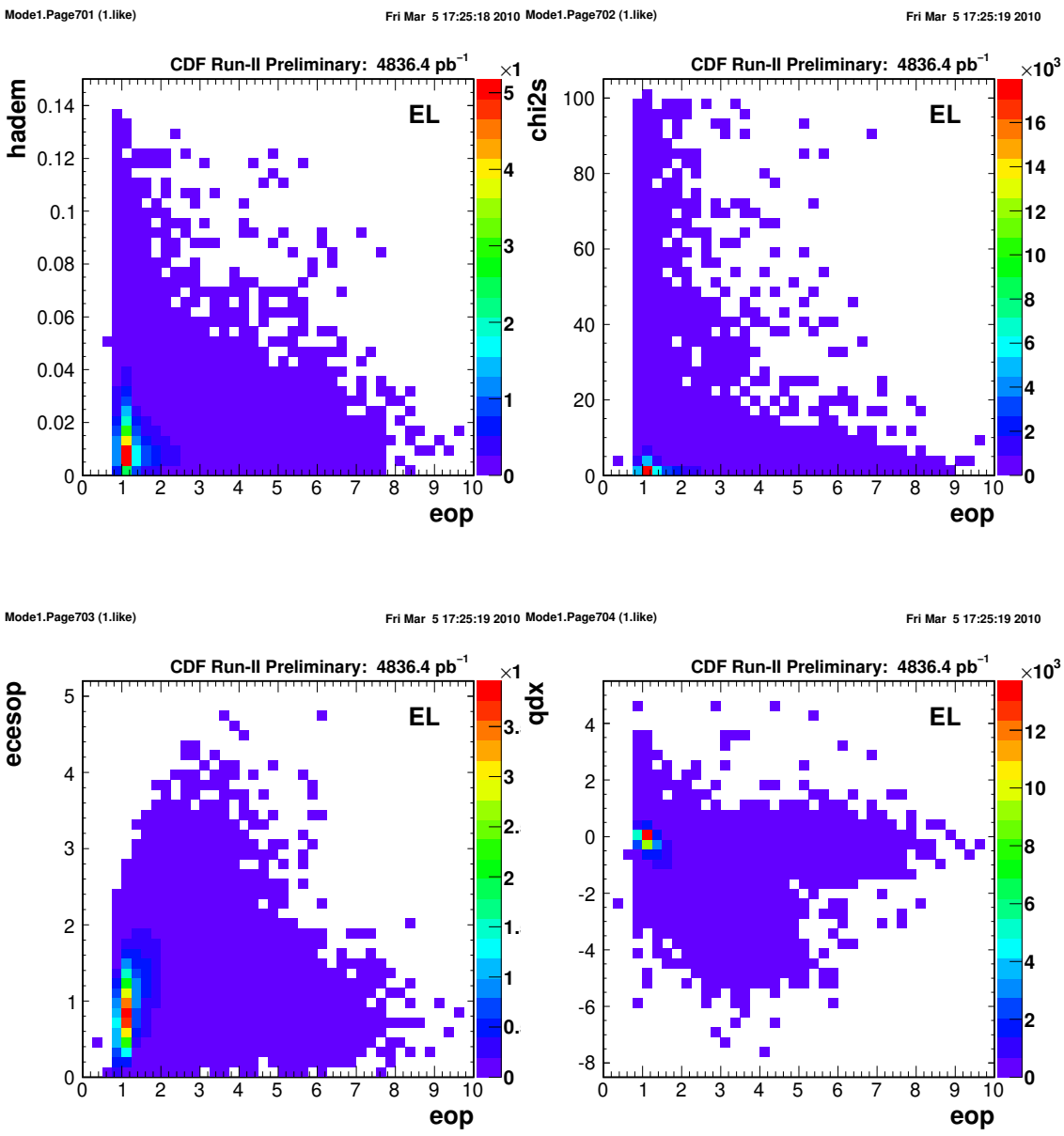

Figure 3.32: The correlation between two variables for Z data.

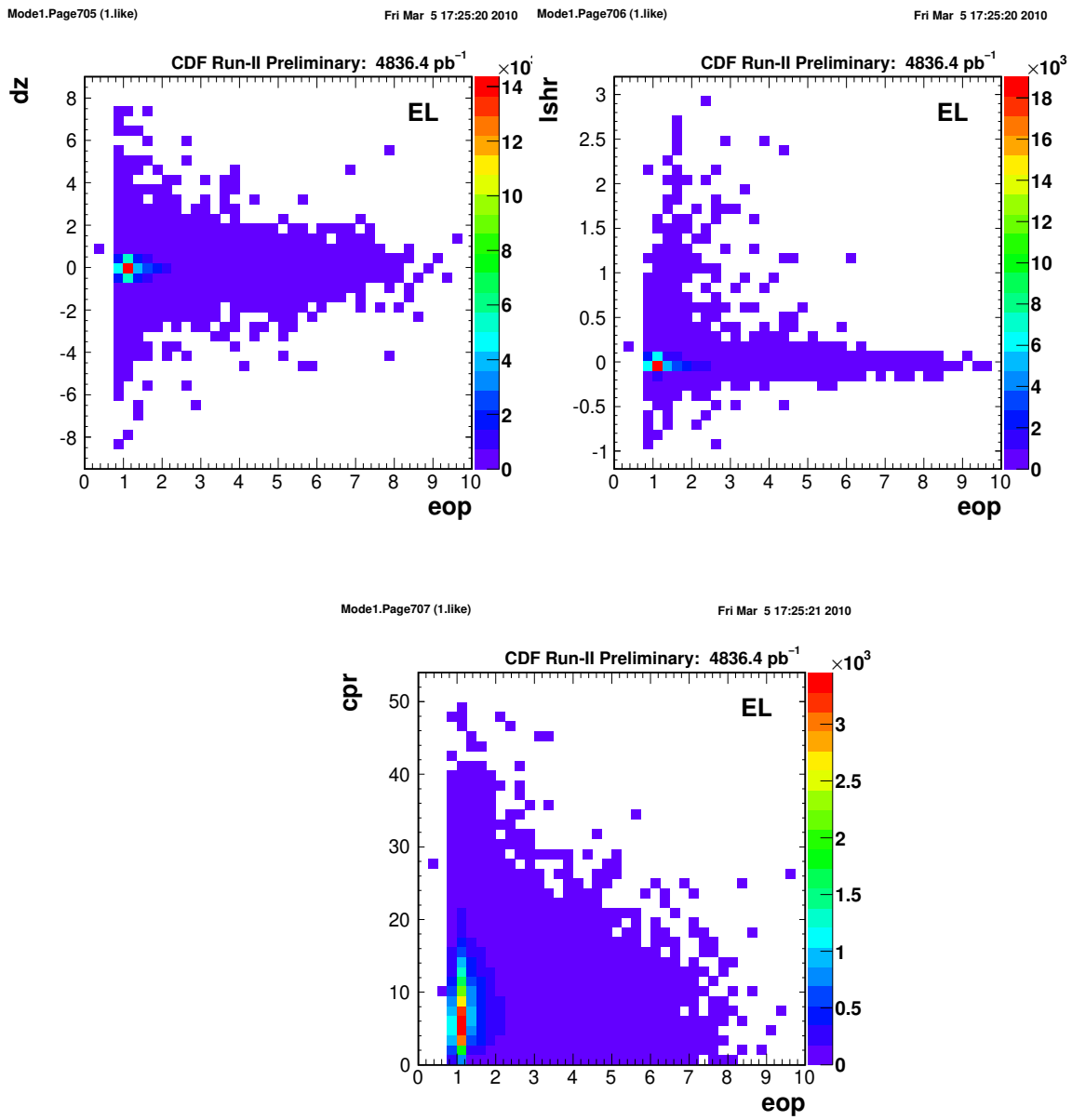

Figure 3.33: The correlation between two variables for Z data.

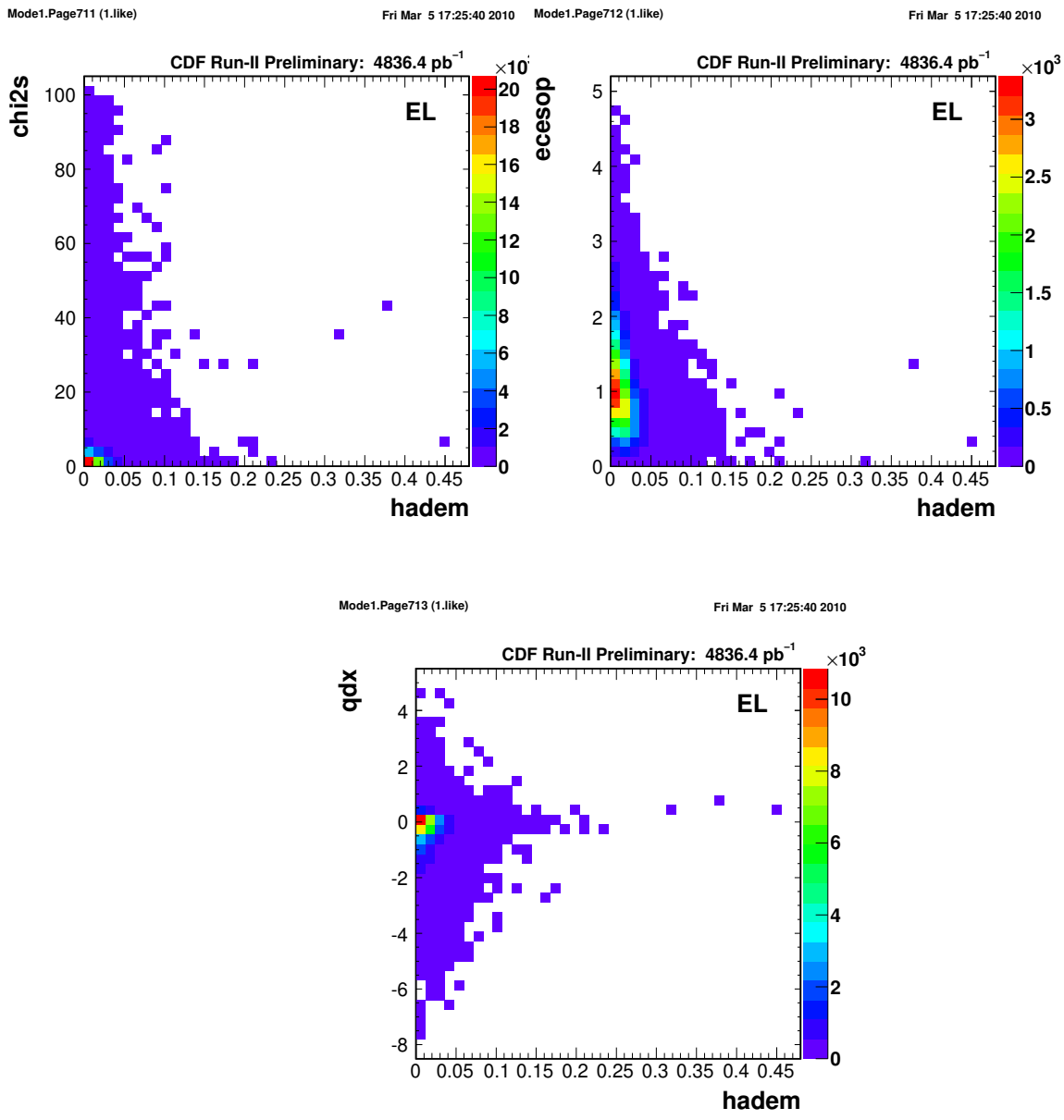

Figure 3.34: The correlation between two variables for Z data.

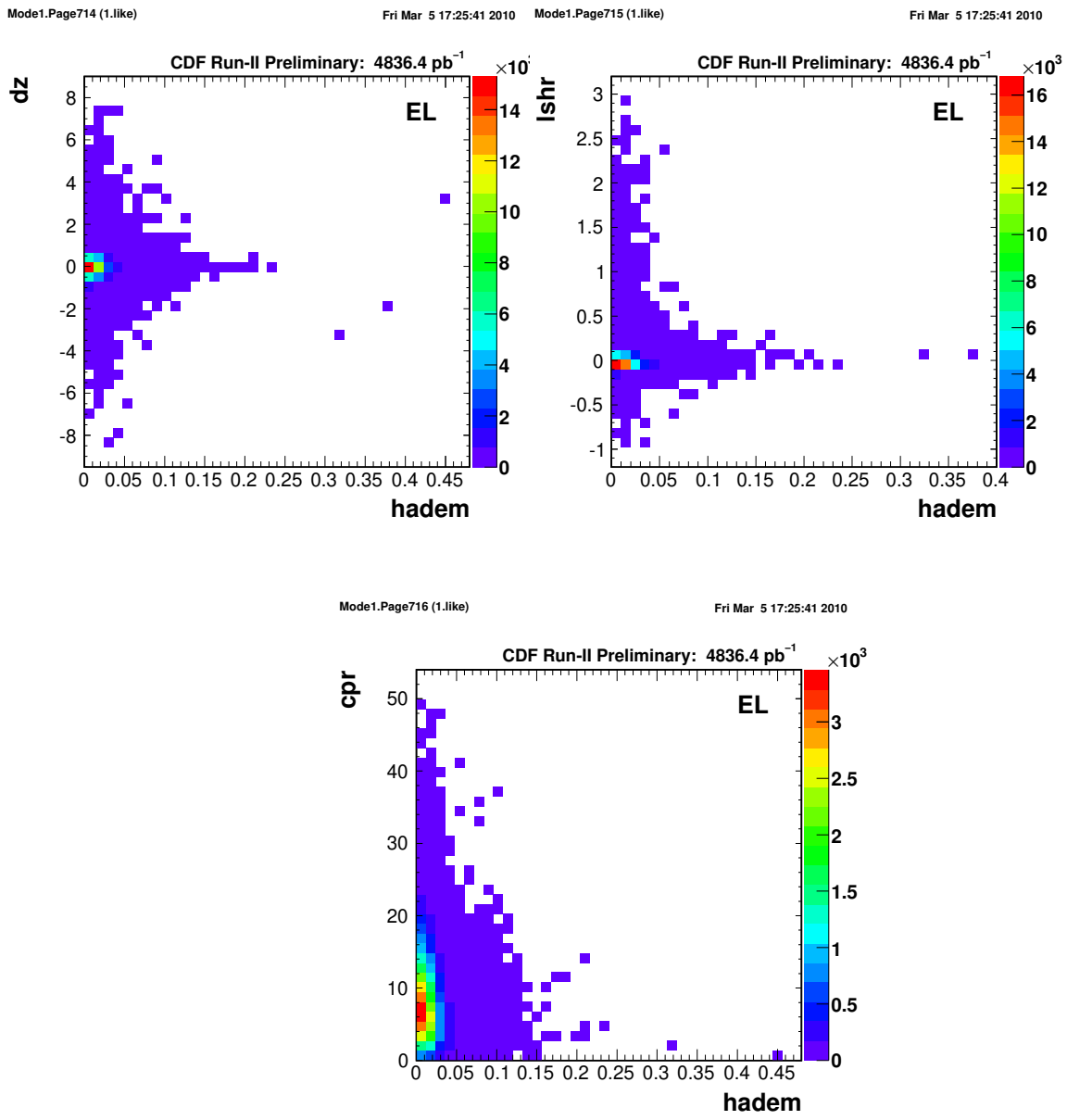

Figure 3.35: The correlation between two variables for Z data.

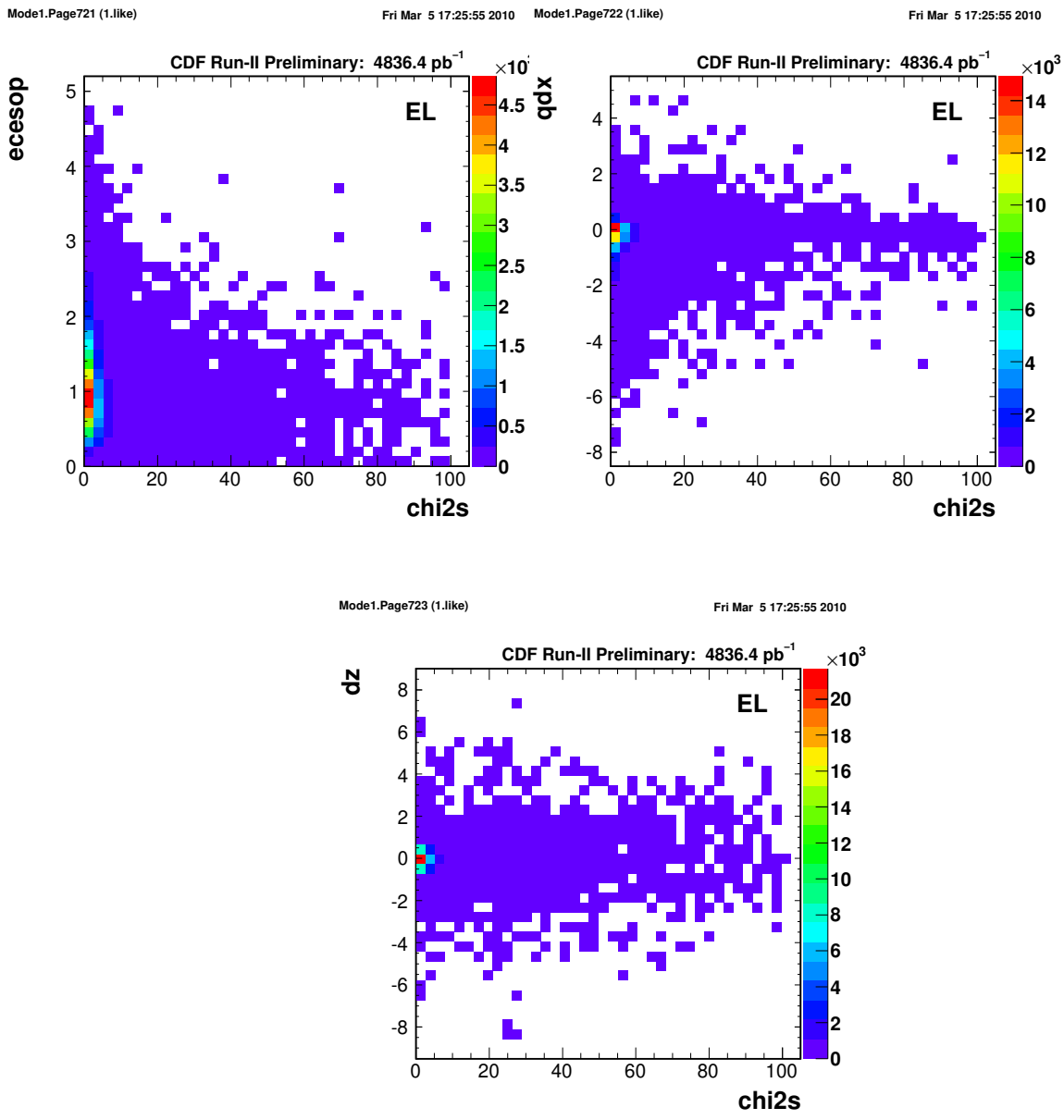

Figure 3.36: The correlation between two variables for Z data.

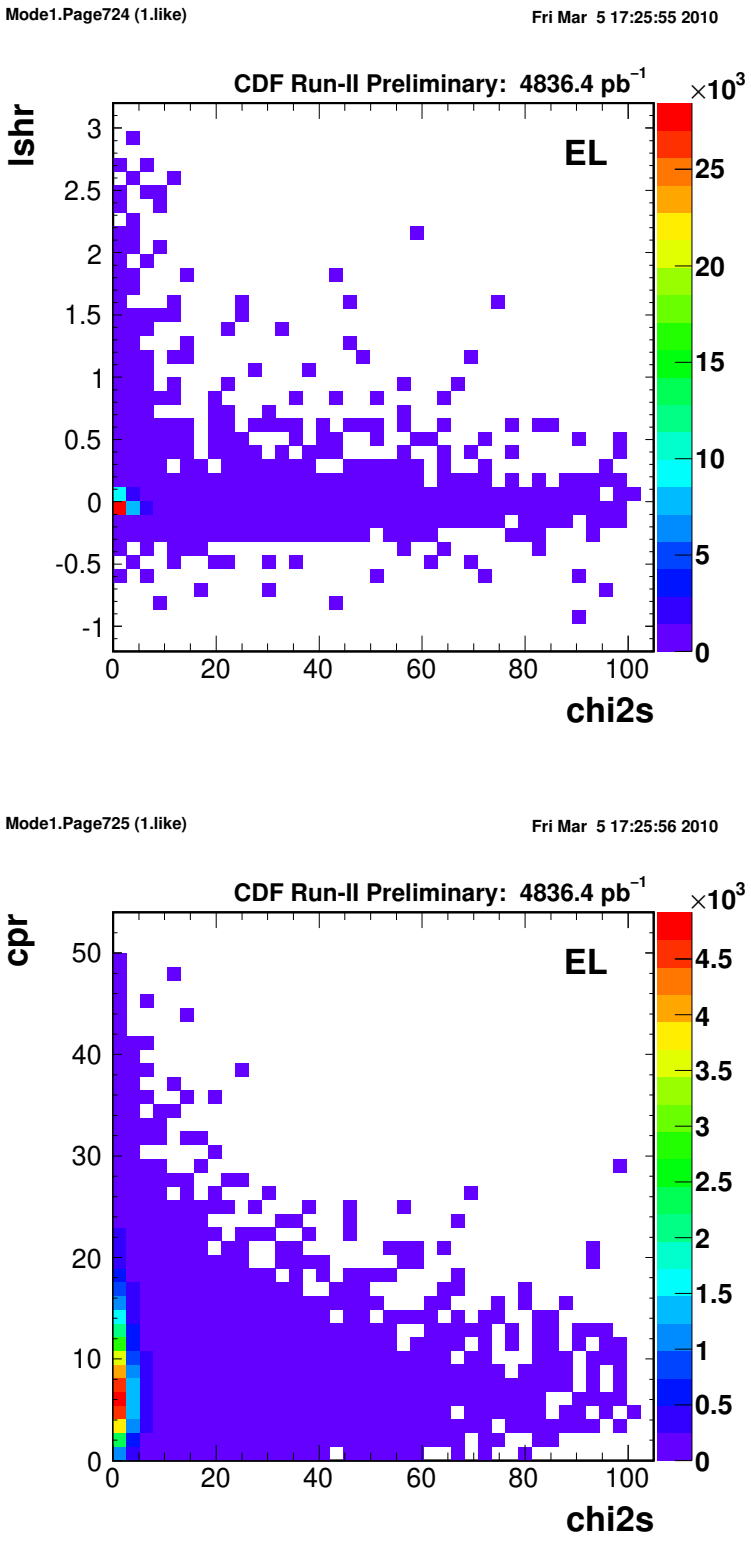

Figure 3.37: The correlation between two variables for Z data.

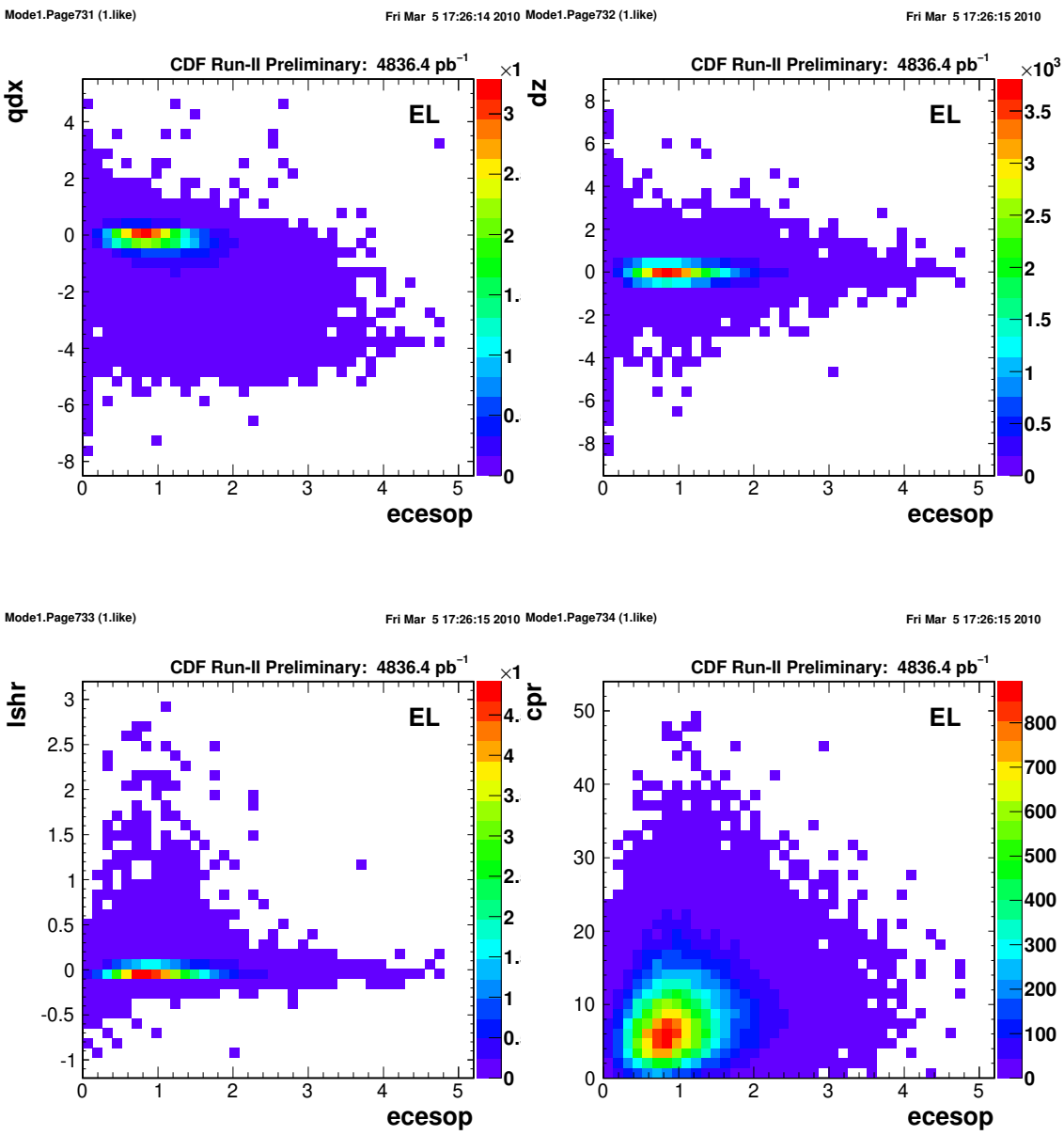

Figure 3.38: The correlation between two variables for Z data.

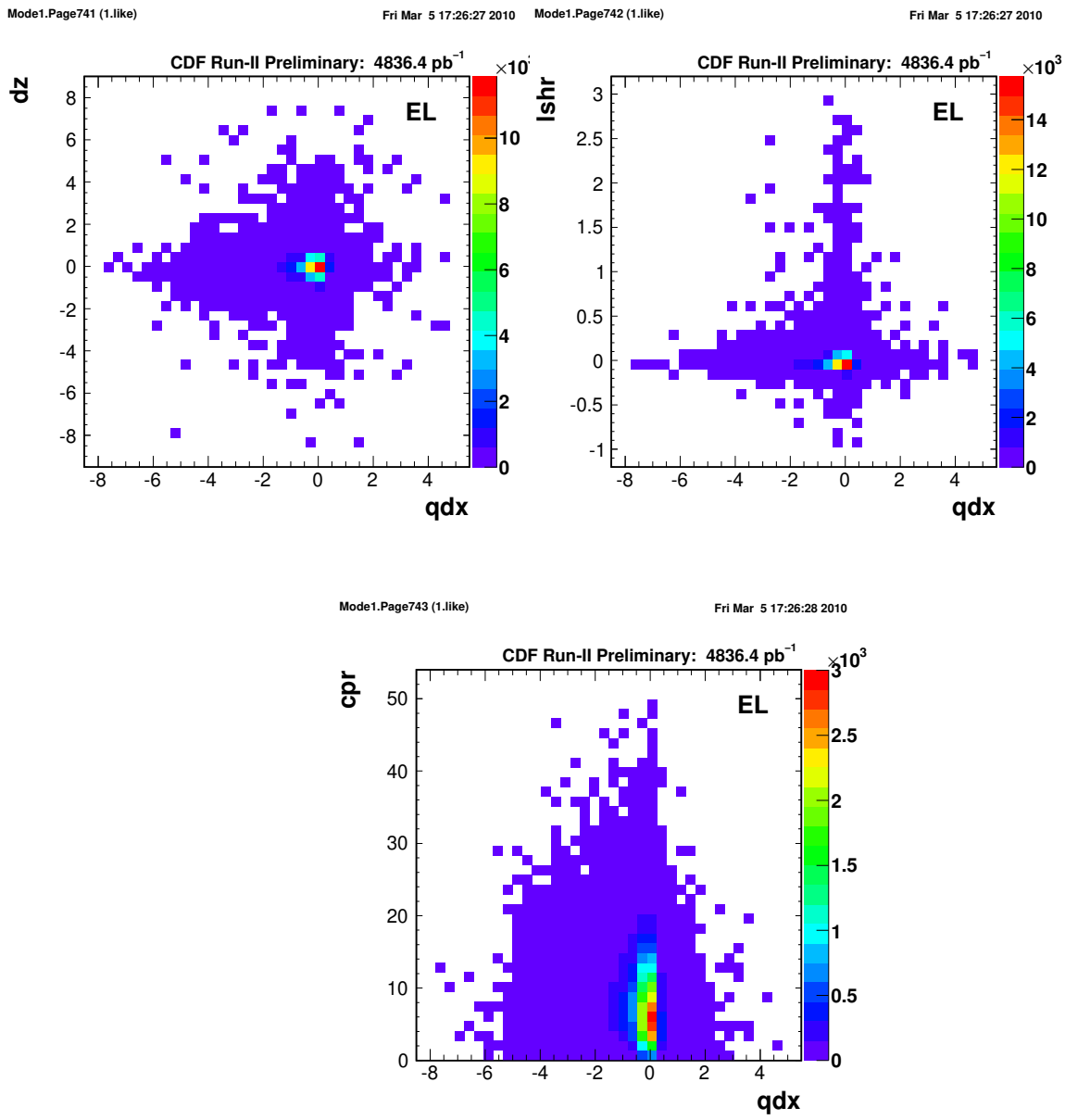

Figure 3.39: The correlation between two variables for Z data.

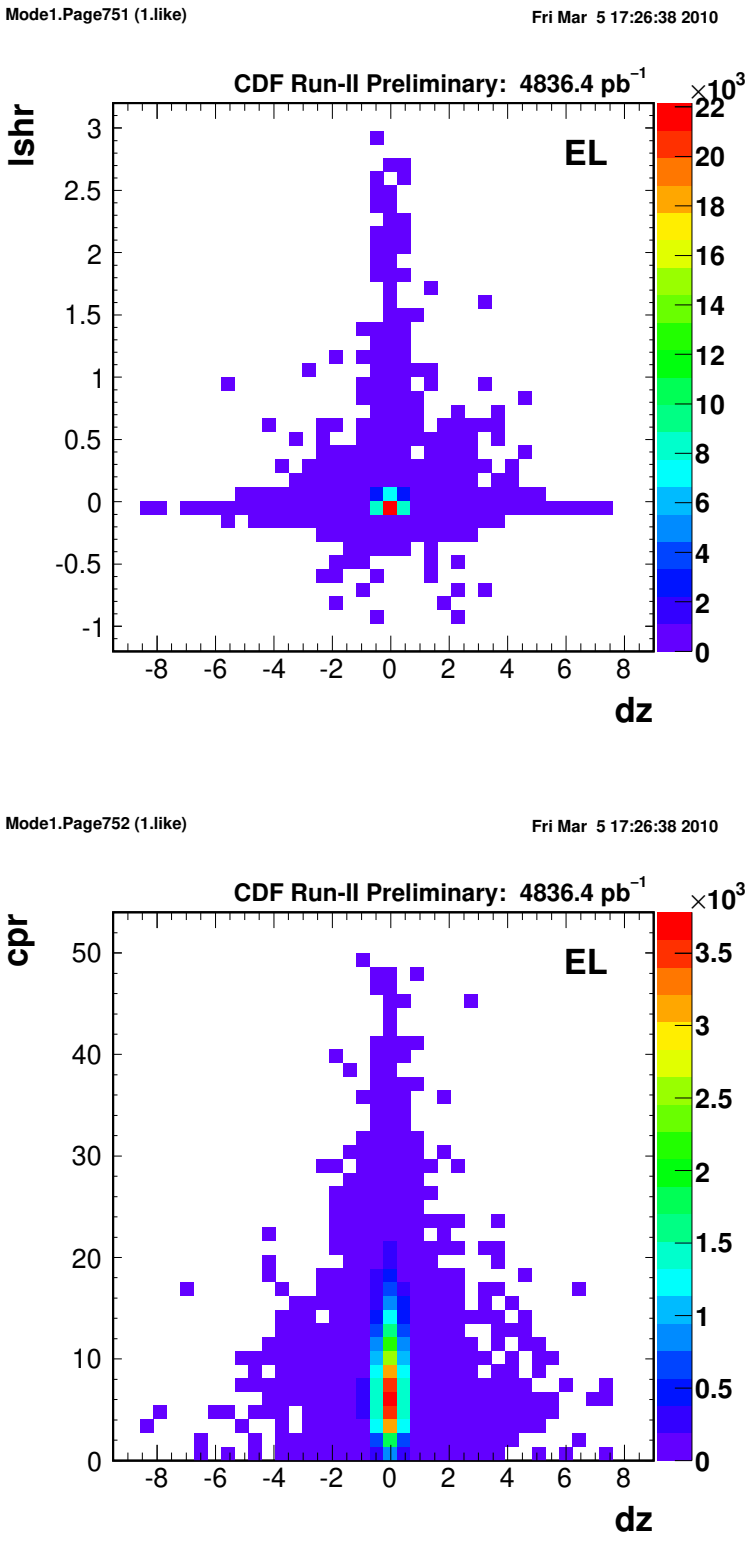

Figure 3.40: The correlation between two variables for Z data.

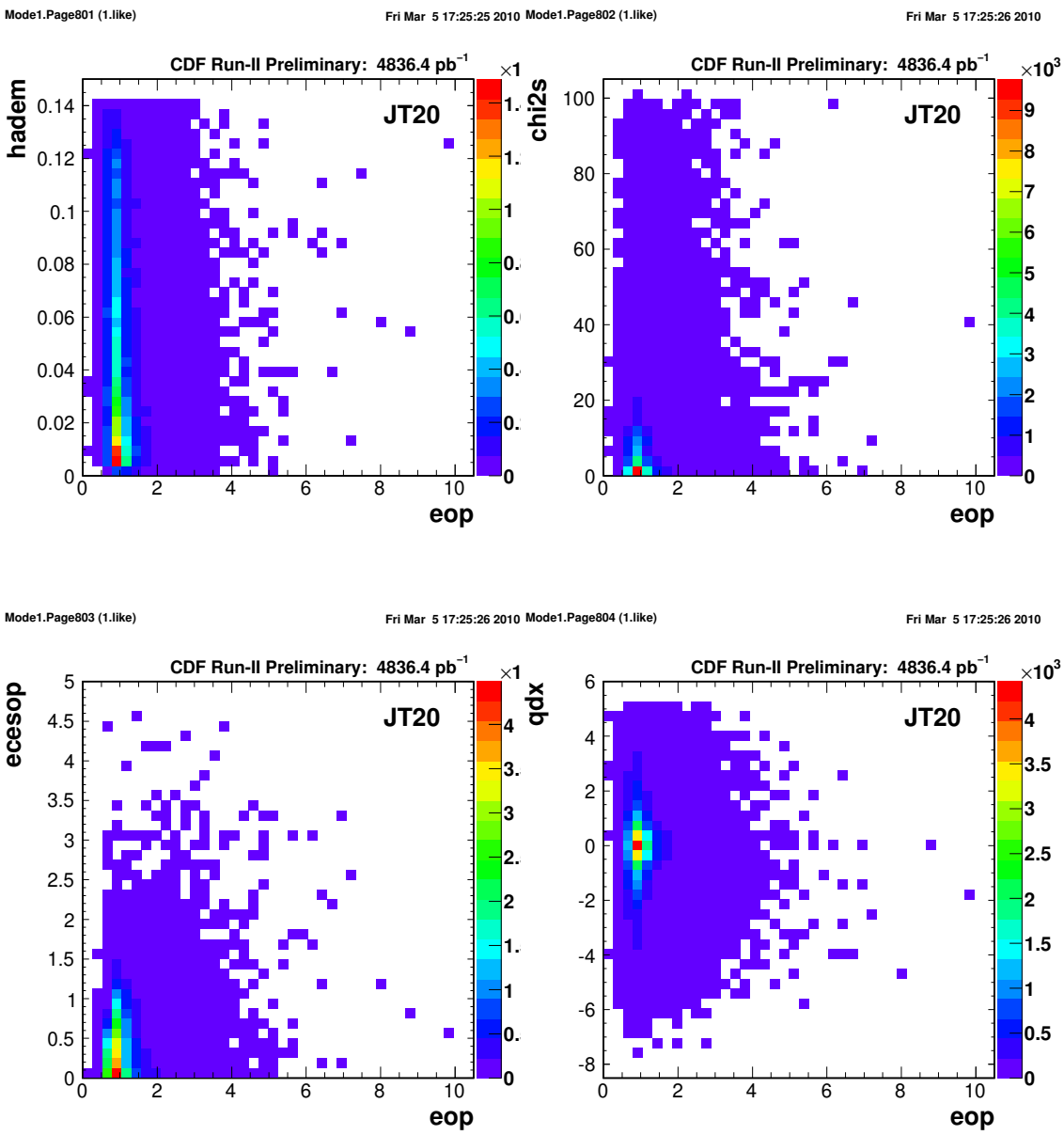

Figure 3.41: The correlation between two variables for Jet20.

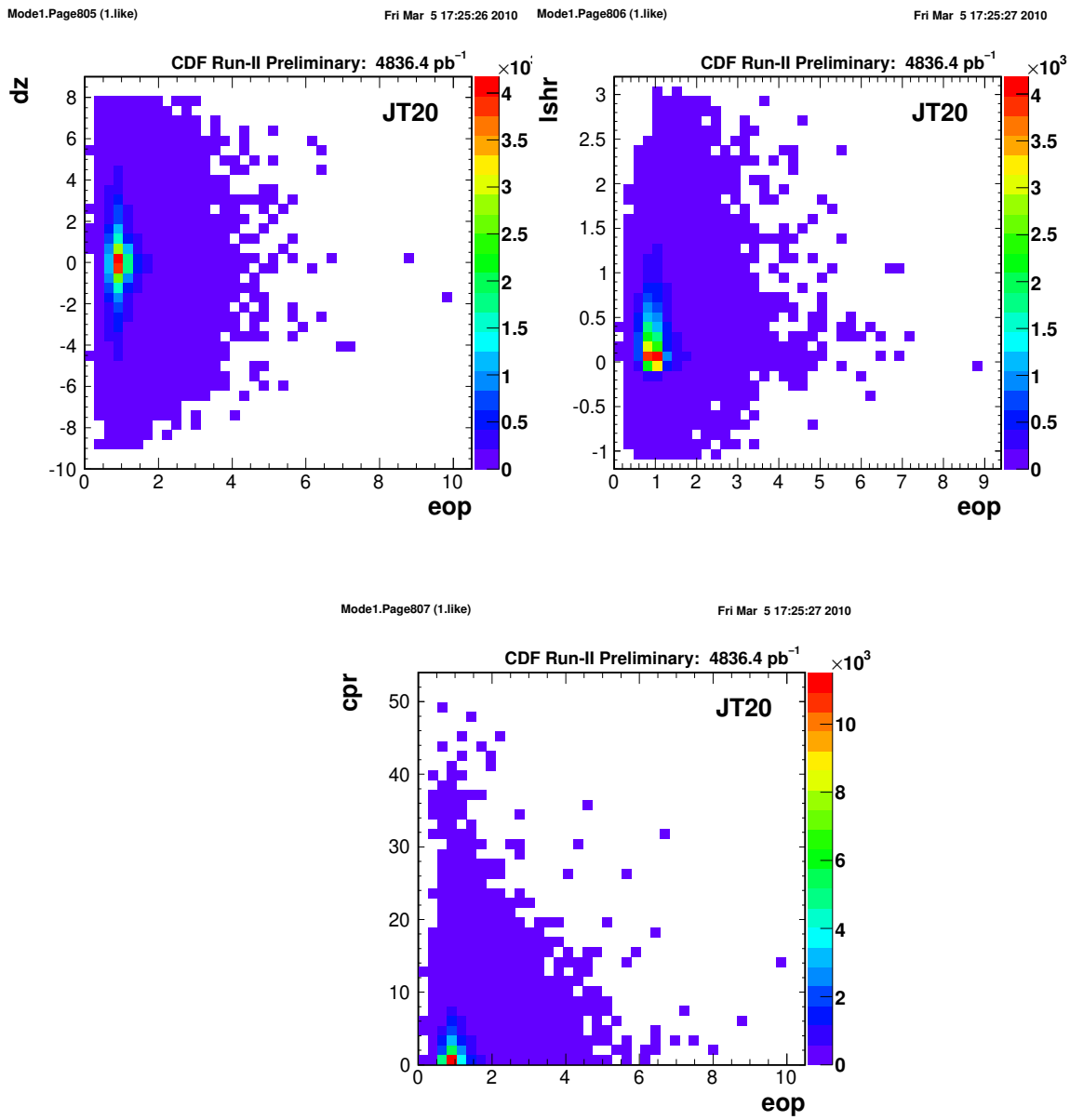

Figure 3.42: The correlation between two variables for `Jet20`.

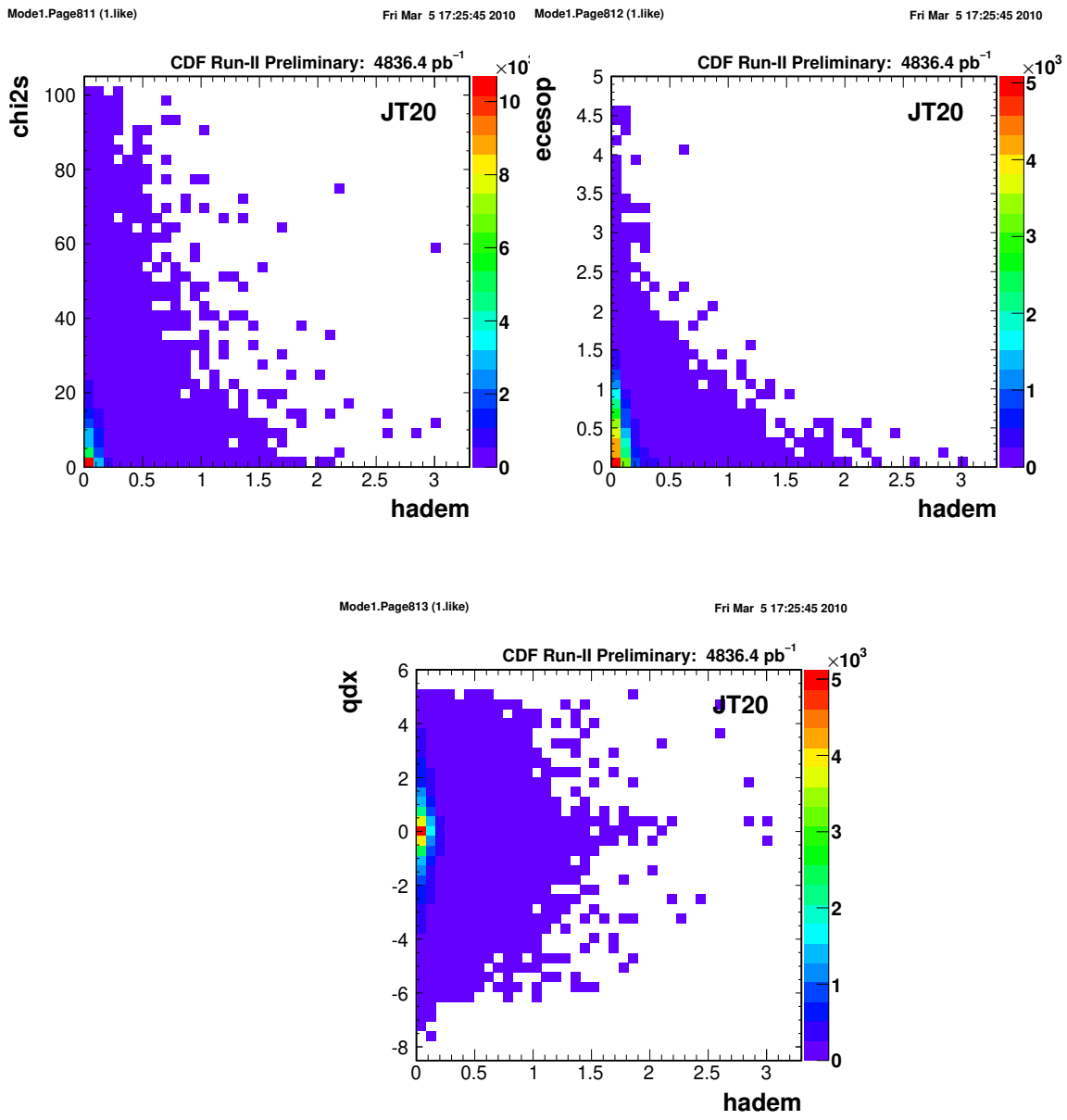

Figure 3.43: The correlation between two variables for `Jet20`.

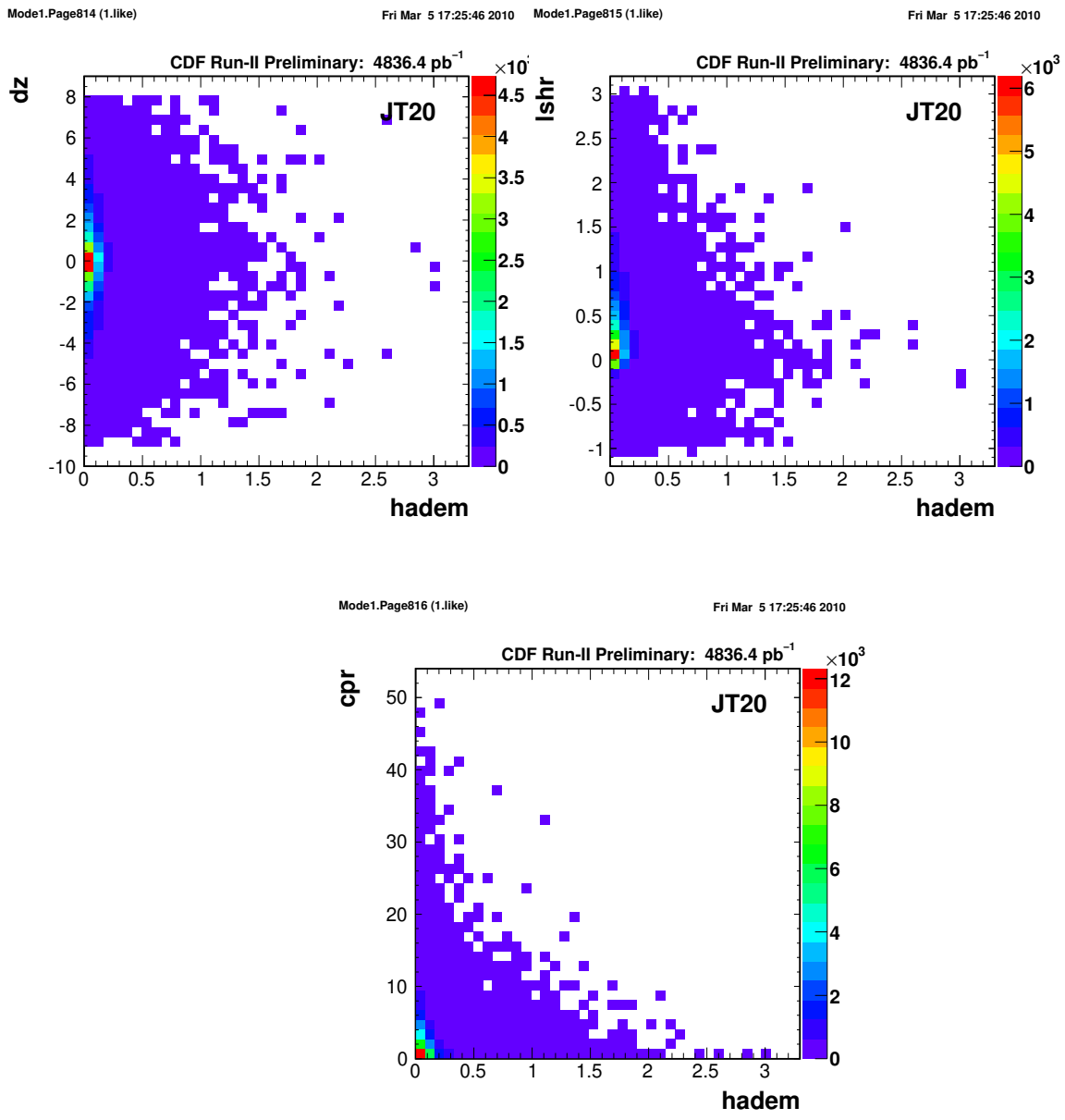

Figure 3.44: The correlation between two variables for `Jet20`.

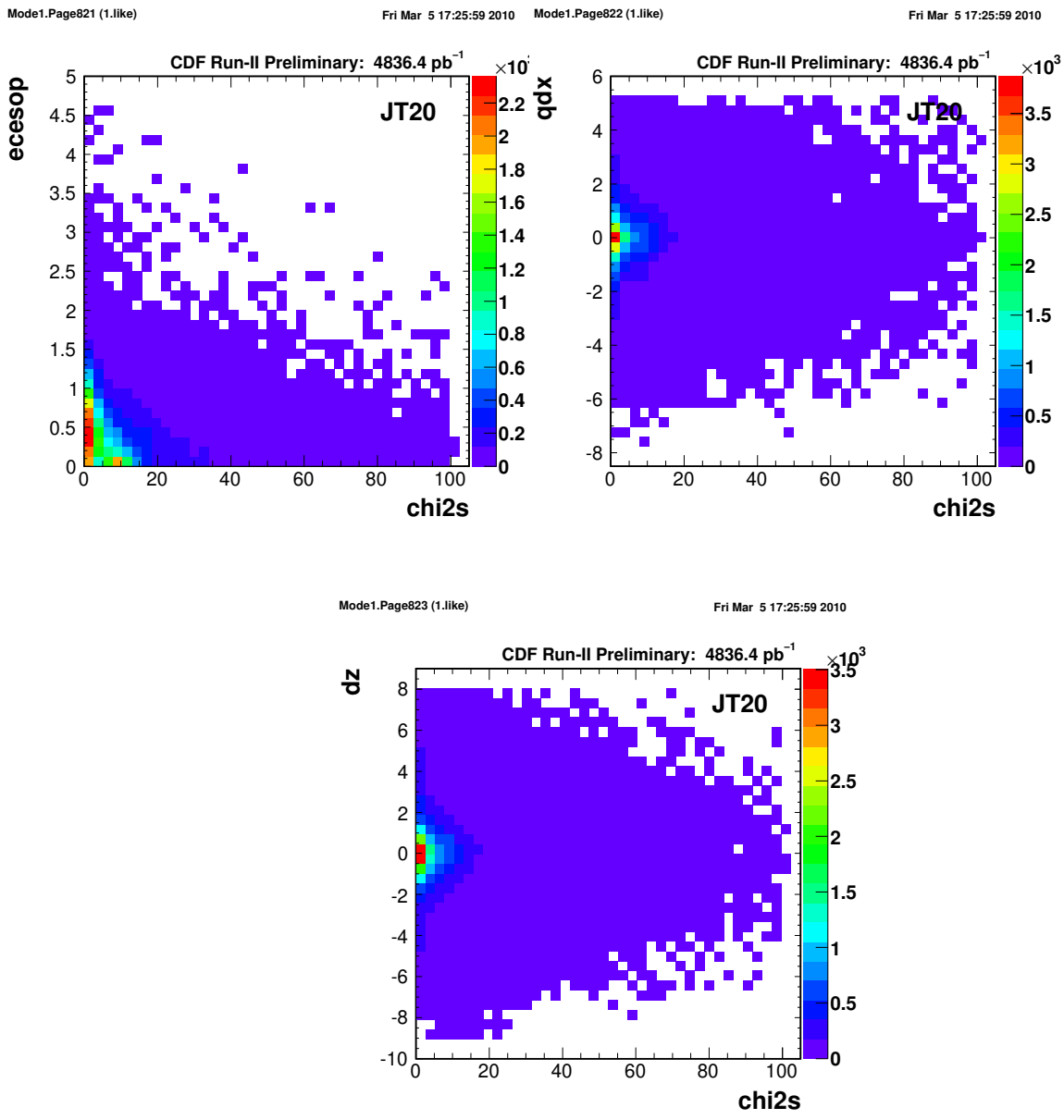

Figure 3.45: The correlation between two variables for `Jet20`.

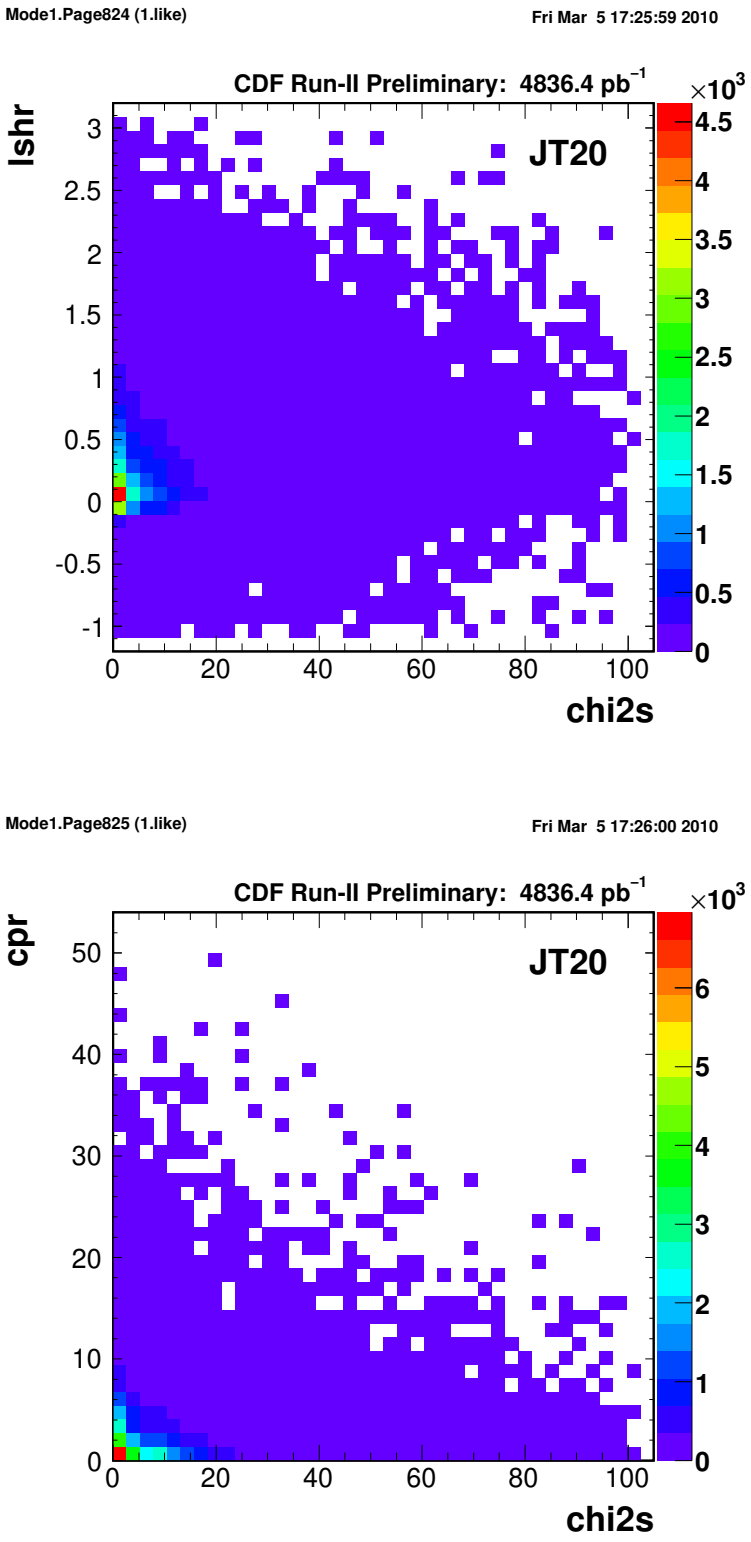

Figure 3.46: The correlation between two variables for `Jet20`.

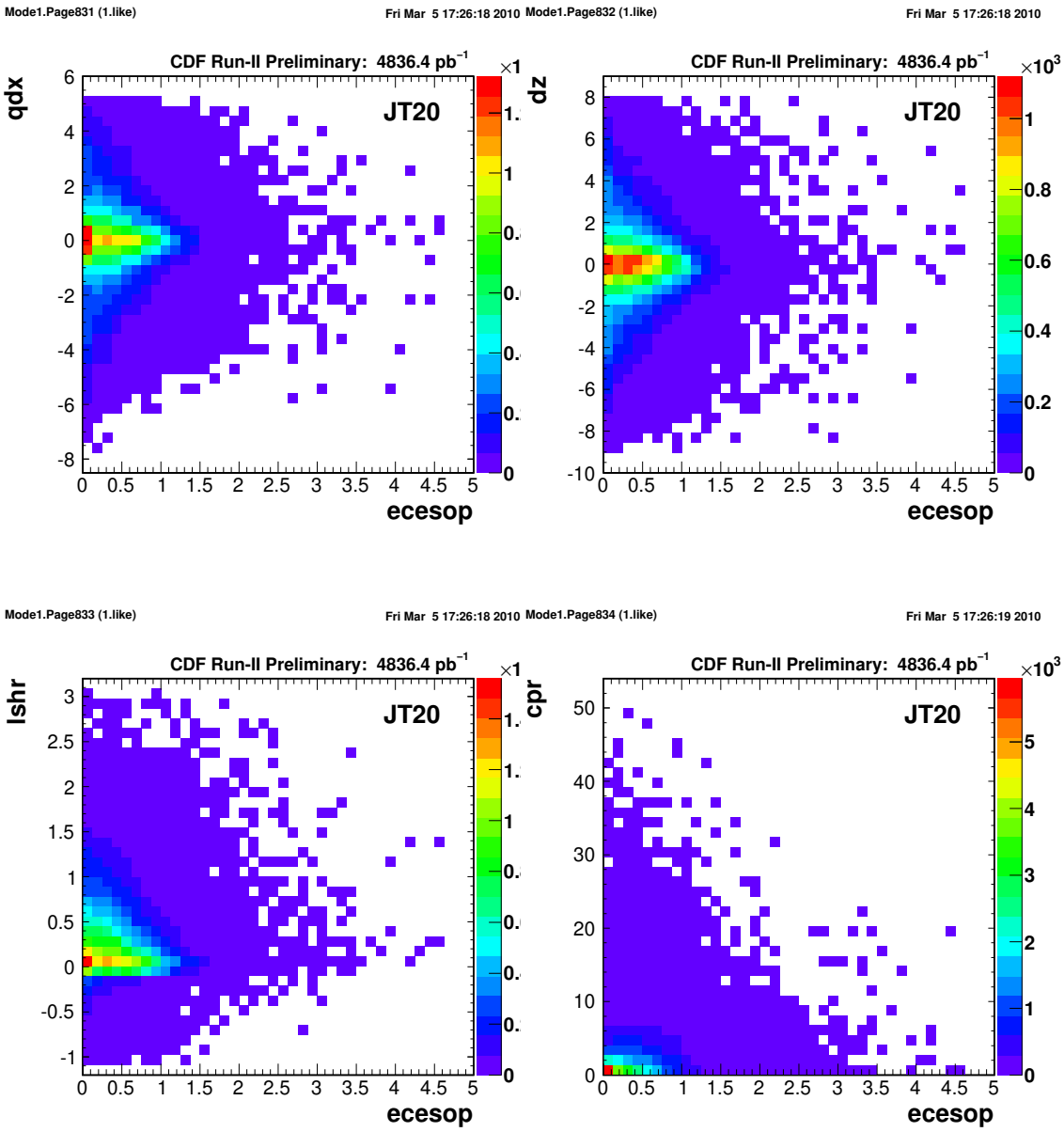

Figure 3.47: The correlation between two variables for Jet20.

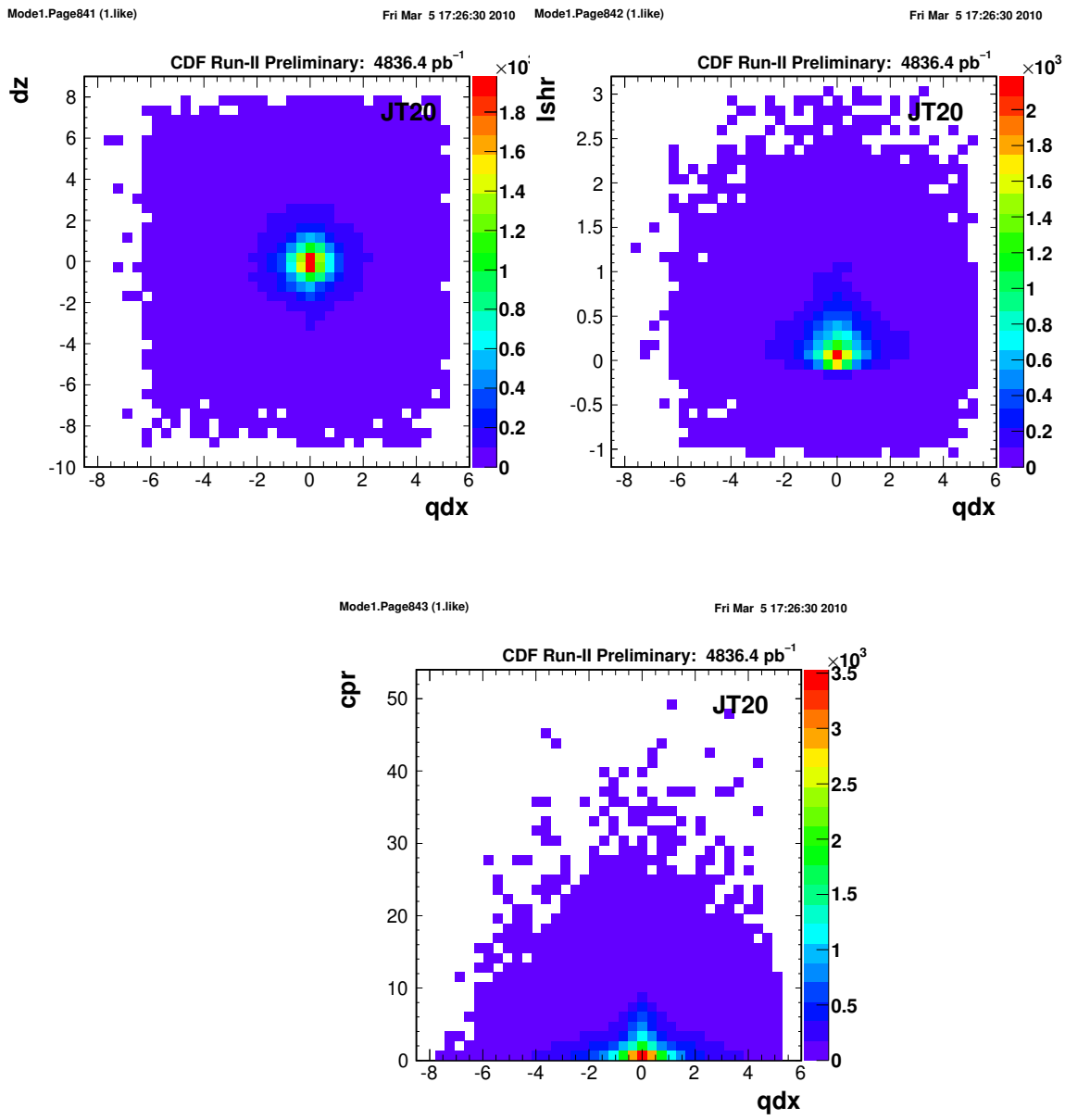

Figure 3.48: The correlation between two variables for `Jet20`.

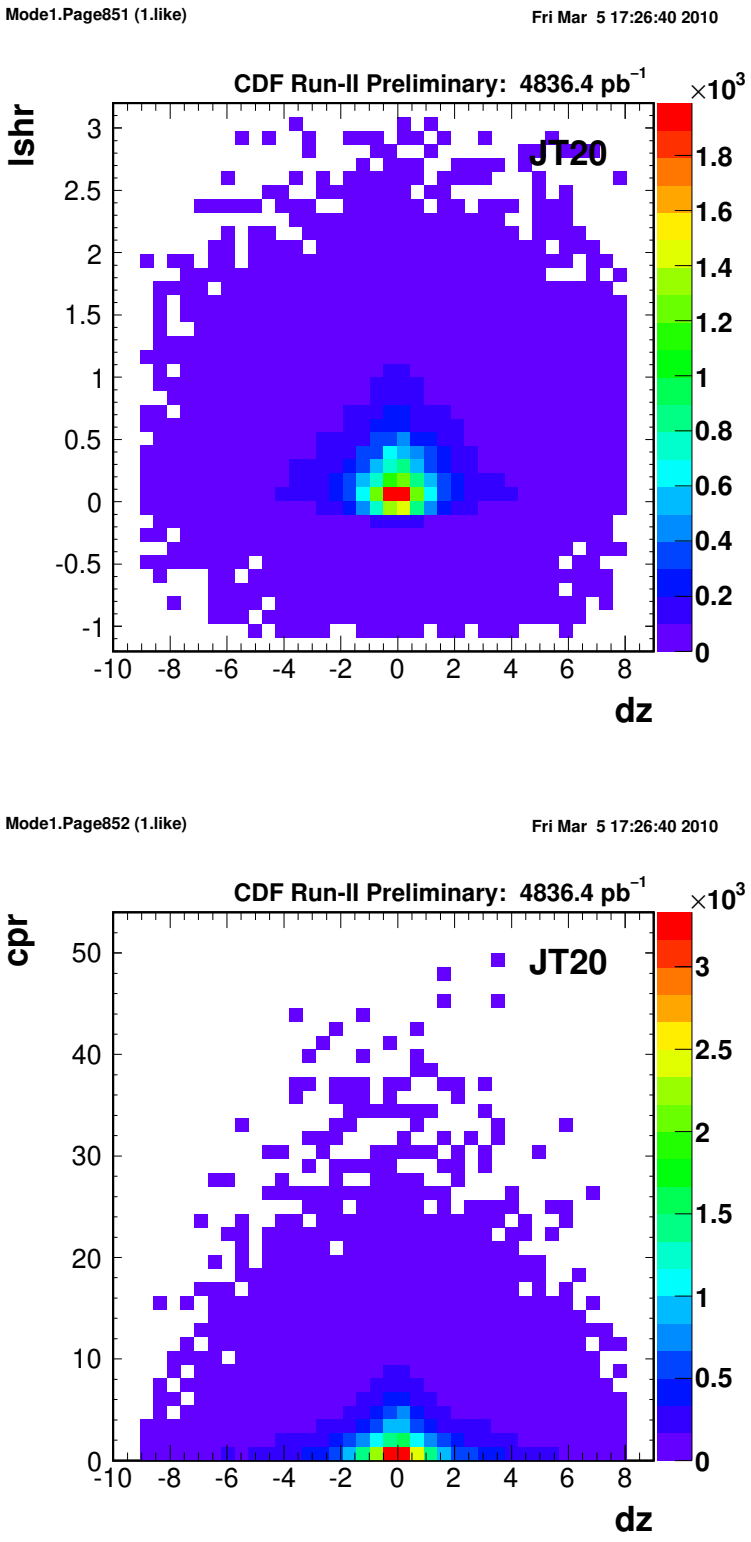

Figure 3.49: The correlation between two variables for `Jet20`.

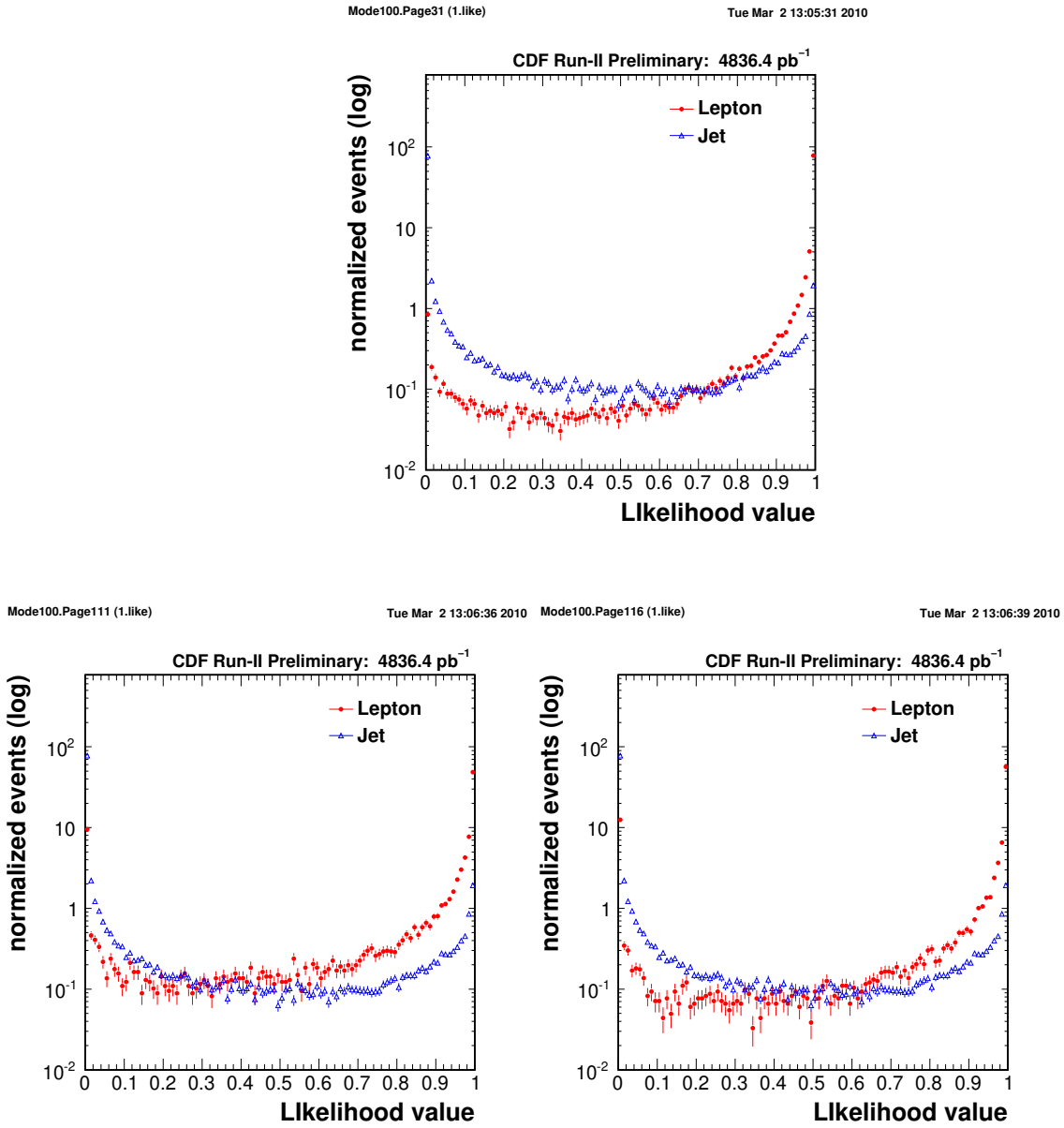

Figure 3.50: The likelihood distributions for leptons and fake leptons after normalized. These plots show the likelihood for electron from Z decays (top), Wh110 events (bottom-left), Wh160 (bottom-right), and Jet20 control samples. The PDF is Z.

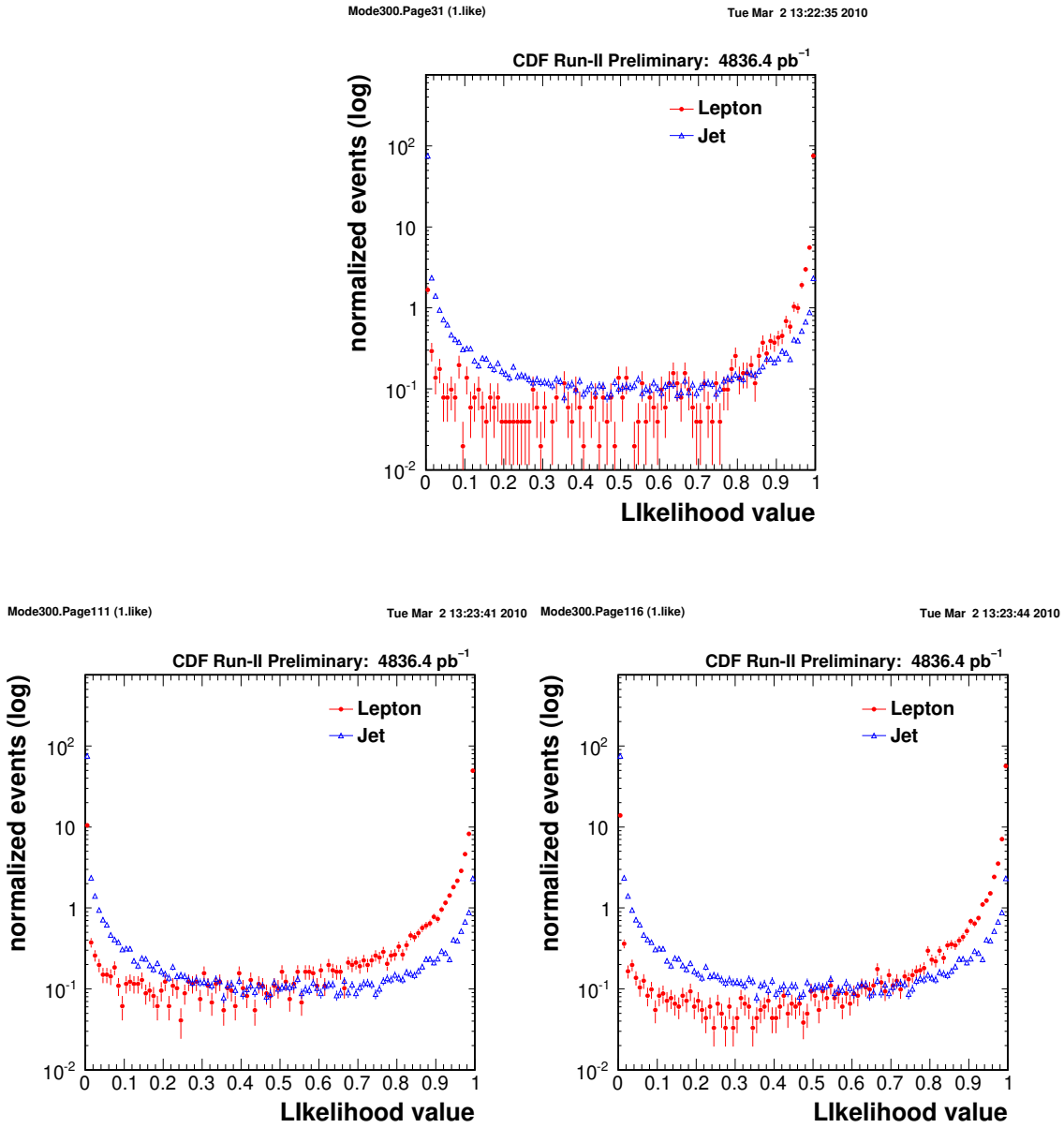

Figure 3.51: The likelihood distributions for leptons and fake leptons after normalized. These plots show the likelihood for conversion electrons (top), Wh110 events (bottom-left), Wh160 (bottom-right), and Jet20 control samples. The PDF is conversions.

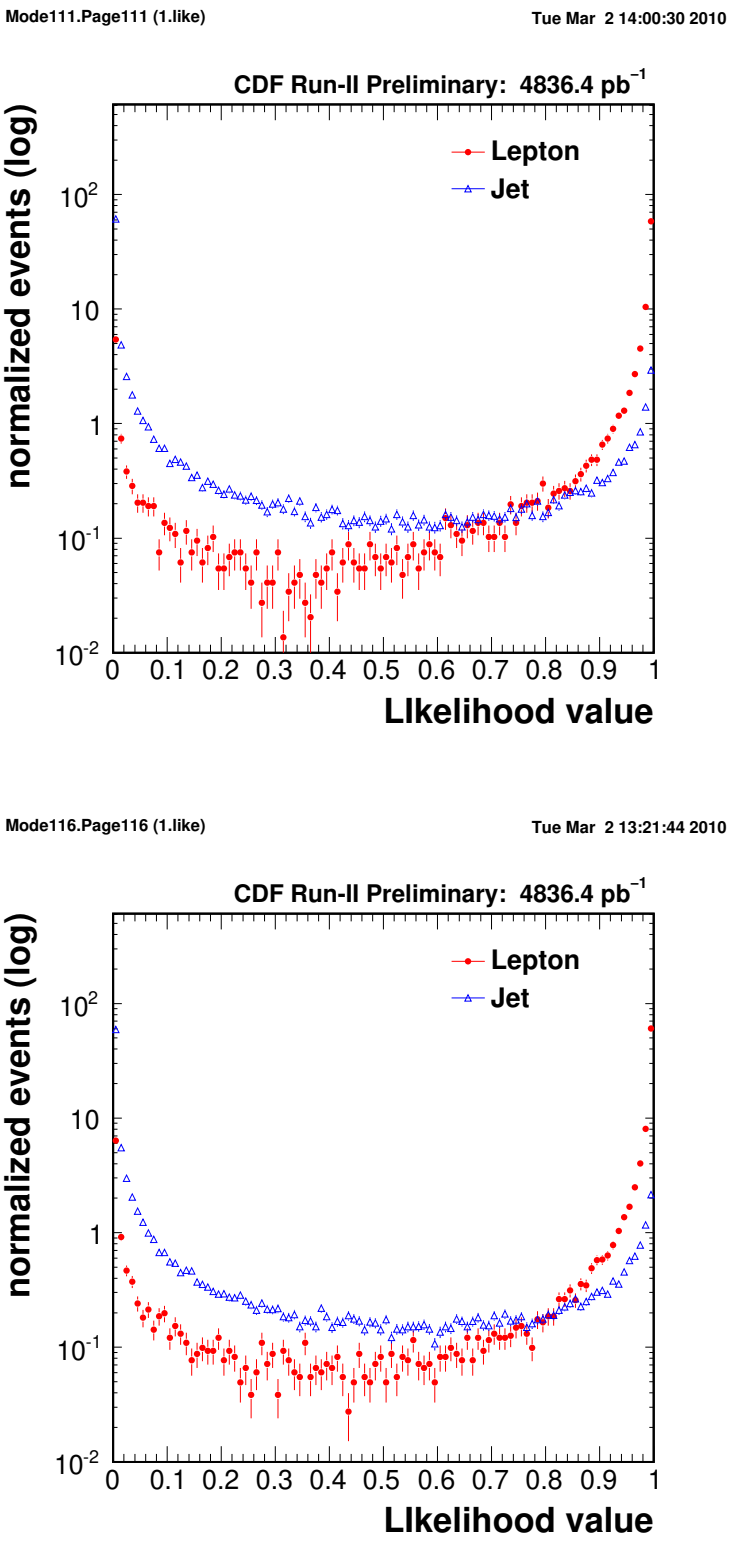

Figure 3.52: The likelihood distributions for leptons and fake leptons after normalized. These plots show the likelihood for Wh110 (top) and Wh160 (bottom) events using the signal PDF of the Wh110 and Wh160, respectively. The background sample is the `Jet20`.

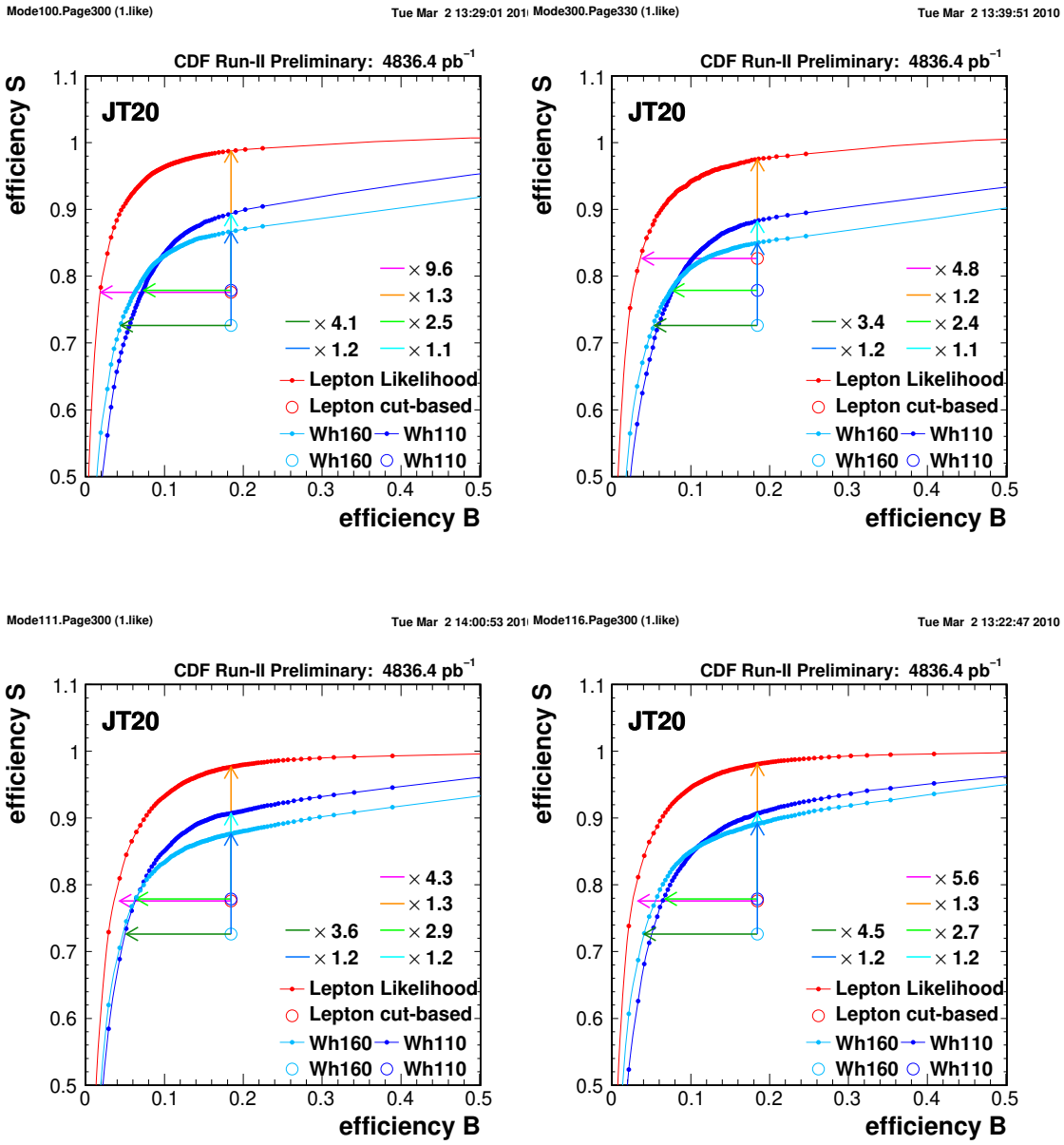

Figure 3.53: Efficiencies of likelihood for Z electrons/conversions, Wh110, and Wh160 samples using the signal PDFs of the Z decays (top-left), conversions (top-right), Wh110 (bottom-left), and Wh160 (bottom-right). The open dots are cut-based efficiency points respectivery. The signal effieiency improvements are indicated by the horizontal arrowed lines. The vertical arrowed lines shows the efficiency reductions of the background.

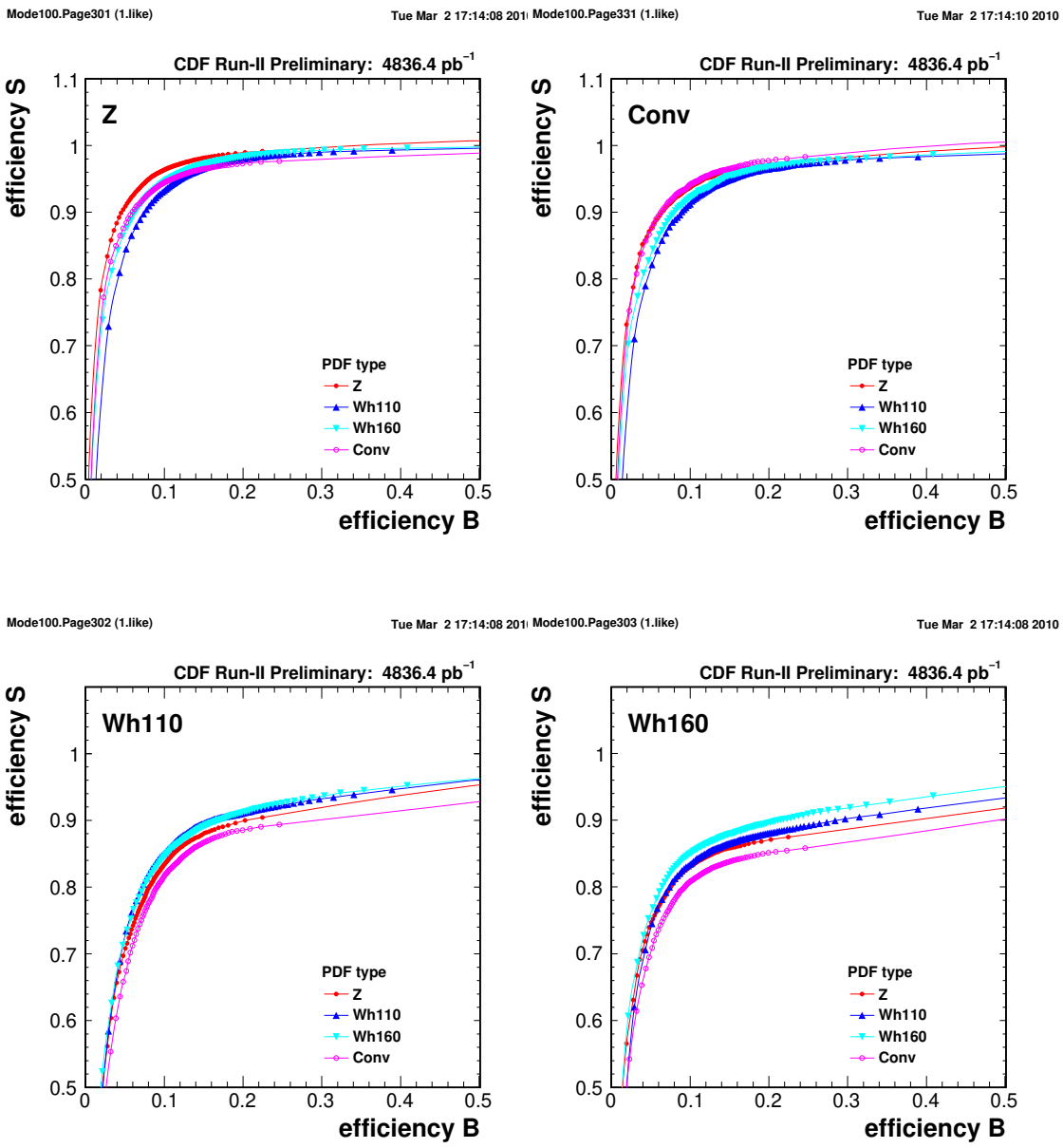

Figure 3.54: The signal-efficiency vs. the background-efficiency curves using the different signal PDFs for a given sample.

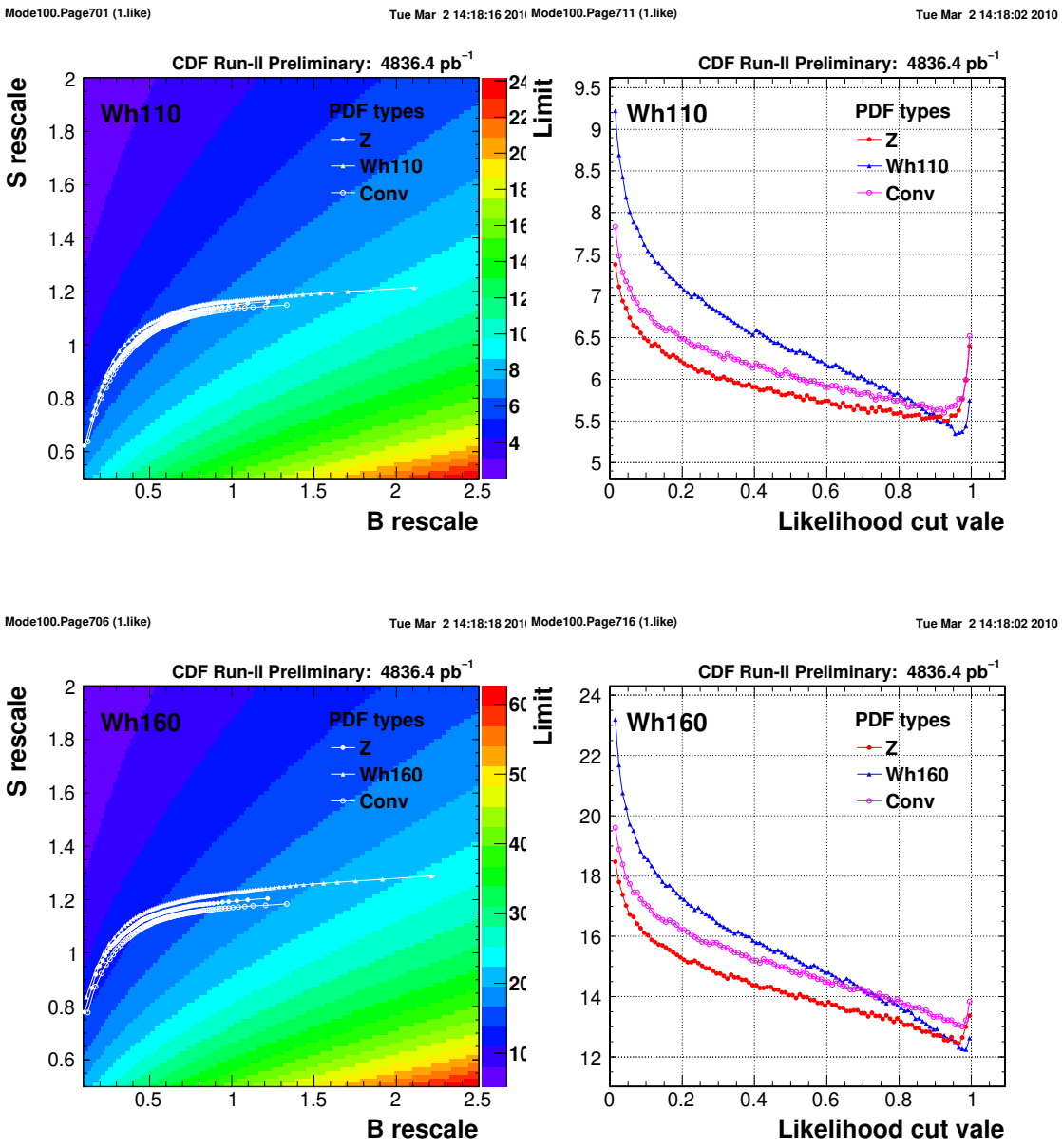

Figure 3.55: Limits for Wh110 and Wh160 samples using signal PDFs of Z (top), photon conversion (middle) and Wh110 (bottom). The background sample is JT20.

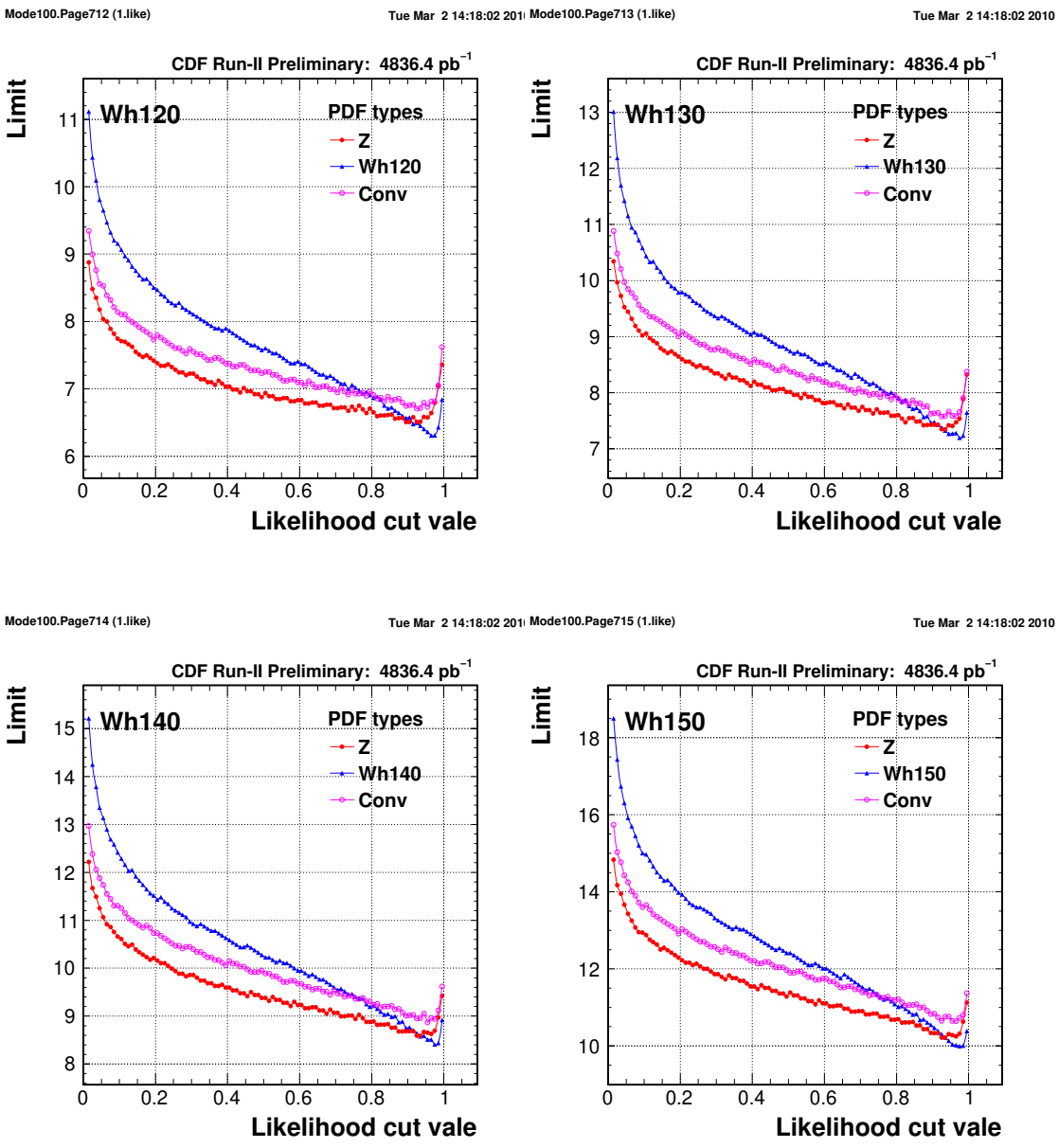

Figure 3.56: Comparison the limits for higgs MC samples using the signal PDFs created from 3 signal types, higgs MCs themselves, Z events and conversion events.

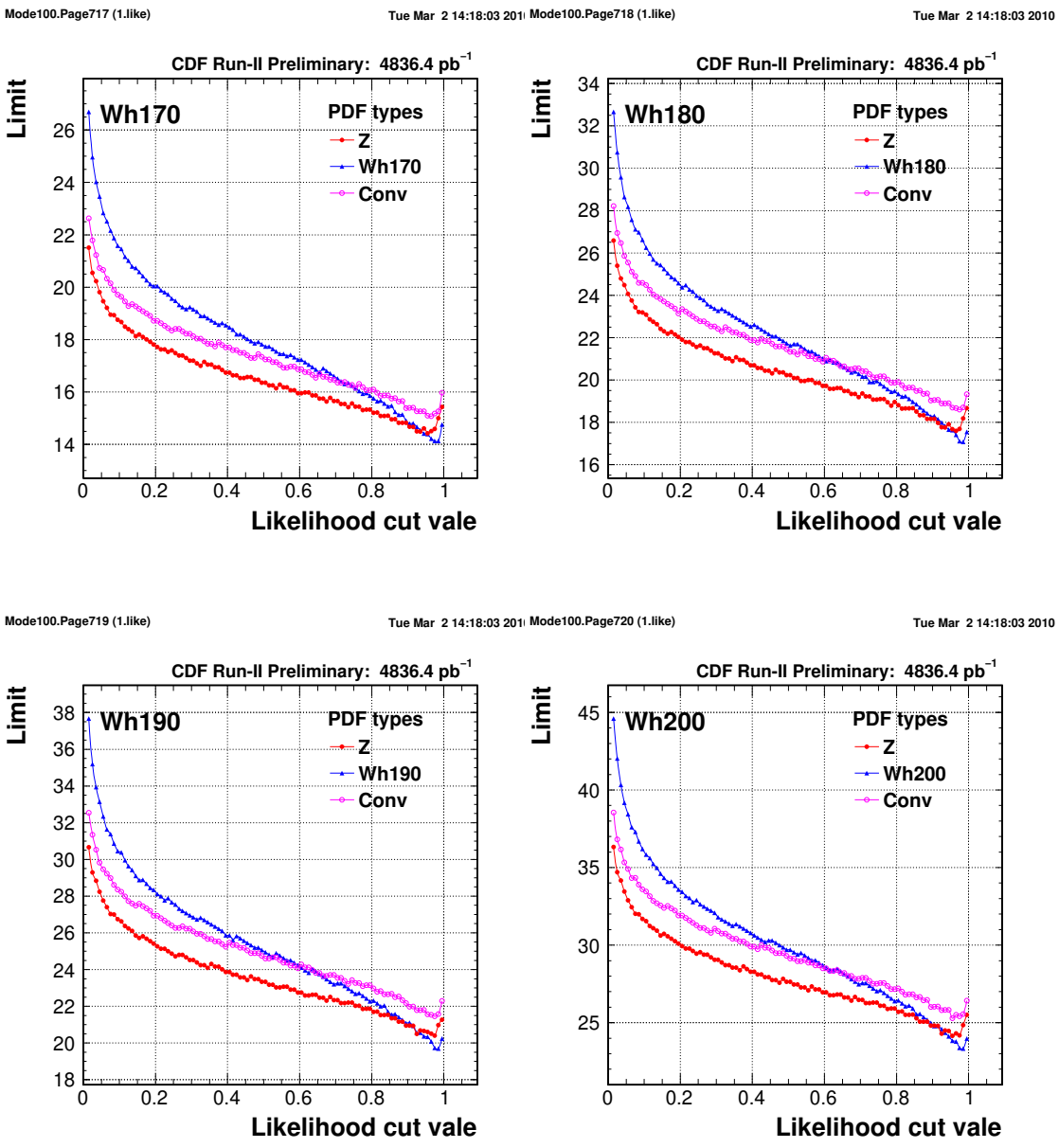

Figure 3.57: Comparison the limits for higgs MC samples using the signal PDFs created from 3 signal types, higgs MCs themselves, Z events and conversion events.

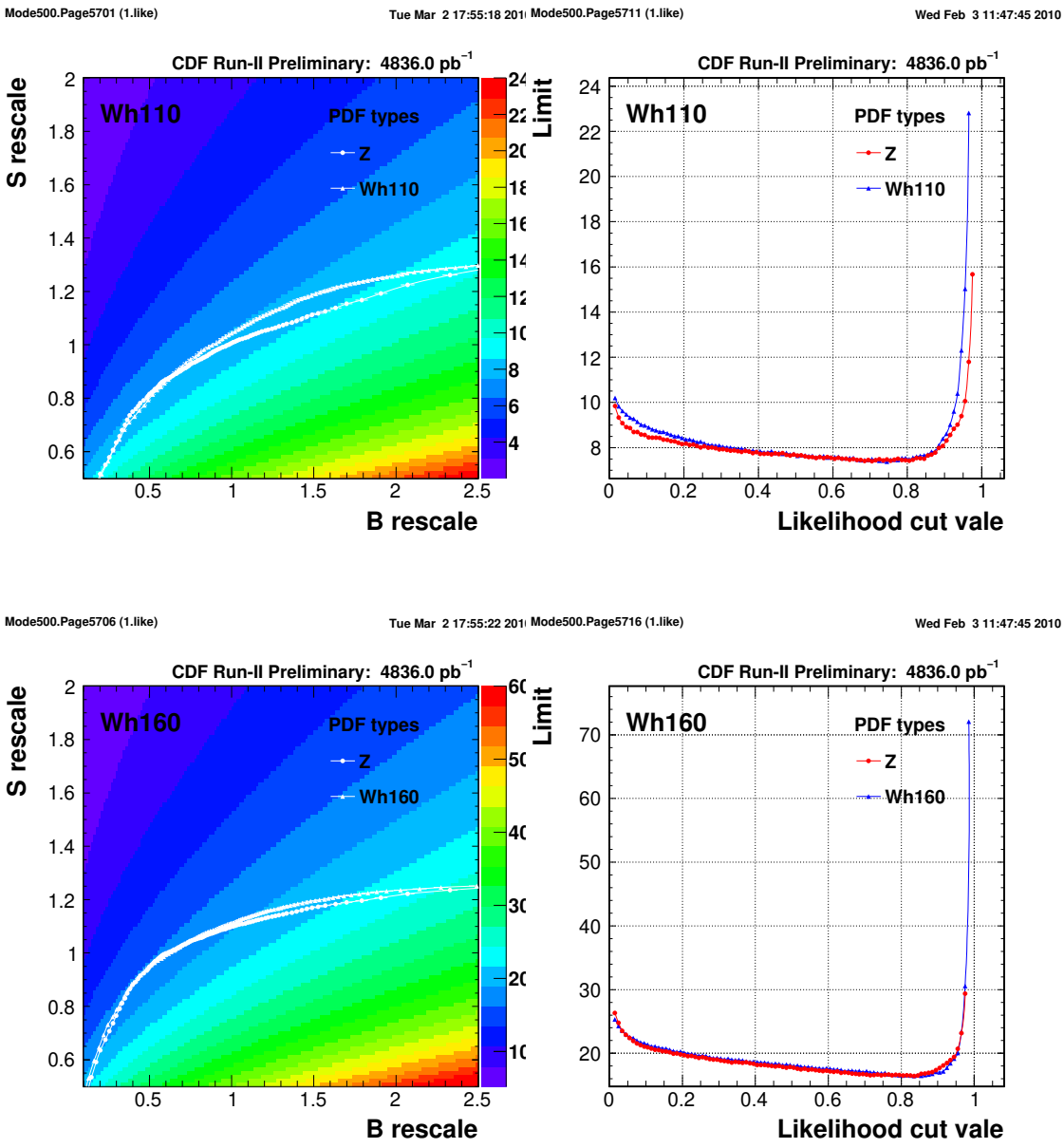

Figure 3.58: Limits for Wh110 sample using signal PDFs of Z (top), and Wh110 (bottom). The backgroud sample is JT20.

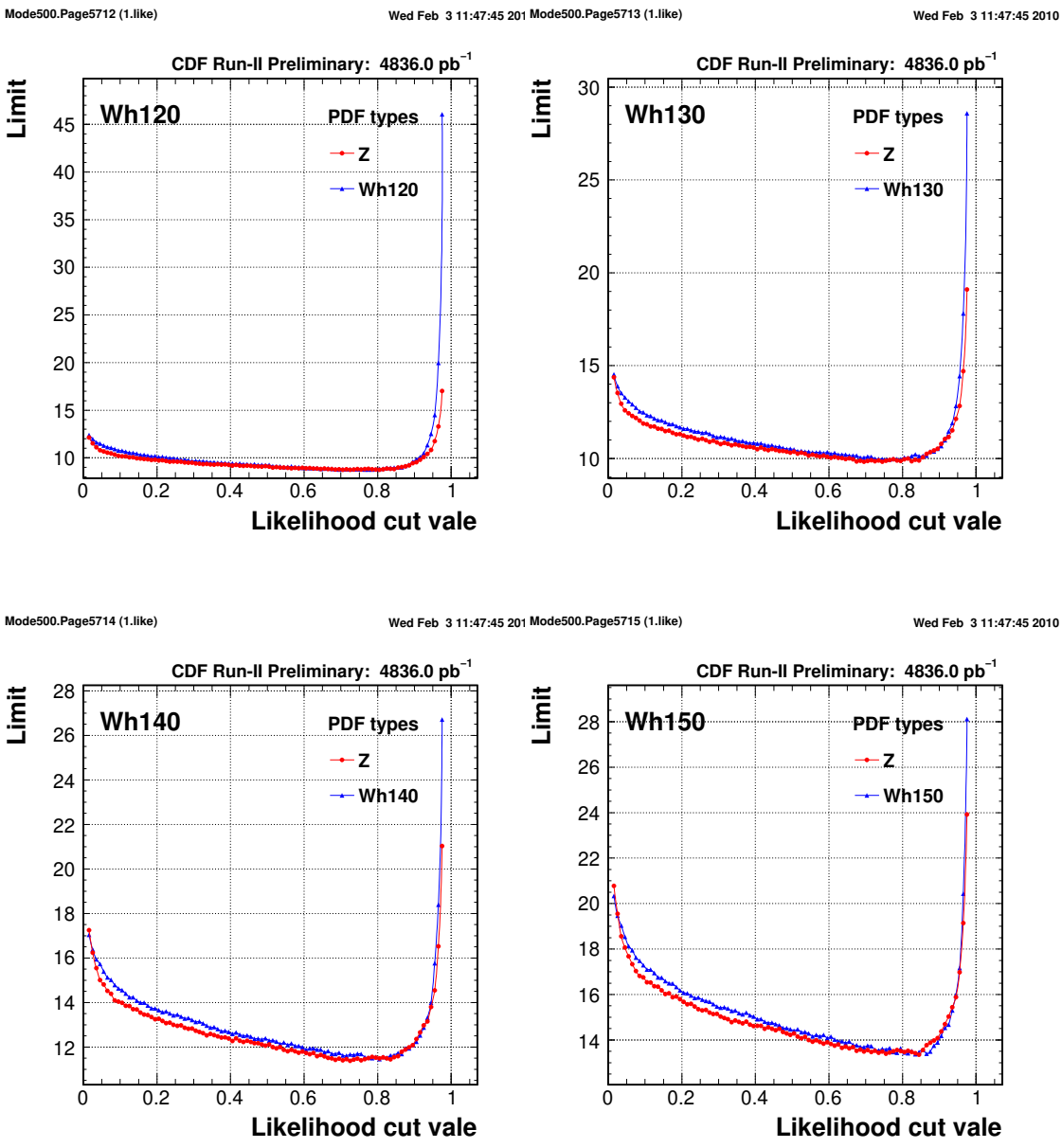

Figure 3.59: Comparison the limits for higgs MC samples using the signal PDFs created from 2 signal types, higgs MCs themselves and Z events.

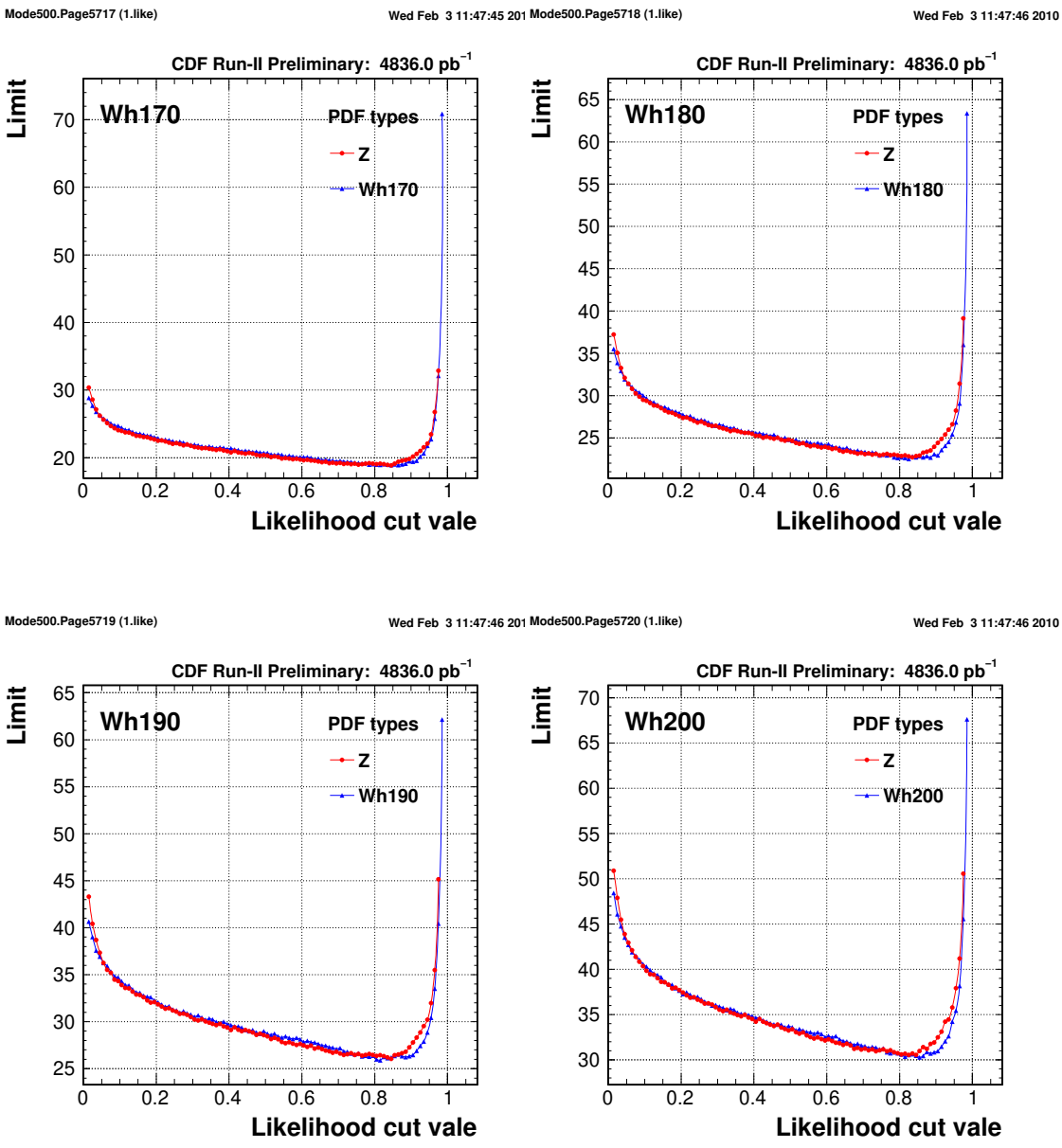

Figure 3.60: Comparison the limits for higgs MC samples using the signal PDFs created from 2 signal types, higgs MCs themselves and Z events.

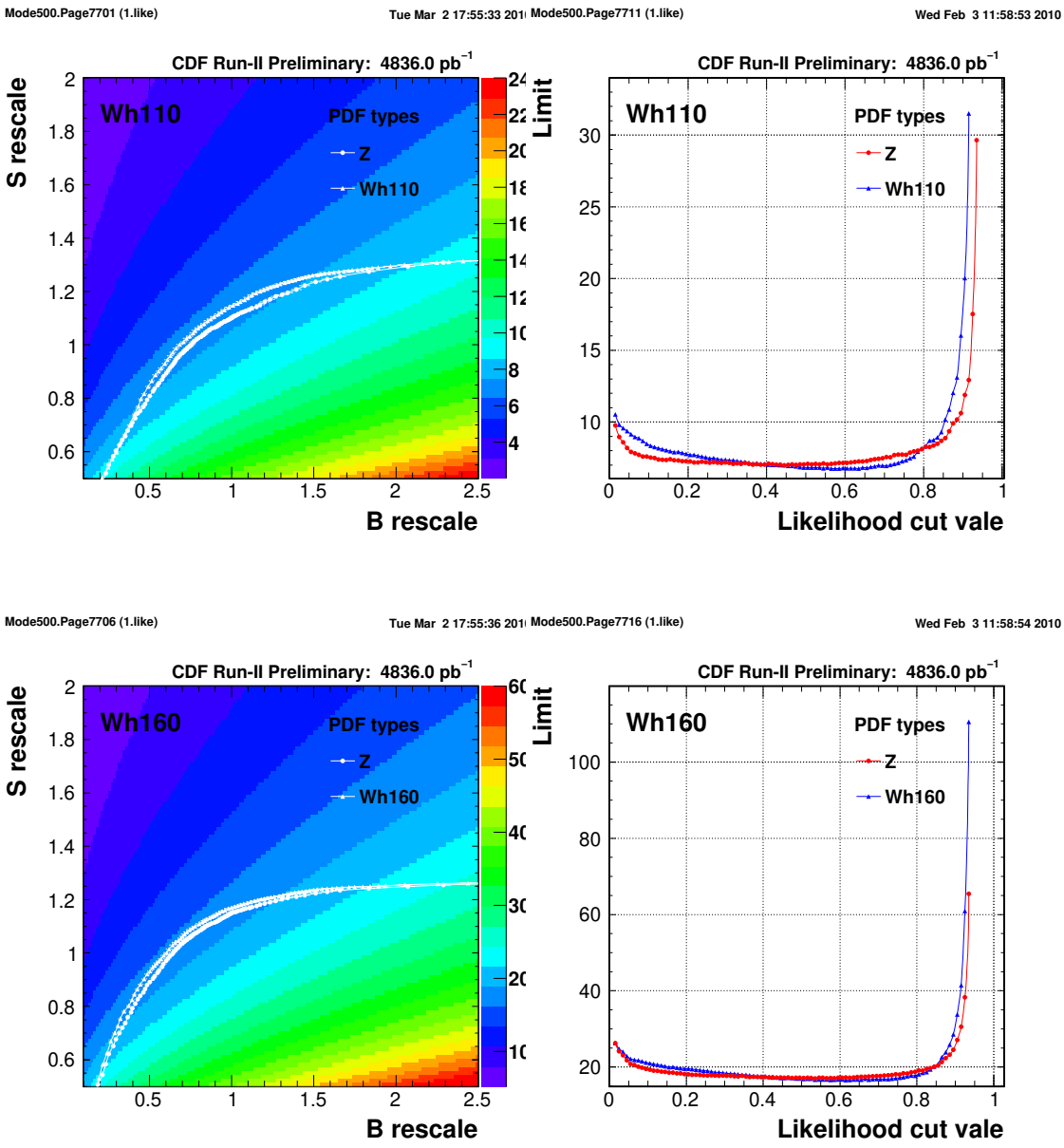

Figure 3.61: Limits for Wh110 sample using signal PDFs of Z (top), and Wh110 (bottom). The backgroud sample is JT20.

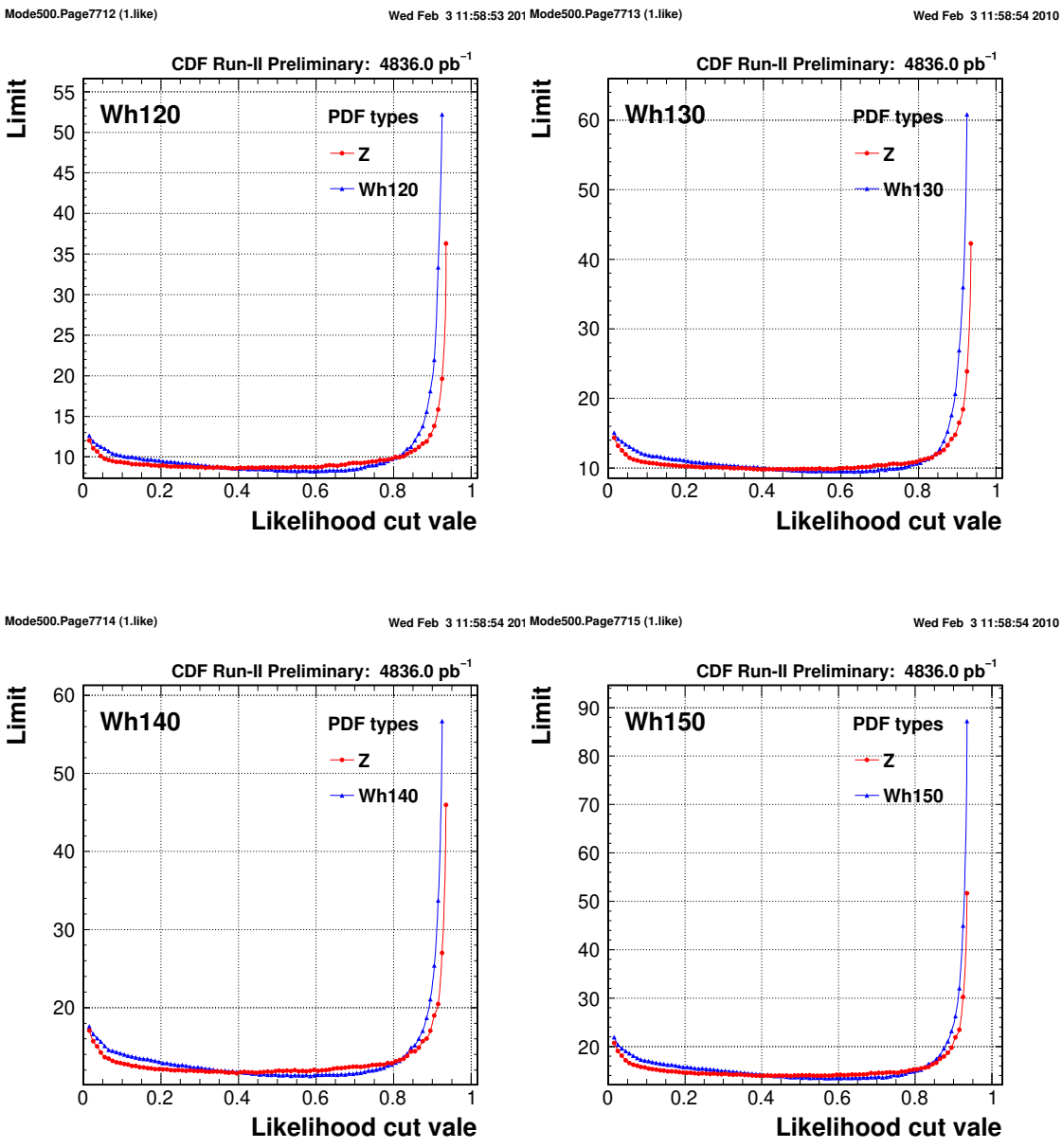

Figure 3.62: Comparison the limits for higgs MC samples using the signal PDFs created from 2 signal types, higgs MCs themselves and Z events.

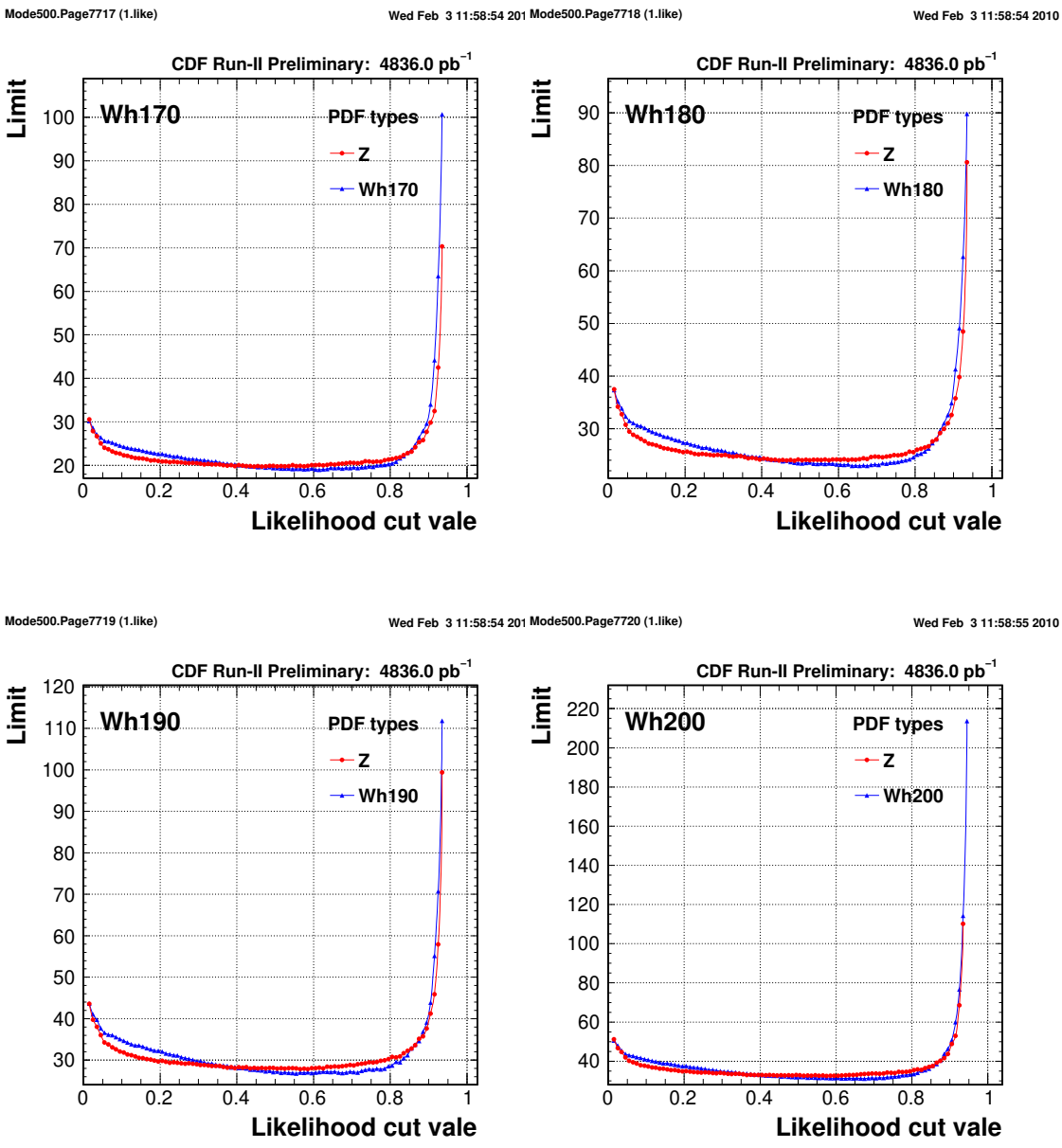

Figure 3.63: Comparison the limits for higgs MC samples using the signal PDFs created from 2 signal types, higgs MCs themselves and Z events.

Chapter 4

Boosted decision tree discriminant

For searches for smaller signal in larger data (background) such as this higgs search has become essential to use as much available information from the data as possible to get it more search sensitivity. The multivariate data analysis can extract maximum of the information. In this search, "Booster Dicision Trees" (BDT) technique which is one of the multivariate data analysis is employed [53, 54]. Desicion trees is a binary-tree-structured classifier such as Fig. 4 : "S" means signal, "B" means background, terminal nodes are call "leaves". The naming for S or B is depending on the majority of events in the each node. A single decision tree is very similar to rectangular cuts. However, whereas a cut-based analysis is able to select only one hypercube as region of phase space, the decision tree is able to split the phase space into a large number of hypercubes, each of which is identified as either signal-like or backgound-like. The tree structure is built up repeatedly splitting the given events to regions that are eventually classified as signal or background. The shortcoming of decision tree is their instability with repect to statistical fluctituations in the training sample from which the tree structure is derived. For example, if tow input variables such E_T and p_T exhibit similar separation power, a fluctuation in the training sample may cause the tree growing algorithm to decide to split on one variable, while the other variable could have been selected without that fluctuation. In such a case, the whole tree structure is altered below this node, possibly resulting also in a substantially different classifier response. This problem is overcome by constructing a forest of single decision trees aand classifying an event on a majority vote of the classifications done by each tree in the forest. All trees in the forest are derived from the same training sample, with the events being subsequently subjected to so-called "Boosting" algorithm, which modifed their weights for events. The boosting invreases the statistical stability of the classifier and typically also improves the separation performance compared to a single decision tree.

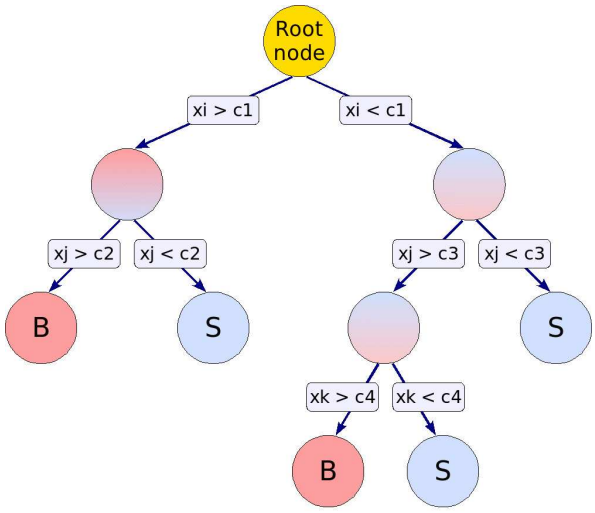

Figure 4.1: Schematic view of a decision tree. Starting from the root node, a sequence of binary splits using the discriminating variables x_i is performed. Each split uses the variable that at this node gives the best separation between signal and background. The same variable may thus be used at several nodes, while others might not be used at all. The leaf nodes at the bottom end of the tree are labeled S for signal and B for background depending on the majority of events that end up in the respective node.

4.1 Desicion trees

The training or building of a decision tree is the process that defines the splitting criteria for each node. The splitting procedure is repeated until the whole tre is built. At each node, the split is determined by finding the variable and corresponding cut that provides the best separation between signal and background. The node splitting is stopped once it has reached a minimum number of events. The end nodes (leaf nodes) are classified as signal or background according to the class the majority of events in the node. The different separation criteria can be configured to assess the performance of a variable and specific cut requirement. For this analisis, the employed splitting criterion is "Gini-Index" to build the decision trees. The Gini-Index is defined as

$$i_{\mathrm{G}} = p(1-p), \tag{4.1}$$

p is purity in a node defined as follows,

$$p = \frac{\sum_s w_s}{\sum_s w_s + \sum_b w_b} \tag{4.2}$$

where $\sum_s$ is the sum over signal events and $\sum_b$ is the sum over background events in a node, assuming the events are weighted with having w_i, so $p(1-p)$ is 0 if the samples

is pure signal or pure background. This criterion chosen is to minimize

$$i_{\mathrm{G}}(\text{left-child}) + i_{\mathrm{G}}(\text{right-child}), \tag{4.3}$$

and to determine the increase in quality when a node is split into two nodes, one maximize

$$i_{\mathrm{G}}(\text{parent}) - i_{\mathrm{G}}(\text{left-child}) - i_{\mathrm{G}}(\text{right-child}), \tag{4.4}$$

where i_G(parent) means Gini index of a node before splitting (parent node), and i_G(left-child, or right-child) means Gini index of a node after splitting from parent node. At the end, if a leaf has purity greater than 1/2 (or whateer is set), then it is called a signal leaf, otherwise a background leaf. The events are classified signal (have score of 1) if they land on a signal leaf and background (have score of -1) if they land on a background leaf. The resulting tree is a decision tree.

The maximum constructed decision tree has some statistically insignificant nodes which leads to reduce the separation performance (overtrainig). Some "pruning" methods are used to avoid the overtrainig as possible. "Cost-complexity pruning" is used to perform the maximum separation. The cost-complexity in a tree T starting at node t is expressed by

$$R_\alpha(T_t) = R(T_t) + \alpha \cdot N(T_t) \tag{4.5}$$

where, $R(T_t)$ is the total error cost in the tree T, the error cost in each terminal node is given by multiplying the $1 - max(p, 1-p)$ by the proportion of data, α is the cost complexity parameter, and $N(T_t)$ is the number of terminal nodes in the tree T, while the cost-complexity at node t is

$$R_\alpha(t) = R(t) + \alpha. \tag{4.6}$$

As long as $R_\alpha(t) > R_\alpha(T_t)$ the tree T has a smaller cost-complexity than the single node t, in other words, it is worth to keep this node expanded. The inequality is also expressed as the follows,

$$\alpha < \frac{R(t) - R(T_t)}{N(T_t) - 1}. \tag{4.7}$$

The node t with the α in the tree T is recursively pruned away as long as violating (4.7). Overtraing is managed by using the pruning method.

4.2 Boosting algorithm

As described before, a signal decision tree has instability for calssifier response due to statistical fluctuation in the samples. The boosting is a general procedure in which the same classifier is trained several times using a successively boosted (reweighted) training event sample. The final classifier is then derived from the combination of all the individual classifiers. The most popular boosting algorithm is "AdaBoost". This algorithm are used to overcome the problem which is one of the boosting algorithms.

In general, the training events that were misclassified during the training of a tree are given a higher event weights in the training of the next tree. This procedure is then repeated for the new tree, as a results many trees are built up. The score from the mth individual tree T_m is taken as $+1$ if the events falls on a signal leaf and -1 if the event falls on a background leaf. The final score is taken as a weighted sum of the scores of the individual leaves.

If there are N total events in the sample, the weight of each event is initially taken as $1/N$. Some notations are defined as the follows,

- x_i is the set of information (for example p_T or E_T) for the ith event
- $y_i = 1$ if the ith event is a signal event and $y_i = -1$ if the ith event is a background event
- w_i is the weight of the ith event
- $T_m(x_i) = 1$ if the set of information for the ith event lands that event on a signal leaf and $T_m(x_i) = -1$ if the set of information for that event lands it on a background leaf.
- $I(y_i \neq T_m(x_i)) = 1$ and $I(y_i = T_m(x_i)) = 0$

where m is index for Mth tree.

4.3 BDT training samples

The BDT discriminant is optimized to well separate between the higgs and the background, so-called "training". The signal training samples are the two leptons from Z decays for Z selection and higgs MC samples for higgs selection, as shown in Table 4.3. While background samples are residual-photon conversion events, and fake lepton events, which are derived from data samples. The training are performed by using each higgs mass sample with the main backgrounds, independently. These samples are passing the same selection criteria of likelihood analysis in §3.3-§3.4.

4.4 Input variales

The BDT is insensitive to the inclusion of poorly discriminating input variables. While for artificial neural networks it is typically more difficult to deal with such additional variables, the decision tree training algorithm will basically ignore non discriminating variables as for each node splitting only the best discriminating input variables is used. We have selected 9 variables to be used as the input variables to construct BDT discriminant.

- E/p

Mass (GeV/c^2)	$\sigma(p\bar{p}\to Wh)$ (fb)	$B_F(h_{\mathrm{FH}}\to WW)$	$B_F(h_{\mathrm{SM}}\to WW)$	Generated (Events)
110	216.0	0.87	0.04	4198567
120	159.0	0.88	0.12	4198567
130	119.0	0.88	0.27	4198567
140	90.2	0.89	0.47	4198567
150	68.9	0.90	0.68	4198567
160	53.1	0.97	0.92	4198567
170	41.3	0.98	0.97	4198567
180	32.4	0.94	0.94	4198567
190	25.5	0.94	0.94	4198567
200	20.3	0.94	0.94	4198567

Table 4.1: Higgs Monte Carlo samples. h_{FH} means fermiophobic higgs, while h_{SM} means Standard Model higgs.

- χ^2_{strip}
- χ^2_{wire}
- HA/EM
- L_{shr}
- $Q \times \Delta x_{\mathrm{CES}}$
- Δz_{CES}
- E_{CES}/p^*

A ranking of the BDT input variables is derived by couting how often the variables are used to split decision tree nodes, and by weighting each split occurrence by the separation gain-squared it has achieved and by the number of events in the node. Table 4.2 shows the variable ranking for the trained channel.

4.5 Distributions of the BDT outputs

We use the output of the BDT trained in the two types of training samples as discriminant for the signal events. The raw output of the BDTs are always in a range inside [-1, 1].

Figure 4.2–4.3 shows normalized BDT outputs distributions for signal and background samples, where the signal samples are Z, higgs MCs for the mass of 100 GeV/c^2, and 160 GeV/c^2. The signal training samples correspoond to each type of samples.

4.6 Efficiency

We estimate and compare the efficiecy between CLID and BDT in the same way as the LLID, see §3.6. The results are shown in Tables 4.3. Figure 4.4 compares the signal-efficiency vs. the background-efficiency curves for 3 samples: Z, higgs with the mass 110 GeV/c^2, and 160 GeV/c^2, for a given type of training, where the background sample is fixed to be the `Jet20`.

We confirm that the BDT is better than the CLID for electrons. Using the BDT trained by the higgs MCs showed better performance than using the BDT trained by the Z data to apply for higgs MCs.

4.7 Cut optimization

We compare the limits on the higgs production using the BDT trained by Z decays, and higgs MCs, as a cut value for the BDT outputs. The limits for the higgs MC of 110 GeV/c^2 and 160 GeV/c^2 are shown in Fig. 4.5. The best performance is obtained by using the BDT trained by the higgs MCs themselves.

4.8 Compare the performance between LLID and BDT

In this section, we compare the performance of efficiency reduction and limits on the higgs production using the LLID and BDT. We use the signal PDFs created from Z decays for selecting Z events, and the PDFs based on higgs MCs for higgs events selection. The BDT training samples are the same for LLID. The signal is the higgs MC of 110GeV/c^2 and background is `JT20`. The fake efficiency reduction using BDT is about 20% better than the LLID for Z selection. But, the fake reduction for the higgs selection is slightly worse than the LLID. Figure 4.6 is the limits with LLID and BDT. For the limit performance of LLID and BDT, we didn't see significant improvements from LLID for the higgs MC of 110GeV/c^2.

Rank	Variable	Importance
trained by Z		
1	lshr	2.761e-01
2	cpr	2.291e-01
3	hadem	2.284e-01
4	ecesop	9.003e-02
5	qdx	8.337e-02
6	eop	6.165e-02
7	dz	2.108e-02
8	chi2w	8.415e-03
9	chi2s	1.937e-03
trained by Wh110		
1	cpr	2.241e-01
2	ecesop	2.041e-01
3	eop	1.447e-01
4	hadem	1.173e-01
5	lshr	9.449e-02
6	qdx	7.737e-02
7	dz	7.272e-02
8	chi2w	3.412e-02
9	chi2s	3.117e-02
trained by Wh160		
1	ecesop	1.993e-01
2	cpr	1.659e-01
3	lshr	1.544e-01
4	eop	1.541e-01
5	hadem	1.334e-01
6	qdx	9.434e-02
7	chi2w	3.738e-02
8	dz	3.729e-02
9	chi2s	2.390e-02

Table 4.2: Variable ranking for BDT training.

Sample	Same background efficiency			Same signal efficiency		
	L cut	new el efficiency	improvement	L cut	new jt efficiency	reduction
JT20	-0.56	0.988 ± 0.0004	× 1.3	0.18	0.013 ± 0.0005	× 15
JT50	-0.44	0.971 ± 0.001	× 1.3	0.18	0.022 ± 0.001	× 7.3
JT70	-0.44	0.971 ± 0.001	× 1.3	0.18	0.030 ± 0.001	× 6.1
JT100	-0.42	0.968 ± 0.001	× 1.2	0.18	0.039 ± 0.001	× 5.1

	L cut	new wh110 efficiency	improvement	L cut	new jt efficiency	reduction
JT20	-0.56	0.818 ± 0.003	× 1.0	-0.50	0.146 ± 0.001	× 1.3
JT50	-0.44	0.749 ± 0.004	× 1.0	-0.50	0.192 ± 0.003	× 0.8
JT70	-0.44	0.749 ± 0.004	× 1.0	-0.50	0.214 ± 0.002	× 0.8
JT100	-0.42	0.737 ± 0.004	× 0.9	-0.50	0.238 ± 0.003	× 0.8

	L cut	new wh160 efficiency	improvement	L cut	new jt efficiency	reduction
JT20	-0.56	0.834 ± 0.003	× 1.1	-0.34	0.085 ± 0.001	× 2.2
JT50	-0.44	0.784 ± 0.003	× 1.1	-0.34	0.120 ± 0.002	× 1.4
JT70	-0.44	0.784 ± 0.003	× 1.1	-0.34	0.134 ± 0.002	× 1.3
JT100	-0.42	0.776 ± 0.003	× 1.1	-0.34	0.153 ± 0.002	× 1.3

Table 4.3: The efficiency performance for BDT trained by Z data samples. The signal samples are Z, the higgs MCs for the mass of 110 GeV/c^2 and 160 GeV/c^2.

Sample	Same background efficiency			Same signal efficiency		
	L cut	new wh110 efficiency	improvement	L cut	new jt efficiency	reduction
JT20	-0.60	0.887 ± 0.003	× 1.1	-0.48	0.079 ± 0.001	× 2.3
JT50	-0.56	0.864 ± 0.003	× 1.1	-0.48	0.101 ± 0.002	× 1.6
JT70	-0.56	0.864 ± 0.003	× 1.1	-0.48	0.112 ± 0.002	× 1.6
JT100	-0.54	0.851 ± 0.003	× 1.1	-0.48	0.131 ± 0.002	× 1.5

	L cut	new wh160 efficiency	improvement	L cut	new jt efficiency	reduction
JT20	-0.66	0.873 ± 0.002	× 1.2	-0.38	0.039 ± 0.001	× 4.7
JT50	-0.58	0.847 ± 0.003	× 1.2	-0.38	0.056 ± 0.002	× 2.9
JT70	-0.60	0.854 ± 0.003	× 1.2	-0.38	0.062 ± 0.001	× 2.9
JT100	-0.58	0.847 ± 0.003	× 1.2	-0.38	0.076 ± 0.002	× 2.6

Table 4.4: The efficiency performance for BDT trained by the higgs MCs themselves. The signal samples are the higgs MCs for the mass of 110 GeV/c^2 and 160 GeV/c^2.

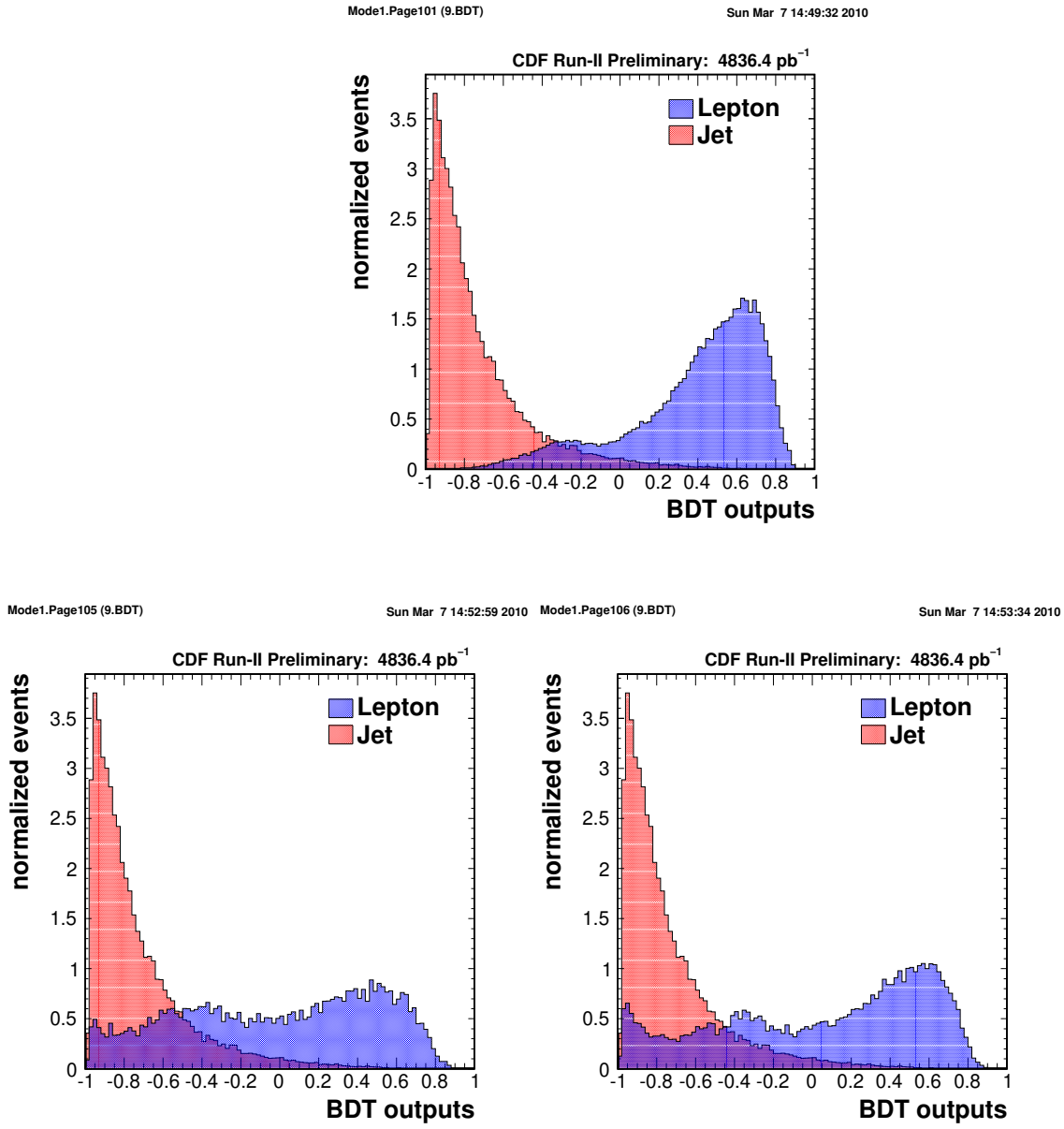

Figure 4.2: The BDT outputs distributions for leptons and fake leptons after normalized. These plots show the BDT outputs for electron from Z decays (top), Wh110 events (bottom-left), Wh160 (bottom-right), and Jet20 control samples. The training sample is Z.

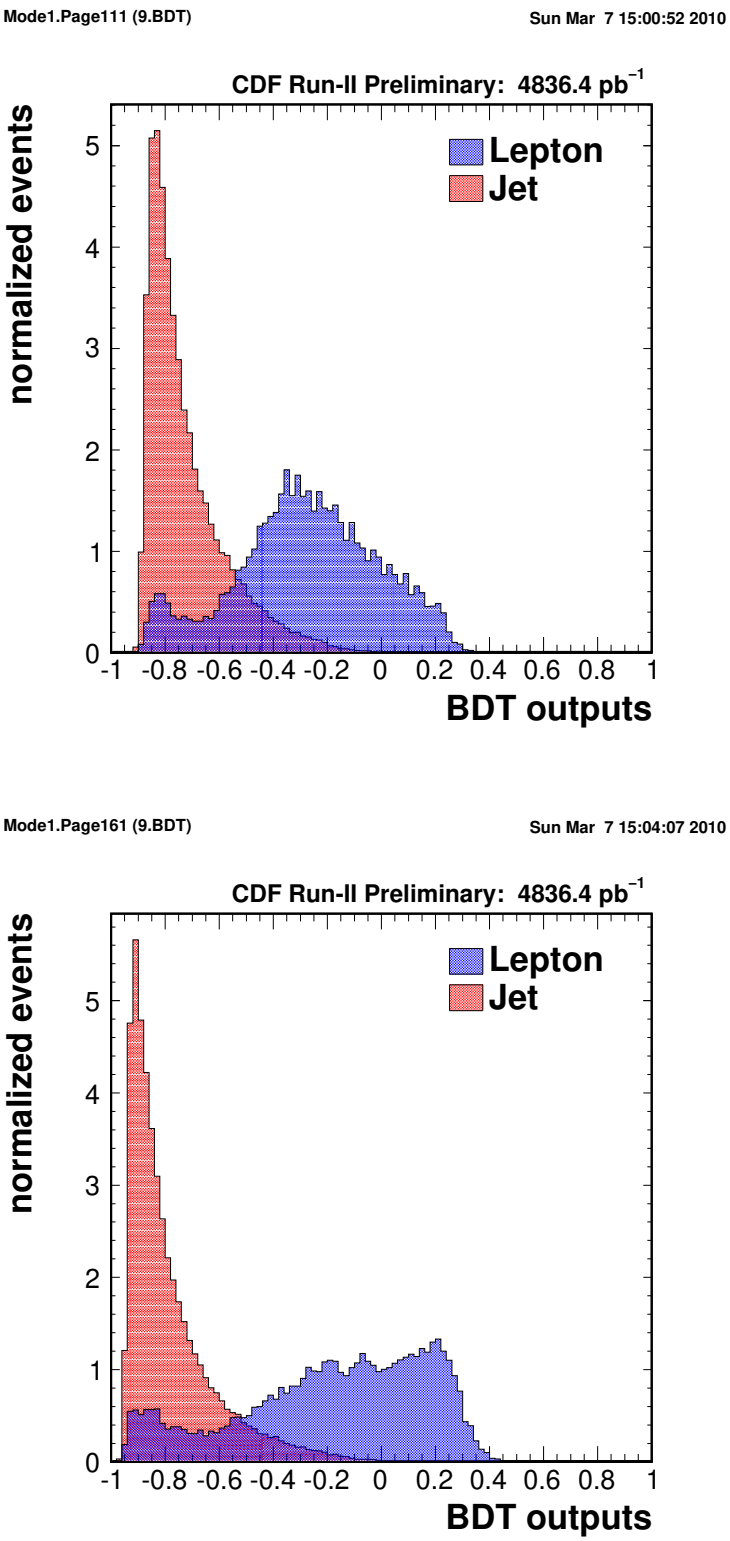

Figure 4.3: The BDT outputs distributions for leptons and fake leptons after normalized. These plots show the BDT outputs for Wh110 (top) and Wh160 (bottom) events using the signal training samples of the Wh110 and Wh160, respectively. The background sample is the `Jet20`.

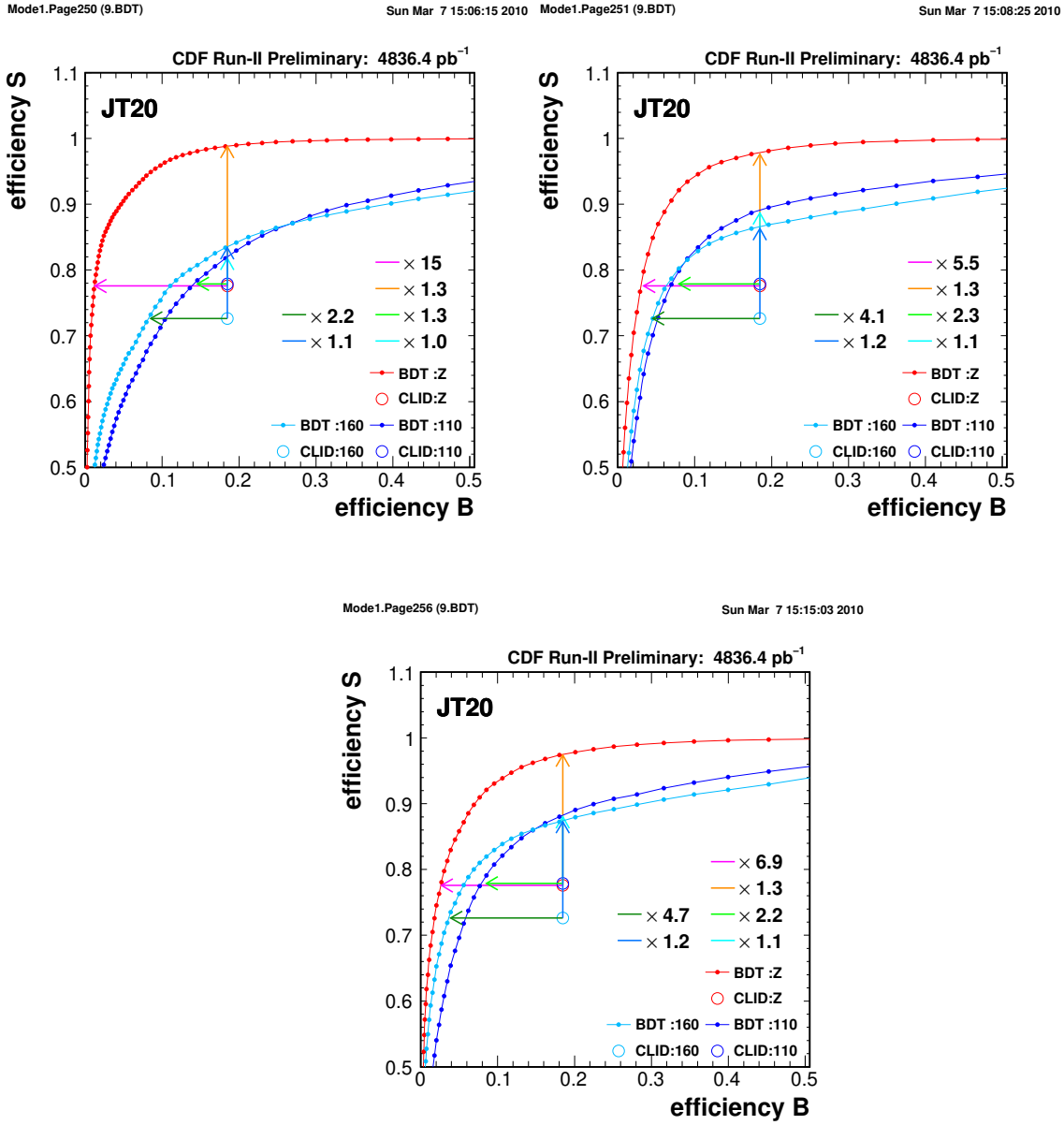

Figure 4.4: Efficiencies of BDT for Z electrons, Wh110, and Wh160 samples using the signal training sample of the Z decays (top-left), Wh110 (top-right) and Wh160 (bottom). The open dots are cut-based efficiency points respectivery. The signal effieiency improvements are indicated by the horizontal arrowed lines. The vertical arrowed lines shows the efficiency reductions of the background.

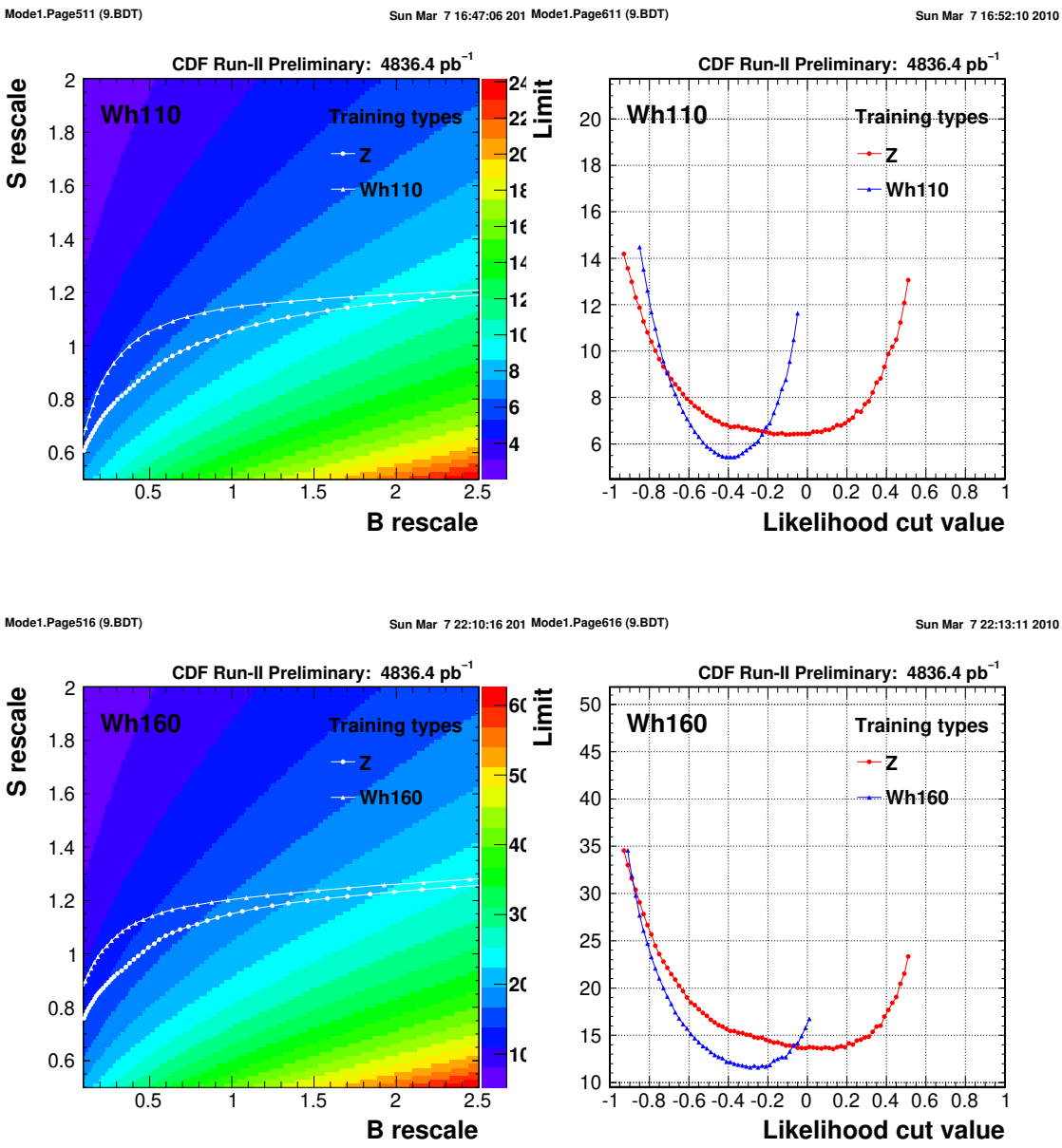

Figure 4.5: Limits for Wh110 (top) and Wh160 (bottom) samples using the BDT trained by Z and the higgs MCs themselves. The background sample is JT20.

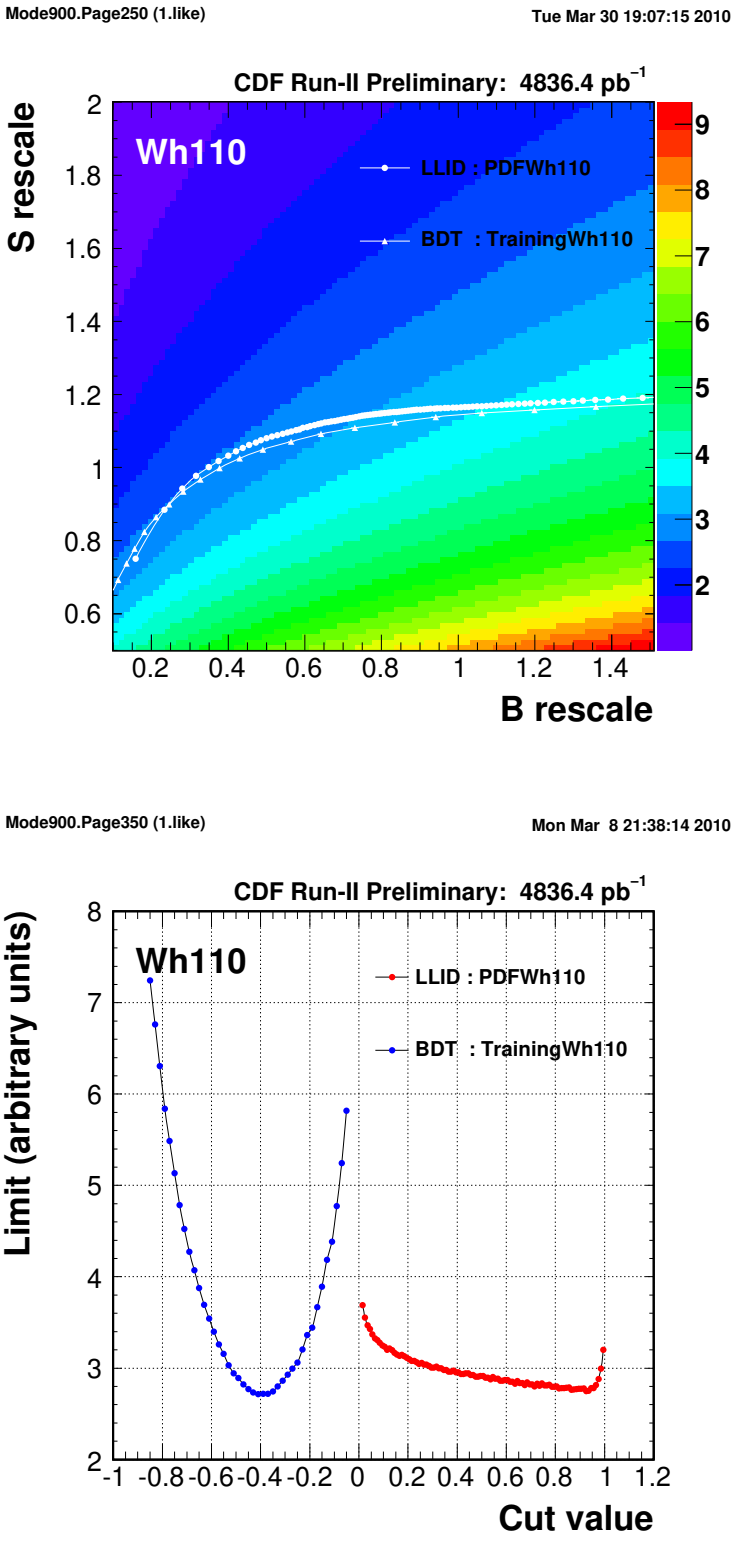

Figure 4.6: Limits for Wh110 sample using LLID and BDT. The background sample is JT20.

Chapter 5

Conclusion

We have developed a likelihood-based method for the electron and muon identification by using the normalized distributions of various identification variables as the probability distribution functions to be combined to form a single likelihood function. We investigated possible choices of the probability distribution functions for real leptons: Z decays, photon conversions for electrons, and higgs Monte Carlo events, while we used lepton candidates in inclusive jet samples as fake leptons. The likelihood-based lepton identification was found to be better than the cut-based lepton identification, especially for electrons. The probability distribution functions created from higgs Monte Carlo events showed the best performances for identifying leptons from higgs decays in terms of the limits on the production cross section. We try the BDT-based lepton identification trained by Z decays and higgs MCs for higgs selection. The background reduction using BDT-based electron identification is better than the likelihood-based electron identification for the Z selection, but no significant difference for the higgs MC with the mass 110 GeV/c^2.

The CDF experiment is also searching the neutral higgs boson using the other channels (total 7 channels) with several analysis techniques (Artificial Neural Network and Matrix Element) [24, 61, 62, 63, 65, 64]. The channels also set the upper limits on cross section, respectively. And the combined upper limits with the 7 channels using from 2.0 to 4.8 fb^{-1} data show more sensitivity to the Standard Model higgs comparing with the upper limit in the individual channel. In addition, the other experiment, so-called the DØ, in the Tevatron is also searching the SM higgs boson using 9 channels from 2.1 to 5.4 fb^{-1} data [27, 28, 31, 66, 67, 68, 68, 69, 70]. The both collaboration have reported the combined upper limits from 110 to 200 GeV/c^2 [71]. In that report, the SM higgs with 163–166 GeV/c^2 was excluded at 95% confidence level as shown in Figure 5.1. The mass range expected to be excluded is 159-168 GeV/c^2. The results has been updated since LEP results for the first time in about 5 years [19], and give us new knowledge for the SM higgs. The Tevatron will run in FY2010 and it will give us total the 6-8 fb^{-1} data, that also give us the hope to "discover" the higgs in the Tevatron.

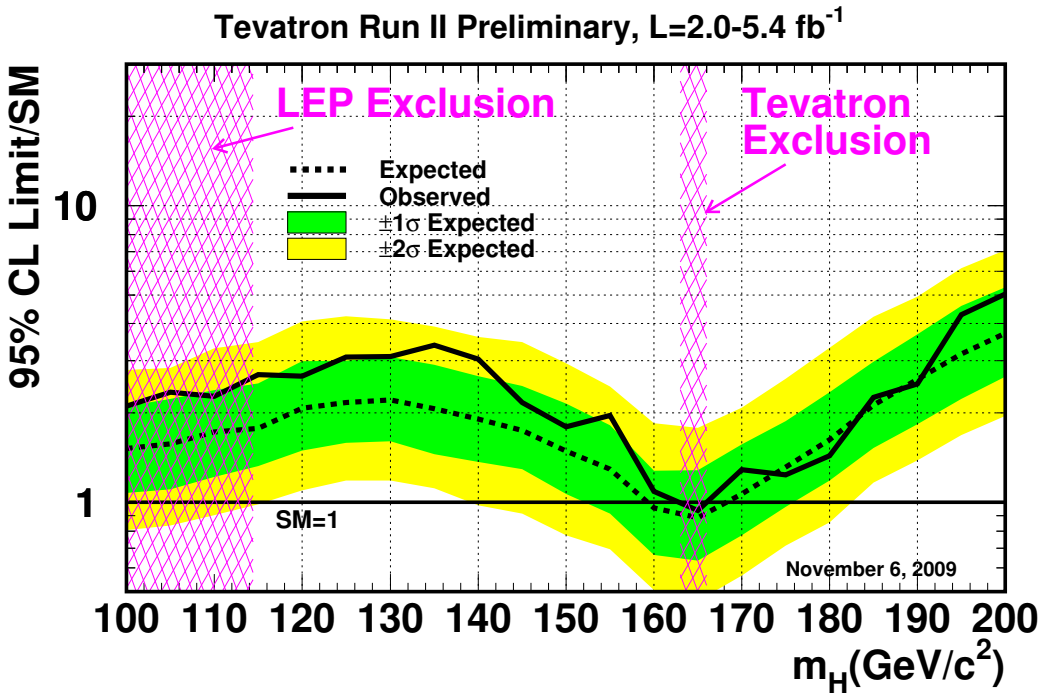

Figure 5.1: The ralative observed and expected upper limit on production cross section to SM prediction as a function of the higgs mass for the combined CDF and DØ results.

Bibliography

[1] I. Newton, "Philosophiae naturalis principia mathematica", ISBN 0674664752 (1833).

[2] A. Einstein, "On the Electrodynamics of Moving Bodies", Annalen der Physik **17** (1905) 891.

[3] A.Einstein, "Does the Inertia of a Body Depend upon its Energy-Content", Annalen der Physik **18** (1905) 639.

[4] C. Amsler *et al* (Particle Data Group), "Review of Particle Physics", Phys. Lett. B **667**, 1 (2008).

[5] F. Halzen and A.D. Martin, "Quarks and Leptons: An Introductory Course in Modern Particle Physics", ISBN 0-471-88741-2 (1984)

[6] S. Glashow, "Partial Symmetries of Weak Interactions", Nucl. Phys. 22 (1961) 579.

[7] S. Weinberg, "A Model of Leptons", Phys. Rev. Lett. **19** (1967) 1264.

[8] A. Salam, in "Elementary Particle Theory", ed N. Svartholm, Almqvist and Wiksells, Stockholm (1969) p.367.

[9] P.W. Higgs, "Broken Symmetries, Massless Particles and Gauge Fields", Phys. Lett. **12** (1964) 132-133.

[10] P.W. Higgs, "Broken Symmetries and The Masses of Gauge Bosons", Phys. Rev. **13** (1964) 508-509.

[11] P.W. Higgs, "Spontaneous Symmetry Breakdown without Massless Bosons", Phys. Rev. **145** (1966) 1156-1163.

[12] H.E. Haber, G.L. Kane, and T. Sterling, "THE FERMION MASS SCALE POSSIBLE EFFECTS OF HIGGS BOSONS ON EXPERIMENTAL OBSERVABLES", Nucl. Phys. B**161** (1979) 493-532.

[13] J.F. Gunion, H.E. Haber, G. Kane, and S. Dawson, "The Higgs Hunter's Guide", ISBN: 0-7382-0305-X (2000)

[14] J.F. Gunion and H.E. Haber, "CP-conserving two-Higgs-doublets model: The approach to the decoupling limit", Phys. Rev. D **67** (2003) 075019.

[15] M. Carena, J.S. Conway, H.E. Havber, and J.D. Hobbs, "Report of the Tevatron Higgs Working Group", arXiv:hep-ph/0010338.

[16] A. Djouadi, "The Anatomy of Electro-Weak Symmetry Breaking TomeI: The Higgs boson in the Standard Model", arXiv:hep-ph/0503172.

[17] P.C. Bhat, H.B. Prosper, and S.S. Snyder, "Top Quark Physics At The Tevatron", arXiv:hep-ex/9809011.

[18] The ALEPH, CDF, DØ, DELPHI, L3, OPAL, SLD Collaboration, the LEP Electroweak working Group, the Tevatron Electroweak Group, and the SLD electroweak ans heavy flavour groups, "Precision Electroweak Measurements and Constraints on the Standard Model", arXiv:0811.4682 [hep-ex]

[19] The LEP Higgs Working Group, ALEPH Collaboration, DELPHI Collaboration, L3 Collaboration, and OPAL Collaboration, "Search for the Standard Model Higgs boson at LEP", Phys. Lett. B **565** (2003) 61-75.

[20] The LEP Higgs Working Group, ALEPH Collaboration, DELPHI Collaboration, L3 Collaboration, and OPAL Collaboration, "Searches for Higgs Bosons Decaying into Photons: Combined Results from the LEP Experiments", LHWG Note 2002-02.

[21] CDF Collaboration, "Combined $WH \to \ell\nu b\bar{b}$ search with 2.7 fb^{-1} of CDF data", CDF Public Note 9596 (2008).

[22] CDF Collaboration, "A Search for $ZH \to \ell^+\ell^- b\bar{b}$ in 2.7 fb^{-1} using a Neural Network discriminant", CDF Public Note 9665 (2008).

[23] CDF Collaboration, "Search for the Standard Model Higgs boson in the $\not\!\!E_T$ plus jets sample", CDF Public Note 9642 (2008).

[24] CDF Collaboration, "Search for the Standard Model Higgs Boson in $H \to \tau\tau$ Channel at CDF Run II $\sim$ Simultaneous Search for $WH/ZH/\mathrm{VBF}/H$ Processes $\sim$", CDF Public Note 9248 (2008).

[25] CDF Collaboration, "Search for $H \to WW^*$ Production at CDF Using 3.0 fb^{-1} of Data", CDF Public Note 9500 (2008).

[26] CDF Collaboration, "Search for the Wh Production Using High-p_T Isolated Like-Sign Dilepton events in Run-II with 2.7 fb^{-1}", CDF Public Note 7307 (2008).

[27] DØ Collaboration, "Search for WH associated production using a combined Neural Network and Matrix Element Approach with 2.7 fb^{-1} Run II data", DØ Note 5828-CONF (2009).

[28] DØ Collaboration, "A Search for $ZH(\rightarrow e^+e^-b\bar{b})$ and $ZH(\rightarrow \mu^+\mu^-b\bar{b})$ Production with the DØ Detector in $p\bar{p}$ Collisions at $\sqrt{s} = 1.96$ TeV", DØ Note 5570-CONF (2008).

[29] DØ Collaboration, "A Search for the Standard Model Higgs Boson in the Channel $ZH\rightarrow\nu\bar{\nu}b\bar{b}$ at $\sqrt{s} = 1.96$ TeV", DØ Note 5506-CONF (2007).

[30] DØ Collaboration, "Search for the Higgs boson in $H\rightarrow WW(*)\rightarrow\ell\ell'\nu\nu$ $(\ell, \ell' = e, \mu)$ decays with 3.0 fb^{-1} at DØ in Run II", DØ Note 5757-CONF (2008).

[31] DØ Collaboration, "Search for the Associated Higgs Boson Production $p\bar{p}\rightarrow WH\rightarrow WWW^*\rightarrow\ell^{\pm}\nu\ell'^{\pm}\nu' + X$ at $\sqrt{s} = 1.96$ TeV", DØ Note 5485-CONF (2007).

[32] DØ Collaboration, "Search for the standard model Higgs boson in $\gamma\gamma$ final states at DØ" DØ Note 5737-CONF (2008).

[33] Tevatron New Phenomena, Higgs working group, CDF Collaboration, DØ Collaboration, "Combined CDF and DØ Upper Limits on Standard Model Higgs Boson Production at High Mass (155-200 GeV/c^2) with 3 fb^{-1}" arXiv:hep-ex/0808.0534 (2008)

[34] T. Affolder, *et al*, The CDF Collaboration, "Search for narrow diphoton resonances and for $\gamma\gamma + WZ$ signatures in $p\bar{p}$ collisions at $\sqrt{s} = 1.8$ TeV", Phys. Rev. D **64** (2001) 092002.

[35] B. Abbott, *et al*, The DØ Collaboration, "Search for Nonstandard Higgs Bosons Using High Mass Photon Pairs in $p\bar{p}\rightarrow\gamma\gamma + 2$ Jets at $\sqrt{s} = 1.8$ TeV", Phys. Rev. Lett. **82** (1999) 11.

[36] CDF Collaboration, "Search for a Fermiophobic Higgs Boson with the Diphoton Final State at CDF", CDF Public Note 9586 (2008),

[37] DØ Collaboration, "Search for Fermiophobic Higgs Boson in $3\gamma + X$ Events", DØ Note 5067-CONF (2007).

[38] The CDF II Collaboration, "The CDF II Detector Technical Design Report", FERMILAB-Pub-96/390-E (1996).

[39] T.K. Nelson *et al*, "The CDF Layer 00 Detector", FERMILAB-CONF-01/357-E (2001).

[40] C.S. Hill *et al*, "Initial experience with the CDF layer 00 silicon detector", Nucl. Instrum. and Meth. A **511** (2003) 118-120.

[41] A. Sill *et al*, "CDF Run II silicon tracking projects", Nucl. Instrum. and Meth. A **447** (200) 1-8.

[42] W. Ashmanskas *et al*, "The CDF silicon vertex trigger", Nucl. Instrum. and Meth. A **518** (2004) 532-636.

[43] A. Affolder *et al*, "Status report of the Intermediate Silicon Layers detector at CDFII", CDF Public Note 5687 (2001).

[44] A. Affolder *et al*, "Intermediate silicon layers detector for the CDF experiment", Nucl. Instrum. and Meth. A **453** (2000) 84-88.

[45] T. Affolder *et al*, "CDF Central Outer Tracker", CDF Public Note 6267 (2003).

[46] L. Balka *et al*, "The CDF Central Electromagnetic Calorimeter", Nucl. Instrum. Meth. A **267**, 272 (1988).

[47] S. Bertolucci *et al*, "The CDF Central and Endwall Hadron Calorimeter", Nucl. Instrum. Meth. A **267**, 301 (1988).

[48] S. Lami *et al* "The CDF calorimeter upgrade for Run IIb", Nucl. Instrum. Meth. A **518** (2004) 39-41.

[49] Y. Seiya *et al*, "The CDF plug upgrade electromagnetic calorimeter test beam results", Nucl. Instrum. Meth. A **480** (2002) 524-546.

[50] D. Acosta *et al*, "The CDF Cherenkov luminosity monitor", Nucl. Instrum. Meth. A **461** (2001) 540-544.

[51] D. Acosta *et al*, "The performance of the CDF luminosity monitor", Nucl. Instrum. Meth. A **494** (2002) 57-62.

[52] B. Rossi, High-Energy Particles, Prentice-Hall.

[53] L.Breiman, J.H.Friedman, R.A.Olshen and C.J.Stone "Classification and regression trees", ISBN: 0-412-04841-8

[54] H.Yang, B.P.Roe and J.Zhu. "Studies of Boosted Decision Trees for MiniBooNE Particle Identification", arXiv:physics/0508045

[55] R.Brun *et al*, "ROOT An Object-Oriented Data Analysis Framework: Users Guide 5.20", (2008)

[56] A.Hocker, P.Speckmayer, J.Stelzer, F.Tegenfeldt, H.Voss, and K,Voss, "TMVA Toolkit for Multivariate Data Analysis with ROOT Users Guide".

[57] K.A.Assamgan *et al*, "THE HIGGS WORKING GROUP: Summary Report", hep-ph/0406152v1.

[58] J.M. Campbell and R.K. Ellis, "An update on vector boson pair production at hadron colliders", Phys. Rev. D **60** 113006 (1999).

[59] A. Bhatti *et al*, "Determination of the Jet Energy Scale as the Collider Detector at Fermilab", hep-ex/0510047v1.

[60] CDF Collaboration, D. Acosta, *et al*, "Search for Electroweak single-top-quark production in $p\bar{p}$ collisions at $\sqrt{s} = 1.96$ TeV", Phys. Rev. D **71**, 012005 (2005).

[61] CDF Collaboration, "Combined $WH \to \ell\nu b\bar{b}$ search with 2.7 fb^{-1} of Data", CDF Public Note 9596 (2008).

[62] CDF Collaboration, "Search fof the Standard Model Higgs Boson in the $\not\!\!E_T$ Plus Jets Sample", CDF Public Note 9642 (2008).

[63] CDF Collaboration, "Search for $ZH \to \ell^+\ell^- b\bar{b}$ in 2.7 fb^{-1} using Neural Network Discriminant", CDF Public Note 9665 (2009).

[64] CDF Collaborationn, "Search for $H \to WW^*$ Production Using 3.6 fb^{-1} of Data", CDF Public Note 9500 (2009).

[65] CDF Collaboration, "A Search for the Standard Model Higgs Boson in the All-Hadronic channel using a Matrix Element Method", CDF Public Note 9366 (2008).

[66] DØ Collaboration, "Search for the standard model Higgs boson τ final states", DØ Note 5883-CONF (2009).

[67] DØ Collaboration, "Search for the standard model Higgs boson in the $HZ \to b\bar{b}\nu\bar{\nu}$ channel in 2.1 fb^{-1} of $p\bar{p}$ collision at $\sqrt{s} = 1.96$ TeV", DØ Note 5586-CONF (2008).

[68] DØ Collaboration, "Search for Higgs production in dilepton plus missing energy final states with 3.0-4.2 fb^{-1} of $p\bar{p}$ collisions at $\sqrt{s} = 1.96$", DØ Note 5871-CONF (2009).

[69] DØ Collaboration, "Search for the standard model Higgs boson in $\gamma\gamma$ final states at DØ with $L = 4.2$ fb^{-1}", DØ Note 5846-CONF (2009).

[70] DØ Collaboration, "Search for the Standard Model Higgs boson in the $t\bar{t}H \to t\bar{t}b\bar{b}$ channel", DØ Note 5739-CONF (2009).

[71] The TEVNPH Working Group, CDF Collaboration and DØ Collaboration, "Combined CDF and D0 Upper Limits on Standard Model Higgs-Boson Production with 2.1 - 5.4 fb^{-1} of Data" arXiv:hep-ex/09113930.